ABSTRACT

Title of Document: A SCANNING SQUID MICROSCOPE FOR IMAGING HIGH-FREQUENCY MAGNETIC FIELDS

Constantine P. Vlahacos, PhD, 2009

Directed By: Professor Frederick C. Wellstood
Department of Physics

This thesis examines the design and operation of a large-bandwidth scanning SQUID microscope for spatially imaging high frequency magnetic fields. Towards this end, I present results on a cryo-cooled 4.2 K scanning SQUID microscope with a bandwidth of dc to 2 GHz and a sensitivity of about 52.4 nT per sample. By using a thin-film hysteretic Nb dc-SQUID and a pulsed sampling technique, rather than a non-hysteretic SQUID and a flux-locked loop, the bandwidth limitation of existing scanning SQUID microscopes is overcome. The microscope allows for non-contact images of time-varying magnetic field to be taken of room-temperature samples with time steps down to 50 ps and spatial resolution ultimately limited by the size of the SQUID to about 10 μm.

The new readout scheme involves repeatedly pulsing the bias current to the dc SQUID while the voltage across the SQUID is monitored. Using a fixed pulse amplitude and applying a fixed dc magnetic flux allows the SQUID to measure the applied magnetic flux with a sampling time set by the pulse length of about 400 ps.

To demonstrate the capabilities of the microscope, I imaged magnetic fields from 0 Hz (static fields) up to 4 GHz. Samples included a magnetic loop, microstrip

transmission lines, and microstrip lines with a break in order to identify and isolate electrical opens in circuits.

Finally, I discuss the operation and modeling of the SQUID and how to further increase the bandwidth of the microscope to allow bandwidth of upwards of 10 GHz.

A SCANNING SQUID MICROSCOPE FOR IMAGING HIGH-FREQUENCY MAGNETIC FIELDS

By

Constantine P. Vlahacos

Dissertation submitted to the Faculty of the Graduate School of the
University of Maryland, College Park, in partial fulfillment
of the requirements for the degree of
Doctor of Philosophy
2009

Advisory Committee:
Professor Frederick C. Wellstood, Chair
Professor Isaak D. Mayergoyz
Professor Romel Gomez
Professor Christopher Lobb
Professor Bryan Eichhorn

Εἰς μνήμην τοῦ πατρός μου

Παναγιώτης Βλαχάκος

Acknowledgements

It may not come as a surprise to anyone, but research is very much a social activity and as such your success depends on the people you interact with. It is strongly influenced by people who may or may not be part of your project or for that matter your lab. By asking a lot of questions and seeking advice I have often received constructive criticism, complaints, clever observations, or assistance which resulted in not only improving my research but more often than not I walked away having learned something new. This dissertation would not have been possible without the help and patience of many people.

There are several people that I would like to acknowledge that have helped me professionally. At the University the person I would like to thank most is my advisor Professor Fred Wellstood whose guidance in everything that he has given me for the many years that I have been at the University. Under Fred's guidance I have built or help to build several scanning probe microscopes, starting with the scanning microwave microscope and ending with the current scanning SQUID microscope that I address in this thesis. At the Laboratory for Physical Sciences I would like to thank my supervisor William Vanderlinde for all his help, unwavering support and patience. Also, I would like to thank Dr. Marc Manheimer, Dr. Kevin Osborn and Dr. Marshall Saylors all at LPS for their advice and generosity to loan me equipment for extended periods of time.

I would like to thank my dissertation committee members, Professors Isaac Mayergoyz, Mel Gomez, Christopher Lobb, and Brian Eichhorn for taking time to read and comment on my thesis. I would like to thank Professor Isaac Mayergoyz for his

guidance and support while I have been a graduate student in the Electrical Engineering department.

I would like to thank the Center for Nanophysics and Advanced Materials which provided a generous and stimulating environment during my stay at the center. In particular I would like to thank Professor Richard Greene. I particularly learned a lot by giving talks and having to explain my work to others in his seminar. I would like to especially thank Professor Steven Anlage for introducing me to microwave microscopy and for his advice and discussions on superconductivity and microwave technology. I would like to thank Professor Christopher Lobb for guidance, support and friendship over the years that I have been at the University.

I would like to thank colleagues and collaborators at Neocera, Inc., who greatly contributed to the 4 K SQUID microscope project. In particular, I thank Dr. Lee Knauss and Dr. Antonio Orozco and the people at Neocera for being very gracious hosts during my time on site working on the microscope.

I would like to thank some of the people I worked closest with. John Matthews and Dr. Soun Pil Kwon both got me stated in working on this microscope and I deeply appreciate their help and advice. I especially thank John for all his help concerning Josephson device physics and writing wonderful software with Labview.

Current students in the subbasement that I am indebted to and would like to thank are Benjamin Cooper, Tony Przybysz and Hyeokshin Kwon. I would like to thank Ben who is always helpful with advice, loaning equipment and an excellent sounding board for ideas, and Tony and Hyeokshin for bringing new ideas and energy into the lab.

Other former students at the Center also helped with important advice and discussion. Dr. Andrew Berkley gave insightful observations and suggested changes in experimental design. Dr. Hanhee Paik offered friendship and useful advice from her experience working on the room temperature scanning SET microscope. I especially want to thank Dr. Sudeep Dutta whom I have known for many years for his always helpful advice on microwave microscopy, SQUIDs, quantum computing and excellent companionship in the lab. I thank Dr. Tauno Palomaki for his advice concerning timing measurements on Josephson junction devices. I also thank Drs. Rupert Lewis and Roberto Ramos who were always available with advice and especially to Rupert who gave me the microwave coaxial lines for my initial proof of concept experiment in a liquid helium dewar.

There are several former students and colleagues I would like to acknowledge who assisted in training me and allowed use of their equipment. I would like to thank Dr. Randy Black whom I originally worked with in Fred's lab. Randy helped on the early room temperature SQUID microscope and microwave microscope. His helpful advice on SQUIDs and all things mechanical is truly appreciated. I thank Dr. Ajay Amar who taught me the how to properly use a leak detector and for his advice and craftsmanship. I would like to thank Dr. Sojiphong Chatraphorn for his great friendship and conversation, and being a good lab partner in the same corner of the lab. I would like to thank Dr. Erin Fleet for his friendship and his advice concerning mechanical design. I have greatly benefited from their experience in scientific prototype design. I would like to thank Dr**.** Su-Young Lee for advice on building scanning SQUID microscopes.

I would like to thank the technical and support staff of the Center for Nanophysics and Advanced Materials. In particular, both Doug Benson and Brian Straugn helped me solve a wide array of technical problems such as the evaporation system, computer software and networking, machining parts, and other things I would throw at them. I would like to extend a very heartfelt thank you to both of them. I would like to thank Belta Pollard, Cleopatra White, and Grace Sewall for all the bureaucratic red tape and paperwork they have handled for me over the years so I could get my work done.

I would like to thank the technical staff of the Physics Department. I would like to especially thank Jack Touart for his excellent help and advice in electronics and allowing me to use many of the Electronic Development Group's equipment. I would like to thank Mr. Russell Wood, a former member of the technical staff of the Physics Department, for his excellent management of the student shop. He provided an excellent shop to allow me to efficiently construct the apparatus for my experiments. His advice on machining and designing scientific apparatus is truly appreciated.

I would like to thank the support staff of the Physics Department. I thank Mr. Robert Dahms and Mr. Jesse Anderson for helping me order equipment and making purchases times on short notice. I thank Mr. Al Godinez for helping me with all my liquid helium orders and hunting me down when the Air Products truck would arrive with a delivery.

Finally, I would like to thank my wife Sophia for her help, support and patience, as well as our daughters Lia and Irene who have brought much happiness to our lives. Finally, I would like to thank my mother for her support and confidence, and I dedicate this thesis to the loving memory of my father, Mr. Peter Vlahacos.

Table of Contents

List of Tables

List of Figures

List of Commonly Used Abbreviations

Symbols used throughout the thesis are listed below.

Fundamental constants

h	Planck's constant, 6.626×10^{-34} J · s
$\hbar$	$h/2\pi$, 1.054×10^{-34} J · s
e	absolute value of the electron charge, 1.602×10^{-19} C
Φ_0	magnetic flux quantum, $h/2e$=2.068×10^{-15} T · m^2
k_B	Boltzmann's constant, 1.381×10^{-23} J/K
ε_0	vacuum permittivity, 8.854×10^{-12} F/m
μ_0	vacuum permeability, $4\pi\times10^{-7}$ H/m
c	speed of light in vacuum, 2.997925×10^{8} m/s

Notation

$\boldsymbol{v}$	vector
$\dot{g}$	derivative of g with respect with time

Junction parameters and controls

γ	Gauge invariant phase difference across a superconducting junction
I_b	bias current
I_0	critical current
V	junction voltage
C_1	capacitance for junction #1
C_2	capacitance for junction #2
ω_p	plasma frequency
β_c	Stewart-McCumber hysteresis parameter
R	shunting resistance
Q	quality factor

SQUID parameters

I_b	total bias current
I_{01}	critical current of junction #1
I_{02}	critical current of junction #2
J	circulating current
Φ_A	applied flux due to current flowing in SQUID modulation coil or sample
Φ_T	total flux due to I_b, any applied magnetic field, and circulating current
L	geometrical inductance of SQUID loop
β	modulation parameter, $L(I_{01}+I_{02})/\Phi_0$
$\vec{\mathbf{B}}_z(x,y,t)$	Magnetic field as a function of position and time

Chapter 1: Introduction

1.1 Scanning Probe Microscopy

Optical microscopy is ubiquitous throughout science and engineering, but makes use of only a narrow band of the electromagnetic spectrum, mainly the visible spectrum. The much longer-wavelength radio-frequency and microwave regime of the electromagnetic spectrum still are relatively unexplored via microscopic techniques. This suggests that a microscope operating in the microwave band would be of scientific and technological interest and a variety of such systems have been built in the last decade or two [1-5].

The use of long wavelengths in microscopy poses certain challenges. The main challenge is that the spatial resolution of a conventional optical microscope is limited by the classical Abbé diffraction limit [6] to approximately $\lambda/2$, where λ is the wavelength of light used. This limit affects conventional optical systems ranging from astronomical telescopes to optical microscopes. The Abbé limit arises from the behavior of light propagating over distances much greater than a wavelength. This region is known as the "far field".

One approach that enables a microscope to operate below the Abbé limit is to give up the use of far-field optics and accept line by line or raster scanned image acquisition in the near field. In the near-field or Fresnel region [7], the field pattern differs substantially from that observed in the far field. The possibility of sub-diffraction limit resolution was first recognized as early as 1928 by Synge [8], who proposed that a sub-wavelength

aperture could be used to confine optical fields. This technique reached fruition in the 1980's with the development of scanning-probe microscopy.

A scanning-probe microscope (SPM) measures an interaction between a small probe and the surface of a sample. The essential feature of all scanning-probe microscopes is that the measurement is performed with a probe in the near field of the sample. Ideally, the probe is scanned over a surface while the probe-sample distance is kept constant. High spatial resolution is achieved by using a very sharp probe and scanning the probe very close to the surface to take advantage of the strong spatial dependence of the probe-sample interaction at close range.

Probes have been designed to measure many physical quantities of interest [9]. The scanning tunneling microscope or STM was the first true SPM that reached atomic resolution [10]. The STM measures surface topography and electron density by utilizing the exponential dependence of the tunneling current on the height of a very sharp conducting tip above a conducting sample. Gerd Binning and Heinrich Roher invented the STM, and in 1986 they received the Nobel Prize in Physics for their work [10]. Many SPMs have followed since the inception of the STM, including:

(1) the atomic-force microscope (AFM) [11,12], which measures the force between a sample and sensing tip. AFM's also routinely reach atomic resolution.

(2) the scanning near-field optical microscope (NSOM) [13,14] is capable of resolving details smaller than the diffraction limit. This is accomplished by passing light down a coated fiber optic transmission line that is tapered to an extremely fine tip at one end. Only the very end of the optical fiber

is left uncoated with metal and hence serves as the aperture of the NSOM. Typically, light is confined to a spot size of approximately 50-100 nm in diameter. When the light exits the fiber, it is absorbed or reflected locally and the resulting scattered or transmitted light is monitored as the tip is moved.

(3) the magnetic-force microscope (MFM) [15,16] measures the magnetic force between a sharp magnetized probe and a scanned surface. MFMs can have a spatial resolution as low as about 25 nm and can resolve field changes as small as a few hundred gauss.

Many other types of scanning probes have been developed. Table 1.1 summarizes the spatial and electromagnetic field resolution for various SPM techniques currently employed.

I should note that some techniques that breach the diffraction limit are quite old. Consider for a moment the common medical binaural stethoscope that originated in the early 1850's. With a stethoscope, the position of a beating heart can be localized to within about 10 cm. For an audio frequency of 30-100 Hz and a speed of sound in water of ~1500 m/sec, the corresponding wavelength is about 15 m. Thus, the common stethoscope has a corresponding resolution of $\lambda/150$! Bearing this in mind, we ask what affects the resolution of the stethoscope? First, the small size of the stethoscope probe compared with the wavelength, and second the distance between the object and the stethoscope is small compared to the wavelength. Therefore, we can expect either the aperture size or probe-sample distance will limit a stethoscope's resolution, whichever is greater. This is a typical feature of practically all scanning probe microscopes.

Table 1.1: Summary of various scanning probe microscopy techniques.

Technique	***Resolution***	***Physical Property***
Scanning Tunneling Microscope (STM) [10]	atomic	topography and electron density
Atomic Force Microscope (AFM) [11,12]	atomic	topography
Near-field Scanning Optical Microscope (NSOM) [13,14]	20 nm	optical absorption and reflection
Magnetic Force Microscope (MFM) [15,16]	25 nm	magnetic field (100 Gauss)
Electron Microscopy		
Scanning Electron Microscope (SEM) [17]	20 nm	topography, voltage, structure, composition
Lorentz Force Microscope [18]	100 nm	magnetic field
HRTEM [19]	atomic	crystal structure, composition
Electron Holography [20]	10 nm	magnetic flux (fraction of Φ_0)
Kerr Microscopy [21,22]	few μm	magnetic field, 10 T, real-time imaging
Optical Microscopy [23]	0.2 μm	optical-infrared absorption and reflection
Localized Energy Deposition [24,25]	few mm	property with temperature or photographic variation
Microwave AFM [26,27]	25 nm	microwave power: 0-40 GHz
Microwave Mixing STM [28-31]	25 nm	microwave power: 0-40 GHz
Near-field Scanning Microwave Microscope [32,33]	1 μm	0-12 GHz, surface impedance, power
SQUID [34]	few μm	B-field, 20 $pT/\sqrt{Hz}$ 0-200 GHz, microwave power, conductivity
Bolometer [35]	few μm	microwave-optical absorption and reflection
Single Electron Transistor (SET) Microscope [36]	100 nm	electric field, 10^{-2} e/Hz
Electric Force Microscope [37]	25 nm	100 e's
Scanning Capacitance Microscope (SCaM) [38]	25 nm	capacitance, sensitivity, 10^{-19} F

With SQUID microscopy we can "view" the "sub-visible" region of the electromagnetic spectrum with high resolution. A wide variety of phenomena can be imaged, including magnetic properties of materials, eddy current imaging of metal parts for the purpose of nondestructive evaluation, and IC circuit operation in the MHz-GHz regime [9].

1.2 A Brief Introduction to SQUIDs and SQUID Microscopy

The Superconducting QUantum Interference Device (SQUID) was invented by R. C. Jaklevic *et al.* in 1964 [42-44]. Since its inception the SQUID has been used in a variety of measurements in physics, electrical engineering and materials research [45-48].

In a scanning superconducting quantum interference device microscope [39], the SQUID acts as an extremely sensitive, approximately point-like, near-field detector of magnetic field. The output from the SQUID is recorded as a sample is moved back and forth under the SQUID, and the resulting data can be used to construct an image of weak magnetic fields from the sample. To be precise the SQUID measures a component of the magnetic field near the surface of the sample. Magnetic field images of a surface that is carrying currents may be further converted into an image of the source currents [40,41].

As mentioned earlier the probe (in my case the SQUID) must be brought nearly in contact with the object generating the field in order to measure the field at maximum strength and with the best spatial resolution. Although the total magnetic field at any point is a sum of the field from all sources, as the distance between the SQUID and an object decreases, the relative importance of more distant field generating sources decreases. As long as the separations between sources are much larger than the size of the

SQUID and the distance between the SQUID and the object surface, then the field may be considered as emanating primarily from local sources. Further, reducing the SQUID sample separation maximizes the measured field strength. Typically, by maximizing the magnetic field strength we maximize the signal to noise ratio (SNR). Increasing the SNR provides for a more precise magnetic field measurement and potentially reduces the overall scanning time. Also, if the field image is used to derive the source image, the uncertainty in the resulting current density will be smaller for a given SNR [40].

The main commercial application of SQUID microscopes is in failure analysis for locating faults in semiconductor microelectronic circuits and multi-chip modules. Images of the source currents can be generated by applying a magnetic inverse technique to the magnetic field images [40,41]. However, advances in microelectronics in the last two decades have made detecting and diagnosing circuit failures technologically important but more challenging. Consider that in present-day integrated circuits, submicrometer line widths and clock speeds in the 2 GHz to 3 GHz range are common. Currently available SQUID microscopes [34] are incapable of imaging or detecting such high-speed signals. Typically, for SQUID microscopy of integrated circuits, single circuit leads are individually activated in the audio range to help differentiate between densely packed circuit elements; i.e. the circuit speeds are artificially slowed down to allow the SQUID electronics to follow the changing magnetic field. Unfortunately, many failure mechanisms only reveal themselves while working under normal operating conditions. Thus, there is a need for high spatial and temporal resolution in circuit failure analysis.

Despite recent advances, the bandwidth of SQUID systems has not exceeded about 100 MHz [55-57]. This limitation is rooted in the feedback electronics used to

monitor the SQUID and not in the SQUID itself. Increasing the SQUID bandwidth to allow imaging from 0 to 3 GHz is desirable since it would enable images to be obtained at the operating speed of current processors. From such images the location and cause of certain types of faults may be determined.

1.3 Statement of the Problem

Currently available SQUID microscopes are limited to detecting magnetic fields of about 1 MHz or less. This could be extended to about 100 MHz if the fastest reported feedback electronics [55-57] was used. However, a bandwidth of 1 GHz or larger is required to image weak magnetic fields from a chip while logic operations are being performed on a nanosecond time scale.

In this thesis I describe a new method for sampling a periodic, time-varying magnetic field using a cryo-cooled hysteretic dc-SQUID [59,59]. This approach eliminates the conventional flux-locked loop electronics [60], and instead uses a pulsed sampling method to acquire data, similar to that used in sampling oscilloscopes. Using this technique, I demonstrate the imaging of magnetic fields up to 3 GHz from room temperature samples. The system achieves a spatial resolution of about 200 μm, limited by separation from sample, and a flux resolution of about $1.9\,\mu\Phi_0/\sqrt{Hz}$. Finally, I note that it may be possible to extend this bandwidth to over 10 GHz through hardware modifications.

1.4 Overview of Thesis

This thesis is comprised of ten chapters. In chapter 2, I give an introduction to scanning SQUID microscopy and discuss some of the principal applications of SQUID

microscopes including failure analysis, measuring magnetic properties of materials, and nondestructive evaluation. In Chapter 3, I give a basic introduction to superconductivity and then discuss the physics of Josephson junctions. I proceed to discuss the [resistively and capacitively shunted] (RCSJ) model for the Josephson junction. This leads into an introduction of basic SQUID physics and electronics. Finally, I review properties of the dc SQUID that are relevant to scanning SQUID microscopy.

In chapter 4, I describe dc SQUID design criteria for high speed and the hysteretic dc SQUIDs that I used in the fast switching experiments. In chapter 5, I cover basic considerations and limitations of the flux-locked loop. I then describe the use of a hysteretic dc SQUID with pulse bias current sampling and its use in a large bandwidth SQUID microscope.

Chapter 6 describes the design and construction of the 4 K cryocooled scanning SQUID microscope. I describe the 4 K cryocooled refrigerator and subsystems, such as the Kevlar suspended cold finger, thermal anchoring, vibration isolation, vacuum apparatus, and scanning mechanism.

In chapter 7, I describe how I simulate the response of a SQUID to a rapidly varying flux signal. The simulation was used to model the critical current versus magnetic flux modulation and SQUID and pulse signal characterization. These simulations are important because they let me estimate the ultimate measurement bandwidth of the microscope.

In chapter 8, I review the basic properties of electromagnetic wave propagation along transmission lines and discuss how I simulated images of circuits at microwave frequencies.

In chapter 9 I describe magnetic field images I obtained from various samples from dc to 3 GHz. These samples include a magnetic loop and microstrip transmission line. I also imaged various sized gaps in a microstrip line to simulate the behavior of open lines in IC circuits. I then compared the imaged test circuits with numerical simulations and use the results to estimate the bandwidth of the microscope. Finally, in chapter 10 I summarize my results and I conclude with comments and suggestions as to possible improvements in future systems.

Chapter 2: SQUID microscopy and Applications

2.1 Scanning SQUID Microscopy

At present the Superconducting Quantum Interference Device (SQUID) and the Spin Exchange Relaxation-Free (SERF) magnetometer [1] are the most sensitive known magnetic field sensing techniques. Compared to a SERF magnetometer, however, a SQUID can achieve a given field sensitivity in a much smaller pick-up area. The combination of small size and high field sensitivity is exploited in the SQUID microscope to create spatially resolved images of very weak magnetic fields.

Scanning SQUID microscopy is performed by raster-scanning a sample under a SQUID and converting the SQUID output signal into a false-color image of a component of the magnetic field [2-8]. Although some imaging at rf and microwave frequencies has been reported [4], the great majority of images are of static or audio-frequency magnetic fields.

A wide variety of samples have been examined in SQUID microscopes over the last decade. SQUID microscopes have been applied to research in biomagnetism [9-10], corrosion detection [11-12], magnetism [13], and non-destructive evaluation [11,14]. SQUID microscopes have also been used for fundamental studies of superconductivity and have been crucial in resolving the d-wave nature of high-T_c superconductors, such as $YBa_2Cu_3O_7$ [15-17]. The application that my research concerns is electrical fault detection in integrated circuits and circuit packages [18-23].

Fig. 2.1. Magma C30 scanning SQUID micro microscope used for failure analysis of integrated circuits and multichip modules (Neocera, Inc.) [24].

The detection of electrical faults in semiconductor circuits is the main commercial applications of SQUID microscopes. Figure 2.1 shows a commercial SQUID microscope from Neocera, Inc., which is principally marketed to semiconductor companies for failure analysis on integrated circuits and multichip modules [24]. The bandwidth of this system is about 100 kHz, which is very typical of SQUID microscopes that have been built. This bandwidth is not an inherent limitation of the SQUID itself but is due to the feedback electronics used to monitor the SQUID.

2.2 Failure Analysis of Circuits

Intel's co-founder Gordon Moore in 1965 predicted [25-26] that the number of transistors on a chip will double about every two years. What has popularly come to be known as Moore's Law describes a long-term trend in the history of computing hardware; The number of transistors that can be placed on an integrated circuit has increased exponentially, doubling approximately every two years. Although originally calculated as a doubling every year, [25-26] the estimate was later refined to a period of every two years [27-28] and is often incorrectly quoted as a doubling of transistors every 18 months. This trend has continued for almost half a century and is not expected to abate for possibly another decade or longer [29].

With the increasing complexity of integrated circuits over the last several decades has also come smaller feature size, more complex design, and new packaging technologies. This has created challenges in analyzing device failure or performing failure analysis, the process of making electrical and physical measurements on circuits in order to determine the location and cause of failure.

An additional complication is that since the first integrated circuit, the number of layers has grown from two to ten or more. Also, this growth of layers is not limited to the substrate (also called the "die") but also to the surrounding circuitry (called the package). Each package typically is made of 6-12 copper layers in an insulator matrix. The main purpose the package is to allow the die to be electrically connected to a circuit board. Further, in flip-chip packaging the die's active surface is directly attached to the package. This results in the die wiring being "buried" under the silicon chip. Thus the final product

typically has no exposed wiring so that optical inspection or scanning electron microscopy cannot be used to view the electrical wiring.

In order for manufacturers to build ever more complicated integrated circuits the need for more powerful tools for failure analysis will be required. These tools will be required to nondestructively and accurately locate buried defects, possibly through the backside of a silicon die or through the package's dielectric matrix. With existing failure isolation tools, non-destructively locating many types of defects with submicrometer resolution is not possible and only a limited amount of information can be obtained from current failure isolation techniques.

2.3 Defects in Semiconductor Circuits

Defects in CMOS IC circuits can be classified into three broad types: bridge, open and parametric [30], as discussed in the next three sections.

2.3.1 Bridge Defects

A bridge defect is an unintentional short circuit between power lines or interconnects (see Fig. 2.2) [30]. A key circuit parameter that determines the impact of a bridge defect on a circuit is the critical resistance $R_{critical}$. Critical resistance is the minimum resistance above which a circuit passes a functionality test. Typically, circuit failures due to bridge defects are not observed unless the bridge resistance is less than $R_{critical} \approx 2\ \text{k}\Omega$ [32].

Bridge defects range in size from submicrometer interline shorts, to many micrometers in length extended structures covering several interconnect lines. Bridge defects can

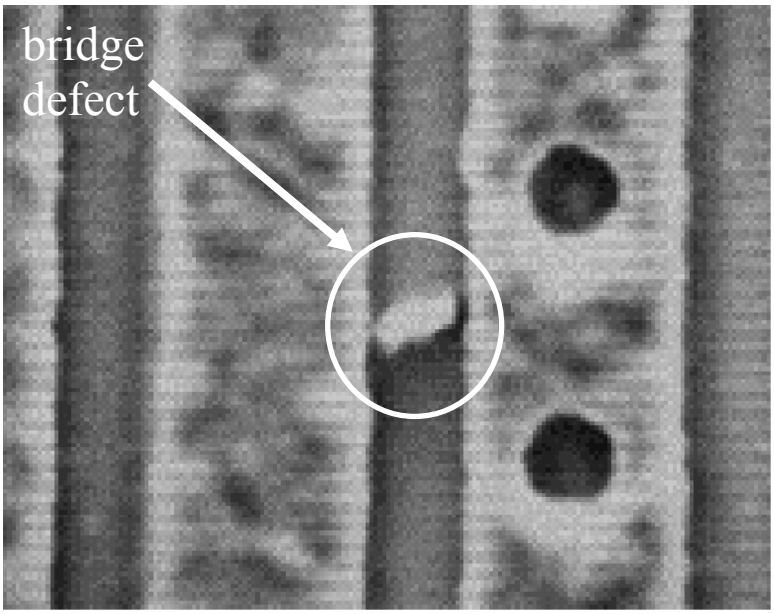

Fig. 2.2. SEM image of a bridge defect between two metal bus lines [33].

be caused by a variety of problems, including dust particles on a photolithographic mask or contamination of photoresist or other chemicals used in processing the chip. In addition, bridge defects can occur between two stacked vertical metal layers and are called “vertical shorts.”

Bridge defects can also occur in a transistor or other active circuit structure due to a gate-oxide short or soft *pn* junction breakdown. A gate oxide short is an undesired electrical path between the gate in a CMOS device and anything under the oxide layer. Gate oxide shorts can be caused by chemical contamination, nitride cracking during oxidation, or crystal defects. Gate oxide shorts can also be created during post-fabrication processing or under operational testing conditions.

2.3.2 Open Defects

Opens or open-circuit defects are more diverse than bridge defects. An open defect is a complete disconnect or electrical discontinuity in an integrated circuit interconnect line [30]. Open circuit defects can occur in interconnect lines in metal, polysilicon or diffusion regions. I will distinguish such complete disconnects from resistive or weak opens, which are classified as parametric failures.

Open defects are classified into six general behavioral types [30,37]:

1. "Transistor on" defect - causes a transistor to be permanently on.
2. "Transistor pair on" defect - defect in a logic gate input that affects two transistors.
3. "Transistor pair on/off" defect – defect in logic gate resulting in one transistor being on and the other off [37].
4. Delay - a defect that introduces a time delay into an interconnect. This type of defect is seen in open circuits having small cracks that allow some flow of current across the barrier. Some IC's can actually operate up to hundreds of MHz with this type of defect [37].
5. "Transistor off memory" – a defect in CMOS IC memory circuits that causes glitches on other input gates as a 2-pattern Boolean test is executed [37].
6. Sequential defect - a large open defect in a sequential circuit that results in degraded voltages with or without Boolean upset or strong clamping to a supply voltage [37].

Open defects in particular present significant challenges to failure analysis. With submicrometer CMOS technologies, the metal line widths are 130 nm or less and via

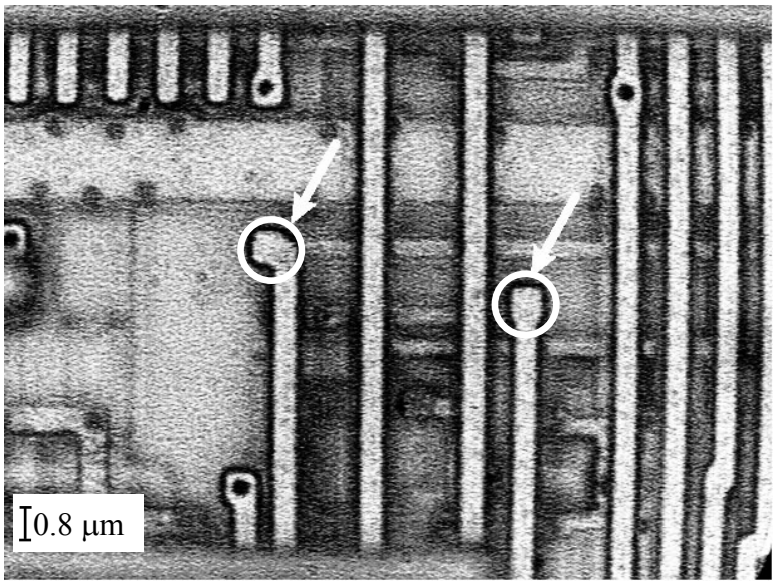

Fig 2.3. White circles and arrows indicate the location in the metal where two vias are missing, producing a CMOS open circuit defect [33].

height-to-width ratios are more than 5:1. This is too small for visual identification of an open. Additionally, via counts on chips range from hundreds of millions to over a billion, with total metal interconnect line lengths of several kilometers. Also, an open does not generate much of a signal in many techniques. For example, an open blocks current, so heating will not be significant and thermal imaging can not be used to localize an open. Finally the shear number of vias and wires suggests that contact-related open defects are likely to be common especially when new processes are being developed.

2.3.3 Parametric Failures

The third type of defect is called a parametric failure [32,37]. Parametric defects arise from variations in IC process parameters. Such defects produce broad behavioral patterns in an IC and can result in timing failures that can be classified into two kinds: (1) intrinsic, where the IC is free of individual defects, and (2) extrinsic, where the IC has individual defects. An IC that has an intrinsic parametric defect will fail because of an

unfortunate combination of variations in the electrical and physical parameters of transistors and interconnects that for example, adversely effects a supply line to a transistor resulting in a logic failure. Extrinsic parametric defects occur on the die due to environmentally sensitive defects. There are five typical extrinsic parametric defect mechanisms [37]:

1. resistive vias and contacts,
2. metal slivers,
3. weak interconnect opens,
4. metal mousebites – mousebites occur when sections of metal are missing from an interconnect line,
5. gate oxide shorts in ultrathin technologies.

There are several fabrication related mechanisms that result in resistive via failures, including incomplete etches that leave a small amount of dielectric layer across the bottom of a via, insufficient metal filling, and ash polymers contaminating the bottom of a via after a reactive ion etch.

Metal slivers are another common extrinsic parametric failure. Metal slivers are due to metal particles that lie between two metal conductors and barely make contact with the signal lines. With the advent of chemical mechanical polishing (CMP) [37], the problem of tiny metal particles lying along interconnect lines has grown. The behavior of such particles can be complicated. Consider a small metal particle between two metal interconnect lines. It may be touching or just barely touching. As the temperature increases, say during burn-in testing, the metal can expand so that a particle ends up touching both signal lines.

2.4 Fault Location Techniques

The ever increasing complexity and decrease in feature size in VLSI circuits means that electrical failures, such as short circuits, opens and high-resistance defects are increasingly a significant cause of IC faults [30]. Failure analysis is a process in which physical and electrical measurements are made in order to determine the cause of failure in a circuit. Once the cause is known, the manufacturing process can be adjusted to prevent the problem and improve yield. In the development and manufacture of integrated circuits, failure analysis plays an important role in a very competitive industry. It allows for shortening time to market, controlling manufacturing costs, and ensuring high reliability. The basic procedure for failure analysis is first to localize the electrical fault to a specific area, and then deprocess, inspect and test the exposed components to determine the cause of the failure [30-37].

Physical fault isolation (PFI) techniques basically use heat, light, electric and magnetic fields to localize defects in circuits. In passive mode techniques a steady-state photon emission, thermal or magnetic field image is made of the defective circuit. Some examples of passive mode techniques are infrared imaging, Schlieren thermal imaging, photon emission microscopy (PEM), and scanning SQUID microscopy (SSM) [36]. After the defect is localized to a reasonably small area, the chip can then be "deprocessed". In deprocessing, the chip is typically removed from its carrier and upper layers etched or polished away as needed to expose the problem layers. After deprocessing more powerful tools can then be used to examine the defective area or component.

A second class of fault isolation techniques uses a circuit's electrical response to a scanned probe, typically a laser or electron beam. The probe induces a thermal potential,

resistance change or photocurrent [38-42]. These changes thereby alter the defect or device's electrical properties, which are recorded via the devices, input, output or supply lines. The corresponding change is recorded as a function of beam position. The most common of these techniques are charge contrast scanning electron microscopy [41], temperature- or light induced voltage alteration (TIVA/LIVA) [34], and optical beam induced current (OBIC) [39]. Also, there are time-dependent physical isolation techniques such as picosecond imaging circuit analysis [42]. This is an extension of photon emission microscopy [34] in which one time resolves the photon emission. As a final example, laser voltage probing involves an incident laser probe that is used to create waveforms from transistors via charge-density modulation [42].

Figure 2.4(a) shows a schematic of a typical physical fault setup with a detector or energy source above the circuit under test [35]. The electrical response of/or stimulus to the device is recorded and the defect signal is shown superimposed on top of the chip layout or microscopy image of the circuit. The inset image in Fig. 2.4(a) shows the signal from a scanning SQUID microscope with background near-infrared image. Figure 2.4(b) shows selected examples of output from PFI techniques: SSM, TIVA, STM, and PEM. Each image in Fig. 2.4(b) shows the approximated background area (W) on which the signal is overlayed. The top-left image is from a conventional scanning SQUID microscope with a background area approximately 15 mm. The top-right image is from a TIVA with a 9 mm background area. The bottom-left image is an example of Schlieren thermal imaging with a background area of 570 μm. The bottom right image is an example of photon emission microscopy of a large area scan of 25 mm.

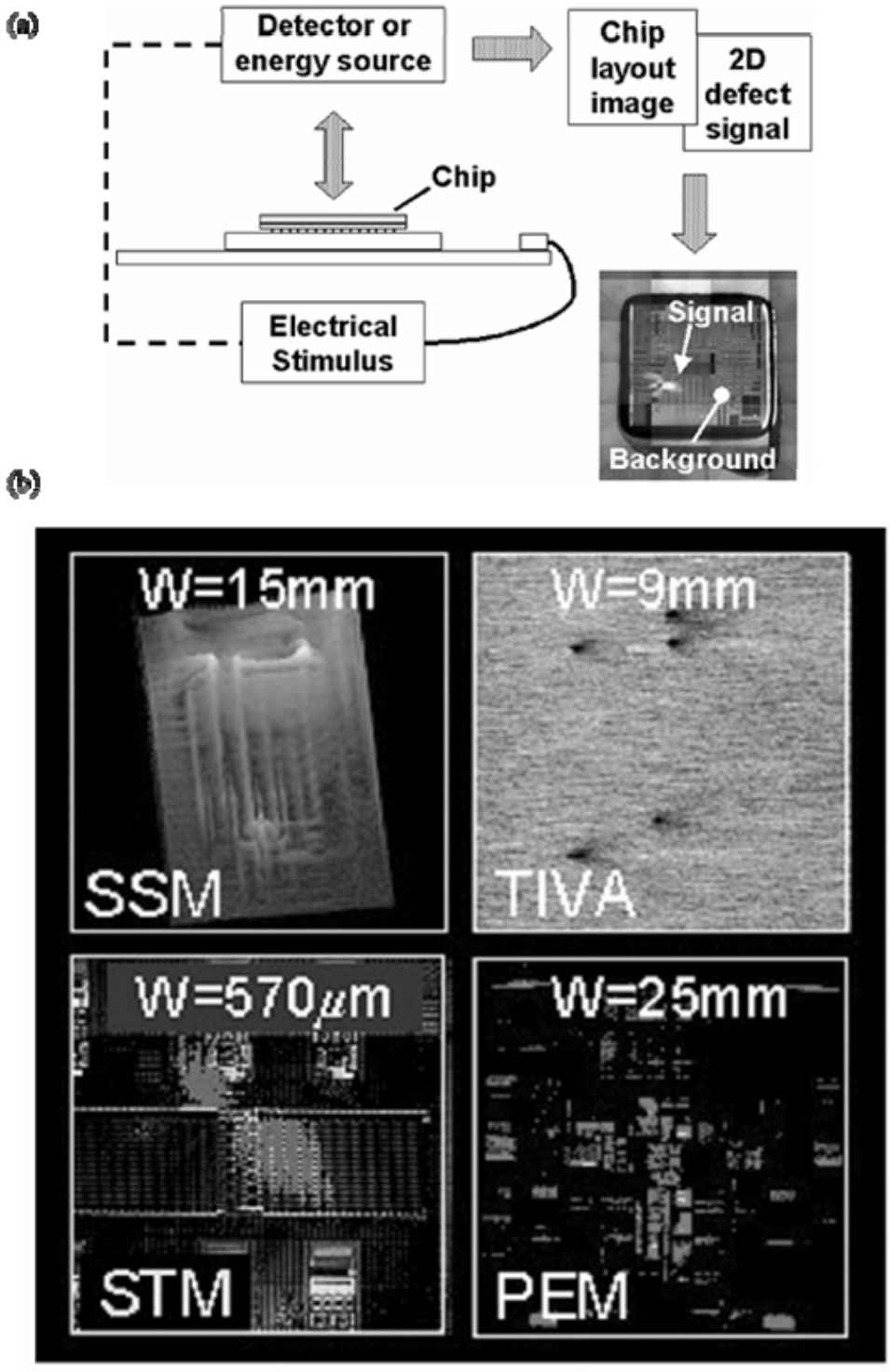

Fig. 2.4. (a) General schematic of physical fault isolation (PFI) setup along with background near-infrared image overlaid on defect signal (scanning SQUID microscopy in this case). (b) Example of four PFI images showing (clockwise) scanning SQUID microscopy, TIVA, STM, and PEM. Width of background area is denoted by W [35].

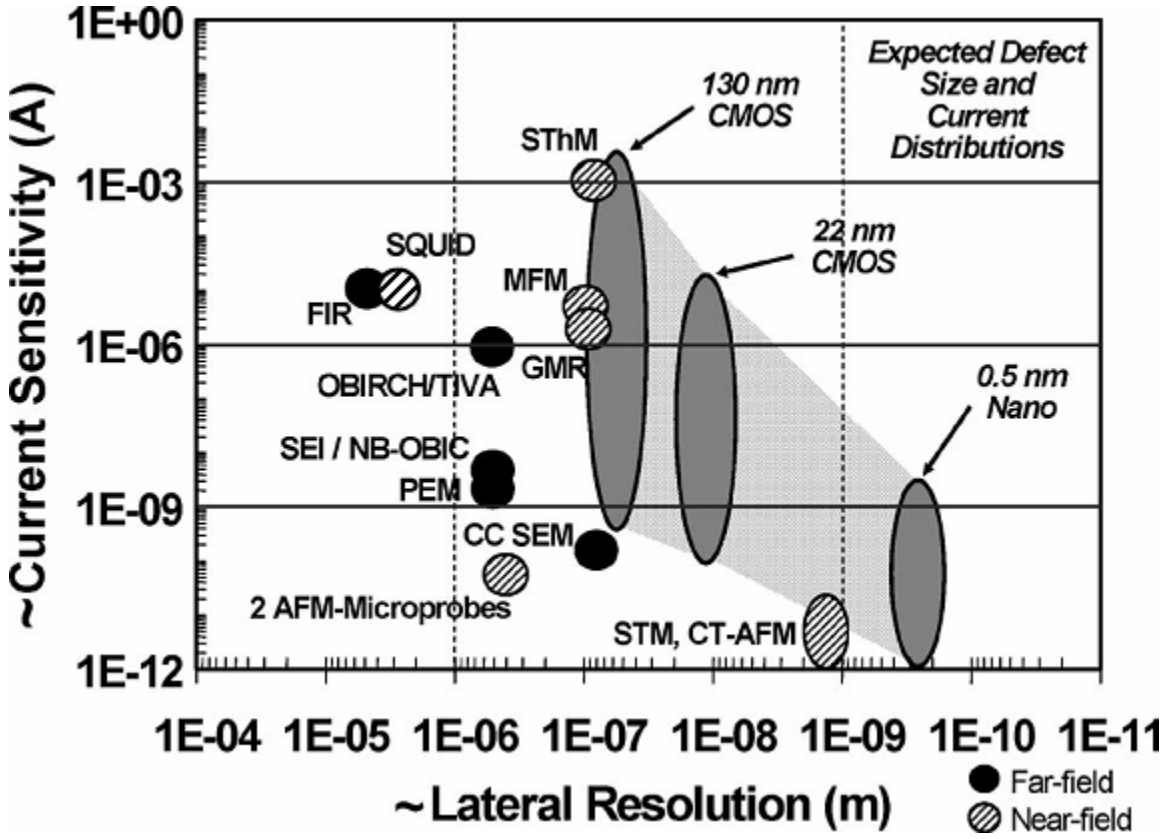

Fig. 2.5. Current sensitivity versus spatial resolution for several physical fault isolation techniques. Also shown is expected defect size and corresponding defect current distribution. (SQUID: superconducting quantum interference device (1 second average); FIR: far-infrared imaging; MFM: magnetic force microscopy; SthM: scanning thermal microscopy; GMR: giant magnetoresistive sensor; TIVA: temperature-induced voltage alteration; SEI: Seebeck-effect imaging; NB-OBIC: nonbiased optical beam-induced current; CC SEM: charge-contrast scanning electron microscopy; STM: scanning tunneling microscopy; CT: conductive tip; PEM: photon emission microscopy; OBIRCH: optical beam-induced resistance change) [40].

One of the great challenges facing the microelectronics industry by advancing IC technology is to precisely locate an electrical fault in three dimensions [40]. Most devices are not designed with built-in test enabled diagnostics. In light of the still shrinking size of devices and the increase of ever more subtle defects, the isolation of even one logic node (which could be hundreds of micrometers in length and extend over multiple wiring levels) is extremely difficult to do. Also, the design of many IC packages makes it

difficult to use close inspection techniques that rely on imaging phenomena associated with defective structures like magnetic density, laser sensitivity or photon emission.

A commonly used metric for a defect's electrical signal strength is the expected defect leakage current. Figure 2.5 shows the relationship between current sensitivity versus spatial resolution for several physical fault isolation techniques. Also, shown in Fig. 2.3 is the expected defect size and corresponding defect current distribution. Notice that some methods like scanning tunneling microscopy, giant magnetoresistive microscopy, and scanning thermal microscopy attain excellent resolution, but only if the sensor can be brought to within nanometers of the signal source. One of the interesting characteristics of the SQUID microscope is that it does not require direct contact with the substrate to create an image, and magnetic fields can penetrate through metal and insulating overlayers.

Manufacturers of integrated circuits (ICs) have developed many techniques to locate wiring defects. These techniques include the use of optical microscopy, scanning electron microscopy, scanning probe microscopy, and microprobes [31]. Thermal imaging with an infrared camera is perhaps the most sophisticated widespread technique for locating short circuits in ICs [35]. This can be a particularly useful technique for locating a short circuit that might be anywhere on a large IC. The technique works well if the circuit draws a large current and generates a "hot spot" in a thermal image. Unfortunately, not all short circuit defects draw large currents and such defects remain a serious problem for integrated circuit manufacturers [33]. Also, the spatial resolution of thermal imaging can be particularly poor, especially on ICs which are "flip chip" mounted and covered by a thick and thermally conductive substrate.

2.5 Summary

In this chapter I described the challenges to failure analysis due to ever decreasing feature size and increasing circuit complexity. With that in mind, Fig. 2.6 shows the spatial resolution for several failure analysis tools compared with expected defect sizes [35]. The techniques are compared with the projected minimum defect sizes (minimum defect size is equal to one-half of the minimum technology feature size) for future microelectronic technology. Without further research and innovation physical fault isolation techniques will lack the spatial resolution to tackle future microelectronics. What is required is innovation into new detection schemes for non-contact imaging of signals in the picoampere to nanoampere range.

The SQUID microscope is one technique that is well-suited to some tasks in fault localization. As mentioned above there are many failure mechanisms and I can broadly divide them into short circuits and open circuits. Open and short circuited electrical connections are a major problem affecting yield and reliability. One expects the problem will only increase as the length of interconnections and the number of wiring levels grow. Since electrical currents produce magnetic fields, nondestructively locating an electrical short circuit is and has been a real niche for SQUID microscopy.

For open circuits the problem is more difficult. Since conventional SQUID microscopy is bandwidth limited to the kH range, and such low frequency current will not pass through an open, “seeing” an open circuit with a conventional SQUID microscope is impractical. On the other hand a SQUID microscope that worked at much higher frequencies might be able to image the location of an open circuit faults via the

magnetic field emanating from current flowing due to capacitive coupling across a gap. This thesis describes such a SQUID microscope and its capabilities.

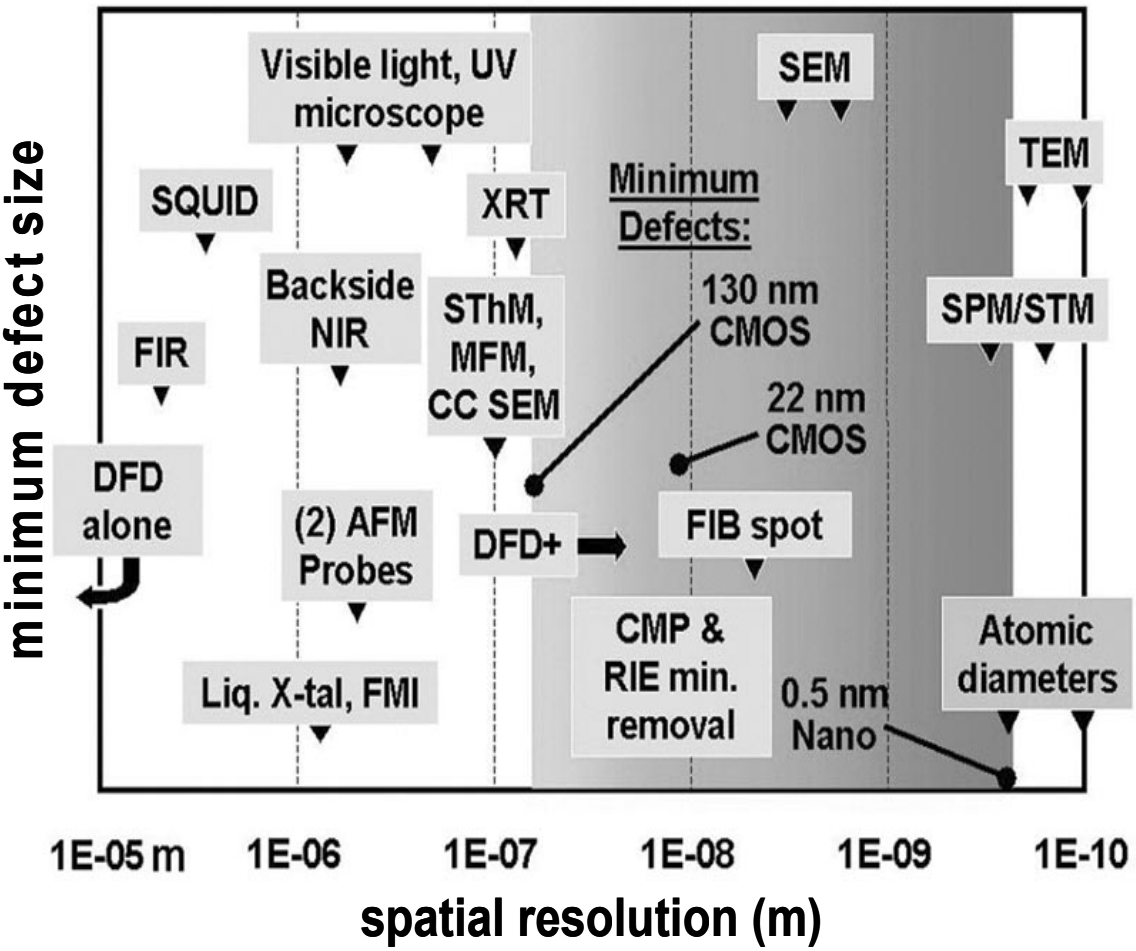

Fig. 2.6. Overall comparison of failure analysis techniques for lateral spatial resolution versus projected minimum defect sizes. The projected minimum defect sizes are labeled and equal to one-half of the minimum technology feature size [35].

Chapter 3: Josephson Junctions and SQUIDs

3.1 Superconductivity

The phenomenon of superconductivity was first observed in 1911 by Kamerlingh Onnes in Leiden [1]. Three years previously he had managed to liquefy helium (the boiling point for helium at 1 atm is 4.2 K). He soon began to use liquid helium as a refrigerant and started studying how the electrical resistance of metals depends on temperature. To his surprise, he found that at 4.2 K the electrical resistance of solid mercury abruptly disappeared. He also found that the electrical resistance of some other metals such as tin and lead completely disappeared. The resistance vanished in a small temperature range at a temperature that depended on the material. This temperature is now called the critical temperature, T_c. Since then, many other metals and alloys have been found to be superconductors as well. The complete disappearance of electrical resistance is one hallmark of superconductivity and an important property for applications such as for high-current transmission lines or high-field magnets.

A second hallmark of superconductivity is the Meissner effect (also known as the Meissner-Oschenfeld effect). The Meissner effect involves the expulsion of magnetic field from a superconductor. The phenomenon was first observed by Walther Meissner and Robert Oschenfeld is 1933 [2]. Their measurements involved applying a magnetic field to tin and lead samples, which were then cooled below their transition temperatures. They found that below T_c the samples would expel all magnetic field lines, leading to zero magnetic flux inside. Thus, the samples became perfectly diamagnetic. The way

superconductors do this is that they produce surface currents that generate an opposing magnetic field which results in a zero net magnetic field inside the superconductor. These currents, called persistent currents, do not decay in time and so perfect diamagnetism implies zero electrical resistance. Persistent currents only flow near the surface of the superconductor and decay on a length scale λ_L with depth, where λ_L is called the London penetration depth. Each superconducting material has a characteristic penetration depth which depends on the density of superconducting electrons (Cooper pairs). As an example, for niobium the transition temperature is $T_c = 9.25$ K and its penetration depth is $\lambda_L = 39$ nm at zero temperature.

Although zero resistance and diamagnetism are key hallmarks of the superconducting state, the underlying physics of the superconducting state is the existence of a condensate wave function of electrons that are paired in momentum space. A quantum mechanical description of superconductivity was developed in 1957 by Bardeen, Cooper, and Schrieffer [3,4]. According to the Bardeen-Cooper-Schrieffer (BCS) model, superconductivity is a macroscopic effect which results from the "condensation" of electron pairs called Cooper pairs [5]. In the BCS model, this pairing is caused by an attractive force between electrons due to exchange of phonons. When one considers many electrons forming pairs, one finds that the pairing opens an energy gap $\Delta(T)$ in the continuous spectrum of allowed energy states of the electrons. Thus, all excitations of the system must possess some minimum amount of energy. If the gap energy, $\Delta(T)$ is larger than the thermal energy, given by $k_B T$, where k_B is Boltzmann's constant and T is the temperature, the Cooper pair is not scattered by the lattice. Hence, Cooper pairs form a superfluid which can flow without energy dissipation, i.e. electrical

resistivity vanishes. A key prediction of BCS theory was that a minimum energy E_g = $2\Delta(T)$ is required to break a Cooper pair and create two quasiparticle excitations. Also, the energy gap parameter $\Delta(T)$ was predicted to increase from zero at T_c to a limiting value

$$E_g = 2\Delta(0) = 3.528kT_c, \tag{3.1}$$

for $T << T_c$. The BCS model quantitatively predicted measured gaps and the shape of the absorption edge above E_g [6]. The BCS theory explained both zero electrical resistivity and the Meissner effect, but also predicted an energy gap in the electronic excitation spectrum and a second-order phase transition to the normal state at a temperature T_c [7].

Prior to BCS theory, Ginzburg and Landau (GL) proposed in 1950 a macroscopic phenomenological theory of superconductivity from a thermodynamic point of view [7,8]. Ginzburg-Landau theory combined Landau's earlier theory of second-order phase transitions with a Schrödinger-like wave equation that quite successfully explained the macroscopic properties of superconductors. Although independent of microscopic aspects of superconductivity, GL theory was quantum-mechanical in that it included coherent, macroscopic effects. In GL theory the free energy density of a superconductor near the superconducting transition can be expressed as a function of a complex order parameter, $\Psi(\mathbf{r})$. The local density of superconducting electrons, $n_s(\mathbf{r})$ is given by the square of the modulus of the order parameter $\left|\Psi(\mathbf{r})\right|^2$. If $\Psi(\mathbf{r})$ is small and varies slowly in space, the free energy density can be expanded in powers of $\left|\Psi(\mathbf{r})\right|^2$ and $\left|\nabla\Psi(\mathbf{r})\right|^2$. By applying a variational method to minimize the free-energy density with respect to fluctuations in the order parameter and the vector potential one arrives at a pair of coupled differential

equations for $\Psi(\mathbf{r})$ and the vector potential $\mathbf{A}(\mathbf{r})$, known as the Ginzburg-Landau equations. Originally Ginzburg and Landau thought of a superconductor as two interpenetrating electron fluids, one was a non-dissipative "superconducting" electron fluid, and the other was the normal dissipative electron fluid.

In 1959, Gor'kov demonstrated that for temperatures sufficiently neat T_c and for spatial variations of Ψ and **A** that were not too rapid one could start from BCS theory and find equations identical to those of GL [9,10]. Further, the GL parameter Ψ could be interpreted (except for a constant of proportionally) as the BCS energy-gap parameter Δ. With this result, we can interpret superconductivity as a macroscopic quantum phenomenon, in which the amplitude and phase are associated with the energy gap parameter $\Delta(T)$. Further, interference and diffraction effects can occur, as we will see in the *Josephson effect*. Thus, we can represent the superconducting fluid by a complex order parameter, $\psi(\vec{r}) = |\psi(\vec{r})| e^{i\theta(\vec{r})}$ where θ is the phase of the electron pairs or Cooper pairs [10]. We can also think of the order parameter as an effective many particle wave function, that has both amplitude and phase and maintains phase coherence over macroscopic distances.

Since $\psi(\vec{r},t)$ is a wavefunction that describes the Cooper pairs, it satisfies the relation

$$\int dV \psi^*(\mathbf{r},t)\psi(\mathbf{r},t) = N^* \tag{3.2}$$

where N^* is the total number of Cooper pairs in the sample and the integral is taken over the volume V of the sample. From this expression, we can interpret the integrand in Eq. (3.2) as the local density of Cooper pairs,

$$\psi^*(\mathbf{r},t)\psi(\mathbf{r},t) = n^*(\mathbf{r},t). \tag{3.3}$$

Hence the order parameter does not describe the probability amplitude for a single particle, but instead the density of pairs. From basic quantum mechanics, we can also write the supercurrent density for a superconductor in an electromagnetic field as:

$$\mathbf{J}_S = q^* \,\mathrm{Re}\left\{\Psi^*\left(\frac{\hbar}{im^*}\nabla - \frac{q^*}{m^*}\mathbf{A}\right)\right\}. \tag{3.4}$$

where q* is the charge of the pairs, m* is the pair's mass, and **A** is the vector potential. As noted above, the order parameter $\Psi(\mathbf{r},t)$ obeys the Ginzburg-Landau equations [7] and approximates the Schrödinger equation for the ensemble in an electromagnetic field:

$$i\hbar\frac{\partial}{\partial t}\Psi(\mathbf{r},t) = \frac{1}{2m^*}\left(\frac{\hbar}{i}\nabla - q^*\mathbf{A}(\mathbf{r},t)\right)^2\Psi(\mathbf{r},t) + q^*\phi(\mathbf{r},t)\Psi(\mathbf{r},t). \tag{3.5}$$

Also, as noted above, we can always write $\Psi(\mathbf{r},t)$ in the form

$$\Psi(\mathbf{r},t) = \sqrt{n^*(\mathbf{r},t)}e^{i\theta(\mathbf{r},t)}, \tag{3.6}$$

where $n^*(\mathbf{r},t)$ is the local density of Cooper pairs and $\theta(r,t)$ is a real-valued function representing the phase of the order parameter. Substituting Eq. (3.6) into Eq. (3.4) yields the supercurrent equation in the form

$$\mathbf{J}_S = q^* n^*(\mathbf{r},t)\left(\frac{\hbar}{im^*}\nabla\theta(\mathbf{r},t) - \frac{q^*}{m^*}\mathbf{A}(\mathbf{r},t)\right). \tag{3.7}$$

To simplify Eq. (3.7), we now define:

$$\Lambda = \frac{m^*}{n^*\left(q^*\right)^2} \tag{3.8}$$

Eq. (3.7) then becomes

$$\mathbf{J}_S(\mathbf{r},t) = -\frac{1}{\Lambda}\left(\mathbf{A}(\mathbf{r},t) - \frac{\hbar}{q^*}\nabla\theta(\mathbf{r},t)\right). \tag{3.9}$$

If we integrate Eq. (3.9) about a closed contour C in the superconductor, we obtain the following expression,

$$\oint_C \mathbf{J}_S(\mathbf{r},t)\cdot d\mathbf{l} = -\frac{1}{\Lambda}\oint_C \mathbf{A}\cdot d\mathbf{l} - \frac{\hbar}{\Lambda q^*}\oint \nabla\theta\cdot d\mathbf{l}\,. \tag{3.10}$$

Now recall that

$$\oint_C \mathbf{A}\cdot d\mathbf{l} = \int_S (\nabla\times\mathbf{A})\cdot d\mathbf{s} = \int_S \mathbf{B}\cdot d\mathbf{s} = \Phi \tag{3.11}$$

where $\mathbf{B}$ is the magnetic flux density associated with the vector potential $\mathbf{A}$, S is the surface defined by the closed contour C and Φ is the total magnetic flux through this contour. Equation (3.10) can now be written as

$$\oint_C (\Lambda\mathbf{J}_S)\cdot d\mathbf{l} + \Phi_S = \frac{\hbar}{q^*}\oint_C \nabla\theta\cdot d\mathbf{l}. \tag{3.12}$$

The integral on the right side of the above expression is simply

$$\int_{\mathbf{r}_a}^{\mathbf{r}_b} \nabla\theta\cdot d\mathbf{l} = \theta(\mathbf{r}_b,t) - \theta(\mathbf{r}_a,t). \tag{3.13}$$

In general, even though a closed path is formed as $\mathbf{r}_b \to \mathbf{r}_a$, the value of the integral need not be zero. To see why, note that there are an infinite number of possible values for the phase which lead to the same value for the order parameter, i.e.

$$\Psi(\mathbf{r},t) = \sqrt{n^*}\,e^{i(\theta_p + 2\pi n)} \tag{3.14}$$

for any integer n yields the same value for the wavefunction Ψ. Thus the phase can only be specified to within modulo 2π of its principal value θ_p, i.e.

$$\theta(\mathbf{r},t) = \theta_p(\mathbf{r},t) + 2\pi n \tag{3.15}$$

where θ_p has its range defined from $-\pi$ to π.

We can thus write in general

$$\oint \nabla\theta \cdot d\mathbf{l} = \lim_{\mathbf{r}_b \to \mathbf{r}_a} \{\theta(\mathbf{r}_b, t) - \theta(\mathbf{r}_a, t)\} = 2\pi n \tag{3.16}$$

Equation (3.12) can now be written as

$$\oint_C (\Lambda \mathbf{J}_S) \cdot d\mathbf{l} + \Phi = n\Phi_0 \tag{3.17}$$

where Φ_0 represents the flux quantum and is defined as

$$\Phi_0 = \frac{h}{q^*} \tag{3.18}$$

The left side of Eq. (3.17) is called the fluxoid and the expression is a statement of fluxoid quantization. Deep inside a superconductor, $\mathbf{J}_S$ will vanish, and Eq. (3.17) reduces to

$$\Phi = n\,\Phi_0. \tag{3.19}$$

This is a statement of flux quantization, i.e. the total magnetic flux passing through a superconductor cannot be arbitrary but instead must be a discrete number of flux quanta.. If the superconductor is not sufficiently thick then we will only have fluxoid quantization (Eq. 3.17) but not true flux quantization (Eq. 3.19).

Flux quantization was experimentally measured in 1961 by two different groups of researchers; B. S. Deaver and W. M. Fairbank at Stanford and R. Doll and M. Näbauer in Germany [11,12]. Deaver and Fairbank electroplated tin on a copper wire which had been wound onto a hollow cylinder. They applied a field to trap flux, removed the field and then rapidly vibrated the cylinder in the axial direction. They measured the resulting magnetic signal by using a pair of coils and found the net magnetic flux trapped inside the loop occurred in quantized steps. Similar results occurred regardless of applied field

strength or when the direction of the applied field was reversed. Their data indicated that the magnetic flux quantum has a value of

$$\Phi_0 = \frac{h}{2e} = 2.068 \times 10^{-15} T m^2, \tag{3.20}$$

where e is the absolute value of the charge of the electron and h is Planck's constant. This was the first experimental evidence for the existence of Cooper pairs, a key component of the microscopic model of superconductivity proposed by J. Bardeen, L. Cooper, and R. Schrieffer in 1957 [3,4].

3.2 Josephson Junctions

Suppose we have two superconductors *#1* and *#2* that are completely isolated. Then the phase of the Cooper pairs in *#1* will be unrelated to the phase of the Cooper pairs in *#2*. Now suppose that the separation between the two superconductors is gradually reduced toward zero. When the separation becomes very small (~1-2 nm), the Cooper pairs will be able to tunnel from *#1* to *#2* and vice versa (see Fig. 3.1). The wave functions will be coupled together and the phases in #1 and #2 become interdependent [13,14].

Josephson analyzed this situation and found some surprising results [14]. Depending on the barrier thickness and the area of the junction, a maximum current can flow without any voltage drop. This maximum current is the critical current I_0. According to the dc Josephson equation the current I through the junction is given by

$$I = I_0 \sin\theta, \tag{3.21}$$

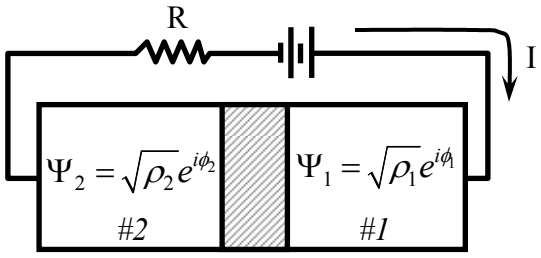

Fig. 3.1. Schematic of Josephson junction composed of two superconducting regions (#1 and #2) separated by an insulating region (shaded region). The insulating region is typically an oxide layer approximately 1-2 nm thick.

where $\theta=\phi_1-\phi_2$ is the phase difference between the two wave functions on each side of the barrier (see Fig. 3.1) [14]. If the current I, through the junction exceeds I_0, a voltage V appears across the junction.

According to the ac Josephson relation, the phase difference θ is related to the voltage V across the junction by [14]:

$$\frac{d\theta}{dt} = \frac{2e}{\hbar} V. \tag{3.22}$$

Josephson derived these results from the BCS model and the ac and dc Josephson effects are a manifestation of quantum phenomenon on a macroscopic scale [15].

3.3 The Josephson Equations

The Josephson relations are somewhat unusual, and it is helpful to have some understanding of how they arise. Feynman [16] provided a simple analysis that captures some of the key physics in a Josephson junction. If the separation between two superconductors *#1* and *#2* is relatively large, the Cooper pair wave function on each side of a junction can be described by a macroscopic wave function

$$\Psi = \left|\Psi(\mathbf{r},t)\right| e^{\left\{ i\theta(\mathbf{r},t) - \frac{2E_F t}{\hbar} \right\}} \tag{3.23}$$

where θ is the phase of the electron pairs and the phases of all the pairs evolve in time at a frequency $2E_F / \hbar$. The phases of the wave functions in the *#1* and *#2* superconductors are unrelated and can only be defined to within an arbitrary additive constant (see Fig. 3.1). If the separation between the two superconductors is reduced the wave functions can penetrate the barrier and couple and the total energy is reduced by this coupling. As the coupling energy increases and exceeds the thermal fluctuation energy, the phases become locked and Cooper pairs can pass from superconductor *#1* to superconductor *#2* without loss of energy. Cooper pair tunneling can also take place with a voltage across the junction. In this case the phases of the superconductors are no longer locked together but rather move relative to each other at a rate that is precisely related to the voltage.

Following these ideas, Feynman wrote the time-dependent Schrodinger equation as

$$\begin{aligned} i\hbar \frac{\partial \psi_1}{\partial t} &= E_1 \psi_1 + K\psi_2 \\ i\hbar \frac{\partial \psi_2}{\partial t} &= E_2 \psi_2 + K\psi_1. \end{aligned} \tag{3.24}$$

The coupling constant K measures the interaction of the two wave functions, while E_1 and E_2 are the energies for the left and right superconductors, respectively.

If we apply a voltage across the two superconductors and assume that the zero of the potential is in the middle of the barrier between the two superconductors, then the potential for superconductor number *#1* will be at $-(1/2)V$ with Cooper-pair potential

energy $+eV$. Similarly for superconductor number *#2* its potential will be at $-1/2V$ and the Cooper-pair potential energy $-eV$. Thus we have:

$$\begin{aligned} i\hbar\frac{\partial\psi_1}{\partial t} &= eV\psi_1 + K\psi_2 \\ i\hbar\frac{\partial\psi_2}{\partial t} &= -eV\psi_2 + K\psi_1. \end{aligned} \tag{3.25}$$

To solve these coupled differential equations, we substitute

$$\Psi_1 = \sqrt{n_1}e^{i\theta_1} \tag{3.26}$$

$$\Psi_2 = \sqrt{n_2}e^{i\theta_2} \tag{3.27}$$

$$\phi = \theta_1 - \theta_2 \tag{3.28}$$

The Cooper-pair densities for the superconductors are n_1 and n_2 respectively, and ϕ is the phase difference across the barrier. Now if we substitute Eqs. (3.26) and (3.27) into the coupled wave equations Eqs. (3.25) and separate the results into real and imaginary components we obtain

$$\hbar\frac{dn_1}{dt} = 2K\sqrt{n_1 n_2}\sin\phi, \tag{3.29}$$

$$\hbar\frac{dn_2}{dt} = -2K\sqrt{n_1 n_2}\sin\phi, \tag{3.30}$$

$$\frac{d\phi}{dt} = \frac{2e}{\hbar}V. \tag{3.31}$$

The above expressions represent the time-dependence of the Cooper-pair densities and the time-dependence of the phase difference.

The current density in the junction can be obtained from the difference between Eq. (3.29) and Eq. (3.30) multiplied by -2*e*. We obtain

$$J = -2e\left(\frac{dn_2}{dt} - \frac{dn_1}{dt}\right) = J_0 \sin\phi, \tag{3.32}$$

where

$$J_0 = \frac{4eK\sqrt{n_1 n_2}}{\hbar}. \tag{3.33}$$

By multiplying Eq. (3.32) by the area of the junction *#1* we obtain the current *I* through the device

$$I = I_0 \sin\phi, \tag{3.34}$$

and where $I_0 = 4eKA\sqrt{n_1 n_2}/\hbar$ is the critical current of the junction. Equation 3.34 is the *dc Josephson effect* and shows that the supercurrent through the junction varies sinusoidally with phase difference ϕ across the junction.

For a fixed voltage across the junction Eq. (3.31) can be integrated directly to give

$$\phi(t) = \phi_0 + \left(\frac{2e}{\hbar}\right)Vt. \tag{3.35}$$

Thus we see that the phase will vary linearly with time for a fixed voltage difference *V* across the junction. If Eq. 3.35 is substituted back into Eq. 3.34 we see that an ac current develops across the junction:

$$I = I_0 sin\left[\frac{2\pi}{\Phi_0}Vt + \phi_0\right], \tag{3.36}$$

where Φ_0 is the flux quantum. The current will have a characteristic frequency f_J also called the Josephson frequency

$$f_J = \frac{2eV}{h} = \frac{V}{\Phi_0} = \left(483.6\,MHz/\mu V\right)\times V \tag{3.37}$$

This effect is called the *ac Josephson effect* and is the basis for the definition of the volt.

An important corresponding time constant for a Josephson junction is the inverse of the *Josephson frequency* or $f_J^{-1} = \frac{h}{2eV}$.

3.4 RCSJ Model of a Josephson Junction

The current-voltage (*I-V*) characteristic for an ideal non-dissipative Josephson junction is hysteretic. Figure 3.2(a) shows a schematic of the situation. Starting from $I = 0$ and increasing *I,* no voltage appears across the junction provided $I < I_0$. When $I > I_0$ the voltage quickly switches to a nonzero value $V \sim 2\Delta/e$, where 2Δ is the energy gap of the superconductor [17,18]. At $V = 2\Delta/e$, the current (2) rises sharply due to quasiparticles formed by breaking Cooper pairs.

My devices were made from Nb and this voltage $V = 2\Delta/e \approx 2.8$ mV (see Fig. 3.2(b). The jump from $V = 0$ to $V = 2\Delta/e$ is discontinuous, as indicated by the dashed line in Fig. 3.2(a). The device shows hysteresis in that for $0 < |I| < I_0$, there are two possible values of the voltage and the voltage will return to zero only when the magnitude of the current $|I|$ is reduced to a much smaller value than I_0. This hysteresis can be eliminated by adding a sufficiently small shunt resistance across the junctions [19-22]. In my case, I use this hysteretic behavior to overcome bandwidth limitations imposed by the feedback electronics.

The current-voltage characteristic of a junction can be understood from the resistively and capacitively shunted junction (RCSJ) model [17,18]. In this model, a junction with critical current I_0 is connected to a current source I and shunted by a capacitance C and a resistance R (see Fig. 3.3).

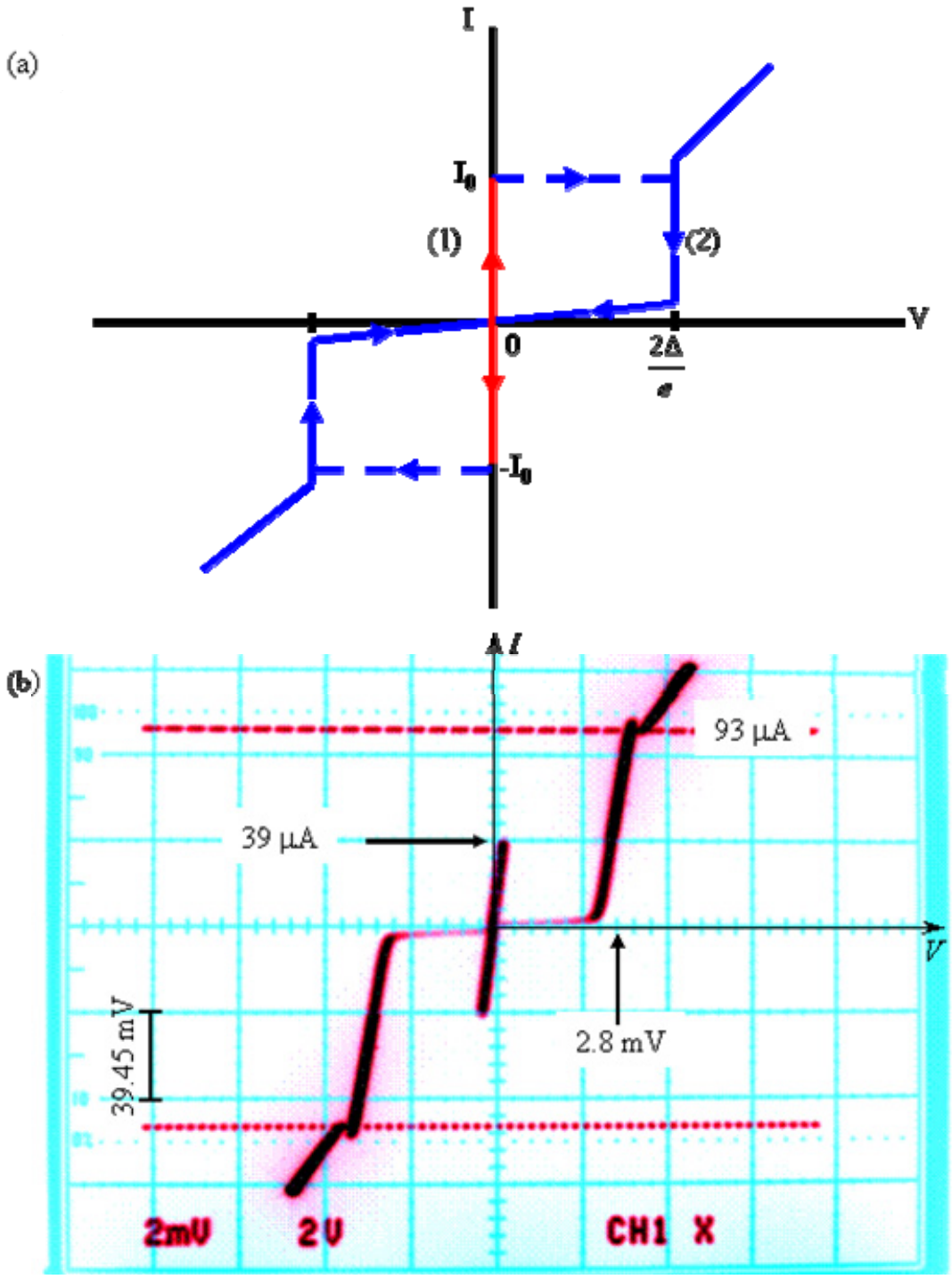

Fig. 3.2. (a) Schematic of current–voltage (IV) characteristic for a hysteretic Josephson junction. Red curves indicate zero voltage state and blue curves represent non-zero-voltage state. (b) Measured IV characteristic for the 4.2 K Nb SQUID (Device HSQ_2) used in the microscope. The critical current is 39 μA and $2\Delta/e \approx 2.8$ mV. Notice that above 93 μA the curve becomes ohmic with resistance $R_N = 34.5\ \Omega$.

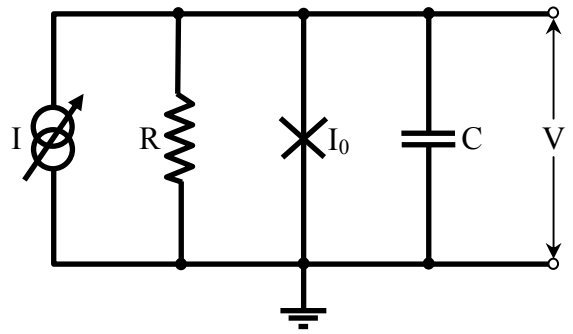

Fig. 3.3. Circuit schematic of RSJ model of a Josephson junction. The junction has a critical current I_0 and is in parallel with shunt resistor R and capacitance C.

Conservation of current gives

$$C\frac{dV}{dt}+I_0\sin\theta+\frac{V}{R}=I. \tag{3.38}$$

From the ac Josephson effect $V=\frac{\hbar}{2e}d\theta/dt$, we obtain

$$\frac{\hbar C}{2e}\frac{d^2\theta}{dt^2}+\frac{\hbar}{2eR}\frac{d\theta}{dt}=I-I_0\sin\theta\equiv-\frac{2e}{\hbar}\frac{\partial U}{\partial\theta}. \tag{3.39}$$

Here I have defined an effective potential energy

$$U=-\frac{\Phi_0}{2\pi}\left(I\theta+I_0\cos\theta\right). \tag{3.40}$$

Equation 3.39 can be transformed into dimensionless form by defining,

$$i=\frac{I}{I_0} \tag{3.41}$$

and

$$\tau=\frac{2\pi I_0R}{\Phi_0}t=\frac{t}{\tau_J}. \tag{3.42}$$

We then find Eq. 3.39 can be written in dimensionless form as

$$i = \beta_c \frac{d^2\theta}{d\tau^2} + \frac{d\theta}{d\tau} + \sin\theta \tag{3.43}$$

where

$$\beta_c = \frac{\tau_{RC}}{\tau_J} = \frac{2\pi I_0 R^2 C}{\Phi_0} \tag{3.44}$$

is the Stewart-McCumber Hysteresis parameter [17,18] and $\tau_{RC} = RC$. Hysteresis occurs if $\beta_c > 1$ and this is the limit I am interested in for my devices.

3.5 Equations of motion of the dc SQUID

Soon after Josephson discovered the effect that now bears his name, the first Josephson junction was made by John Rowell and Phillip Anderson at Bell Labs [16]. One year later in 1964, Robert Jaklevic, John Lambe, Arnold Silver, and James Mercereau of Ford Research Labs described their invention of the dc Superconducting Quantum Interference Device or SQUID [23-25].

A dc SQUID is a closed superconducting loop interrupted by two Josephson junctions (see Fig. 3.4). Current bias leads and voltage output leads are connected to the top and bottom of the loop. The maximum supercurrent I_0 that can flow through the SQUID without a voltage appearing is determined by the critical current of both junctions and the flux Φ_a applied to the SQUID. For a symmetrical SQUID (identical junctions and arm inductances) the critical current I_0 is a maximum for $\Phi_a = n\Phi_0$, where n is an integer, and a minimum for $\Phi_a = n\Phi_0 + \Phi_0/2$. In fact I_c is periodic in Φ_a. Biasing the device into the finite voltage state (by applying $I > I_0$) causes high-frequency circulating supercurrents to flow around the ring due to the ac Josephson effect.

Since I_0 depends on the applied flux, a dc SQUID can be used as a magnetometer and it turns out to be extremely sensitive [26-30]. For a 4.2 K SQUID with 16 Ω shunts and a 1 mm^2 pick-up area, the flux sensitivity is of order fT/√Hz [26]. By going to lower temperature or using a separate pick-up coil with a large area and a flux transformer, orders of magnitude more sensitivity is obtainable. For comparison, the maximum magnetic field produced outside the body by a beating human heart is on the order of 10^{-10} T and large signals from the human brain are on the order of 10^{-13} T. Such signals are routinely detected by SQUID systems.

The behavior of a SQUID can be understood by analysis of its circuit. Figure 3.4 shows two identical Josephson junctions connected in parallel and driven by a current source. An external applied magnetic flux Φ_a is threading through the SQUID loop [26]. The total current I applied to the SQUID can be written as

$$I = I_1 + I_2 \tag{3.45}$$

where I_1 is the current through the left arm of the SQUID and I_2 through the right (see Fig. 3.4). From current conservation in the left arm, for example, we have

$$C_1 \frac{dV_1}{dt} + I_{01} \sin\theta_1 + \frac{V_1}{R_1} = I_1 \tag{3.46}$$

Setting $\dot{\theta}_1 = {2eV_1}/{\hbar}$ from the ac Josephson relation for the left junction, we obtain for the total current through the left arm of the SQUID,

$$\frac{\hbar C_1}{2e}\frac{d^2\theta_1}{dt^2} + \frac{\hbar}{2eR_1}\frac{d\theta_1}{dt} + I_0 \sin\theta_1 = I_1 \tag{3.47}$$

Here, the resistor R_1 accounts for dissipative losses in the left junction (#1). These losses may occur from quasiparticle tunneling, tunneling of normal electrons due to the breakup

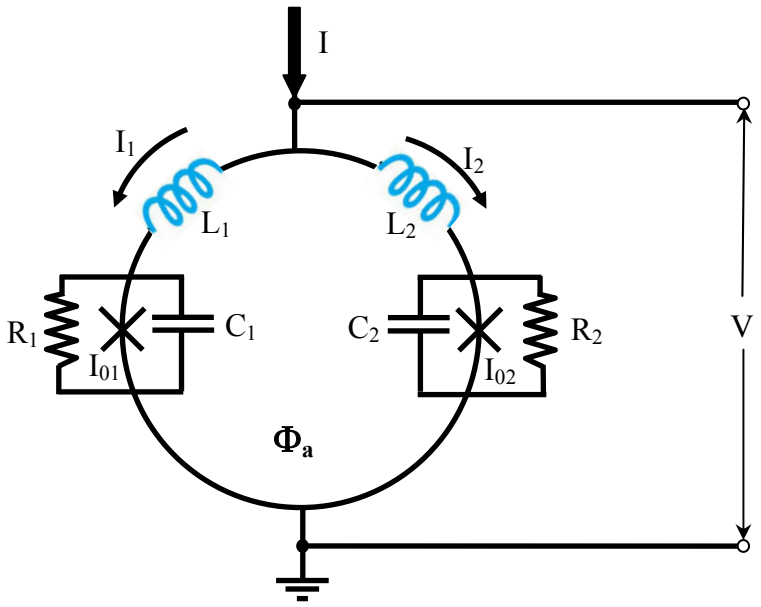

Fig. 3.4. Schematic of dc SQUID. Two Josephson junctions are connected in parallel in a superconducting loop of inductance $L = L_1+L_2$. Each junction has a critical current $I_0=I_{01}=I_{02}$ and is in parallel with its self-capacitance $C=C_1=C_2$ and shunting resistance $R=R_1=R_2$.

of Cooper pairs, or from current flow through a shunting resistance if one has been added to the device.

Similarly for the right arm of the SQUID, from current conservation we have

$$C_2 \frac{dV_2}{dt} + I_{02} \sin\theta_2 + \frac{V_2}{R_2} = I_2. \tag{3.48}$$

Setting $\dot{\theta}_2 = {}^{2eV_2}\!/_{\hbar}$ from the ac Josephson relation for the right junction we obtain for the total current I_2 through the right arm of the SQUID,

$$\frac{\hbar C_2}{2e}\frac{d^2\theta_2}{dt^2} + \frac{\hbar}{2eR_2}\frac{d\theta_2}{dt} + I_0 \sin\theta_2 = I_2 \tag{3.49}$$

Finally, we will require that wavefunction in the superconductor be single-valued. This imposes an additional constraint on the phase differences θ_1 and θ_2 [28]:

$$\theta_1 - \theta_2 = \frac{2\pi}{\Phi_0}(\Phi_a + LJ) = \frac{2\pi}{\Phi_0}\Phi_T. \tag{3.50}$$

Here Φ_T is the total flux through the SQUID loop, with contributions from the applied magnetic flux Φ_a and the current $J = I_1 - I_2;$ circulating in the SQUID loop. The flux from the circulating current can be written as LJ where $L_1 = L_2$.

Equations 3.47, 3.49 and 3.50 can be solved numerically to find the voltage across the SQUID as a function of the current I, the applied flux Φ_a and the time t [31]. The maximum critical current is found to be $I_0 = I_{01} + I_{02},$ and this occurs for $\Phi = n\Phi_0$ if $L_1 = L_2$. Figure 3.4 shows a schematic of the IV curves. Here, I have assumed the junction resistance changes from R to R_n when $V > 2\Delta/e$. In fact I_0 and R_n are related to each other by $I_0 R_n = (\pi\Delta/2e)\tanh(\Delta/2kT)$ [14].

As was the case for a single junction, a hysteretic SQUID can be biased in different regimes. If the current through the SQUID is below the critical current I_0, a supercurrent can flow through the loop with no voltage being developed. For $I > I_0$ a supercurrent can no longer be sustained through the junction, and a voltage will appear even when I is decreased much below I_0. One can represent the behavior of V as approximately,

$$V \cong \begin{cases} 0, \ for \left|I\right| < I_0 \ in \ the \ zero-voltage \ state \\ \dfrac{2\Delta}{e}, \ for \ I_r < \left|I\right| < I_0 \ in \ the \ voltage \ state \\ IR_n, \ for \ \ I > I_0, \end{cases} \tag{3.51}$$

and where R_n is the normal state tunneling resistance of the junction [14].

The vertical red curve in Fig. 3.5 at $V = 0$ represents the supercurrent across the junction for the zero-voltage state. The solid blue curve represents the behavior when the current has switched to the finite voltage state. The dashed blue curves in Fig. 3.5 show the switching between the zero-voltage state and the voltage state. Figure 3.6 shows measurements of the *IV* characteristic of a real Nb SQUID for different applied flux.

As in a single junction, the switching from the zero-voltage state to $2\Delta/e$ is extremely rapid. There are several time constants that arise in the analysis of the SQUID current, and it is not immediately obvious which determines this switching time. One time constant is set by the characteristic oscillation frequency of the system when it is subjected to a small perturbation. This plasma frequency is [14]:

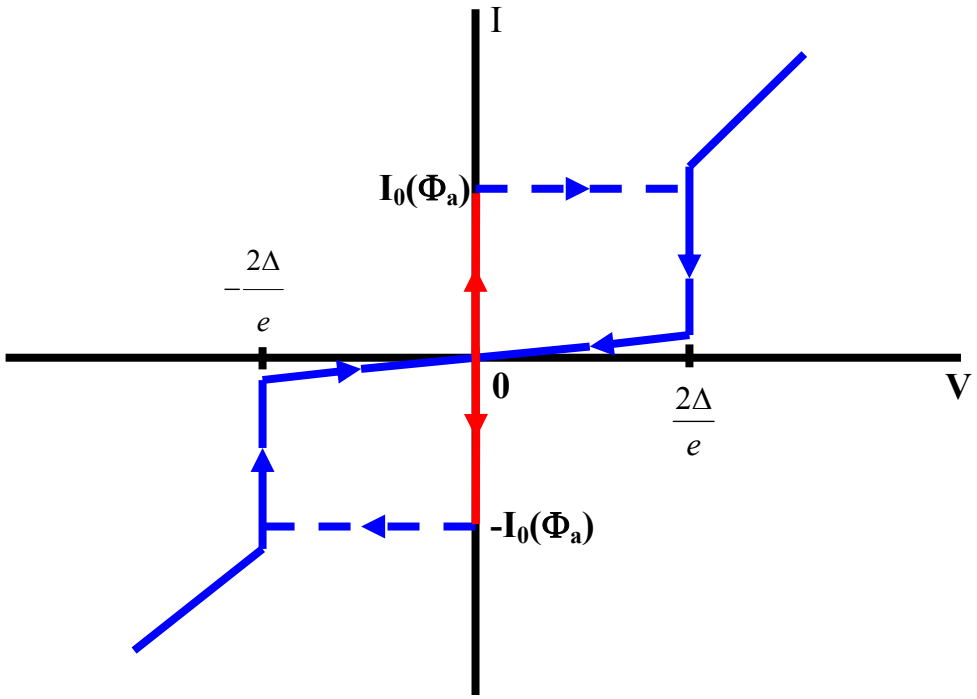

Fig. 3.5. Schematic of current-voltage relationship for a hysteretic SQUID. The critical current I_0 is a function of the flux Φ_a applied to the SQUID.

$$f_p = \frac{\omega_p}{2\pi} = \sqrt{\frac{I_0}{2\pi\Phi_0 C}}\left(1-\left(\frac{I}{I_0}\right)^2\right)^{1/4}. \qquad (3.52)$$

This defines a characteristic time scale $\tau_p = \frac{1}{\omega_p} = \sqrt{\frac{\Phi_0 C}{2\pi I_0}}\left(1-\left(\frac{I}{I_0}\right)^2\right)^{-1/4}$.

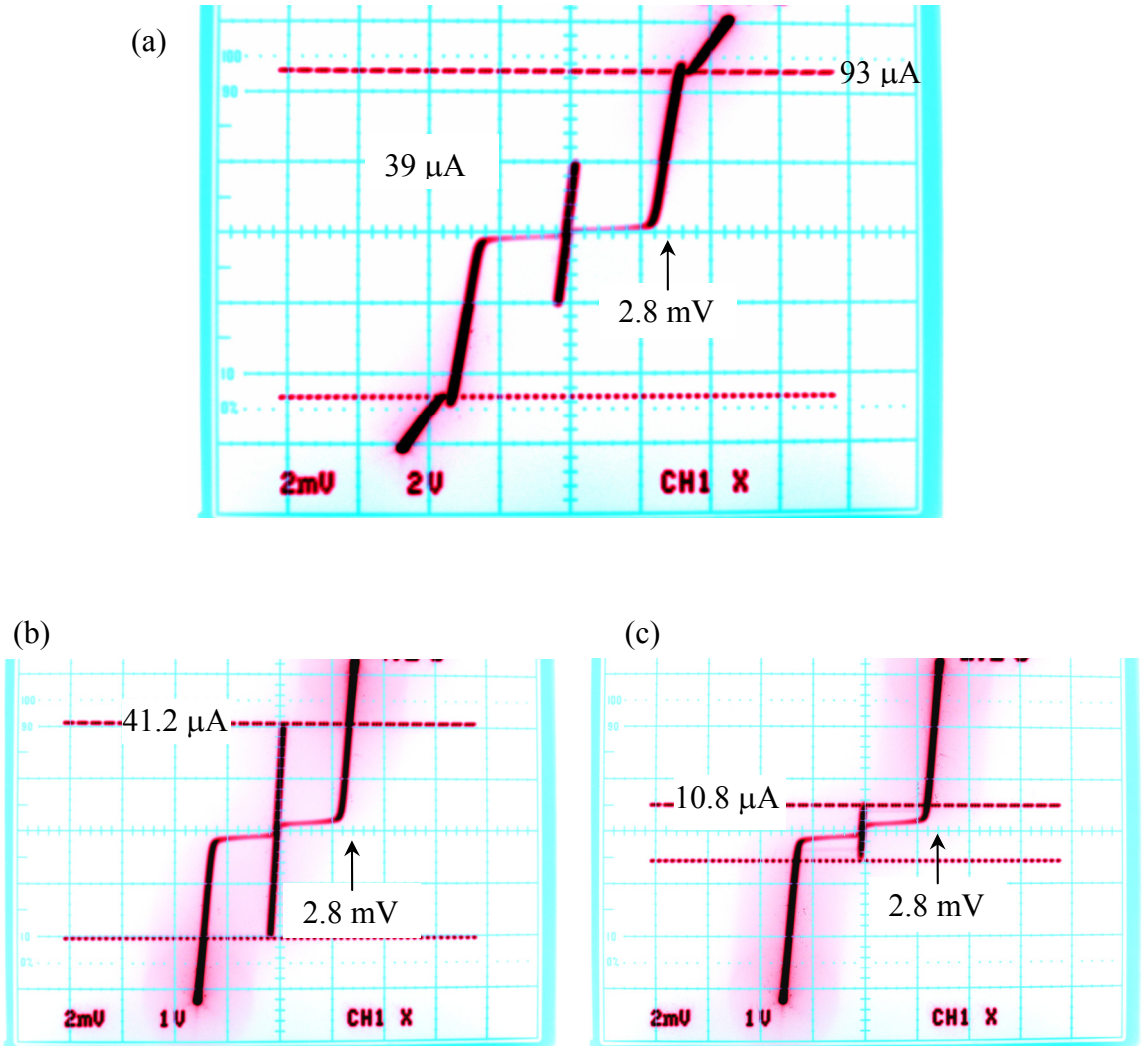

Fig. 3.6. (a) Measured current-voltage characteristic for Nb dc SQUID (Device HSQ_2) at 4.2 K showing (b) maximum and (c) minimum modulation with applied magnetic flux. (b) Maximum modulation at $\Phi = 0$ gives $I_{01} + I_{02} = I_0(\Phi_0 = 0) = 41.2$ μA. (c) Minimum modulation at $\Phi = \Phi_0/2$ gives $I_0(\Phi_0 = \Phi_0/2) = 10.8$ μA. Notice the switch to the voltage state takes place at approximately $2\Delta/e \approx 2.8$ mV.

Another time scale is set by the *RC* time constant $\tau_{RC} = RC$. We can construct a third time constant $\tau_c = \frac{2\Delta C}{e I_0}$ which is the time it takes the current supply set at $I = I_0$ to charge up the capacitance *C* to the gap voltage $2\Delta/e$. For a device with $\beta_c >> 1$, it is this last time constant that sets the time scale to switch from the zero-voltage state to the gap. Note that for

$$\frac{2\hbar I_0 R^2 C}{\Phi_0} >> 1 \tag{3.53}$$

we find:

$$\tau_{RC} = RC >> \frac{\Phi_0}{2\hbar I_0 R} >> \frac{\Phi_0 e}{2\hbar 2\Delta} \tag{3.54}$$

3.6 Simplified Model of SQUID Behavior

In the limit of zero voltage, the behavior of the SQUID simplifies considerably. In this limit, we can neglect current through the resistors and the capacitors and write the total current through the SQUID as

$$i = i_1 + i_2 = I_0 \sin\theta_1 + I_0 \sin\theta_2 \tag{3.55}$$

$$= 2I_0 \cos\left(\frac{\theta_1 - \theta_2}{2}\right)\sin\left(\frac{\theta_1 + \theta_2}{2}\right) \tag{3.56}$$

where we have assumed $I_{01} = I_{02} = I_0$ (see Fig. 3.7). Using the flux-phase relation (Eq. 3.49)

$$\theta_1 = \theta_2 + 2\pi n + \frac{2\pi\Phi}{\Phi_0} \tag{3.57}$$

we can rewrite the total current as given in Eq. 3.55 as

$$I = 2I_0 \cos\left(\frac{\pi\Phi}{\Phi_0}\right)\sin\left(\theta_1 + \frac{\pi\Phi}{\Phi_0}\right). \tag{3.58}$$

If the flux due to the circulating current is negligible, then the total flux Φ is just the externally applied flux Φ_a. So long as the condition $LJ << \Phi_a$ holds, the maximum current I_0 can be obtained by maximizing Eq. 3.61 with respect to θ_1. The minimum of the current happens when the derivative with respect to θ_1 of Eq. 3.61 vanishes and this takes place when

$$\cos\left(\theta_1 + \frac{\pi\Phi_a}{\Phi}\right) = 0. \tag{3.59}$$

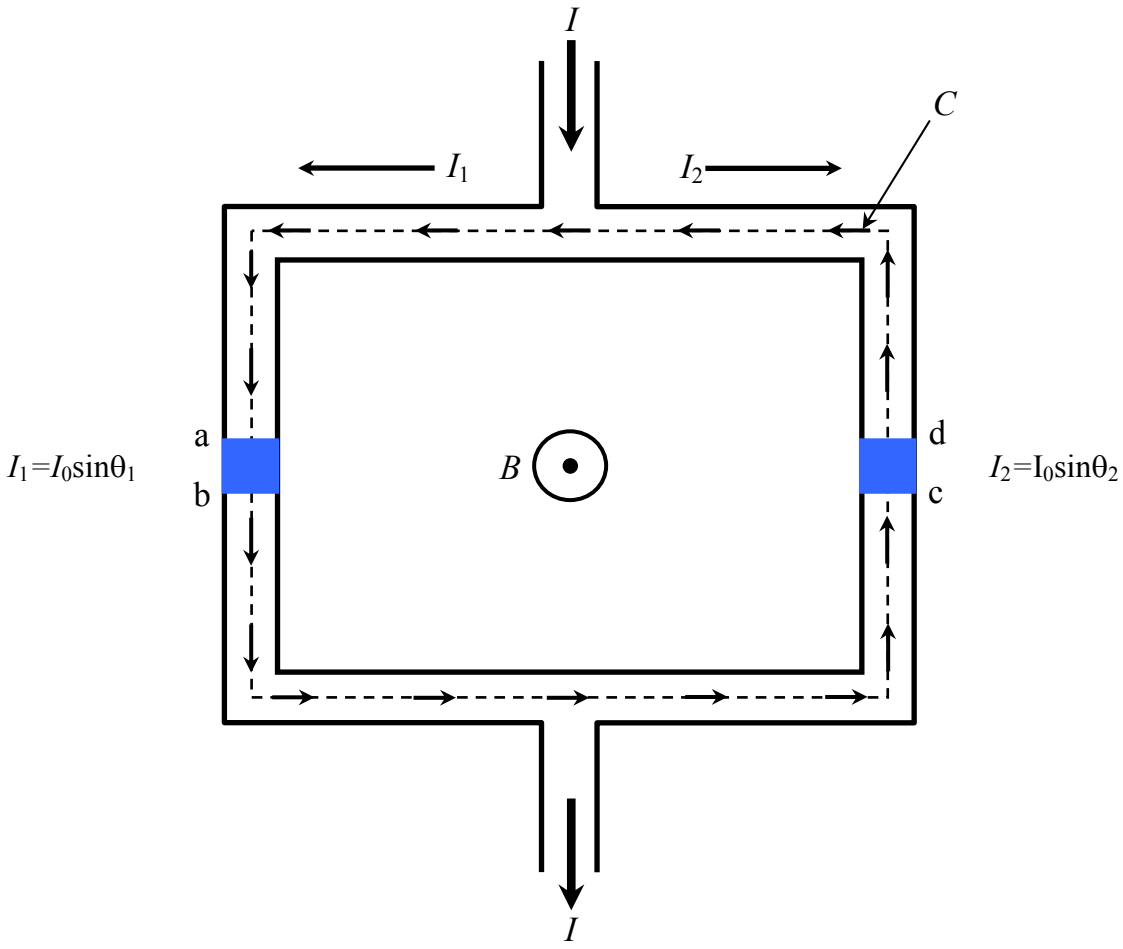

Fig. 3.7 Two identical Josephson junctions connected in parallel by superconducting wire. The integration path C is shown by the dashed line.

Thus, the maximum current, I_c is

$$I_c = 2I_0 \left| \cos\left(\frac{\pi \Phi_a}{\Phi} \right) \right| \tag{3.60}$$

which is periodic in the applied flux Φ_a with a maximum of

$$\Phi = n\Phi_0. \tag{3.61}$$

In general, the total magnetic flux is the sum of the flux generated by the flowing currents in the loop, and the externally applied flux Φ_a. In my SQUIDs I have designed two identical junctions and two identical sides of the loop. For $V = 0$, I can write the currents on each side of the loop as

$$I_1 = \frac{I}{2} + J \tag{3.62}$$

and

$$I_2 = \frac{I}{2} - J \tag{3.63}$$

The average current I results in no net flux in the loop, while the circulating current, $J = (I_1 - I_2)/2$ generates a flux LJ. Thus, the total magnetic flux is

$$\Phi = \Phi_a + LJ \tag{3.64}$$

or

$$\Phi = \Phi_a + \frac{LI_c}{2}\left(\sin\theta_1 - \sin\theta_2\right). \tag{3.65}$$

If this relationship is substituted into Eq. 3.61, one finds a complicated equation that for $L > 0$ can be solved numerically to find I_{max} as a function of Φ_a.

3.7 Nb SQUID

Figure 3.8(a) shows a close-up of the SQUID that I used in my SQUID microscope (Device HSQ_2). Each junction is 3 μm wide by 25 μm long, and the loop is a square washer with 10 μm inside length and 30 μm outside length. Figure 3.8(b) shows the overall SQUID chip with contact pads. The gold contact pads are 200 μm by 500 μm. The gold contact pads on the bottom and left-hand side of Fig. 3.8(b) are the current bias lines to the SQUID, and the top and right-hand side gold contact pads connect to a 1-turn coil that is fabricated on top of the SQUID loop and is used for applying magnetic flux to the SQUID.

The device was fabricated by Hypres, Inc [32]. The Hypres IC fabrication process uses only refractory materials, with the exception of the Ti/Pd/Au metallization layer used primarily for contact pads. Niobium is used as the superconducting material because of its relatively high critical temperature (T_c = 9.2 K) and because it can withstand being thermally cycled many times without suffering degradation. The fabrication process [24] starts with a 6-inch (150 mm) diameter oxidized silicon wafer as the substrate. The niobium/aluminum-oxide/niobium Josephson tunnel junctions are made by depositing an *in-situ* trilayer across the entire wafer and subsequently defining junction areas by 1x photolithography and etching. The trilayer base electrode of niobium is 135±10 nm thick. The next two layers of the trilayer are the insulating aluminum oxide tunnel barrier (1 nm) and Nb counter-electrode (200 nm). Electrical connection from one Nb layer to another Nb layer is accomplished by vertical channels (vias) that are also made of Nb through sputtered SiO_2 insulation layers. A detailed description of the electronic behavior of device HSQ_2 can be found in chapter 4.

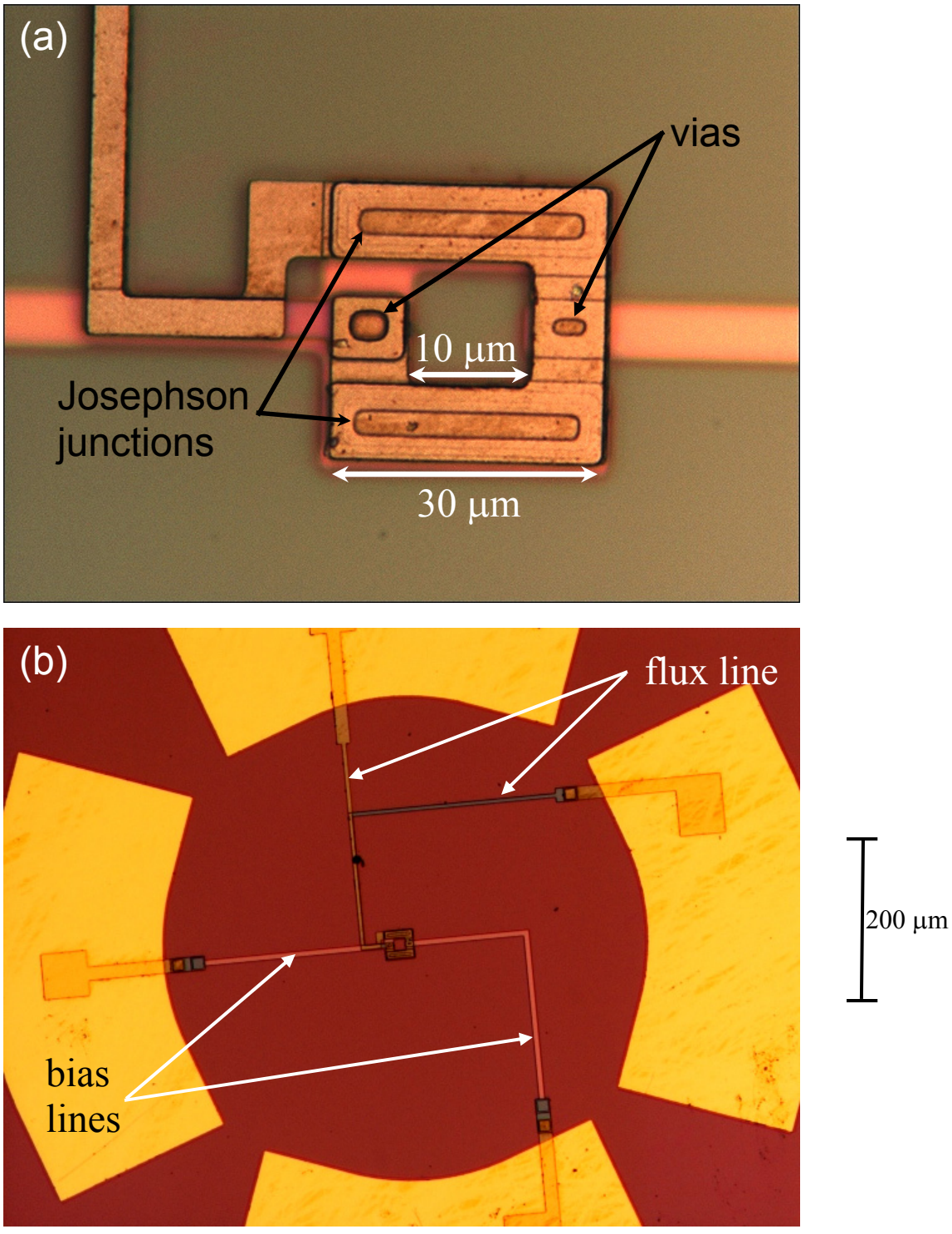

Fig. 3.8 (a) Close-up of SQUID (Device HSQ_2) with junctions at the top and bottom of the square washer. (b) Photograph of hysteretic dc SQUID showing four gold contact pads (200 μm x 500 μm) with SQUID in center.

3.8 Summary

In this chapter, I briefly reviewed the phenomenon of superconductivity and the basic physics involved in the Josephson effect. I also presented a simple derivation of the dc and ac Josephson effects. I then reviewed the resistively-shunted junction (RSJ) model for the Josephson junction and used this model to construct a model of the dc-SQUID. In this model, I obtained a set of coupled, nonlinear differential equations whose solution requires numerical methods. Finally, I described the classical behavior of the dc-SQUID and briefly described one of the devices I used.

Chapter 4: Designing SQUIDs for high-speed microscopy

4.1 Design Considerations

There are three main performance parameters that arise in designing a SQUID for a high-bandwidth scanning SQUID microscope: the spatial resolution, the temporal resolution and the flux resolution. In this chapter, I examine how each of these factors affects the design of the dc SQUID, starting with the spatial resolution.

4.1.1 Spatial Resolution

Since a SQUID is sensitive to the total magnetic flux that is linked through its loop, variations in the magnetic flux on scales less than the dimensions of the hole tend to be lost. However since magnetic field strength is inversely proportional to the distance from the source, this is not the only factor. Roughly speaking, the raw (unprocessed) spatial resolution s of a SQUID is set by the greater of the lateral dimensions b of the SQUID inner hole and its distance d from the magnetic source. In my system, $b \sim 30$ μm whereas typically I imaged with $d \sim 200$ μm, so the spatial resolution in an unprocessed image of magnetic field is limited by the SQUID-to-sample separation, i.e. $s \approx d$.

The detailed geometry of the SQUID can also affect the spatial resolution. In particular, when the line width w of the SQUID loop is equal or greater than inner hole size b, "Flux focusing" will channel some magnetic flux into the inner hole that would have otherwise not reached it. Flux focusing is due to the Meissner effect [1-3]. The result is that for holes with large line widths, the spatial resolution tends to worsen somewhat. On the other hand, larger line widths increase the SQUID's effective area

which increases the field through the SQUID hole and thus results in increased field sensitivity. In order to strike a balance between spatial resolution and field sensitivity one can determine the minimum spatial resolution and flux resolution required and then adjust inner and outer hole size accordingly.

The SQUID geometry also affects the SQUID inductance. Since the SQUID loop is superconducting, most of the current will tend to flow along the inner edge of the hole that forms the SQUID loop. This results in the SQUID's inductance being mainly determined by the size of the inner hole. Indeed Jaycox and Ketchen [4] have shown by numerical calculation that once the line width w of the loop conductor is equal to or greater than the length b of the inner side length of the square hole, the inductance for a square loop approaches a limiting value expressed by

$$L = 1.25\mu_0 b. \tag{4.1}$$

Due to the flux focusing, for a square hole SQUID washer of outer width $D = b + 2w$, the effective area is given by $A_{eff} = b \cdot D = b(b + 2w)$ [4,5]. Thus for a given effective area, the inductance can be decreased by decreasing the inner hole width b while increasing the line width w so as to keep fixed A_{eff} fixed.

4.1.2 Temporal Resolution

In order for the microscope to have adequate temporal resolution its bandwidth must be large enough. My aim is to use a SQUID to image magnetic fields from microelectronics which typically have operating frequencies up to 3 GHz. From the analysis of the SQUID presented in chapter 3, we saw that there are several time constants that arise. As in a single junction, the switching time from the zero-voltage state

to $2\Delta/e$ is extremely rapid and of the order $\tau_c = 2\Delta C/eI_0$ where C is the capacitance, I_0 the junction critical current, Δ the gap energy and e the charge of an electron. Another time constant is set by the ring-down time of the junction $\tau_{RC} = RC$. Yet another time constant is the Josephson time constant $\tau_J = \Phi_0/2\pi I_0 R$. Roughly speaking, the bandwidth is limited by the smaller of $1/\tau_{RC}$ and $1/\tau_J$, while τ_J determines the time it takes for the output signal to develop.

I note that the Stewart-McCumber Hysteresis parameter β_C [6,7] is defined as

$$\beta_C = \frac{\tau_{RC}}{\tau_J} = \frac{2\pi I_0 R^2 C}{\Phi_0} \tag{4.2}$$

For $1/\tau_{RC} < 1/\tau_J$, one finds $\beta_c > 1$ and

$$\Delta f < \frac{1}{\tau_{RC}} = \frac{1}{RC} = \frac{f_p}{\sqrt{\beta_C}}. \tag{4.3}$$

where the plasma frequency $f_p = \omega_p/2\pi$. The plasma frequency is related to the above two time constants by $f_p = \frac{1}{2\pi\sqrt{\tau_{RC}\tau_J}}$. For $1/\tau_{RC} < 1/\tau_J$, one finds $\beta_c < 1$ and

$$\Delta f < \frac{1}{\tau_J} = \frac{2\pi I_0}{\Phi_0} \tag{4.4}$$

where Δf is the SQUID bandwidth.

We can obtain another limit on the bandwidth by noticing that it must be less than the longer of the two time constants τ_{RC} and τ_J. Thus we can express an upper bound on the bandwidth Δf as

$$\Delta f < f_p = \frac{1}{2\pi\sqrt{\tau_{RC}\tau_J}} = \frac{1}{2\pi}\sqrt{\frac{2eI_0}{\hbar C}}. \tag{4.5}$$

I note that this upper bound on the bandwidth Δf does not depend on the shunt resistance of the Josephson junction. Further, in the above expression, the critical current I_0 and junction capacitance C are both approximately proportional to the junction area. Thus the ratio I_0/C is an intrinsic junction parameter that does not depend on the junction area and will be a constant for a given fabrication process.

4.2 SQUID Parameters and Noise

The ability of a SQUID to detect a small magnetic flux signal is limited ultimately by the noise in the SQUID. This noise can be categorized into two distinct types. The first type of noise is called "1/*f* noise" or excess low-frequency noise [8]. 1/f noise increases with decreasing frequency, with the noise power scaling inversely with the frequency *f*. In typical SQUIDs, 1/*f* noise is visible below about 100 Hz to 1 kHz. The impact of 1/*f* noise is important in SQUID applications where the signals are at low frequencies. In particular, NDE and biomagnetism require high sensitivity at low frequency, often lower than 10 Hz. On the other hand, the microscope I describe in this thesis operates from dc up to many orders of magnitude above the frequency where 1/*f* noise is visible. Since I am mainly interested in the high speed response of the system, I will ignore 1/*f* noise. The second source of noise is broad-band "white noise" that originates from Nyquist noise in any resistance in the circuit, including any resistance shunting the SQUID tunnel junction. White noise is also called intrinsic noise because it arises naturally from resistive components in the SQUID and cannot be reduced by changing materials or fabrication techniques. In the following discussion, I will assume that the performance is

not limited by external noise or by the read-out electronics or amplifiers attached to the SQUID.

Consider an ideal Josephson junction that is shunted by a resistance R (a shunt resistor) [see Fig. 3.3]. Provided the frequency $f < k_B T/h$, the Nyquist voltage noise power spectral density produced by the resistor is [9],

$$S_V(f) = 4k_B TR. \tag{4.6}$$

Equivalently, we can assume the noise is produced by a current noise source in parallel with the resistor with current noise power spectral density:

$$S_I(f) = \frac{4k_B T}{R}, \tag{4.7}$$

where f is the frequency, k_B is Boltzmann's constant, T is the temperature and R is the effective or shunt resistance. The dimensions for S_V and S_I are respectively voltage $\left(V^2\right)$ and current $\left(A^2\right)$ squared per unit bandwidth (Hz) [9]. If S_V is integrated over a bandwidth Δf, one finds the mean squared voltage in this bandwidth. Notice also that in their expressions S_V and S_I are independent of frequency, *i.e.* this is white noise.

The effects of this current noise on a junction can be simulated by adding a noise term $I_n(t)$ to Eq. (3.39). One obtains the Langevin equation [10]:

$$\frac{\hbar C}{2e}\frac{d^2\theta}{dt^2} + \frac{\hbar}{2eR}\frac{d\theta}{dt} + I_0 \sin\theta = I + I_N(t). \tag{4.8}$$

In the classical thermal limit, the noise current $I_n(t)$ has a white power spectral density given by the Nyquist current noise power spectral density Eq. (4.7). The noise term in Eq. 4.8 has the effect of causing the tilt of the washboard potential to fluctuate with time. This fluctuation results in three effects that I will need to consider.

First, when $I < I_0$ and the junction is in the zero-voltage state, from time to time thermal fluctuations will cause the total current $I + I_N(t)$ to exceed I_0 and the junction will escape to the voltage state. For an underdamped junction $(\beta_c > 1)$, this results in the junction voltage switching from zero to the gap voltage $2\Delta/e$. This is just the thermal activation over the barrier from the trapped state *t* the running state[10]. For an over-damped junction the noise term $I_n(t)$ causes random tilting of the potential and randomly produced voltage pulses. This shows up in the *I-V* characteristic curve as "noise rounding"; most of the time the particle or "phase ball" is confined to a potential well, but occasionally it makes a transition to the next well resulting in a small voltage pulse. In this case, for $I < I_0$, the time average of the voltage is nonzero.

Thus current noise reduces the observed current at which the device switches. We distinguish the switched current parameter I_0 from the switching critical current I_c. For a well-defined switched critical current I_c to be observable, the Josephson coupling energy should obey [11,12]:

$$E_J > 5k_BT, \tag{4.9}$$

where

$$E_J = \frac{I_0\Phi_0}{2\pi}. \tag{4.10}$$

From simple thermal considerations, we would expect $E_J \leq k_BT$, rather than the factor of 5 found in Eq. 4.9, which was found from numerical simulation by Clarke and Koch [12]. Combining equations 4.9 and 4.10, we will thus require that the junction critical current I_0 obey

$$I_0 > I_0^{\min} = \frac{10ek_BT}{\hbar}. \tag{4.11}$$

For a typical Nb junction temperature of $T = 4.2$ K one finds $I_0^{\min} = 0.9\mu A.$

The second major impact of Nyquist noise is that it leads to voltage noise across the SQUID. In the nonhysteretic limit $\beta_c << 1$ with the device in the voltage state ($I > I_0$), this noise is given by [13,14]

$$S_V(f) \cong \frac{4k_BTR_d^2}{R}\left(1+\frac{1}{2}\left(\frac{I_0}{I}\right)^2\right), \tag{4.12}$$

where f is the measurement frequency which is much less than the Josephson frequency f_J and R_d is the dynamic resistance of the SQUID $(R_d = \partial V/\partial I)$.

The third impact is that the Johnson noise current S_I causes fluctuations in the current flowing through the junctions and hence also will cause fluctuations in the measured switching current of a hysteretic junction. In my SQUID microscope I measure the switching current of the SQUID to keep track of the flux in the SQUID. In this case, flucuations in the measured critical current will lead to effective flucuations in the measured flux.

Following Tinkham, Eq. (4.8) can be used to obtain an expression for the effective flux noise density [15]. The critical current of a SQUID is similar to that of a single Josephson junction except that the critical current is modulated by the total magnetic flux through the SQUID loop. For a symmetric SQUID with $\beta = 2LI_0/\Phi_0 \ll 1$ the magnitude of the SQUID critical current is given by

$$I_C(\Phi) = 2I_0\left|\cos\left(\pi\frac{\Phi}{\Phi_0}\right)\right|, \tag{4.13}$$

Thus the critical current is modulated by the total magnetic flux Φ and is periodic with period Φ_0. The transfer function between the critical current and magnetic flux is given by $\left|\partial I_C/\partial\Phi\right| = \left(2\pi I_0/\Phi_0\right)\sin\left(\pi\Phi/\Phi_0\right)$ and thus the maximum transfer function is when $\Phi \sim \Phi_0/2$ where

$$\left|\frac{\partial I_C}{\partial\Phi}\right|_{\max} = 2\pi\frac{I_0}{\Phi_0} = \frac{\pi\beta}{L}, \tag{4.14}$$

and the expression is valid for $\beta \ll 1$. Using equations (4.7) and (4.14) we obtain for the effective magnetic flux noise power spectral density:

$$S_\Phi^{\min}(f) = \frac{S_I(f)}{\left|\frac{\partial I_C}{\partial\Phi}\right|_{\max}^2} \approx \frac{4}{\pi^2\beta^2}\frac{k_B T L^2}{R}, \tag{4.15}$$

where R is the shunting resistance across the junction. The above argument is only approximate and only valid in the limit of $\beta << 1$. Numerical simulations reveal for $\beta \sim 1$ that a SQUID in the voltage state has a flux noise density of [16,17]

$$S_\Phi(f) \cong \frac{18 k_B T L^2}{R}. \tag{4.16}$$

Other computer simulations on SQUIDs operated in the voltage state indicate somewhat higher values [1,12,17,18]. Nevertheless, all these results indicate that the flux noise decreases with decreasing temperature, decreasing SQUID loop self-inductance, and increasing resistance R.

4.3 Layout of Niobium SQUIDs

The SQUIDs that I designed and used were fabricated by Hypres, Inc., in Elmsford, New York [19]. HYPRES has been engaged in the development and commercialization of superconducting microelectronics since 1983, and has a complete self-contained superconducting microelectronics fabrication facility. Their standard niobium trilayer process is available to academic customers who submit patterns conforming to their design rules.

Two hysteretic SQUID devices were used in this thesis. The first SQUID device which was used on a dip probe and inserted into liquid helium I refer to as HSQ_1. That chip was made using design "spk3h" and was taken from Hypres Mask 292, Lot 6102, Wafer KL493, which was fabricated with their 1000 A/cm^2 process [19]. The second SQUID which was installed into the microscope I refer to as HSQ_2. That chip was made using design "umqc0205" and was taken from Hypres Lot 040605, Wafer KL820 and it was fabricated with their 30 A/cm^2 process [19].

Specifically the SQUIDs were fabricated using a Nb-AlO_x-Nb oxide trilayer process. The process includes three superconducting wiring layers and two additional metal layers fabricated on oxidized silicon substrates (see Table 4.1 for a summary of the SQUID parameters). Niobium has a superconducting transition temperature of T_c = 9.25 K and a gap voltage $2\Delta / e \cong 2.8 mV$ for temperatures $T << T_c$ [20]. Additionally, niobium trilayer junctions can have a large sub-gap resistance which allows for the fabrication of hysteretic Josephson junctions. This is critical for the pulse sampling measurement technique I use.

Fig. 4.1(a) shows the computer-aided design layout for the SQUID chip I used for my microscope. I created the layout using ICED [21] with Hypres design rules [19]. There are nine SQUIDs with two different layouts. The different layouts are intended for making measurements of magnetic flux in two different orientations. The SQUIDs along the main diagonal are designed to fit at the end of a tapered sapphire rod and measure magnetic flux vertically incident from the object of interest ($\boldsymbol{B}_z$). These SQUID are called "*z*-SQUIDs". The other six SQUIDs are designed to fit on the side of a shaped sapphire rod to measure magnetic flux perpendicular to the axis of the sapphire rod in (the "*x*" direction). These are called "*x*-SQUIDs". For all the data presented in this thesis, I used a *z*-SQUID.

Figure 4.1(b) shows a close-up view of the CAD layout for a *z*-SQUID. There are four Au contact pads. All the pads are approximately 180 μm x 400 μm. The lower and right most pads are the current bias lines. These also serve as the voltage output lines. The top and left most contact pads are the flux bias lines.

Fig. 4.2(a) shows a detailed view of the CAD layout for the Josephson junctions along with the vias and conducting paths which would form the bias and flux lines. The grid of red dots is spaced by 1 μm. The Josephson junctions are outlined in yellow and green rectangles which represent the contact via between layer I1B and the counter-electrode (junction area) layer I1A. The Josephson junctions outlined by the green rectangles are 3 μm x 25 μm. The blue outline represents the SQUID loop in the M3 metal layer. The red outline represents the single-turn flux loop designed in the M2 metal layer. The small cyan rectangle is the I2 layer which is a via connecting the M2 and M3 metal layers.

(a)

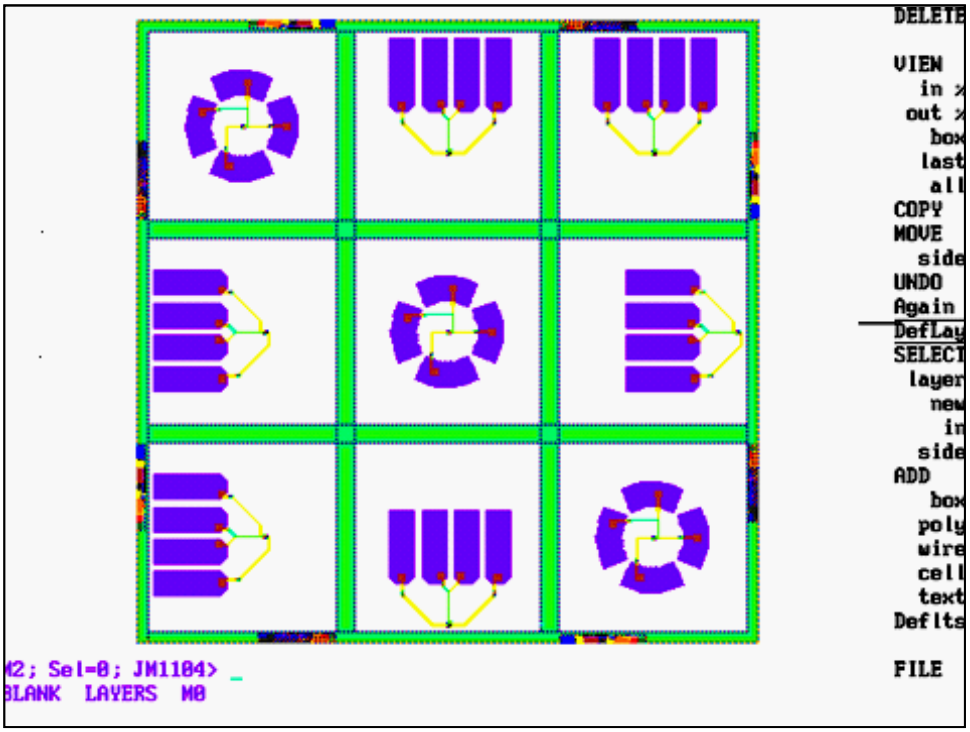

(b)

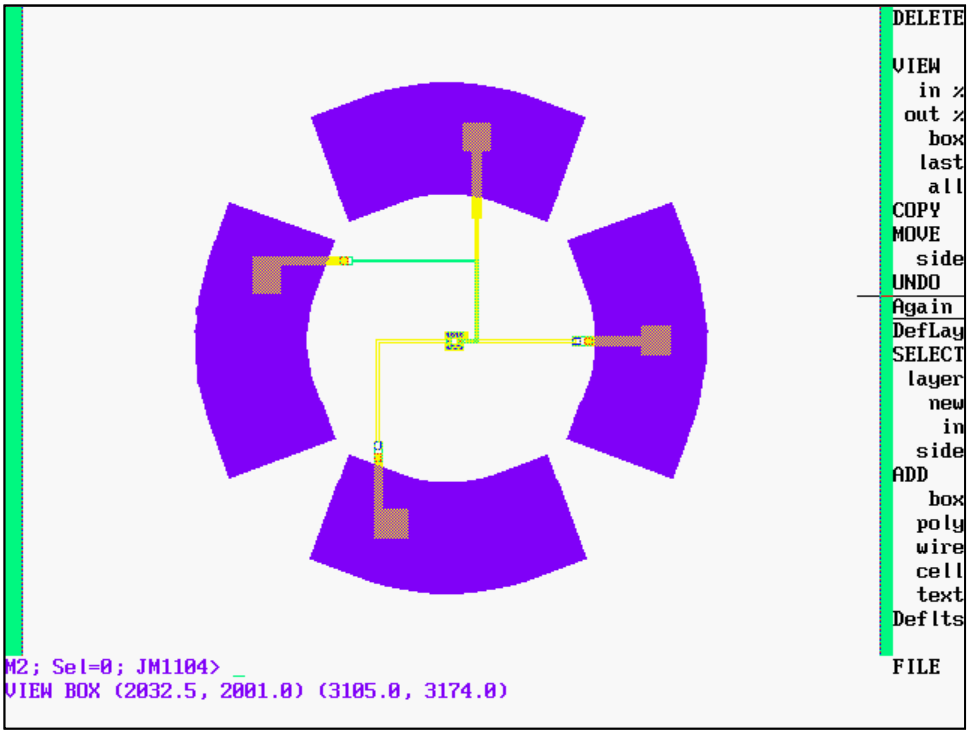

Fig. 4.1. (a) Design of nine HYPRES niobium SQUIDs on a silicon chip designed using ICED CAD software. (b) Close-up of ICED layout of a *z*-SQUID used for the microscope. Current and voltage lines are the bottom and right contact pads, and the left and top contact pads are for the flux coil.

(a)

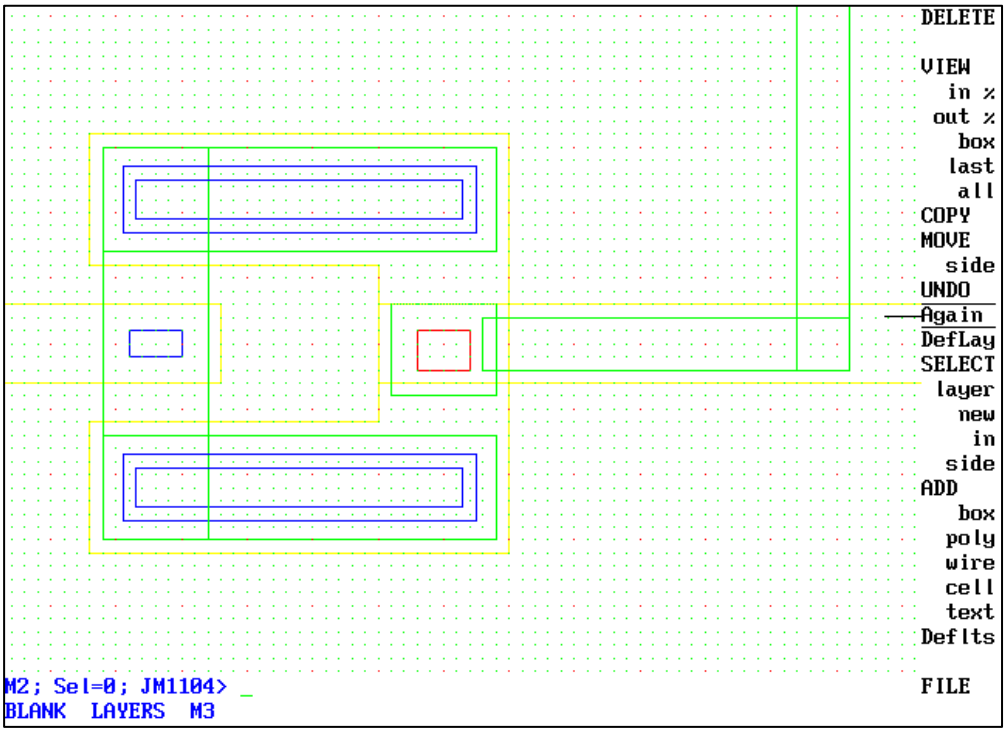

(b)

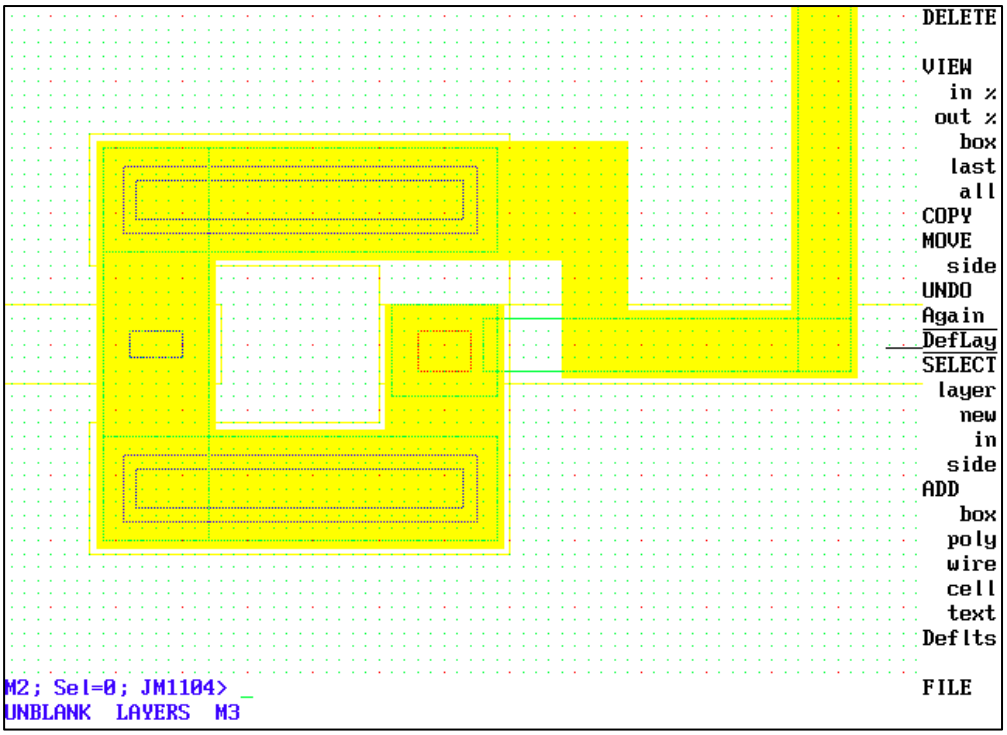

Fig. 4.2. (a) z-SQUID layout from ICED CAD software. (b) CAD layout of single-turn flux line highlighted in solid blue.
formula [19]

Figure 4.2(b) shows the single flux line highlighted in solid yellow. The inner square of the flux line is 12 μm x 12 μm and the width of the flux line is 9 μm. The input is over a metal layer M2 and the output line is directly over it, in layer M3. The coil itself is directly on top of the SQUID loop to produce good coupling.

4.4 Niobium SQUID Characteristics

Table 4.1 summarizes the nominal design parameters for the SQUIDs used in this thesis. With a SQUID inner hole of 10 μm x 10 μm the loop inductance is $L \simeq 15.7\, pH$. The outer dimension is 30 μm and this gives an effective pick-up area of 300 μm^2. The capacitance of the low-T_c junctions can be calculated using Hypres's capacitance

$$C_s = \frac{1.0}{24.7 - 2.0 \ln j_c} \ (pF / \mu m^2) \tag{4.17}$$

where C_s is the capacitance per unit area in pF/μm^2 and the critical current density j_c is in units of μA/μm^2 [19]. For the SQUID used in the microscope (device HSQ_2), the nominal critical current density was j_c = 0.3 μA/μm^2 and each junction area was 3 μm x 25 μm. This results in C_s = 2.8 pF and $2I_0$ = 41 μA. With R = 25 Ω, this gives

$$\beta_c = \frac{2\pi I_0 R^2 C}{\Phi_0} = 121 \tag{4.18}$$

The ratio I_0/C = 8.0x10^6 A/F and this gives a plasma frequency from Eq. 3.51 of $f_p \approx$ 20.4 GHz. For a hysteretic SQUID we can then use Eq. 4.3 to estimate that the SQUIDs bandwidth will be

$$\Delta f_{\beta_c} \leq \frac{f_p}{\sqrt{\beta_c}} \cong 1.85\, GHz. \tag{4.19}$$

Table 4.1: SQUID parameters. The capacitance and critical current of the junctions are C_s and I_0. The self-inductance of the SQUID loop is L. The SQUID screening or modulation parameter is β and the Stewart-McCumber parameter is β_c. The switching time is τ_c and the ring-down tine is τ_{RC}. The effective SQUID loop area is A_{eff} and Δf expected bandwidth

Parameters	SQUID #1	SQUID #2
Device name	HSQ_1	HSQ_2
Loop size (outer)	30 μm x 30 μm	30 μm x 30 μm
Loop size (inner)	10 μm x 10 μm	10 μm x 10 μm
Junction area	3 μm x 3 μm	3 μm x 25 μm
J_c	11.60 μA/μm^2	0.30 μA/μm^2
A_{eff}	300 μm^2	300 μm^2
L	15.7 pH	15.7 pH
C_s	0.45 pF	2.8 pF
β_c	90	121
β	1.6	0.34
$I_0=(I_{01}+I_{02})/2$ (designed)	104.4 μA	22.5 μA
$2I_0$ (measured)	180 μA	41.22 μA
ΔV	2.8 mV	2.8 mV
R	25 Ω	25 Ω
τ_J	13 ps	59 ps
τ_c	12 ps	352 ps
τ_{RC}	11 ps	71 ps
Δf_{β_C}	11.5 GHz	1.85 GHz
$S_\Phi^{1/2}$	6.0 x10^{-8} $\Phi_0/\sqrt{Hz}$	2.7 x10^{-8} $\Phi_0/\sqrt{Hz}$

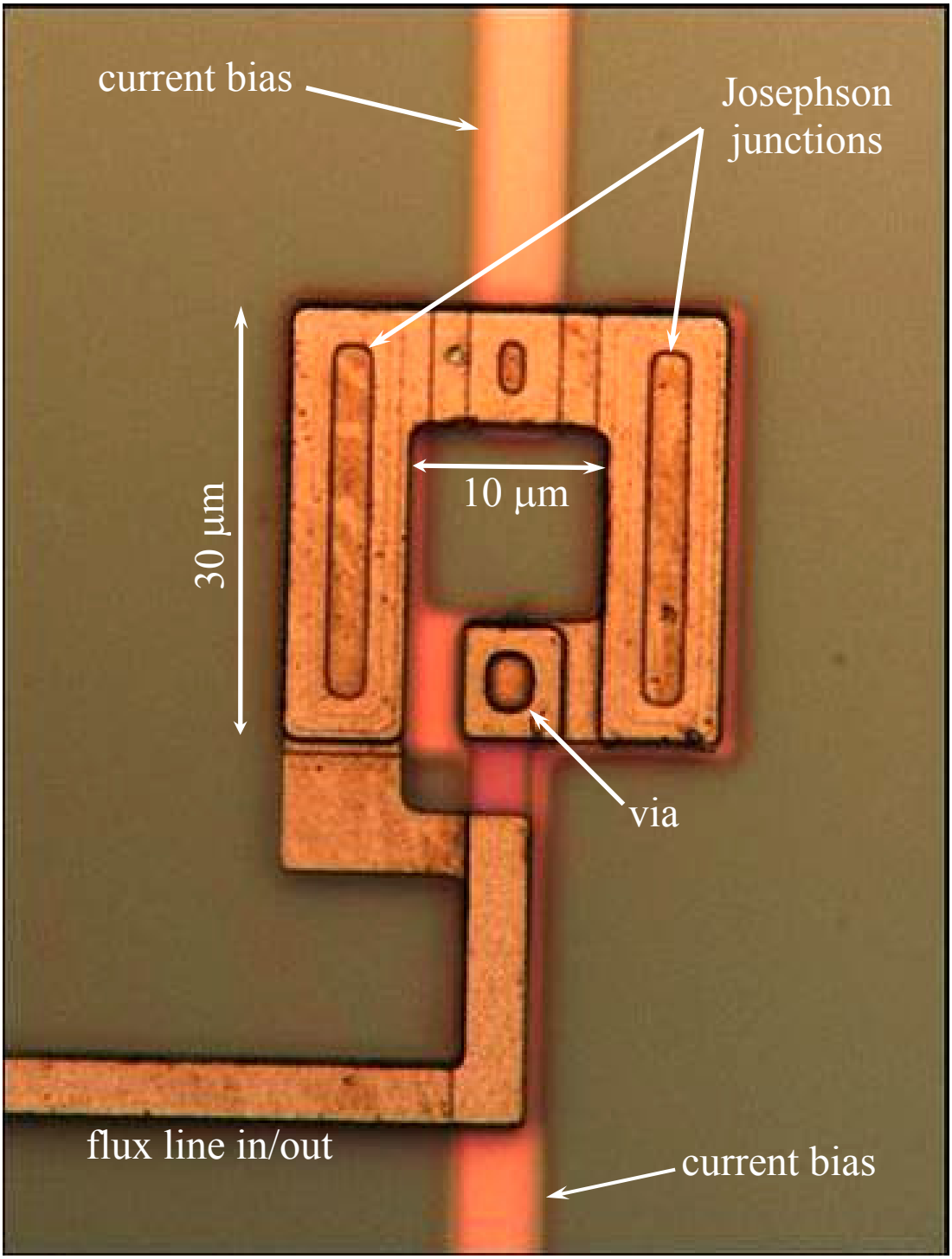

Fig. 4.3. Photograph of niobium z-SQUID (device HSQ_2). The center hole is 10 μm x 10 μm and the outer washer is 30 μm x 30 μm. The Josephson junctions are 3 μm x 25 μm Nb/AloOx/Nb trilayer junctions.

The magnetic flux noise can be estimated using equations (4.17) and (4.16). For $L \approx 15.7$ pH, $R_{subgap}=100\ \Omega$, and at a temperature of $T = 4$ K the rms magnetic flux noise power spectral density is about $\sqrt{S_\Phi}=5.5 \times 10^{-23}\ \mathrm{T \cdot m^2} \cong 2.7 \times 10^{-8}\ \Phi_0 / \sqrt{Hz}$. For a bandwidth of 2 GHz, this yields an rms flux noise of about $8.5 \times 10^{-3}\ \Phi_0$.

4.5 Summary

The SQUID I used was designed to have a bandwidth of approximately 3 GHz. This bandwidth can be understood by noting that a hysteretic SQUID acts in certain ways like an underdamped harmonic oscillator. For a SQUID to be hysteretic (underdamped) we require that the Stewart-McCumber parameter $\beta_c > 1$ [6,7].

For the SQUID I used, $C = 2.8$ pF and $2I_0 = 41.22\ \mu$A for each junction. Although the device is unshunted, it is wired directly to leads that connect to a 50 Ω coaxial line. Assuming an impedance $Z = 25\ \Omega$ divided equally across both junctions, I obtain $RC \approx 71$ ps. For signals that are applied much more slowly than this, any transient oscillations setup in the SQUID have time to damp out. With these junction parameters the Stewart-McCumber parameter is $\beta_c \approx 121$. The Q or quality factor of the SQUID is then obtained from

$$Q = \omega_p R C = \sqrt{\frac{2\pi I_0}{C \Phi_0}} R C = \sqrt{\frac{2\pi I_0 R^2 C}{\Phi_0}} = \sqrt{\beta_c} \cong 11. \tag{4.20}$$

The estimated bandwidth is then

$$\Delta f \cong \frac{f_p}{Q} \approx \frac{1}{2\pi R C} \approx 1.85\, GHz \tag{4.21}$$

where $f_p = \omega_p / 2\pi$ is the junction plasma frequency. For my device, the plasma frequency is $f_p \approx 20.4$ GHz. Finally, the switching time is:

$$\tau_c = \frac{\Delta}{2e}\frac{C}{I_0} \approx \frac{2.8\,mV}{20.61\,\mu A}(2.8\,pF) = 380\,ps. \tag{4.22}$$

I also described how the spatial resolution may be improved if the SQUID loop size is minimized. This also decreases the self-inductance of the loop which improves the flux sensitivity. The SQUID bandwidth can be increased by maximizing the ratio of critical current to capacitance, I_0/C. Finally, in order to have hysteresis in the *I-V* characteristic of the SQUID the Stewart-McCumber parameter β_c needs to be much larger than one. This entails maximizing the resistance of the shunt resistors across the junctions or by eliminating the junction shunt resistors altogether.

Chapter 5: Design of Large Bandwidth SQUID Electronics

In this chapter I describe how I designed the large bandwidth SQUID microscope electronics. I first review the operation of a conventional SQUID flux locked loop electronics and show it is too slow for the job at hand (detecting flux with a 1 GHz bandwidth). Next, an alternative technique is presented that is based on a technique used in recent quantum computing experiments. This new approach uses a hysteretic dc SQUID with pulsed bias current sampling. Finally, I discuss how I used this technique to measure magnetic flux by detecting the critical current of the SQUID.

5.1 Operation of a SQUID in a Flux-Locked Loop

The scanning SQUID microscope consists of the SQUID itself, the microscope cryogenics and vacuum assembly, the scanning assembly, and the SQUID electronics. The purpose of the electronics is to monitor the flux applied to the SQUID. The SQUIDs electronics needs to take into account the nonlinear response of the SQUID to flux and produce an output corresponding to changes in flux. One way to accomplish this is to use a negative feedback loop, referred to as a "Flux Locked Loop" (FLL) [1].

Operation of a conventional SQUID FLL requires a non-hysteretic current-biased dc SQUID [2,3]. Typically the bias current is set somewhat greater than I_c so the device is running in the voltage state at a flux of $\Phi \sim \Phi_0/4$. For low noise performance, the SQUID is coupled to a preamplifier through a cold transformer that matches the SQUID output impedance ($\sim R$) to the noise resistance ($R_{opt} = V_n/I_n$) of the preamplifier [3].

Figure 4.1 shows a typical FLL arrangement. A modulating magnetic flux of amplitude $\Phi_{ac} \sim \Phi_0/4$ is applied to the SQUID at a modulation frequency f_m that is typically in the range of 100 kHz to 500 kHz. The voltage signal from the SQUID is amplified and sent to a mixer that acts as a lock-in detector at the modulation frequency. The output of the mixer is sent to an integrator. The current output $I_{f/b}$ of the integrator is connected to the modulation feedback coil through a series resistor R_f. With the feedback loop closed, if a slowly varying magnetic flux $\delta\Phi_a$ is applied to the SQUID, the feedback circuit will generate an opposing flux $-\delta\Phi_a$ that almost exactly cancels the applied flux. In this case, the voltage across the resistor R_f is just $V_{out} = \frac{R_f}{M_f}\delta\Phi_a$, *i.e.* it is directly

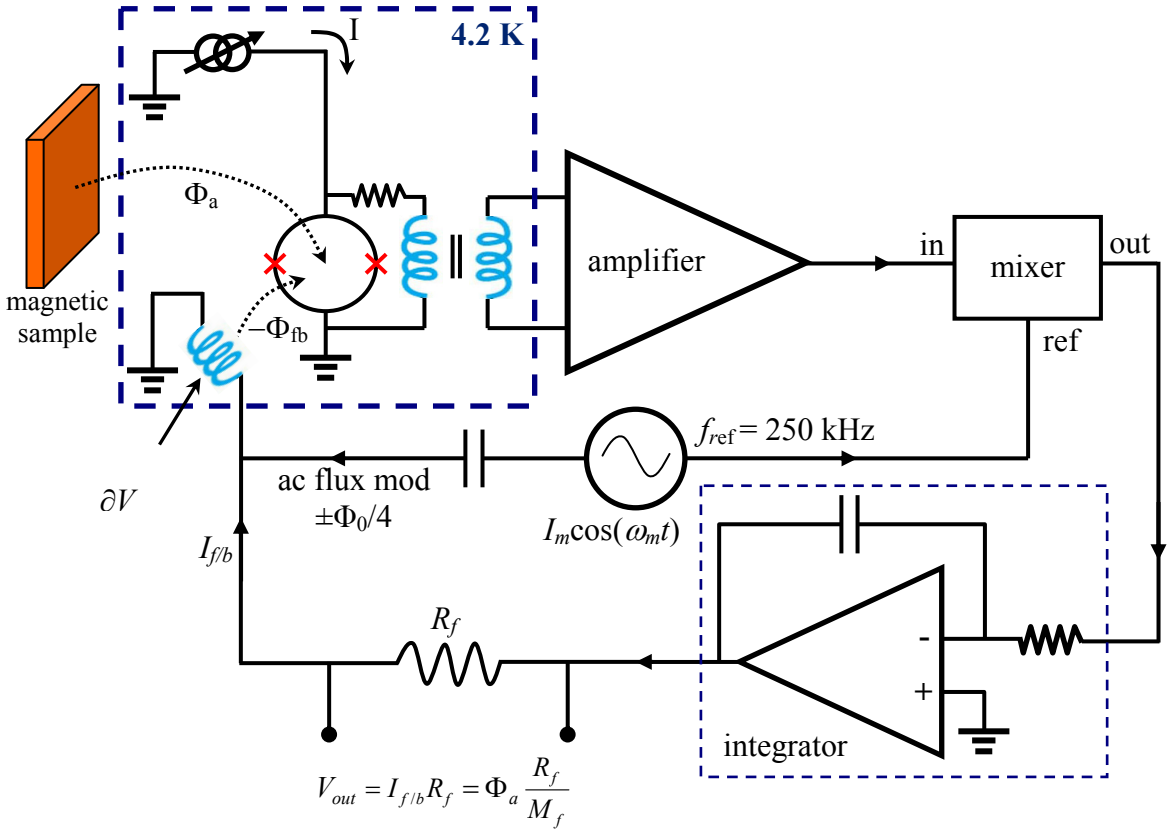

Fig. 5.1. Block diagram of ac modulated flux-locked loop (FLL) SQUID electronics.

proportional to the applied flux, and the total quasi-static (slowly varying) flux in the SQUID is kept constant or "locked". In this way one can measure changes in magnetic flux ranging from very small fractions of a flux quantum to many flux quanta.

To understand why I could not use a flux locked loop for my measurements, we need to take a closer look at how a FLL works. First, we will suppose there is no static flux applied and there is an oscillating modulation flux, $\Phi_m \cos(\omega_m t)$ applied to the SQUID by the feedback coil. As noted above, the modulation frequency is typically $f_m = \omega_m/2\pi$ = 100 kHz to 500 kHz. The flux modulation amplitude is adjusted to $\Phi_m = \pm\Phi_0/4$ (see Fig. 5.2). With the SQUID biased above its critical current, the voltage V across the SQUID is an even function of the applied flux Φ_a and the voltage is equal at the two turning points. Thus, with zero static flux in the SQUID, the time-dependent voltage across the SQUID will not have a component at the modulation frequency. As shown in Fig. 5.2(a), when the static applied flux is zero, the resulting SQUID voltage will vary with a frequency that is twice the modulation frequency, i.e. $f_{outpout} = 2f_m$ (plus higher harmonics). When this is fed to the mixer and multiplied at the reference signal at frequency f_m, the result will have no component at dc and the integrator will produce no change in its output.

Next, consider what happens if the static flux Φ_a is increased by a small amount ($\Delta\Phi << \Phi_0$). The total applied flux Φ then oscillates between $\Delta\Phi \pm \Phi_0/4$. The resulting voltage across the SQUID is shown in Fig. 5.2(b). In particular, there will now be a component at frequency f_m. The output of the mixer will then show a dc output (proportioanal to the amplitude of the components at f_m), and this will be subsequently integrated to produce a steadily increasing positive signal at the output of the mixer.

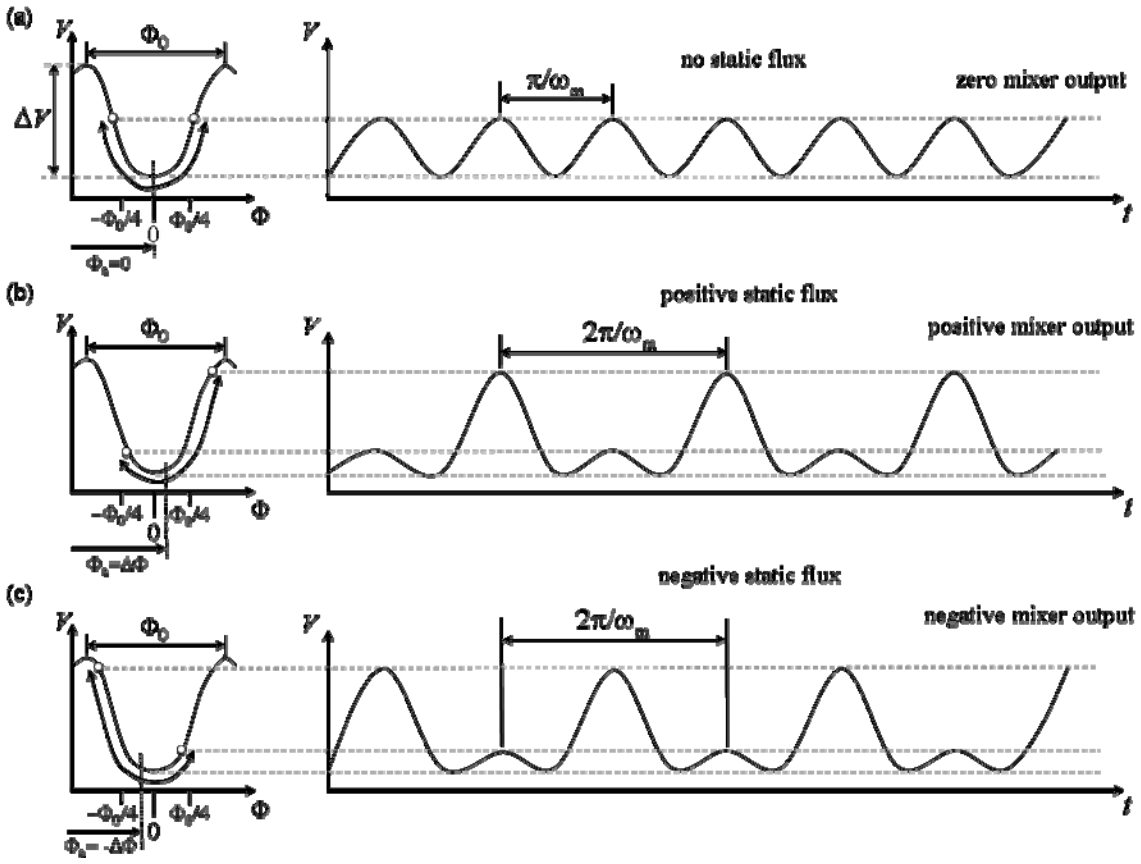

Fig. 5.2. Basic operation of a flux-locked loop (FLL) [4]. (a) V-Φ curve with modulation flux with zero-offset flux and corresponding voltage versus time t. (b) Positive offset flux. (c) Negative offset flux.

Finally, if the static flux is decreased by a small amount $-|\Delta\Phi|$, the total flux Φ again oscillates between $\Delta\Phi \mp \Phi_0/4$. The voltage across the SQUID in this case is shown in Fig. 5.2(c), and results in the mixer output being negative and the integrator output steadily decreasing.

The last step in the FLL involves feeding back to the SQUID a flux proportional to the negative of the output from the mixer. This acts to oppose the applied flux. Provided the overall loop gain (SQUID, amplifier, mixer, integrator) is high enough, the integrator output will keep changing until the feedback flux has cancelled the applied

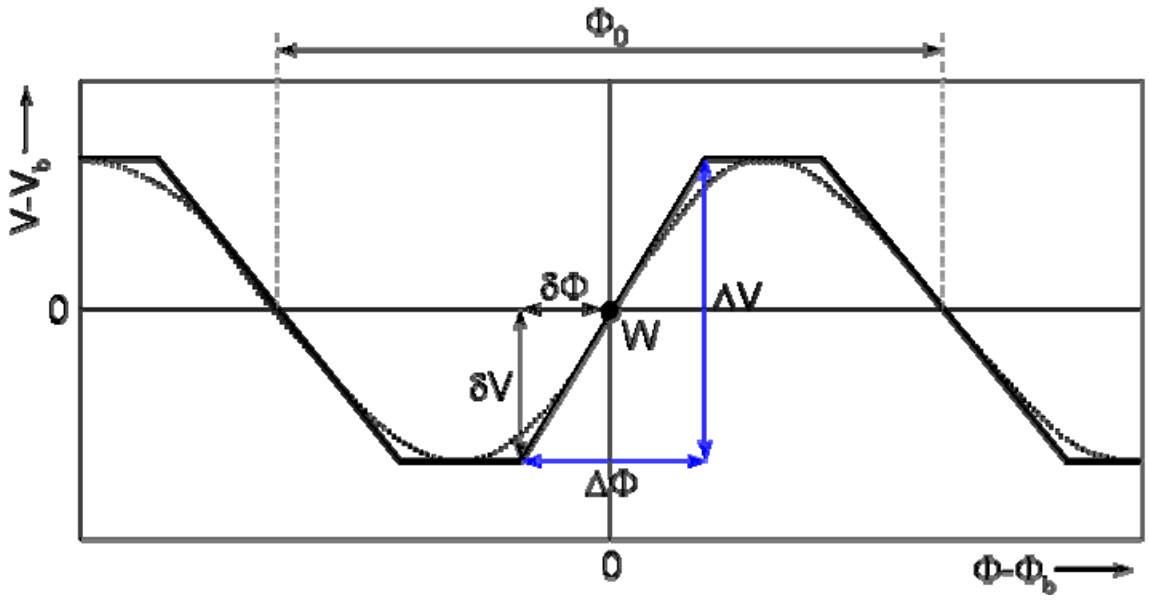

Fig. 5.3. Characteristic voltage-flux SQUID response, idealized (solid line) and real (dashed line).

flux. Thus, the FLL acts so that a given small change in applied magnetic flux $\Delta\Phi$ will generate an opposing flux that nearly exactly cancels the original applied flux change.

5.2 Limitations of the Flux-Locked Loop

To understand the limitations of the flux-locked loop, we now consider a simple model. In this simplified model, the SQUID is assumed to be an infinitely fast flux-to-voltage converter with a periodic V-Φ characteristic (see Fig. 5.3). The straight line segments in Fig. 5.3 are piecewise line approximations to a real V-Φ characteristic (dotted line). We assume that at the working point W the voltage V across the SQUID is equal to the bias voltage V_b, and the applied flux Φ in the SQUID loop is equal to the bias flux Φ_b. Typically, the usable voltage swing $2\delta V$ and the voltage-flux transfer function $V_\Phi = (\partial V / \partial \Phi)_W$ at the working point are kept as large as possible to simplify the readout electronics. If the working point lies symmetrically between the minimum and maximum

voltage of the V-Φ characteristic, then ΔV is equal to the usable voltage swing $2\delta V$. Also, around the working point W (see Fig. 5.3), the SQUID has a roughly linear characteristic in the flux range $\pm\Phi_{lin}/2$.

We can now analyze the dynamic behavior of a FLL using the closed-loop model depicted in Fig. 5.4 [5,6]. The model is composed of three basic components: the SQUID, a preamplifier, and a one-pole integrator (an amplifier with a limited bandwidth). The input is the applied flux Φ_a and the output is the feedback flux Φ_{fb}. The total flux in the SQUID is just

$$\Phi_e = \Phi_a - \Phi_{fb}, \tag{5.1}$$

which we can think of as being the "error" flux. The error flux needs to remain within $\pm\Phi_{lin}/2$ in order for the SQUID to behave as a linear element; keep in mind that the error flux signal saturates when $|\Phi_e| > \Phi_{lin}/2$.

The open loop gain $G_0(f)$ of the open feedback loop, which includes the gains of the SQUID, integrator and any preamplifier, can be represented by

$$G_0(f) = \frac{f_1}{if} \tag{5.2}$$

where f_1 is the unity-gain frequency of the open feedback loop and where $i = \sqrt{-1}$.

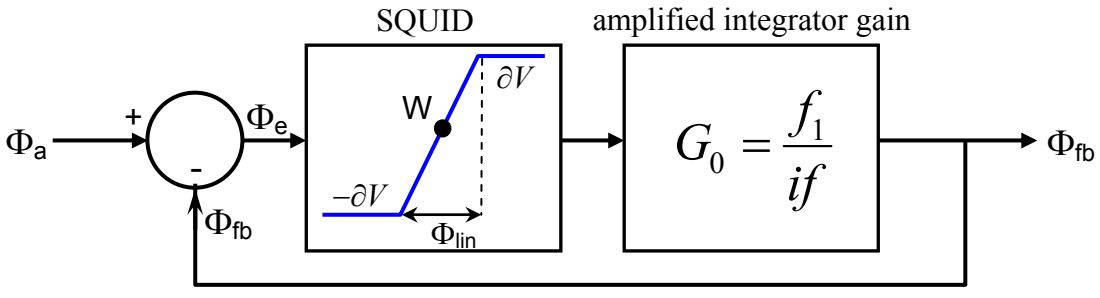

Fig. 5.4. Simplified model of the flux-locked loop [6].

This assumes a 1-pole integrator, which is fairly typical of FLL's. We can also write the open-loop gain as

$$G_0(f) = \left(\frac{V_\Phi M_f}{R_f} \right) \frac{A}{if} \tag{5.3}$$

or

$$f_1 = \frac{A V_\Phi M_f}{R_f}. \tag{5.4}$$

where V_Φ is the flux-to-voltage transfer function of the SQUID, M_f is the mutual inductance between the SQUID and its feedback coil, A is the gain of the integrator and preamplifier at 1 Hz, and R_f is the feedback resistor. For example, if R_f= 10 kΩ, M_f= 210 pH, and $V_\Phi = R/L = 10 \mu V / \Phi_0$ and A=1000, the unity gain frequency is f_1=100 kHz.

The closed loop gain $G(f)$ of the FLL can be written as

$$G(f) = \frac{\Phi_{fb}}{\Phi_a} \tag{5.5}$$

where $\Phi_{fb} = G_0(f)\Phi_e = G_0(f)(\Phi_a - \Phi_{fb})$. Thus

$$G(f) = G_0(f)\left(1 - \frac{\Phi_{fb}}{\Phi_a} \right) = G_0(f)(1 - G(f)). \tag{5.6}$$

Solving for the closed loop gain, we find

$$G(f) = \frac{G_0(f)}{1 + G_0(f)} = \frac{1}{1 + if/f_1}. \tag{5.7}$$

Examination of Eq. 5.7 reveals that the closed-loop frequency response $G(f)$ with an ideal one-pole integratror is identical to that of a first-order low-pass filter with a 3-dB cutoff frequency $f_c = f_1$. From Eq. 5.7 the absolute value of the closed-loop frequency response is

$$|G(f)| = \sqrt{\frac{1}{1+\left(f/f_1\right)^2}}. \tag{5.8}$$

Notice that the closed loop gain depends on the unity-gain frequency. Figure 5.5(a) shows a plot of the frequency response [Eq. (5.8)] of the closed-loop gain for various values of the reduced unity-gain frequency f_1.

In principle, it seems that one could obtain a FLL with an arbitrarily large bandwidth simply by increasing the f_1. However, in practice this is not possible. One limitation to the bandwidth is the delay time in the feedback loop. The delay time is the total time propagation delay in the transmission lines between the SQUID and the room-temperature feedback electronics. The delay time t_d (or dead time) causes phase shifts at high frequencies. For example, if we assume a 1 m long transmission line connecting the SQUID to the room-temperature electronics, a typical delay time is $t_d \approx 10$ ns. A one-pole integrator feedback loop with delay-time has a closed-loop gain given by [5,6]

$$G_0(f) = \frac{f_1}{if} e^{-i2\pi f t_d}. \tag{5.9}$$

From Eqs. (5.7) and (5.9) the absolute value of the closed-loop frequency response is [5,6]

$$G(f) = \frac{1}{\sqrt{1+\frac{f}{f_1}\left(\frac{f}{f_1} - 2\sin\left(2\pi f_1 t_d\right)\right)}}. \tag{5.10}$$

For low frequencies $f \to 0$, the closed-loop gain [Eq. (5.10)] to second order is given by

$$|G(f)| = 1 - \frac{1}{2}\left(1 - 4\pi f_1 t_d\right)\left(\frac{f}{f_1}\right)^2. \tag{5.11}$$

For $f_1 t_d = 1/4\pi = 0.08$ the closed-loop response is optimally flat, *i.e.*, has no resonance peak. The corresponding system bandwidth is

$$f_{3dB,\max} = \frac{0.18}{t_d}, \tag{5.12}$$

and the corresponding unity bandwidth is [5,6]

$$f_{1,\max} = \frac{f_{3dB,\max}}{2.25} = \frac{0.08}{\tau_d}. \tag{5.13}$$

Figure 5.5(b) shows a plot of the gain curves in this case. Attempting to use a higher f_1 will yield an increasingly larger resonance peak [see Fig. 5.5(b)] until the system starts to undergo self-oscillation (positive feedback) at the resonance.

The above equations give a practical estimate of expected SQUID system bandwidth. For example, if the SQUID system has room temperature electronics and the distance between the SQUID and electronics is approximately 1 m, then the bandwidth is limited to about 20 MHz. Further, suppose we use the above model to design a digital SQUID with on-chip feedback in order to further reduce the delay time t_d. In this case the loop delay is minimized due to the on-chip feedback design, but even with t_d = 1 ns the expected bandwidth is increased to 180 MHz. Finally, from Eq. 5.13, we see that to increase the bandwidth of a SQUID system up to 1 GHz, the time delay t_d would need to be reduced minimized down to 180 ps or less. Needless to say this would be very challenging to do with conventional electronics, and we also would need to be able to run the circuit at cryogenic temperatures.

The bandwidth of any feedback loop such as an FLL is also limited by the Nyquist sampling criterion [7]. This criterion says that the sampling modulation frequency (f_m in our case) must be at least twice the signal frequency. Also, for the

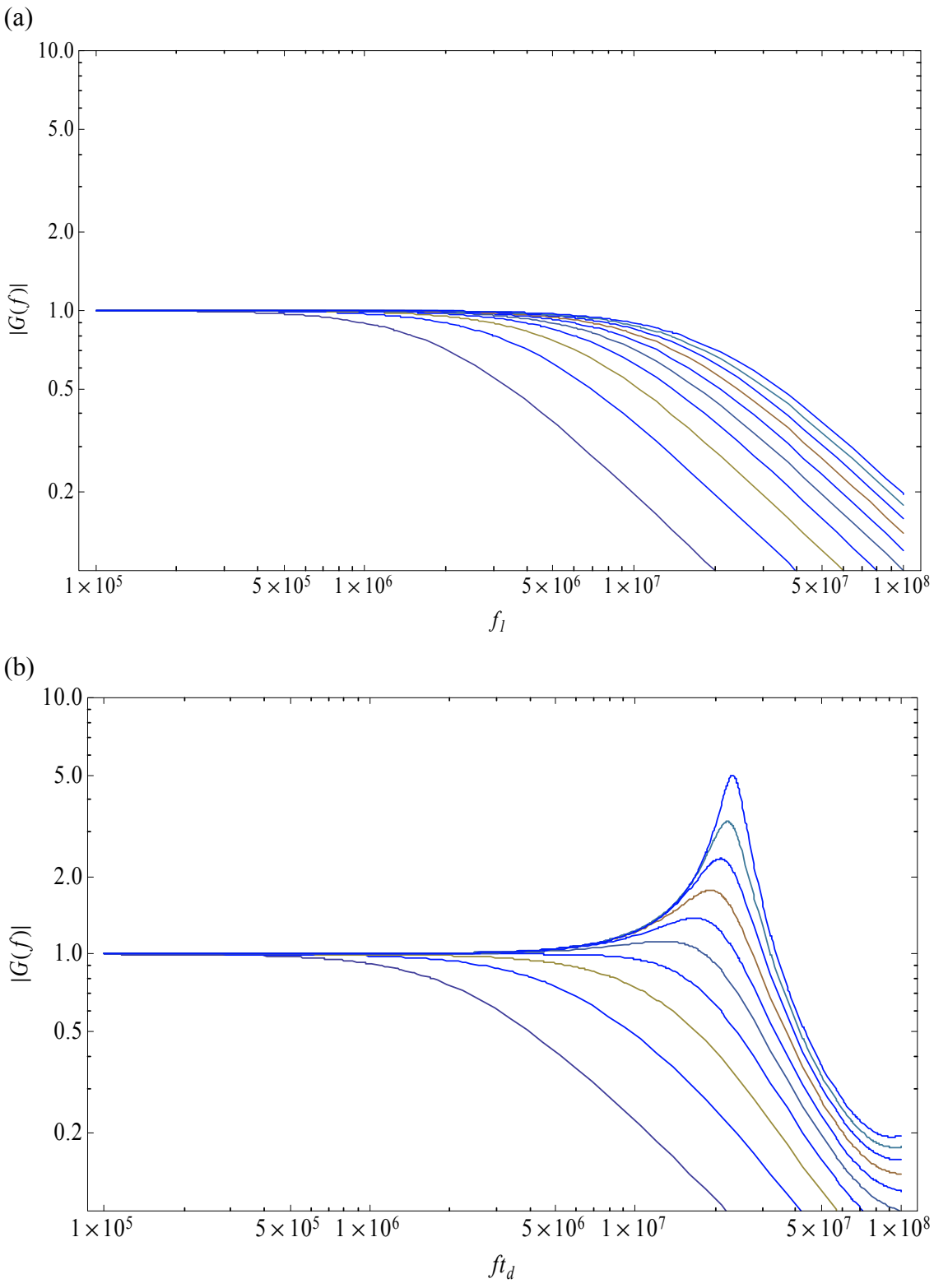

Fig. 5.5. (a) Closed-loop gain of the FLL for f_l= 2,4,6,...,20MHz, and no time delay. (b) Closed loop gain $G(f)$ for reduced frequency f_l values range from 2 to 20 MHz in steps of 2 MHz from left to right for a time-delay t_d = 10 ns.

feedback to be effective at a given frequency, one needs the open loop gain G_0 at that frequency to be much greater than one. Further, in order to maintain loop stability the open loop gain G_0 of the loop – including the SQUID, amplifier and integrator – should roll-off like 1/ω at $|G_0| = 1$. To reach a 1 GHz bandwidth these conditions imply a modulation frequency of at least 2 GHz and an amplifier with a well-controlled frequency response from 0 Hz up to about 10 GHz. To state the problem in simple terms, the feedback electronics must be able to feed back corrections for slowly varying signals as well as high frequency signal. In practice it is very hard to achieve such a wideband frequency response while maintaining low noise operation, which means this approach is not technologically viable.

5.3 A Hysteretic dc SQUID with Pulsed Current Sampling

Instead of attempting to build a FLL with a GHz bandwidth, a new approach was sought. This meant abandoning the conventional readout electronics and FLL feedback scheme. Instead, I chose a sampling technique that is similar to an approach used in recent quantum computing experiments [8,9]. In this scheme, a short bias current pulse is sent to a hysteretic dc SQUID. During the pulse the SQUID will either stay in the zero voltage state or switch to the voltage state, with the switching depending on when the current pulse exceeds the SQUIDs critical current $I_c(\Phi_a(t))$ at the time t the pulse is applied. Only if the critical current of the SQUID is lower than the pulse amplitude will a voltage appear across the SQUID. Since the critical current I_c of a SQUID depends on the flux Φ_a at time t, by monitoring I_c at time t we can infer Φ_a at time t.

In practice, one must send many current pulses to deduce the critical current precisely. For example, Fig. 5.6 illustrates how the critical current can be measured as a function of applied static flux using a pulse approach. With the flux fixed, one sends a brief current pulse to the SQUID. The SQUID is then checked to see if it switched to the voltage state. If it does, this is recorded as a "count". This is repeated of order of 10^4 times to get a well-defined switching probability for a given current pulse size. I then increase the pulse size and again determine the switching probability. I keep repeating this process until the pulse is so large that the SQUID is switching during every pulse (red in Fig. 5.6). For small amplitude pulses, the device never switches (blue in Fig. 5.5). The critical current I_c can be determined as the current pulse amplitude that yields switching 50% of the time. Figure 5.5(b) shows a false-color plot of such switching data where I measured the response as a static flux Φ_a was varied by several Φ_0. From such a plot I can directly measure the critical current and calculate the transfer function $\partial I_c / \partial \Phi_a$ at any flux bias.

The above process is also the basic idea behind measuring a rapidly varying flux signal [see Fig. 5.7]. To measure a rapidly varying flux, the SQUID is biased with a static flux at approximately one-quarter flux quantum (where I_c changes rapidly with Φ_a) and with current somewhat below the critical current. If a small rapidly varying magnetic flux signal is present [see Fig. 5.7(a)], this will modulate the critical current [see Fig. 5.7(b)]. A current pulse of about 400 ps duration is then applied to the SQUID. If the amplitude of this pulse (and any static bias current) is less than $I_C\left(\Phi(t)\right)$, the SQUID does not switch, implying that $I_C(\Phi(t) > I_{pulse}$ (see Fig. 5.6(c)).

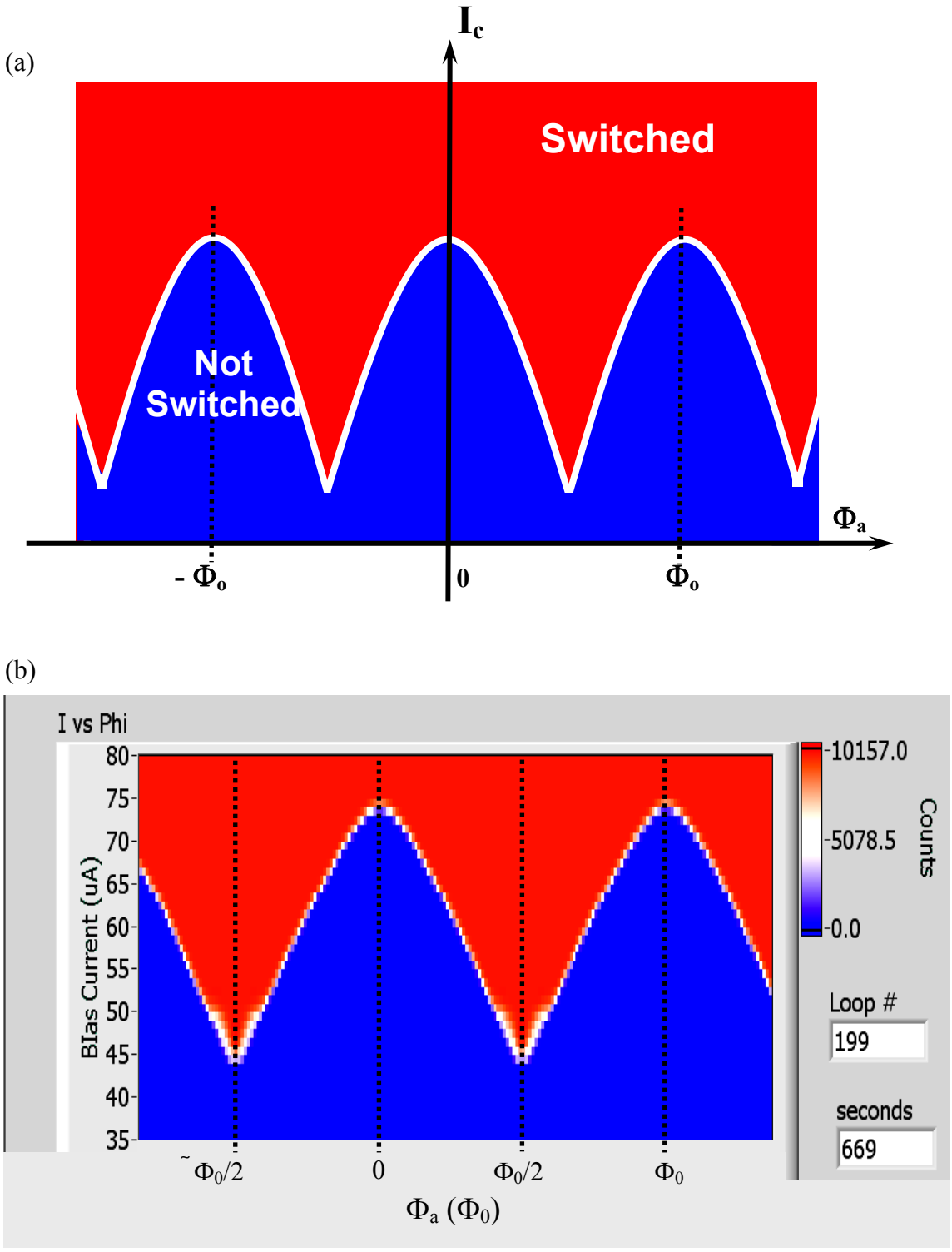

Fig. 5.6. (a) Schematic of SQUID switching current versus applied flux. (b) False-color plot showing measured number of switching events versus current (*y-axis*) and flux (*x-axis*).

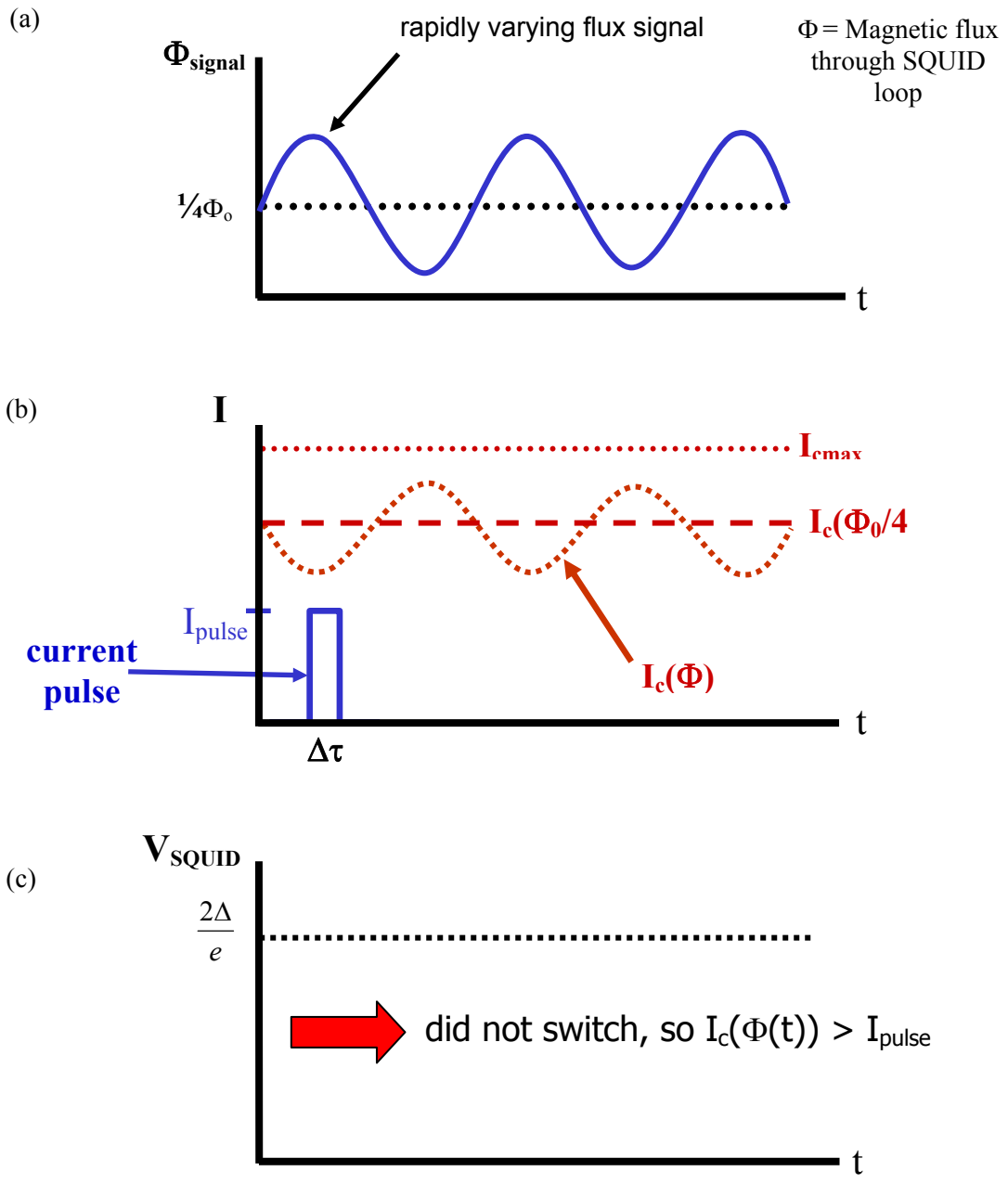

Fig. 5.7. Pulse sampling technique for measuring a small, rapidly time-varying flux signal, $\Phi_{signal}(t)$ applied to the SQUID loop. (a) SQUID is biased at ¼ Φ_0, and a small time-varying flux signal is generated by a sample. (b) A short current pulse I_{pulse} is applied to the SQUID and (c) if the amplitude of this pulse is less than the flux modulated critical current, the SQUID does not switch and the voltage across the SQUID is effectively zero, *i.e.* $I_c(\Phi(t)) > I_{pulse}$.

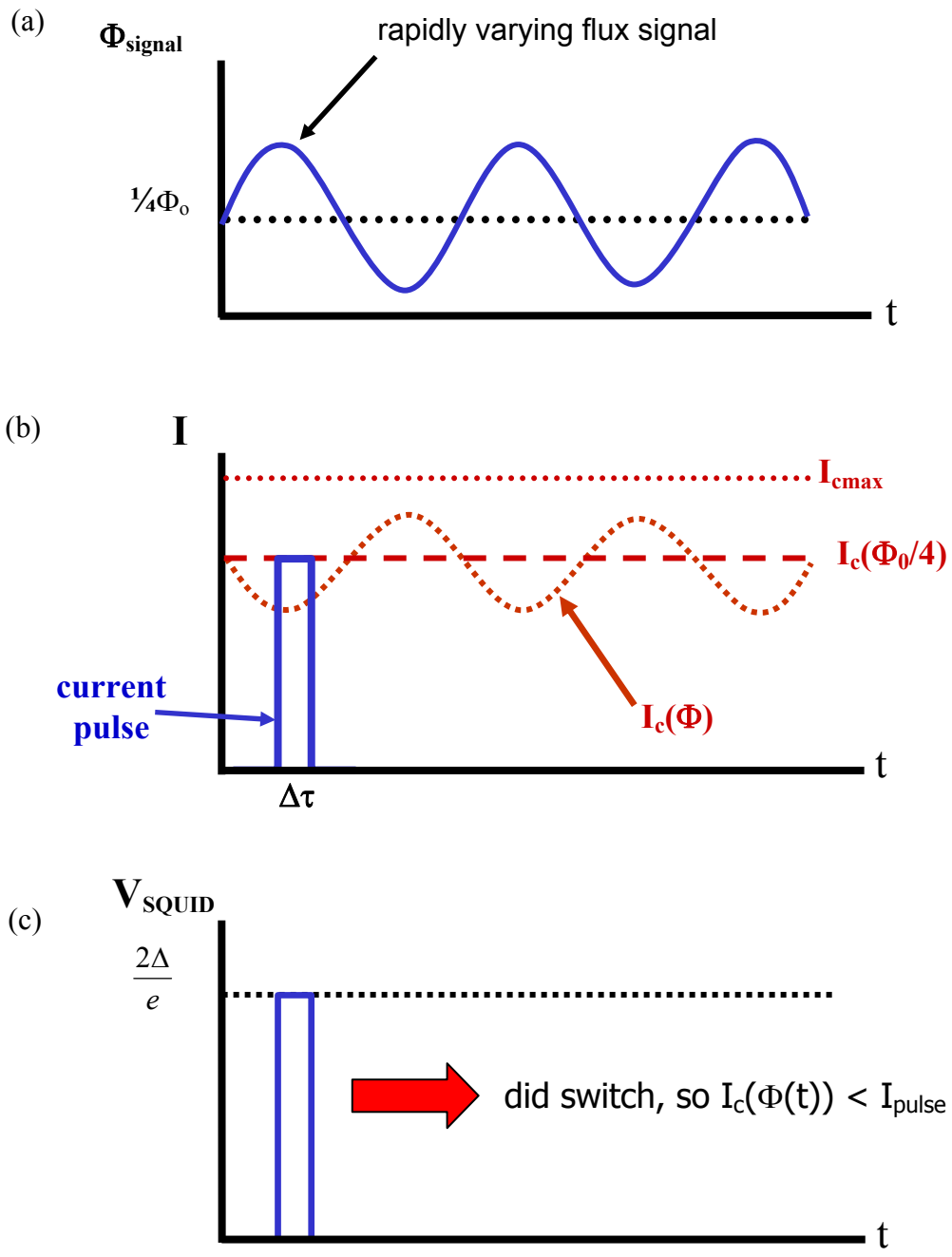

Fig. 5.8. (a) The SQUID is dc biased at ¼ Φ_0, and a small rapidly varying flux signal is applied by a sample. (b) A short current pulse is applied to the SQUID. (c) In this case the amplitude of the current pulse is greater than the critical current I_c (Φ(t)) of the SQUID at time *t* and the SQUID switches to the gap voltage during the pulse.

On the other hand, if the current pulse amplitude is greater than $I_c(\Phi(t))$, then the SQUID switches to the voltage state and I can conclude $I_C\left(\Phi(t)\right) < I_{pulse}$ (see Fig. 5.8). In practice, I must repeat the process many times for different pulse amplitudes to accurately pin down $I_C\left(\Phi(t)\right)$. The last wrinkle in this process is to add a time delay to subsequent current pulse so that it effectively steps through the time varying flux signal. If this process is repeated many times, and at each spatial location over a sample, a time-dependent magnetic flux image is obtained.

It is important to recognize that this process only works if the signal is repetitive and can be reliably synchronized to the pulses so that the flux signal can be repeatedly interrogated at equivalent points in time. Also the signal must not change significantly during the pulse itself or so rapidly that the SQUID does not have time to respond. I note that since SQUIDs are made from superconductors and the SQUID I use has a very small inductance, the voltage response is practically zero if the bias current pulse is less than the critical current. On the other hand, if the pulse exceeds I_c, a 2.8 mV pulse will be generated, and this is easy to detect and count with conventional room-temperature electronics.

In order for this technique to be successful for large bandwidth applications the bias current pulses must have a pulse width on the order of the temporal resolution desired or the inverse of the band width. So, for example, to have a 1 GHz bandwidth, the pulse width should be 1 ns or less. Limitations to the achievable or useable pulse width originate from the pulse generating circuit, the wiring, and the SQUID bandwidth. The wiring to the SQUID needs to have sufficient bandwidth, minimal dispersive effects, and be of uniform impedance to not generate undesirable reflected pulses. Of course, the

SQUID also needs to be able to react in a timely manner in order for the electronics to discriminate between switched and unswitched states. A hysteretic SQUID satisfies this condition. The voltage rise time of a hysteretic SQUID (see Chapter 4) is

$$\tau_c = \frac{2\Delta C}{e I_0}. \tag{5.14}$$

This is one measure of a SQUIDs reaction time. For my hysteretic niobium SQUID I find $\tau_c \cong 250\,ps,$ so the SQUID quickly ramps up to the gap voltage on the scale of a 1 GHz signal.

We can understand the importance of using a hysteretic SQUID by examining the transition from the zero-voltage to the resistive state. First, for my hysteretic SQUID, the transition time given by Eq. (5.14) is quite short with a rise time of τ_c = 0.25 ns and the voltage change is $2\Delta/e$ (≈ 2.8 mV). For typical laboratory electronics, this large voltage is easily measured. Also, the voltage persists until the bias current decreases below the retrapping current, *i.e*. as long as the current bias pulse is applied. For a nonhysteretic SQUID, the transition from the zero voltage to the resistive state is more gradual and near the transition the voltage change is on the order of $\sim I_c R$, which is typically of order 100 μV and thus much smaller than Δ/e [3]. So for a given change in applied magnetic flux, the voltage response of a hysteretic SQUID is much larger than a nonhysteretic SQUID and persists for the duration of the current pulse.

5.4 Measuring Flux by Detecting the Critical Current

The pulsed sampling scheme described above requires that one make multiple measurements; a single measurement can only determine if the SQUID's critical current is greater or less than the bias current pulse height. This begs the question as how to best

follow the SQUID's critical current produced by a flux signal that is varying rapidly in time.

The scheme I used involves setting the current pulses to a fixed height $I_p = I_c(\Phi_0 / 4)$ while a static flux of $\Phi_0/4$ is applied. With this choice, in the absence of any flux signal, the SQUID shows a voltage pulse for approximately 50% of the current pulses. If the bias current pulse amplitude is set too low or too high, the SQUID will either never show a voltage pulse, or show continuous pulsing, respectively. For example, Matthews *et. al.* applied this technique and mapped out the switching probability at different flux feedback values [10].

In practice I make a histogram of switching events versus bias flux. As the bias flux is adjusted, some of the pulses leave the SQUID in the zero voltage state and the remaining pulses trigger the SQUID into the voltage state. In particular, if the bias flux plus the signal flux add up to $\Phi_0/4$ then the current pulse will cause the SQUID to switch 50% of the time. One downside to this technique is that it requires more measurements than some other schemes; measurements must be made at all flux values between $\pm\Phi_0 / 2$. The approach we followed can best be called synchronous pulsed sampling.

In synchronous pulsed sampling the current pulses are synchronized to the start of the repetitive test magnetic flux signal. This periodic signal represents our signal-under-test, and we externally trigger the bias current pulse from this test signal. By adjusting the delay of the bias current pulse relative to the test signal, the SQUID responds to the signal at different times. To measure the test-signal flux as a function of time, we fix the bias current at an optimum location [in the middle of its range corresponding to

$I_c(\Phi_0/4)$]; then, for a given delay between the signal and the bias pulse, we sweep the dc flux level over the range which we expect to see the SQUID switching turn on or off. We record the number of counts from the counter at each flux value. We then increment the delay (typically by one pulse width) and sweep the dc flux again. By repeating this process we can generate a 2D histogram of the number of switching events as a function of both flux and delay time. For each value of the delay, we then interpolate the value of the flux for which the counts were at 50% of full scale. The result is a map of the flux from the test signal as a function of time. Details on the hardware I use to perform pulsed sampling are given in Chapter 7.

5.5 Summary

In this chapter I first described the operation of a SQUID that uses flux-locked loop electronics and then discussed the limitations to the bandwidth imposed by the flux-locked loop electronics.

I next described a method for sampling small high-frequency periodic magnetic fields using a hysteretic SQUID with a pulsed bias current sampling technique. Further, I described how the SQUID's critical current is detected using the pulse scheme.

Finally, I note that the current pulse technique has some advantages which are not immediately apparent. First, it does not require precise timing measurements. For example, it does not matter when during a pulse the SQUID switches. What is important is whether or not the SQUID has switched to the resistive state. Second the output pulses are readily counted using standard pulse counters. Third, the generation, propagation and detection of pulses is very well-known and employs readily accessible technology.

Finally, the transition to a voltage state is fast, relatively large and easily measured using room-temperature electronics.

Chapter 6: 4 K Cryocooled Scanning SQUID Microscope

In this chapter I first provide an overview of the SQUID microscope design and then describe the main parts. Three issues needed to be addressed in the design: vibration isolation, thermal radiation, and thermal anchoring of the SQUID. After the main system components are discussed I describe the sample translation system hardware and how I operated this with the SQUID electronics and other instrumentation. I also discuss the basic system maintenance and care.

6.1 Overview of Microscope Design

Before giving a detailed description of the major parts, it is useful to have an overview of the entire system. A photograph of my scanning SQUID microscope is shown Fig. 6.1. The main parts of the microscope are the SQUID and its associated electronics, the cryogenics and vacuum hardware, and the sample translation stages.

Figure 6.2 shows a cut-away schematic of the lower half of the microscope. Note that the cold finger is not directly connected to the cryocooler but instead attached by Kevlar strings to the room temperature frame. Figure 6.2 also shows the double radiation shields that thermally isolate the cold finger from thermal radiation, as well as the window assembly that allows the thin sapphire window to be brought close to the SQUID.

Figure 6.3 shows an outside view of the SQUID window assembly on the lower section of the vacuum chamber. A G-10 fiberglass cone is attached to an aluminum vacuum flange that is bolted to the stainless steel vacuum jacket. The bottom apex of the

cone has a 2 mm diameter hole where a 25 μm thick sapphire window is attached. The SQUID-window assembly has a stainless steel bellows which allows for vertical adjustment of the sapphire window; three 1/4-28 inch threaded rods allow the window to be raised and lowered with respect to the SQUID, which is fixed inside the vacuum chamber. Once the SQUID-window distance has been set the sample is placed on a *z*-stage and raised to the sapphire window. Two of my main tasks was developing and implementing this design for the microscope.

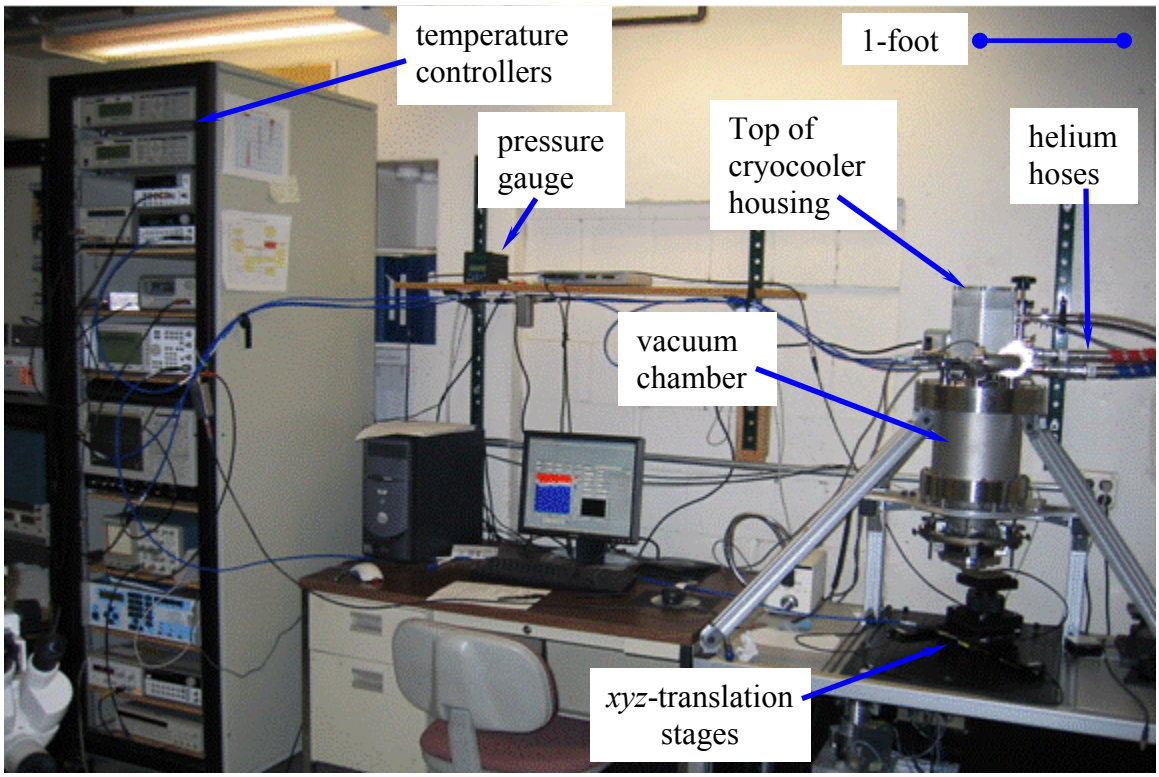

Fig. 6.1. Photograph showing overall system comprising the scanning SQUID microscope. On the left is a rack containing the electronic instrumentation such as pulse and microwave generators, a function generator, universal counter, and oscilloscope. In the middle of the photograph is the computer that controls the microscope and collects data. On the right is the scanning SQUID microscope with the top of the cryocooler housing visible on top of the vacuum chamber and the translation stages underneath.

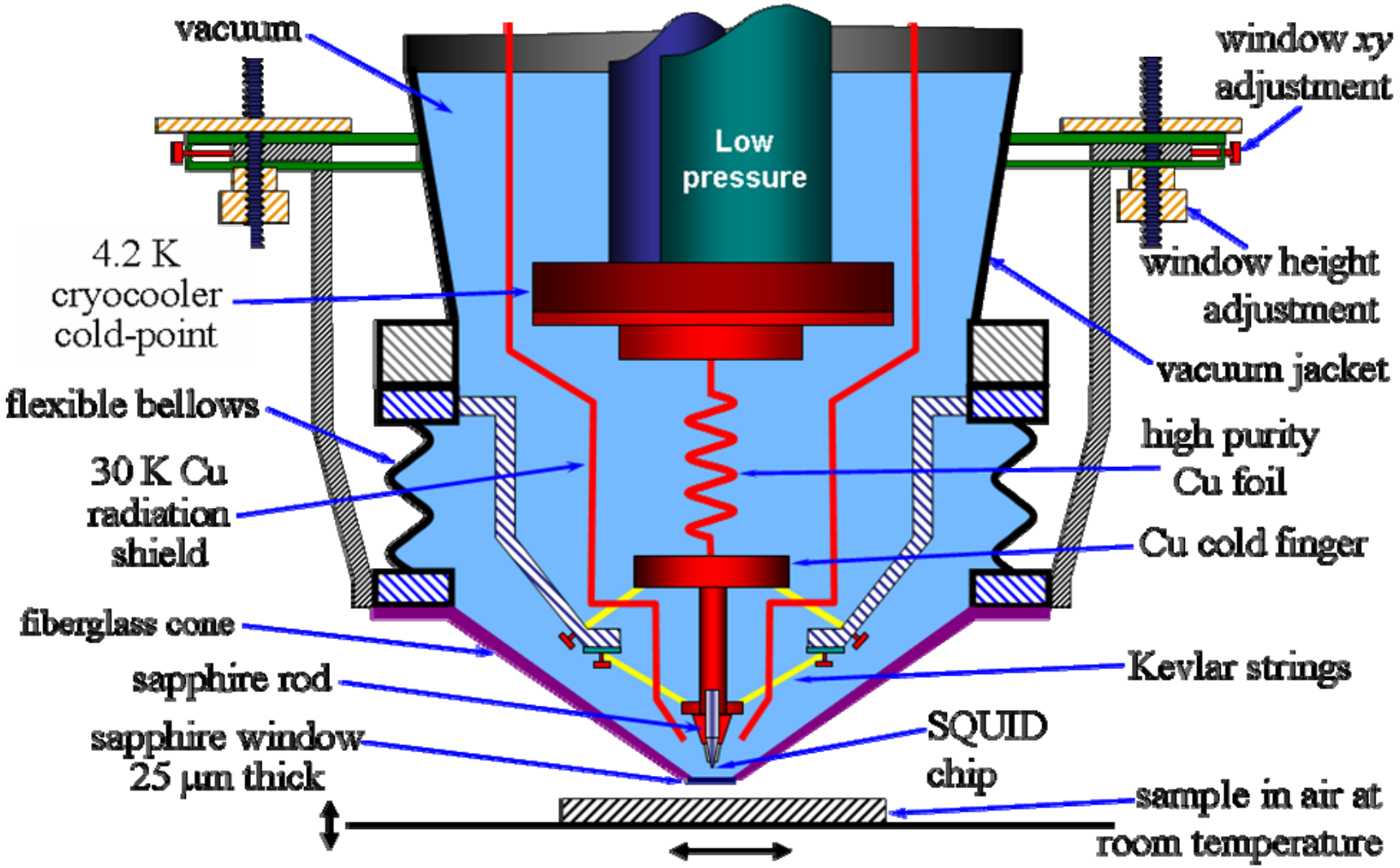

Fig. 6.2. Cut-away schematic of lower section of SQUID microscope showing SQUID, cold finger, and window assembly.

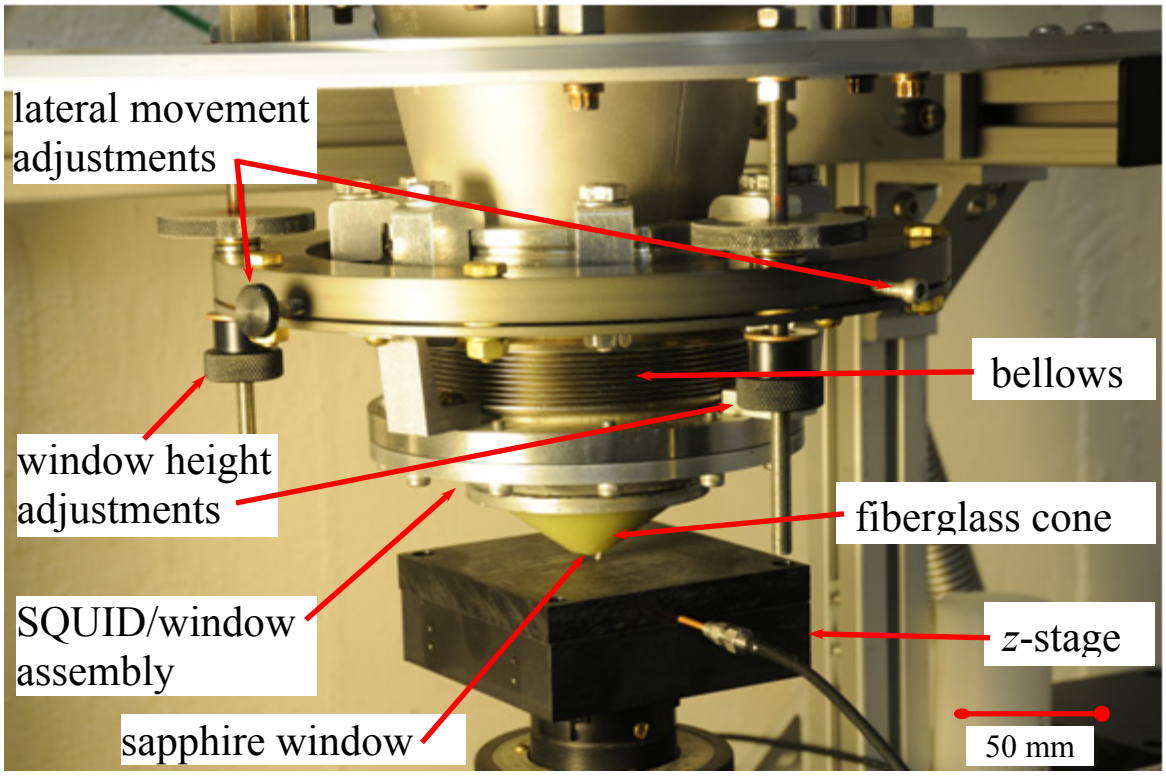

Fig. 6.3. Bottom portion of the assembled vacuum chamber showing the window assembly and z-stage that supports the sample.

There were several broad design criteria that the microscope needed to satisfy. Since we decided to use a hysteretic Nb SQUID, the SQUID needed to operate at liquid helium temperature. Also, it would be best if the microscope could be operated and serviced by one person. In particular, we wanted a compact instrument that was simple to operate. Another main requirement was that we wanted to measure samples at room temperature and permit changing and mounting samples without needing to shut down the microscope [1,2]. In particular, electronic failure analysis is typically conducted on samples that are mounted and operating at room temperature.

To address some of the above criteria, we chose to use a large-capacity cryocooler to cool the SQUID rather than a liquid helium dewar. Compared to a dewar, a cryocooler is more compact, relatively simple to use, and would not require daily filling of liquid

helium. Currently available closed-cycle cryocoolers can reach temperatures below 4 K, which allows for the use of low-temperature superconductors such as niobium. In particular, it is a major advantage to only need electrical power to cool the SQUID. Once we chose to use a cryocooler, we had to deal with the significant levels of vibration created during ordinary operation of the cooler. How we mitigated the vibrations is discussed in detail in the following sections.

Another broad design constraint was that the system needed to be magnetically quiet so as not to affect the performance of the SQUID. Magnetic noise could potentially originate from several sources in the system. For example, vibrations from the cryocooler would cause the SQUID to move in the Earth's magnetic field producing a large flux noise. Electrical or magnetic noise from the pumps, the scanning stage and associated laboratory electronics also needed to be addressed.

6.2 Cryocooler and Vacuum System

6.2.1 The Pulse Tube Cryocooler

In our microscope the SQUID is cooled using a Cryomech PT405 two-stage pulse-tube refrigerator [3-5] (see Fig. 6.4) with a cooling power of 500 mW at 4 K [6]. This is a relatively large cooling power at 4 K and one of the reasons we chose this system.

The pulse-tube system also does not use magnetic thermal storage elements, such as found in Gifford-McMahon refrigerators, and this makes the pulse-tube relatively quiet magnetically [3]. On the other hand, while the refrigerator is operating, the cold head vibrates with an amplitude of about 3 μm to 25 μm. Actually, this vibration amplitude is

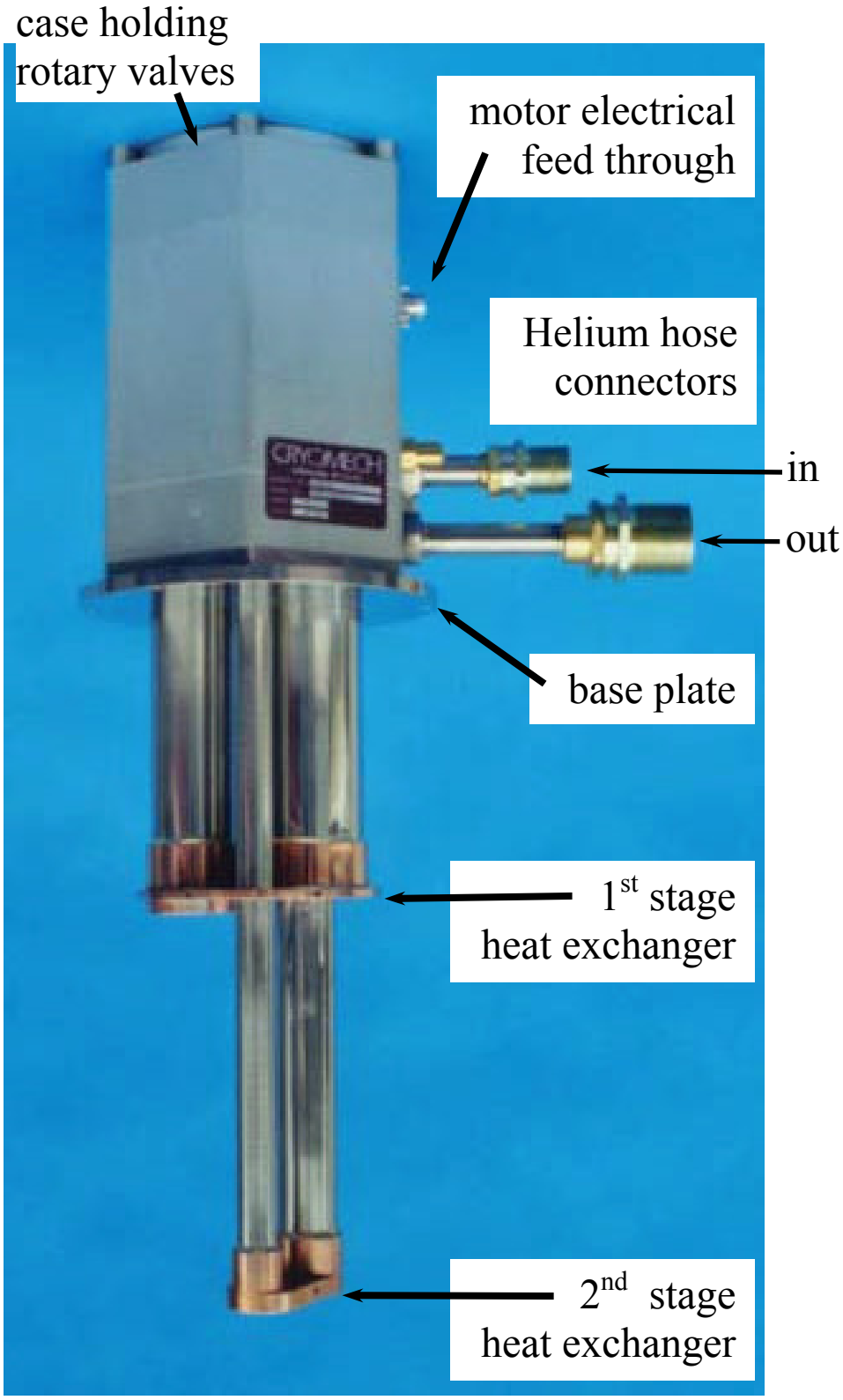

Fig. 6.4. Cryomech PT405 4 K pulse tube cryocooler.

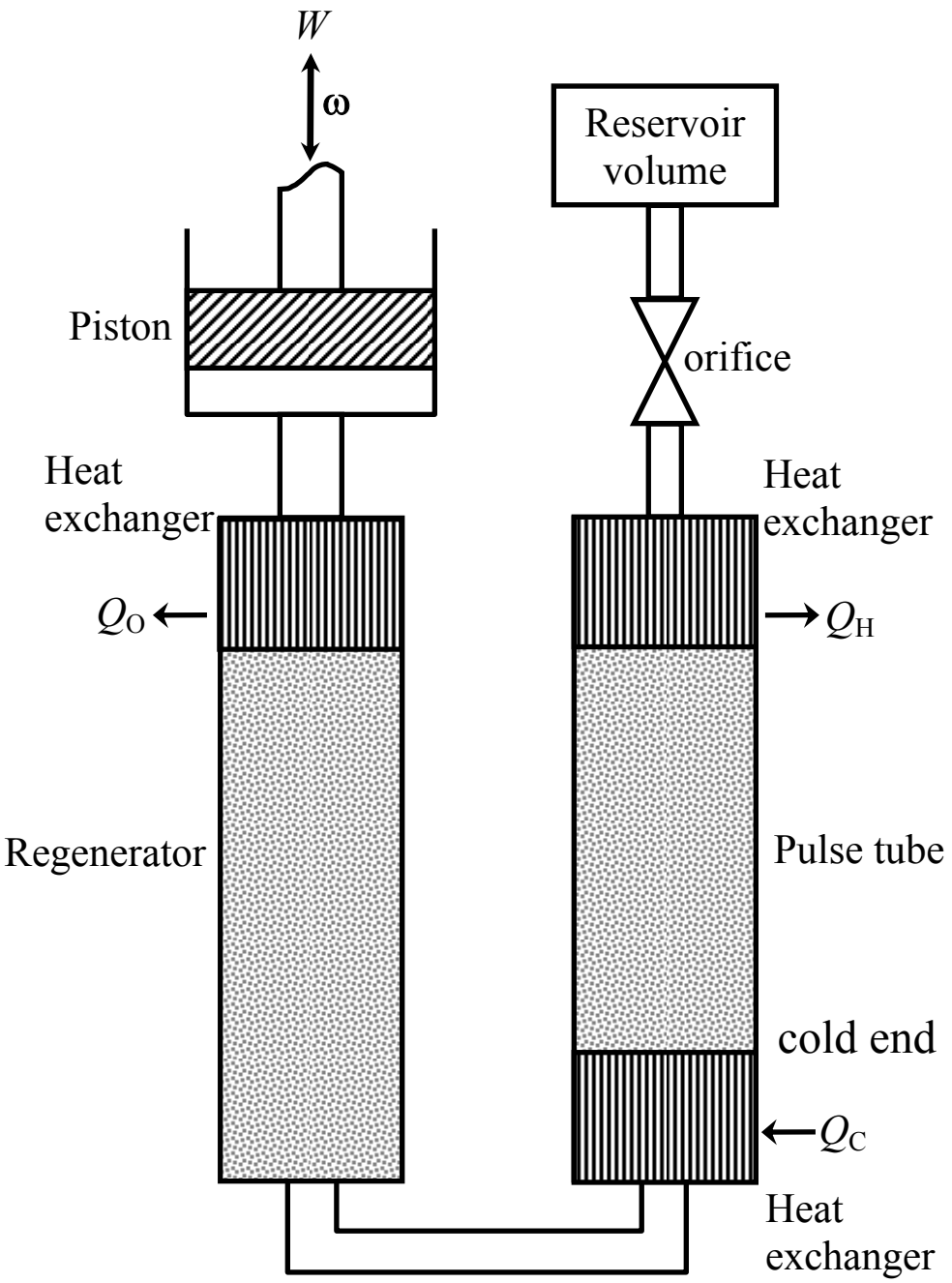

Fig. 6.5. Schematic diagram of an orifice pulse tube refrigerator [8].

relatively small for a closed-cycle refrigerator due to the fact that pulse-tube refrigerators lack a displacer and this was another reason why we used a pulse tube system. However, if the SQUID moved by micrometers it would produce serious problems (noise) and my design needed to suppress this motion [5].

The basic idea of a pulse-tube cryocooler was first described by Gifford and Longsworth in 1963 [7]. The working gas in the PT405 is 99.9999% pure ^{4}He. Unlike many other closed-cycle refrigerators, there are no moving parts in the low-temperature region of a pulse-tube cooler. This significantly reduces vibrations and also increases the lifetime of the cooler. Although they are called pulse-tube coolers there are no pulses. The cooling takes place via smooth, periodic, nearly adiabatic pressure variations while gas moves in the pulse tube.

A schematic diagram of an orifice pulse tube refrigerator is shown in Fig. 6.5. There are four stages in the operation of the refrigerator. First, an "acoustic pulse" is produced in the gas (helium) in the regenerator of the pulse tube by a compressor with a room temperature rotary output valve. In step two the compressed gas flows through the orifice (see Fig. 6.5) to the reservoir volume. This results in heat Q_H being transferred out of the gas at the hot end of the pulse tube through the heat exchanger. The orifice and reservoir store gas during a half-cycle and the gas flow is in phase with the pressure. Additionally, the reservoir volume acts to reduce any pressure oscillations during the flow, and the oscillating gas flow through the orifice separates the heating and cooling effects [8]. Next, the rotary valve opens to the compressor input, causing the gas in the pulse tube to expand and cool adiabatically. Finally, the cooled low-pressure gas in the pulse-tube is forced towards the cold end by the flow out of the reservoir via the orifice

into the pulse tube. During this expansion phase, the gas exits the pulse tube towards the compressor, removing heat from the regenerator. The resulting pressure cycling results in transferring heat Q_C from the cold end towards the hot end.

One very attractive feature of pulse tube refrigerators is the separation of the compressor unit from the expansion unit and the cold head. The PT405 uses a low frequency pulse tube that operates at approximately 1.3 Hz. Two flexible stainless steel hoses deliver compressed helium gas from the compressor to the cold head and then the gas is returned to the compressor. In our system the compressor is water cooled with a TekTemp TKD-100 series re-circulating water chiller and both the water cooler and compressor are located in a separate room from the rest of the system to reduce noise.

The above description of the basic operation was for a single-stage pulse tube cooler. The PT405 uses two such stages to increase its cooling efficiency and reach temperatures below 4 K. The first stage acts as a heat sink for hot side of the second stage and is situated between room temperature and the second stage. The first stage can reach temperatures down to 30 K and the second stage can reach temperatures down to 2.8 K with no load. The first stage has a rated cooling power of 25 watts at 65 K while as noted above, the second stage has a cooling power of 0.5 watts at 4.2 K (the cooling power reaches zero at the base temperature of about 2.6 K). One final point of interest is that there is no liquid-gas interface in the pulse-tube. This is because the operating pressure of 250 psi is greater than the critical pressures for ^{4}He of 33.1 psi.

6.2.2 The vacuum system

To reach cryogenic temperatures, it is essential that all cryogenic components in the microscope be maintained in a good vacuum. Figure 6.6 shows the vacuum chamber for our system. The chamber is a 30.5 cm diameter stainless steel cylinder with a nonmagnetic stainless steel flange at each end. An extruded aluminum support structure is used to hold the vacuum chamber (see Fig. 6.6). The base plate of the cryocooler is installed onto the top flange of the vacuum chamber and sealed using an OFHC copper gasket. The bottom flange of the chamber is sealed with the SQUID-window assembly.

As shown in Fig. 6.7(a), the SQUID/window assembly is comprised of a flexible metal bellows that is suspended by three support arms. The bottom of the SQUID/window assembly is closed with a fiberglass (G-10) cone [see Fig. 6.7(b)]. The fiberglass cone has a 2 mm hole at its apex. The sapphire window [9] which is 25 μm thick is supported by a sapphire disk that is affixed to the apex of the fiberglass cone with epoxy [10].

The SQUID/window assembly is designed to allow the sapphire window to have six degrees of freedom. The assembly has four screws (on a circle at 90° to each other) to provide the window with lateral (x-y) movement (±2 mm) so it can be centered under the SQUID. In Fig. 6.7(b) one can also see one of three height adjustment knobs that allow the sapphire window to be tilted and raised (z) to bring it close to the SQUID tip. These seven adjustment screws (4 lateral, 3 tilt and z) give the window assembly the necessary flexibility to both center the sapphire window and raise it to within close proximity of the SQUID. Typically, I use the screws to position the sapphire window to within approximately 50 μm of the SQUID tip.

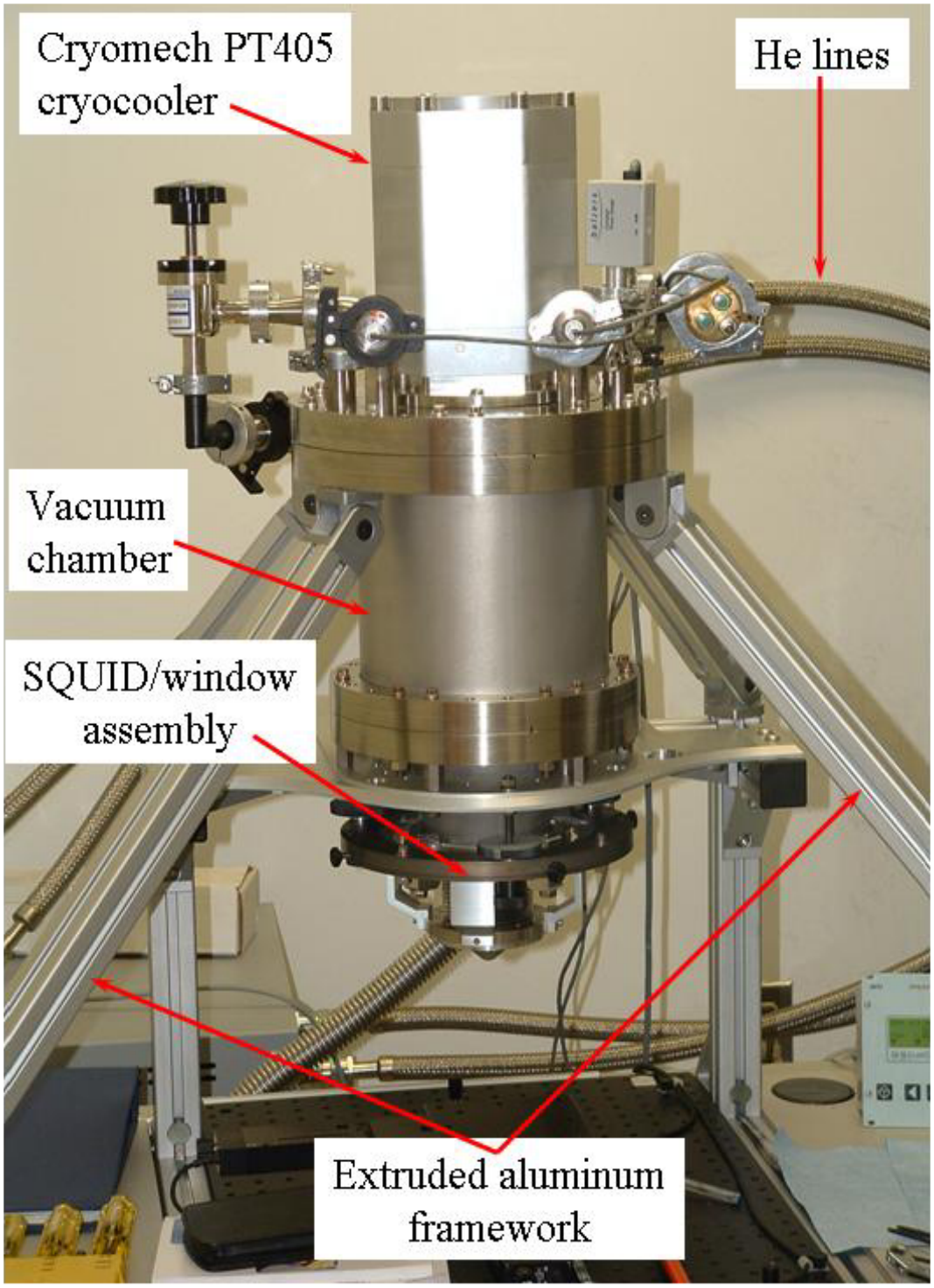

Fig. 6.6. Photograph of assembled microscope showing Cryomech PT405 cryocooler on top of vacuum chamber. The vacuum chamber rests on an extruded aluminum frame in the shape of a pyramid.

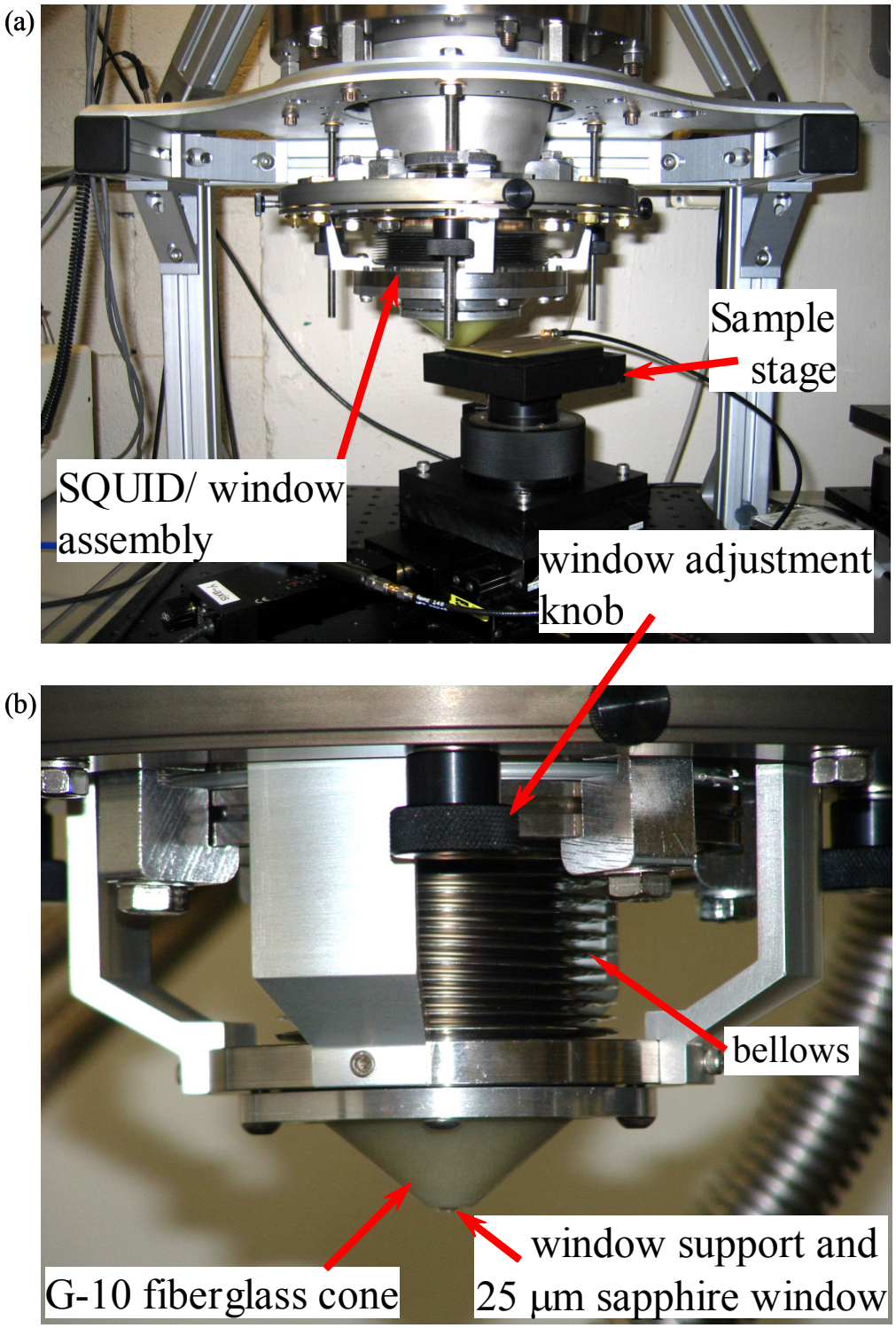

Fig. 6.7. (a) Photograph of SQUID/window assembly and the sample stage. (b) Close-up of the SQUID/window assembly showing flexible bellows in the center of the assembly and the fiberglass G-10 cone.

As I noted above, the bottom of the window assembly is enclosed by a cone made from G-10 fiberglass (see Fig. 6.8). The cone is 3.175 mm thick, 73.3 mm in diameter and 36.7 mm tall. In order to minimize thermal radiation from or through the cone, I covered the inside of the cone with a single layer of aluminized Mylar with the aluminum layer facing outward. To reduce vacuum leaks through the fiberglass cone I coated the outside of the cone with a thin layer of KL-5 vacuum leak sealant from Kurt J. Lesker [11].

The purpose of the fiberglass cone was to seal the vacuum space and allow samples to be brought close to the SQUID. The fiberglass is strong enough to withstand atmospheric pressure but is electrically insulating and so will not support eddy currents. At the smaller end of the cone I epoxied a 5 mm diameter disk shaped sapphire washer using Master Bond EP30FL epoxy [10]. The washer purchased from Sapphire Engineering [14] is 1 mm thick and is optically clear. A hole is drilled in the center of the washer using a 1 mm diamond coated drill bit.

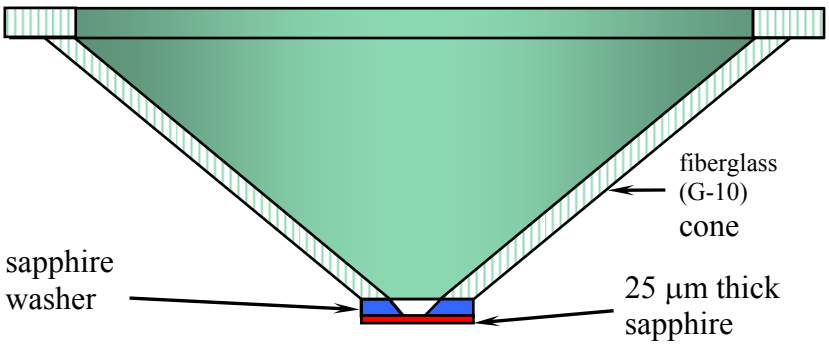

Fig. 6.8. Schematic of fiberglass (G-10) cone showing location of sapphire washer and sapphire window.

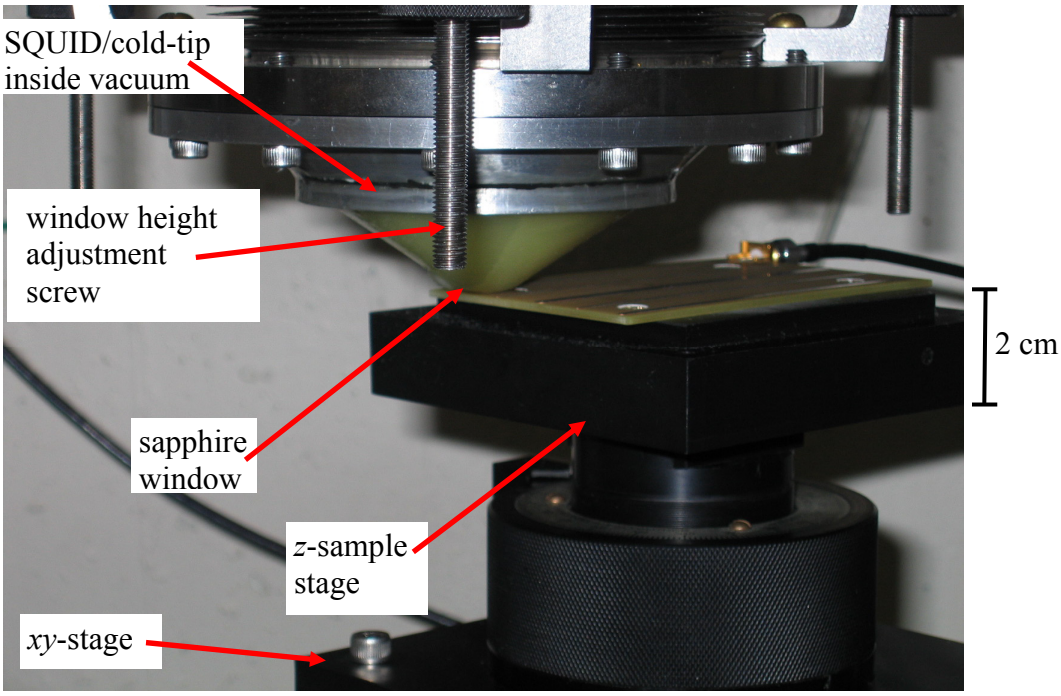

Fig. 6.9. Photograph of SQUID/window assembly for the microscope.

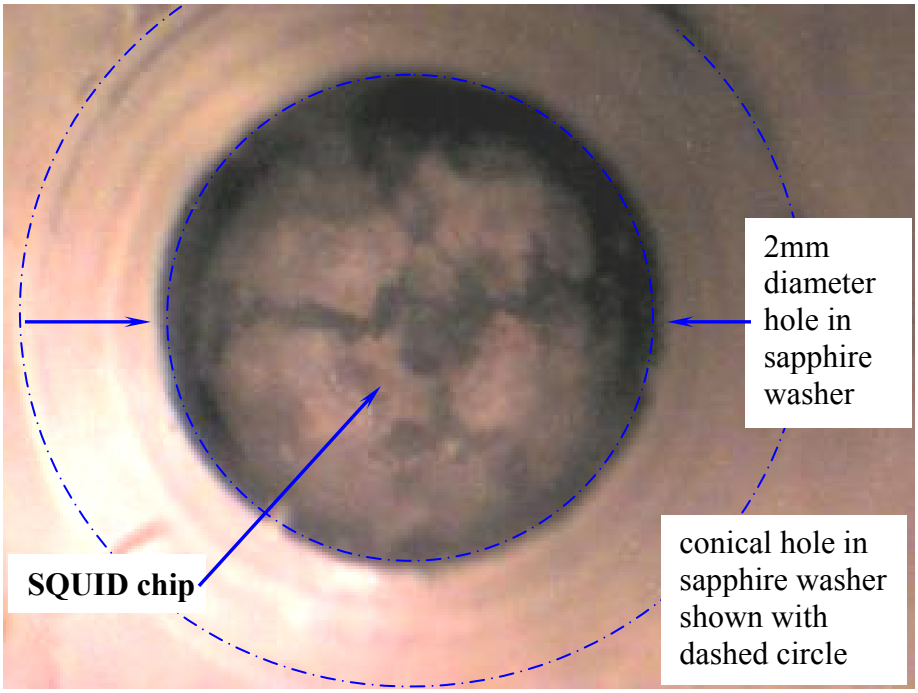

Fig. 6.10. Photograph showing close-up of sapphire window moved very close to SQUID. The sapphire washer is epoxied to the top of the fiberglass cone, and it has a 2 mm diameter hole. The 25 μm sapphire window is epoxied on top of the sapphire washer centered about the hole.

Afterwards, I used a diamond-coated conically-shaped grinding tool to enlarge the 1 mm hole to a 3 mm diameter hole which tapers down to a 2 mm diameter hole. This sapphire washer supports the 25 μm thick sapphire window that covers the conical hole. The sapphire window obtained from Princeton Scientific Corp. [9] was optical grade, with orientation (0001), diameter 5 mm +0/-0.1 mm, thickness 25 μm, both sides optically polished, with surface quality 60/40 (S/D). The washer is also important because its thermal expansion matches that of the 25 μm thick sapphire window (see Fig. 6.9 and 6.10) so that small temperature changes do not put stress on the thin window. Needless to say, it is the thinness of this thin window that allows the SQUID to be brought very close to a room temperature sample that is in air.

I used an Alcatel Drytel 31 to pump out the vacuum system. This is a completely oil-free turbo-drag high-vacuum pumping system. This stand-alone system can operate from atmosphere to $1x10^{-6}$ torr. It is designed for use with vacuum chambers up to 50 liters in size and has a maximum pumping speed of 16 cfm in the high vacuum range. It has a 7.5 liters/s turbo-drag pump (which rotates at 27,000 rpm full speed) and is backed by a 1 m^3/hr diaphragm pump. The diaphragm pump carries the main burden of pumping from atmosphere down to 10 torr. Prior to starting the cryocooler, I use the Drytel 31 to evacuate the vacuum chamber to approximately $2x10^{-4}$ torr. Once the cryocooler is started, the pressure further decreases because of cryopumping and levels off at a nominal gauge pressure of $5x10^{-7}$ torr.

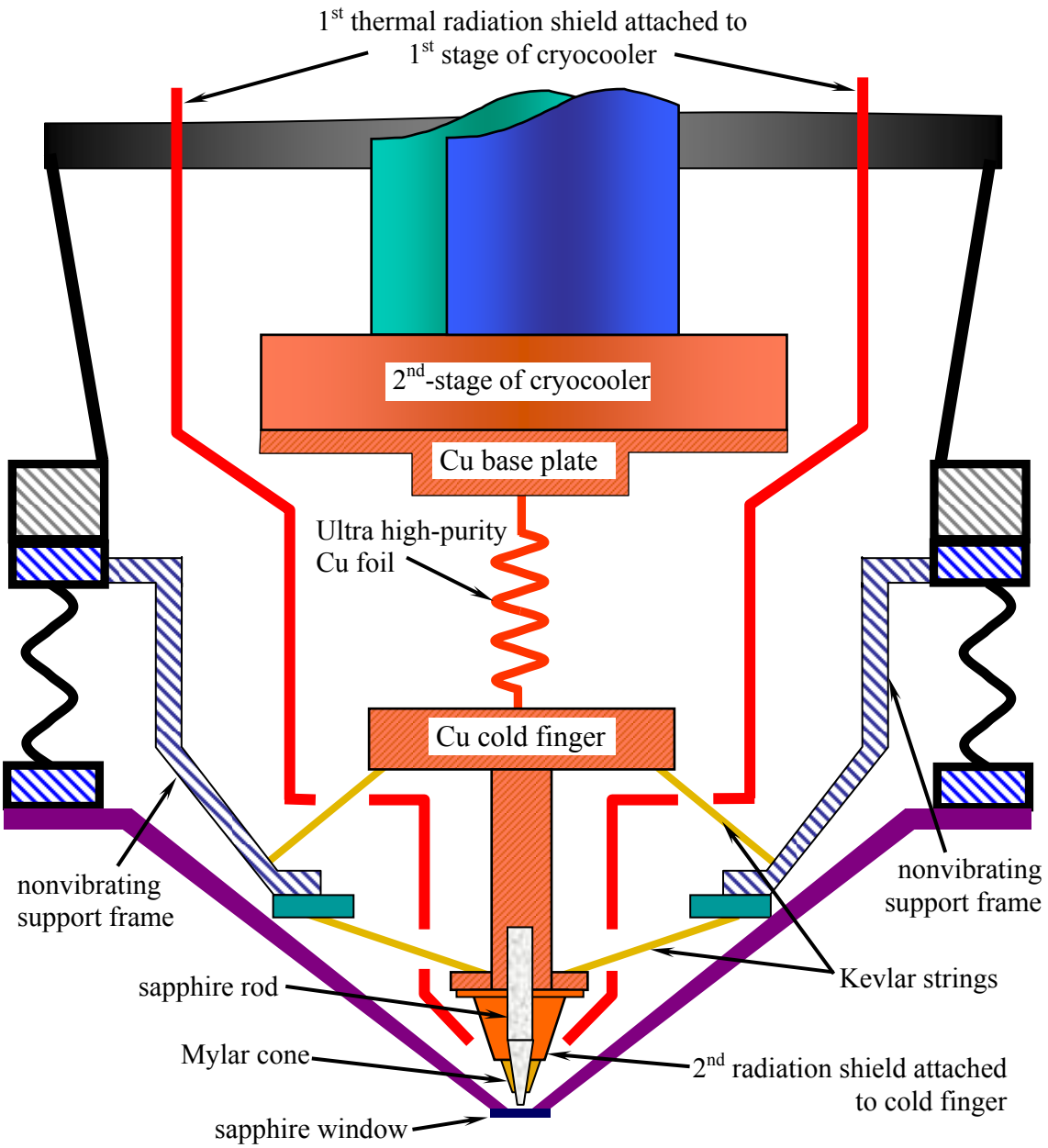

Fig. 6.11. Schematic of cold finger showing location of thermal radiation shields and other components inside the vacuum chamber. There are a total of six Kevlar strings, but only four strings are shown. The cold finger is tightly suspended from an independent support frame inside the vacuum chamber. The 1st thermal radiation shield is attached to the 1st-stage of the cryocooler. The cold finger is comprised of three components. First is the copper base plate that is screwed to the 2nd-stage of the cryocooler. Second a high-purity foil link is soldered to the base plate and to the cold finger. Finally, a 50 mm diameter copper disk and copper rod are used to hold the sapphire SQUID tip. The 2nd thermal radiation shield is attached to the bottom of the cold finger. There are holes in the 1st radiation shields in order to allow the Kevlar strings to pass through and not make contact with this shield as it vibrates.

6.3 Cold Finger, Thermal Anchoring and Radiation Shielding

6.3.1 Fabricating the SQUID tip and cold finger assembly

Figure 6.11 shows a schematic of the microscope's cold finger, thermal anchoring and thermal radiation shielding. The cold finger is connected to the cryocoolers 2nd stage by means of a flexible, high-purity Cu foil. The cold finger is surrounded by the first radiation shield, which is attached to the cryocooler's 1st stage. A small second radiation shield is attached to the end of the cold finger to shield the SQUID tip. Finally, the cold finger is held stationary by means of Kevlar strings that are anchored to a non-vibrating frame inside the vacuum chamber.

The cold finger has four main functions. First, it must provide excellent thermal conductivity between the refrigerator cold point and the SQUID chip to allow the SQUID to cool to its operating temperature. Second, the cold finger must end in a point that is rigidly fixed and to which the SQUID can be attached. In particular, the cold finger needs to be mechanically isolated from the cryocooler so that vibrations of the cryocooler aren't transmitted to the SQUID. Finally, metals should be kept away from the end to prevent eddy currents.

Building the cold finger and attaching the SQUID to it requires considerable care and preparation. The process starts with the SQUIDs. The SQUID chips I received from Hypres were on 5 mm x 5 mm silicon substrates with nine SQUIDs patterned on one substrate. I first diced the substrate using an automated chip dicing machine located at the Laboratory of Physical Sciences. For each single *z*-SQUID chip I left contact pads and a small area around the chip as a safety margin for a final size of 1.5 mm x 1.5 mm [12].

After dicing the SQUID chip, I then selected one of the chips for cleaning. The cleaning procedure is performed by soaking for a few minutes first in acetone, followed by a methanol rinse and finally an isopropanol rinse. After cleaning I used nitrogen gas to dry the SQUID chip.

Next, I attached the SQUID chip to a sapphire rod using STYCAST 2850FT epoxy with catalyst 9 from Emerson & Cuming [13]. STYCAST 2850FT is a two component thermally conductive epoxy. Further, this epoxy offers excellent chemical resistance to solvents and adheres well to sapphire even after repeated thermal cycling. I allowed the epoxy to cure for about 72 hours to ensure the bond between the SQUID chip and epoxy reached maximum strength.

The rod supports the chip at the end of the cold finger and I chose sapphire for its high thermal conductivity, its transparency (less heating from room temperature radiation) and because it is non-magnetic and insulating. The rod is 6.35 mm in diameter [14], 25 mm long, and at one end tapers to a 1mm x 1mm square tip. The SQUID chip is attached to the 1 mm x 1 mm square end. After the epoxy has cured, I grind and polish the SQUID chip so that it matches the end of the tapered sapphire rod. Prior to grinding I coat the SQUID chip with a layer of photoresist to protect the chip from debris and damage. I grind the chip by hand using 800 and 1200 grit polishing pads. Great care and patience needs to be exercised at this point because it very easy to grind away one of the contact pads if one does not constantly monitor progress. Following grinding the SQUID chip was cleaned again by rinsing first in acetone, then in methanol, and then isopropanol to remove debris and the protective layer of photoresist.

Attaching the SQUID chip at the end of the tapered sapphire rod, and cutting the chip to a small size, allows the sapphire window to be positioned close to the SQUID without touching any surfaces. The other end of the sapphire rod is installed into the copper cold finger. The hole for the sapphire rod in the cold finger is a carefully machined 6.35 mm diameter hole that is 10 mm deep. The sapphire rod is installed into the hole using silver paint in order to ensure a tight thermally conductive connection.

6.3.2 Making Electrical Connections to the SQUID

Figure 6.12(a) shows a schematic and photo of the basic features at the end of the tapered sapphire rod. Three electrical connections must be made to the SQUID. One is the current bias line, the other the voltage line, and the third the flux line. Each line starts at the top flange of the vacuum system as a semi-rigid UT-34 stainless steel coax transmission line that is thermally anchored to the first stage. At the first stage I transition to flexible, stranded stainless steel coaxial transmission lines. The flexible lines allow for some "give" in the transmission lines so they don't pull apart from thermal contraction. At the second stage, the lines transition to twisted pair. The twisted pair are easier to connect to the SQUID chip and also help minimize the heat load on the cold finger and SQUID chip. I use one twisted pair for the flux line to the SQUID chip. A second twisted pair has one line connected to the two center conductors of the current and voltage coax lines (tying them together electrically) and the other line is connected to the shared ground return on the outer jacket of the coax lines. Thus the current bias and voltage output leads are shared for this twisted pair section. This allows me to attach just four wires to the sapphire rod (two for flux, and two for IV) instead of six.

Figure 6.12 shows the wires and components on the end of the sapphire rod. The first component attached to the sapphire rod was a Cernox thermometer (model CX-1010) from Lakeshore. I used a small amount of STYCAST 2850FT epoxy to give a thin bond layer and assure good thermal contact. To electrically connect to the Cernox thermometer, I used Lakeshore QuadTwist QT-36 cryogenic wire. It is formed from two twisted pairs (4 leads) of 36 AWG phosphor bronze wire (each pair has 8 twists per inch and each pair is entwined into 4 twists per inch). This allows me to use a four-wire configuration with the Cernox thermometer. The electrical current is carried in one pair of leads while the sensor voltage is measured across the other pair. This typical four-wire configuration is used to minimize lead resistance and the pickup of electromagnetic noise and allows more accurate temperature measurements.

The current/voltage bias lines are glued to the sapphire rod using GE varnish. There is one line to each tapered side of the sapphire rod, aligned with the bias contact pads on the SQUID chip (see Fig. 6.12). Similarly, I attached the two flux lines with a thin layer of GE varnish to the other two tapered sides of the sapphire rod; each wire was aligned with respect to the contact pads that go to the single-turn flux loop on the SQUID chip. I used silver paint to make the final electrical contact between these lines and the pads on the SQUID chip. This involves painting a thin layer of silver paint from the gold contact pads on the front surface of the SQUID chip, over the edge of the chip and down the tapered sides of the sapphire rod. This was a delicate and difficult step that required great care. Using silver paint to make electrical contact is not always reliable and I found the contacts tended to degrade with time (over a few months). In particular, the silver

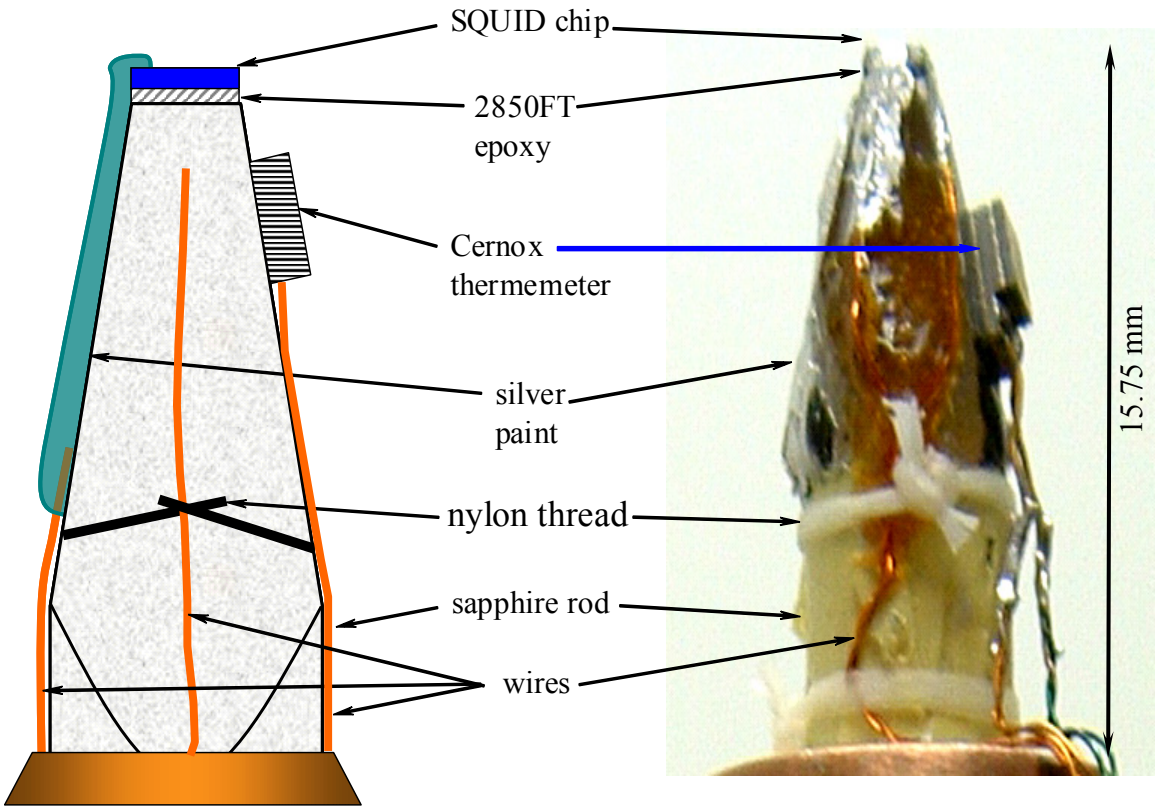

Fig. 6.12. (a) Schematic of cold tip used in microscope showing location of SQUID chip on top of sapphire rod, wiring and thermometer. (b) Photograph of actual cold tip used in microscope. The sapphire rod is 6.35 mm in diameter and extends 15.75 mm beyond the top of the cold finger.

paint has little mechanical strength and degrades with thermal cycling, and you risk an open circuit after repeated thermal cycles.

6.3.3 Thermal anchoring

In the design of the cold finger, there are three important but competing criteria that need to be addressed very carefully. The cold finger needs to be in excellent thermal contact with the cryocooler, but it also has to be isolated mechanically from vibrations of the cryocooler. Further, the cold finger also needs to be thermally isolated from the rest of the environment, including the walls of the vacuum chamber which are at room

temperature. I will discuss shielding from thermal radiation in the next section while this section covers thermal anchoring.

In order to provide excellent thermal contact between the cryocooler and the cold finger assembly, I fabricated a thermal link from four sheets of flexible 100 μm thick 99.999% high-purity copper foil [15]. The sheets are stacked on top of each other and then bent into a sinusoidal shape (see Fig. 6.11). I then soldered one end of the this stack to the base of the cold finger and the other end to an (OFHC) copper base plate that attached to refrigerator cold point (see Fig. 6.11). The thinness of the foil and the sinusoidal folds in the link help it to act like a very floppy "spring" between the cryocooler and cold finger; it creates a weak mechanical coupling between the cold-point of the cryocooler and the cold finger and reduces the transmission of vibrations to the SQUID tip.

In order to cool the SQUID to 4 K, the copper foil needs to have a high thermal conductivity. The heat carried by a copper link of cross-section A and length L with a thermal conductivity coefficient κ is given by [16]

$$\dot{Q} = \frac{A}{L}\int_{T_1}^{T_2} \kappa(T)dT. \tag{6.1}$$

where T_2 and T_1 are the temperatures of the ends of the link. For a narrow temperature $T_2 \sim T_1 \sim T$ range Eq. (6.1) can be approximated by

$$\dot{Q} = K\Delta T \tag{6.2}$$

and K is the thermal conductance of the copper foil at the temperature $T = (T_1 + T_2)/2$ and is given by

$$K = \frac{nA\kappa}{L}. \tag{6.3}$$

Also, $\Delta T = T_2 - T_1$ equals the difference in temperature between the second stage and the cold finger and n is the number of layers of foil. While the microscope is operating, I found that the temperature at the cold tip was typically T_2 = 3.9 K and the temperature at the 2nd stage was T_1 = 2.7 K for a temperature difference ΔT = 1.2 K. The copper link used four rectangular sheets each with a width w= 5 cm, length L = 8.25 cm and thickness t = 0.01 cm for a cross sectional area of each foil is A = 0.05 cm^2. One then finds from Eq. (6.3) that $K \cong 3.9 W/K$ where the number of layers is n = 4 and the thermal conductivity of high purity copper at 4 K is κ = 162 W/(cm-K) [16].

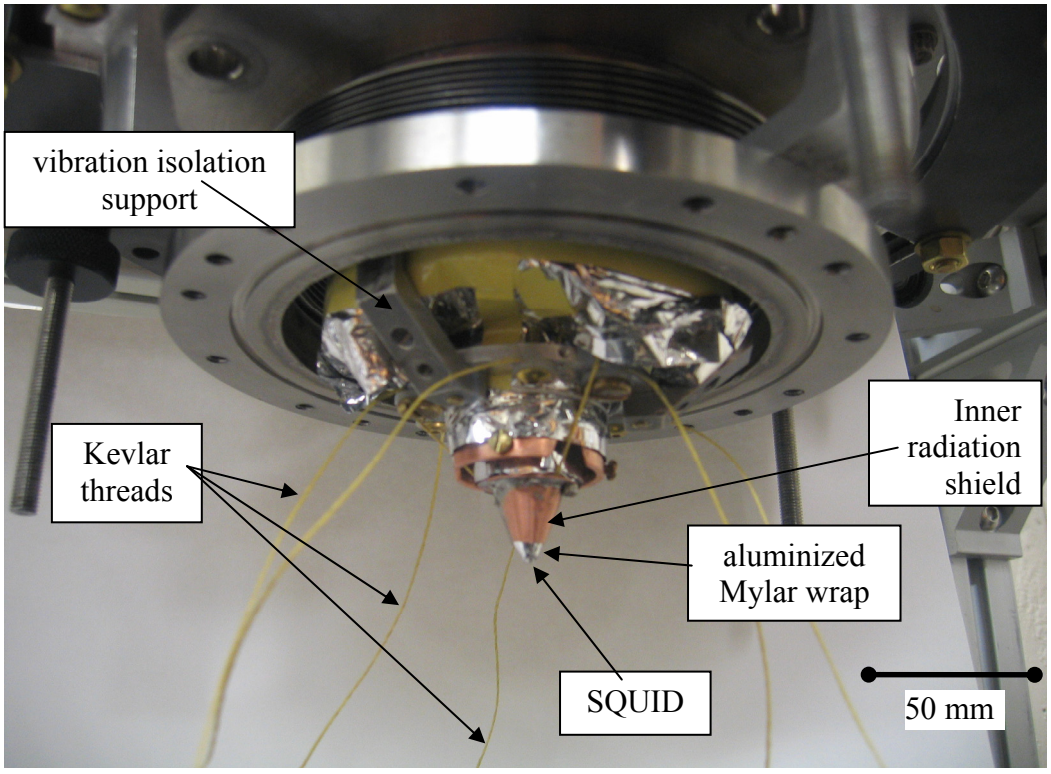

Fig. 6.13. Photograph of SQUID at the bottom of the cold-tip with Kevlar threads prior to attaching the threads to the vibration isolation supports.

Since the cold-finger cannot be fixed rigidly to the vibrating cold-point, some other means must be used to keep it fixed. To do this, I used a network of six Kevlar threads (strand size 207) [17] to rigidly suspend the cold finger [see Fig. 6.11 and Fig. 6.13] inside the SQUID/window assembly. One end of each string attaches to the cold finger while the other end of each string is attached to support arms that are bolted to the (non-vibrating) outer vacuum jacket of the microscope. As can be seen from Figs. 6.11 and 6.12 some threads pull up and some pull down, and this produces a very rigid holding of the cold finger. Developed by Dupont, Kevlar is a light, strong para-aramid synthetic fiber, related to other aramids such as Nomex and Technora. For cryogenic applications, Kevlar is particularly useful because it maintains its strength and resilience down to cryogenic temperatures.

The Kevlar threads satisfy two very important criteria in the microscope: the threads have a very low thermal conductivity and a high tensile strength. The low thermal conductivity is very important because the threads go directly from 300 K to 4 K in just a few centimeters. The tensile strength is important because the more tension that can be applied, the less the tip will move when the cold-point vibrates. The 0.64 mm diameter Kevlar thread that I use [17] has a thermal conductivity of 1.97 x 10^{-4} W/cm-K at 4 K [18,19] and heats the cold finger by:

$$\dot{Q} = \frac{A\kappa}{L}\Delta T \cong \frac{\left(3.2\times10^{-3}\,cm^2\right)\left(1.97\times10^{-4}\,\frac{W}{cm-K}\right)}{2\,cm}\left(296K\right) \cong 94\mu W \qquad (6.4)$$

or a heat load of 94 μW per thread. With 6 threads this gives a total heat load of 0.6 mW, which is small compared to the cooling power of the refrigerator at the cold point.

In section 6.4 I discuss the vibration isolation further, and some of the difficulties associated with this Kevlar suspension system.

6.3.4 Thermal radiation shielding

A serious complication introduced by operating at 4 K is the need to minimize heating of the SQUID by thermal radiation from room temperature and from parts of the apparatus that are at the temperature of the first stage (~70 K).

Two copper radiation shields are used to cut out this radiation; one is attached to the first stage of the cryocooler (at 30 K) and the other is attached to the end of the cold-tip (at 4 K) [see Figs. 6.11 and 6.14]. The first stage is used to cool the outer thermal radiation shield or "first" radiation shield. The first radiation shield is made of oxygen-free high thermal conductivity copper (OFHC) and surrounds the second stage as well as the cold finger. The bottom of the 1st radiation shield is formed into an OFHC cone (see Fig. 6.15). The second or inner radiation shield is a cone made of OFHC copper and is attached to the bottom of the cold finger. It surrounds about 60% of the exposed sapphire rod (see Figs. 6.13, 6.14, 6.15, and 6.16).

To further reduce the heat load on the tip, I cover the sapphire rod by a layer of reflecting aluminized Mylar so that all but 2 mm of the SQUID tip is covered. By the Stefan-Boltzmann Law, the power P incident on the exposed tip of the cold finger from room temperature radiation is

$$P = \varepsilon\sigma A\left(T_2^4 - T_1^4\right) = \varepsilon\left(5.67\times10^{-8}\,\frac{W}{m^2\,K^4}\right)\left(2\times10^{-5}\,m^2\right)\left(300^4 - 4^4\,K^4\right) \cong 9.2\,mW, \quad (6.5)$$

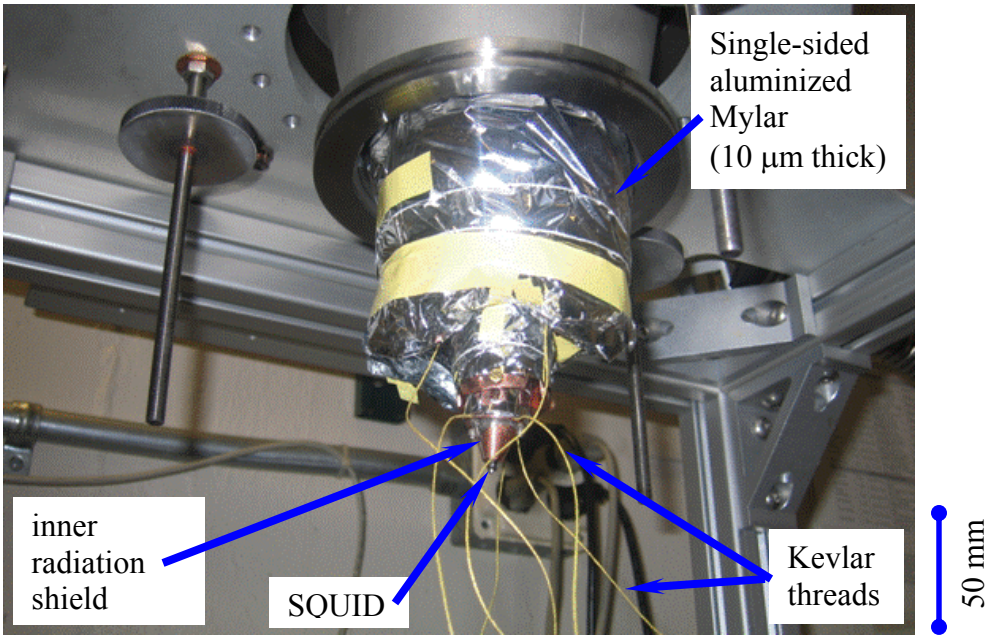

Fig. 6.14. Photograph of aluminized Mylar insulation wrapped around the outer radiation shield installed on the cryocooler. The cryocooler has been lowered into the vacuum chamber prior to the window assembly being installed. The Kevlar strings can also be seen hanging from the cold finger.

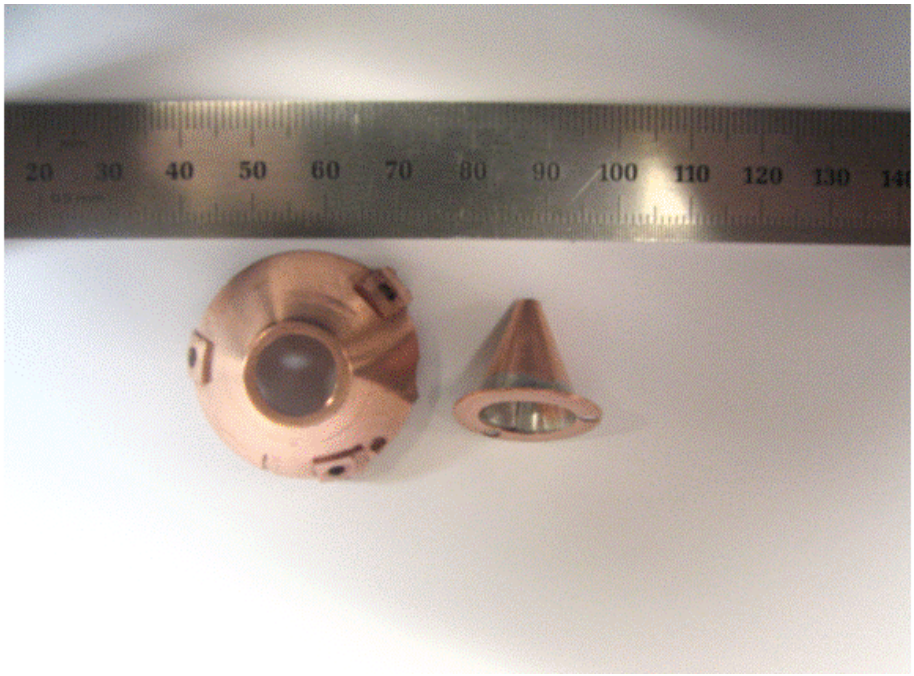

Fig. 6.15. Photograph of the bottom cone of the outer radiation shield (left) and the inner radiation shield (right). Scale is in mm.

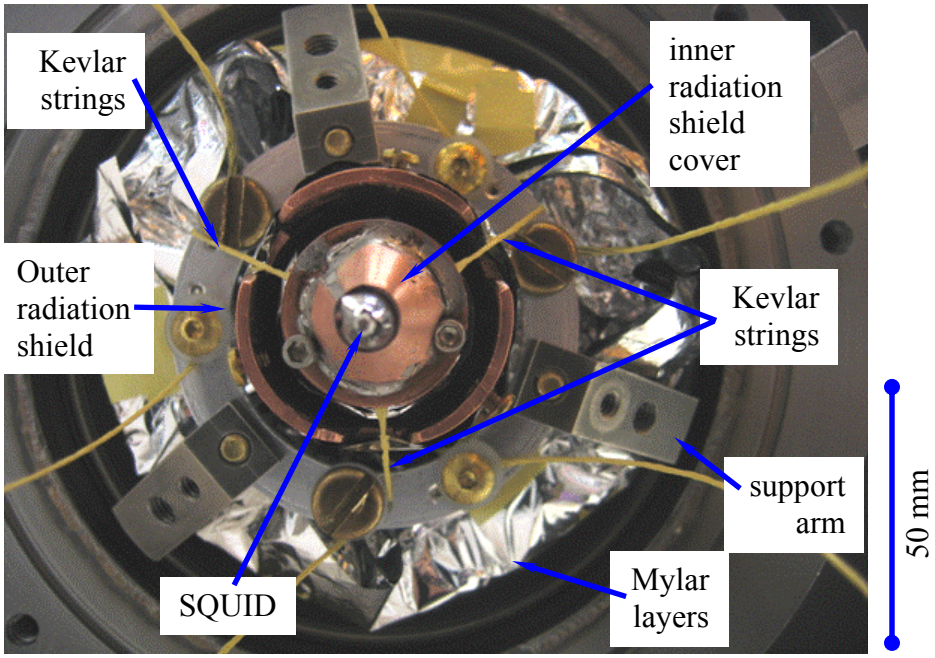

Fig. 6.16. Photograph looking straight up at the cold finger. The outer radiation shield is not installed, but the inner radiation shield and Mylar wrap around the SQUID tip can be seen.

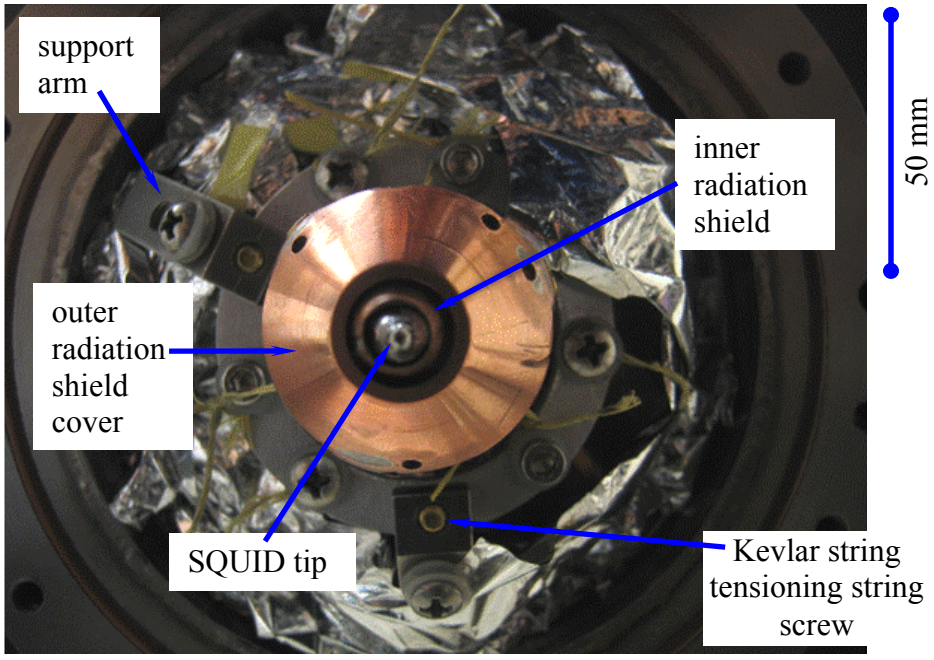

Fig. 6.17. Photograph showing completed assembly of radiation shields and suspended cold finger prior to installing the window assembly.

where σ is the Stefan-Boltzmann constant, $A = 2\times10^{-5}\,m^2$ is the exposed area of the sapphire rod and SQUID chip, T_2 = 300 K is the room temperature radiation, T_1 = 4 K the temperature of the cold finger, and I have taken the emissivity ε = 1. This level of power is not negligible and results in a $\Delta T \approx$ 2.4 mK across the Cu-foil thermal link

Heat transfer due to the residual gas molecules in the vacuum chamber is small as long as the pressure is kept low. We can estimate an upper bound on the heat conductance using [20]

$$\dot{Q} \approx CaPA\Delta T \le 44\,mW \tag{6.6}$$

where the constant C = 1.2 for air, the pressure $P \le 9\times10^{-4}\,Pa$, the accommodation coefficient is set to a maximum value a = 0.5, A = 0.275 m^2 is the total surface area of the cold end of the microscope, and the temperature difference between the outer wall of the vacuum chamber and the cold end of the microscope is $\Delta T \approx$ 296 K.

To reduce the heat load, I also wrapped thirty layers of single-sided aluminized Mylar insulation around the first shield (see Fig. 6.14). I also added six layers of Mylar to the sapphire tip, down to about 1 mm from the SQUID chip. With this arrangement, I found that when the SQUID was within a few hundred μm of the room temperature sapphire window, the temperature of the SQUID only increased by about 0.15 K (as determined from the *I-V* curve) above the temperature (about 4 K) registered by a thermometer located on the Cu cold finger a few millimeters from the SQUID [see Fig. 6.12(b)].

6.4 Vibration Isolation

The system I developed for isolating the cold finger from vibrations of the cold-point of the cryocooler has two main parts. As described in the previous section, I used six high-purity copper foils to make a thermal link between the cold finger and cryocooler and a network of six Kevlar threads to hold the cold finger (see Figs. 6.11). These strings are equilaterally distributed (120° apart) about the cold finger with one end of each string attached to a (non-vibrating) room temperature frame in the vacuum chamber (see Figs. 6.16, 6.17) and the other end tied to the cold finger. On the support frame, the threads are attached to brass screws (see Fig. 6.17) which can be turned to apply about 30 lbs of tension.

To give the thermal link flexibility, the 4 sheets were stacked on top of each other and formed into a sinusoidal pattern. I did this by pressing the foil stack using a 6.35 mm diameter rod to form 8 semicircular curves. The resulting final dimension of the thermal link including the sections for soldering to the cold finger was 52.07 mm wide x 52.32 mm in length.

The six Kevlar threads were used to rigidly suspend the cold finger (see Figs. 6.16, 6.17) inside the SQUID/window assembly. I chose Kevlar because it maintains its strength and resilience down to cryogenic temperatures and because of its very low thermal conductivity.

To understand the mechanical behavior of the cold finger, I modeled the above arrangement of Kevlar strings as shown in Fig. 6.18. Let k_{Cu} be the Cu link's spring constant and k_{kevlar} the Kevlar support system's effective spring constant. I will assume

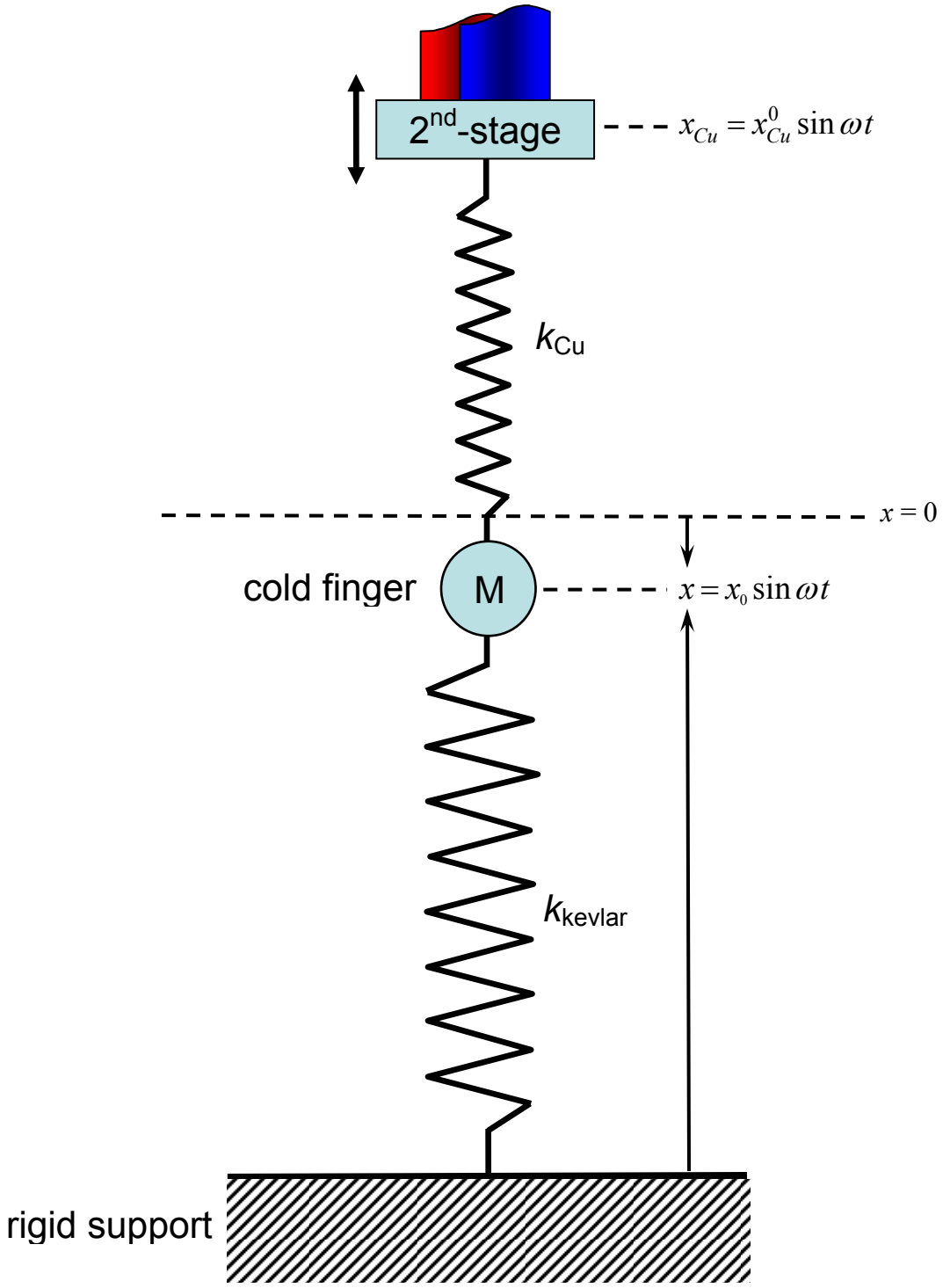

Fig. 6.18. Simple mechanical model of the Cu foil, cold finger and Kevlar strings. The cryocoller causes 2nd-stage to move the top of the Cu link. The position x of the cold finger with mass M is attenuated because the effective Kevlar spring constant k_{kevlar} is much greater than the Cu link's spring constant k_{Cu}.

that vibrations of the cryocooler cause the top of the Cu link to move as $x_{Cu} = x_{Cu}^0 \sin \omega t$. Then the differential equation governing the motion of the system is given by

$$M \frac{d^2 x}{dt^2} = -k_{kevlar} x - k_{Cu}(x - x_{Cu}), \tag{6.7}$$

where M = 0.13 kg is the mass of the cold finger. Since the resonance frequency $\omega = \sqrt{k/M}$ of the cold-finger was much larger than the oscillation frequency $\omega \cong 2\pi \, rad/\sec$ of the cryocooler, the steady-state amplitude of the motion of the cold finger is:

$$x_{kevlar}^0 = \frac{k_{Cu}}{k_{Cu} + k_{kevlar} - M\omega^2} x_{Cu}^0 \cong \frac{k_{Cu}}{k_{kevlar}} x_{Cu}^0. \tag{6.8}$$

From separate measurements on the Kevlar strings and copper foil, I found

$$\frac{k_{Cu}}{k_{kevlar}} \sim \frac{1}{1000}. \tag{6.9}$$

Thus, the system reduces the level of vibrations by a factor of 1000 in going from the cold point to the end of the cold finger.

One drawback of this 6-string design is that it is rather complicated, and I have to be very careful when putting the system together. In particular the threads go from the cold finger through small holes in the 30 K outer heat shield before attaching to support arms on the outer jacket of the window assembly. Three threads pull the cold finger up and the other three threads pull the cold finger down. This arrangement ensures that the cold finger is held rigidly to the outer jacket (by the threads) while being mechanically weakly coupled (by the Cu foil) to the vibrating cold point. Needless to say, it is critical in this arrangement that the Kevlar lines don't touch the outer heat shield since it is vibrating. Although it was complicated, the vibration isolation was so effective that under

34x magnification I was unable to discern any movement of the SQUID tip. The system was also stable; I found I could operate for months at a time.

Other sources of vibration must also be minimized, including mechanical pumps and the compressor. To minimize the transmission of vibrations coming from the Alcatel Drytel turbo pump, I filled a plastic container with 200 lbs of play sand and buried the vacuum line (from the turbo pump to the vacuum chamber) in the middle of this container. I then placed a 50 lb bag of sand on top of the container to keep the hose from vibrating out of the container. This approach is quite effective at damping most of the vibrations. To reduce noise, the helium compressor for the cryocooler was located 20 feet away in a room above the room where the microscope resided. Mechanical vibrations due to the compressor were mitigated by using flexible hoses and by clamping of the hoses to the pass-through conduit between the two rooms. Another key factor was relatively large mass and high rigidity of the vacuum assembly (~ 35 kg), so that the fairly small external forces from the hoses resulted in only very small motion of the apparatus.

6.5 Sample Scanning Mechanism

6.5.1 Translation System

In order to form two-dimensional images of spatial variations in the magnetic field from a sample, it is necessary to support and translate the sample with respect to the SQUID. The translation system is made up of four main components: a Dell Dimension 6400 personal computer, a *z*-stage, precision *xy*-translation stages, and the actuator controller which reads position data and converts instructions from the computer into electrical signals that control individual actuators.

The microscope is designed to collect data using a raster scan method; *i.e*. one line at a time. Prior to the scan the user selects the step size in the *x* and *y* directions and the number of the steps to take. Measurements of the magnetic field are taken beginning at the selected origin of the scan and the sample is scanned along one axis, say the *x*-axis. After all the steps in a line are taken, the sample is moved back to the beginning of the *x*-axis and then moved along the *y*-axis by one step. This process is repeated until the specified scan area has been covered. When selecting the step size, a basic consideration is that features of interest will be lost if the step size is made larger than the feature size. Thus the step size should be decreased until features of interest can be resolved.

One noteworthy feature of our system is that we chose to move the sample under the SQUID and not move the SQUID over the sample. One reason for this choice is that the SQUID is attached to the cryocooler which is attached to the vacuum chamber and compressor hoses so that it is not so easy to move the SQUID. More importantly, if the SQUID moves, it will see variations in the magnetic field just from spatial variations in the ambient field and these would act as an additional noise source. Thus, fixing the SQUID's position and moving the sample relative to the SQUID allows for a better measurement of the field due to just the sample.

6.5.2 Translation System Hardware

In order to image magnetic field variations over a sample, the translating system needs to be able to perform three-dimensional positioning. Typical samples range in size from millimeters to centimeters, and the magnetic field variations may dictate sub-micrometer positioning. To position the sample as close as possible to the SQUID

window in the *z*-direction, I use a custom made, non-magnetic *z*-stage mounted on top of the *xy*-stages, see Fig. 6.7(a). With this set up, I can control *z* to about 1 μm.

The *xy*-scanning stage is comprised of two model 850G actuators with linear horizontal translation stages, ESP6000 drivers, and an ESP6000 motion controller all made by Newport, Inc. [21-23]. The 850G actuators have a minimum step size of 1 μm with an absolute accuracy of 50 μm over the full range of motion of 25 mm. I used a precision machinist's right-angle in order to precisely align the two stages to form the *xy*-translation horizontal stage.

6.5.3 Scanning Software and Scanning Parameters

The software I used to control the microscope is called "Switched_xy μWave Flux vs Time" and was written in LabView version 6.0.1. Figure 6.19 shows an image of the control screen [24]. The software runs under Microsoft Windows XP on a Dell Dimension 4600 personal computer. The software is responsible for positioning and translating the sample, controlling the application of pulses, recording the output from the SQUID (counts) and storing the position information from the actuators. After each line scan the flux versus delay data is displayed so the user can monitor the progress of the scan (see Fig. 6.19).

To operate the software the user first needs to manually position each translation stage and then input that position as the origin. The other positioning parameters that need to be given are the step size for each axis and the total number of steps to take.

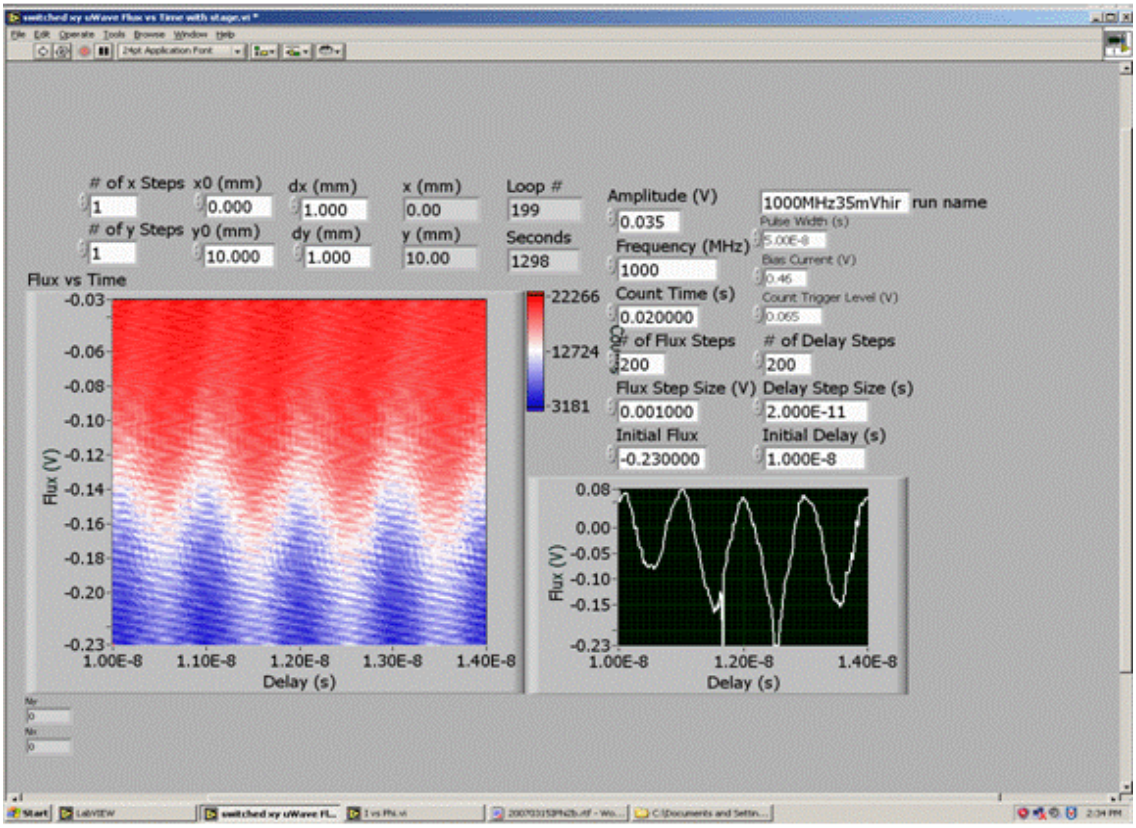

Fig. 6.19. Image of screen used to control scanning and data collection for the SQUID microscope.

Besides controlling the scanning, I also set the initial flux applied to the SQUID, the flux step size, and the total number of flux steps to take. This information will set the limits of the flux transmitted to the 1-turn coil on the SQUID chip. In addition, I set the initial delay time, the delay step size, and the number of delay steps to take. This sets the limits of the region in time to be examined. Another parameter I need to set is the voltage trigger level that determines where a signal triggers a count. To do this, I examine the voltage response of the SQUID on the oscilloscope; this trigger voltage level is generally set so the counter is recording 100% of the possible counts but not triggering when the SQUID does not switch. Once the voltage level is determined I can use the software to further refine the level for the scan.

The scanning software also allows me to set the file name where the data will be recorded, and record the amplitude and frequency of the signal of interest. The total scan time (typically between 0.25 and 3 hrs) depends on the grid size and the measurement time per pixel. The time spent at each pixel is dependent on the count time set for the counter (typically ~ 20 ms). Ultimately, the scan time is limited by the scanning hardware, but also by the time it takes LabView to process commands. LabView is a text based command language. That is, each command is a text string that the instrument processes and then responds back as to its state. This takes quite a bit of time (typically ~500 ms); it would be faster if during the scanning the data were held in a buffer until the entire scan was complete and only then uploaded to a file.

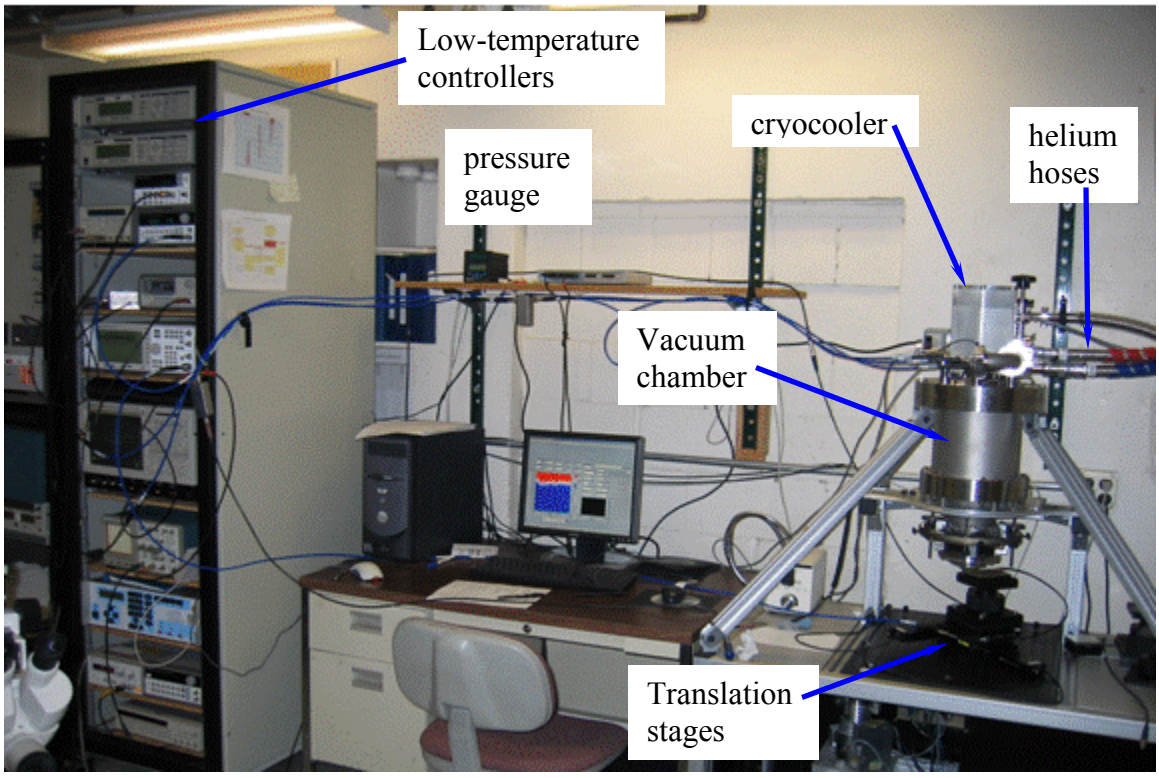

Fig. 6.20. Photograph showing overall system comprising the scanning SQUID microscope.

6.6 SQUID Electronics and Instrumentation

6.6.1 Experimental setup

The overall layout of the SQUID microscope system is shown in Fig. 6.20. On the left resides the rack containing the electronic instrumentation, including the pulse generator, microwave generators, function generator, universal counter, and oscilloscope. In the middle of the photograph is the computer that controls the microscope and collects data. On the right is the scanning SQUID microscope with the vacuum chamber and translation system visible. The cryocooler has two hoses for the helium from the compressor which can also be seen in the photograph; the red and blue braiding designate the high and low pressure lines, respectively.

Figure 6.21 shows a block diagram of my experiment. An Agilent E4426B microwave signal generator sends a repetitive test signal to the sample. The test signal acts as the master clock. I use the 10 MHz reference signal from the microwave generator as the trigger signal, while the clock sends a trigger signal with a 10 MHz repetition rate, the pulse generator can only respond at 1 MHz maximum. [I note this maximum depends on the pulse delay time, *i.e*. if the pulse delay is set high, this 1 MHz repetition rate gets reduced.] Thus, the pulse generator is triggered by every 10th trigger signal from the 10 MHz clock signal.

The signal generator also sends a delay trigger to an Avtech AVPP-1-B pulse generator. Each time a trigger signal is detected by the pulse generator, it sends a rectangular current pulse with 400 ps duration to the SQUID.

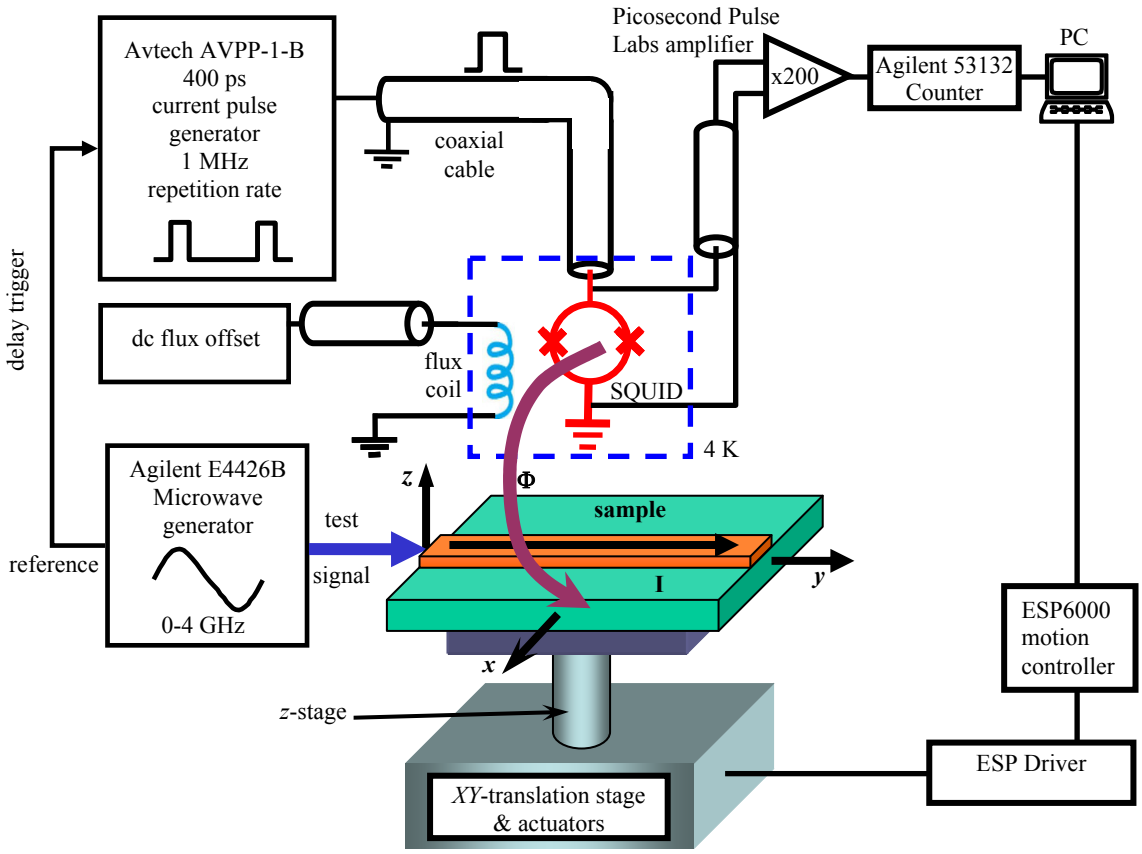

Fig. 6.21. Schematic of experimental arrangement for high-bandwidth SQUID microscope. The test signal (a GHz sine wave) is provided by a microwave generator connected to the sample. A controllable dc offset flux is coupled to the SQUID via a one-turn on-chip loop. The SQUID current source is a 400 ps pulse generator. A counter detects the number of voltage pulses from the SQUID in a given time interval (10-20 ms).

I also use a Hewlett-Packard 33120A function generator to send a dc magnetic flux offset to the one-turn coil that couples flux to the SQUID.

The voltage amplitude of the pulse generated if the SQUID switches is approximately 2.8 mV. This is fed into a Picosecond Pulse Labs [25] high frequency amplifier with a gain of 200, producing an output pulse of almost 0.5 V.

The output pulses are fed to an Agilent 53132 counter that sums the number of voltage pulses above a 150 mV threshold received in a given time (typically between 1

and 20 ms). I typically use a pulse repetition rate of 1 MHz that yields a maximum of 1000 to 20,000 counts for 1 and 20 ms counting interval.

The bias current pulse amplitude and the dc flux are set such that, in the absence of any signal flux, the SQUID produces a voltage pulse for 50% of the current pulses. If the bias current pulse amplitude is set too low or too high, the SQUID will either never show a voltage pulse, or show continuous pulsing, so some care must be taken in setting up the pulse generator.

6.6.2 Temperature and Pressure Monitoring

To keep track of the system's behavior, I kept a daily record of the temperature of the 1^{st}-stage, 2^{nd}-stage and cold finger, as well as the pressure in the vacuum chamber. With this data I could tell how well the cryocooler was performing and if the SQUID was at a reasonable operating temperature. Excessive drift in temperature affects the characteristics of the SQUID (the critical current modulation changes). An increase in either the temperature or pressure can be an indication of a problem with the vacuum chamber or the thin sapphire window.

The pressure in the vacuum chamber was monitored using the KPDR900 vacuum controller with a KJLC 979 ATV gauge, both from the Kurt J. Lesker Company [28]. The KPDR900 is a stand alone single channel power supply and display. The KJLC 979 ATV combines a Pirani and mini ion Bayard-Alpert gauge, providing a wide measuring range from ultra high vacuum (10^{-10} Torr) to atmospheric pressure.

I used three different thermometers to monitor the temperature of different parts of the microscope. I placed a platinum thermometer on the 1^{st}-stage and Cernox thermometers [26] on the 2^{nd}-stage and the sapphire SQUID point. I recorded the

temperature using two Neocera LTC-21 low temperature controllers [27]. All three thermometers have resistances that change as a function of temperature. The thermometers were wired up in a four-point configuration using Lakeshore QuadTwist QT-36 wire (two pairs of twisted 36 gauge wire). The leads from each thermometer were thermally anchored to gold coated thermal bobbins on each stage, and each thermometer was attached using STYCAST 2850GT epoxy [13].

6.7 Operation and Maintenance

6.7.1 Cool down procedure

Once the microscope was assembled I connected the vacuum chamber to the Alcatel Drytel 31 pump and pumped out the chamber. Under normal conditions it takes a few hours for the pressure in the chamber to reach 5×10^{-4} Torr.

Prior to starting the cryocooler, I would go through a safety checklist. First, I would record the minimum and maximum helium pressure on the gauges of the cryocooler compressor. I would then visually check the helium high pressure gas lines, the water lines from the water chiller, and the 240 Volt electrical supply lines to the compressor and water chiller. Next, I would check that the sapphire window was moved several millimeters away from the SQUID tip. Fourth, I turned on the water chiller. The water bypass system I built allowed me to regulate the flow rate into the cryocooler compressor; I would set it to the manufacturer's specifications of 1.8 gallons per minute. Also, I set the water temperature to 20° C on the water chiller and recorded both the water flow rate and temperature. With the water chiller running and cooling the compressor, the helium compressor can be started. The cryocooler normally makes a slow chugging sound with a frequency of 1.3 Hz. Also, at start-up the pressure on the

high-pressure gauge will normally oscillate in the range of 330-340 psi and the low-pressure gauge will oscillate in the range 80-90 psi. As the cryocooler reaches operating temperature the gauges will stabilize to 250-260 psi for the high pressure gauge and 95-110 psi on the low pressure gauge. Once the cryocooler starts to cool, cryopumping will further reduce the pressure in the vacuum chamber, which eventually settles to approximately 5 x 10^{-7} Torr.

It takes about three hours for the system to cool down and all three thermometers on the system to level off. At this point, the 1st-stage will read about 29.5 K, the 2nd-stage 2.7 K and the cold tip will reach about 4 K. A typical set of cool down curves is shown in Fig. 6.22.

6.7.2 Scanning Procedures

Once the SQUID has reached its operating temperate of about 4 K, I use an oscilloscope to record an *IV* trace. I use this trace to determine some key SQUID parameters such as the minimum and maximum critical current, the contact resistance and the retrapping current.

With the SQUID at its operating temperate, I next positioned the thin sapphire window very close to the SQUID. Since the window is transparent, it is possible to observe the SQUID point through the window as the window is adjusted. To do this I placed a mirrored 90° prism on the *z*-axis stage and used an optical microscope while guiding the window up to the SQUID [see Fig. 6.23(a)]. The window has four lateral positioning screws to allow the window to be centered relative to the SQUID and three

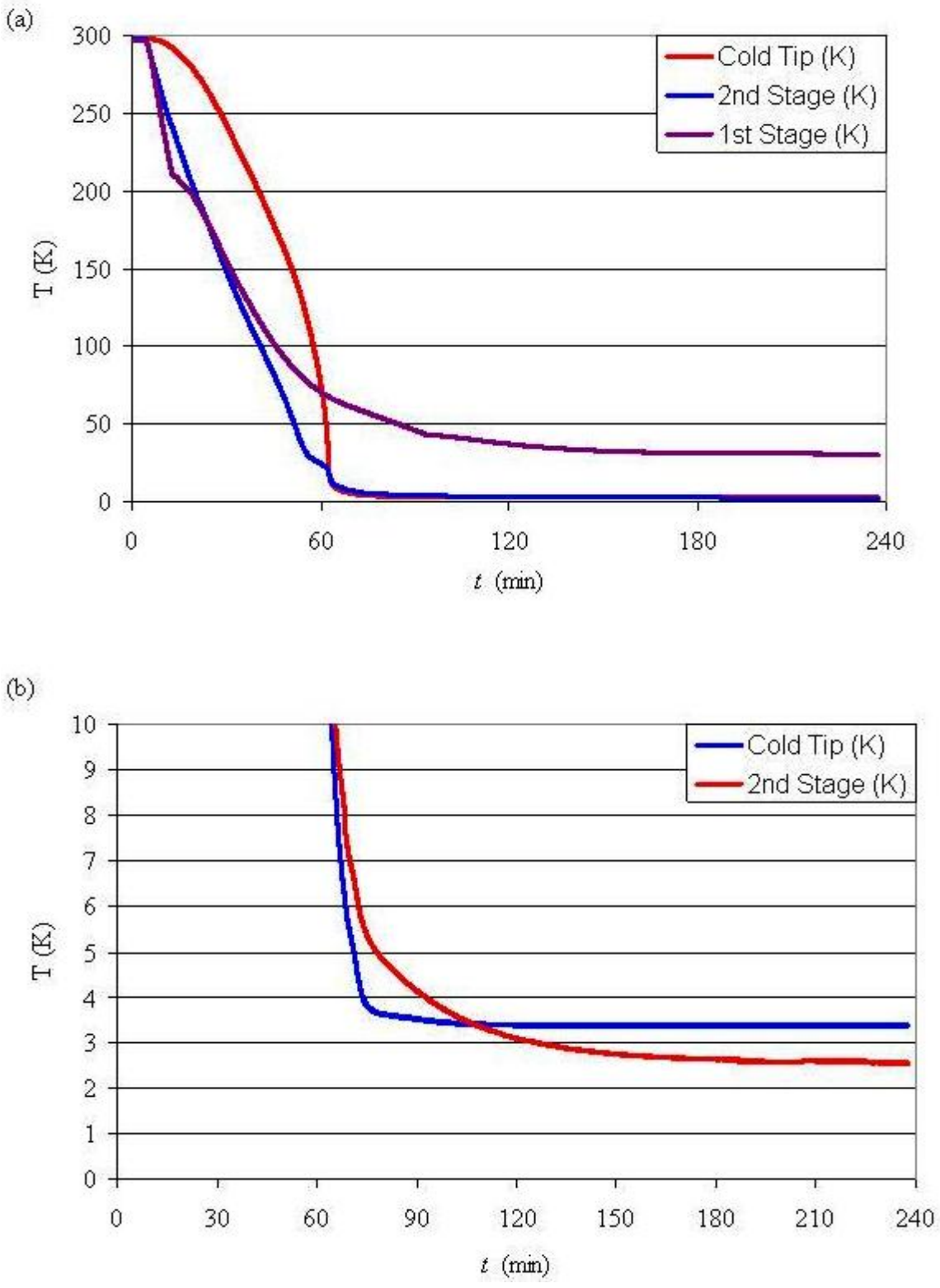

Fig. 6.22. (a) Typical set of cooldown curves for the cryocooled SQUID microscope. Notice that within about three hours all three thermometers have leveled of. (b) Expanded temperature scale from 0 to 10 K for 2nd stage and cold tip.

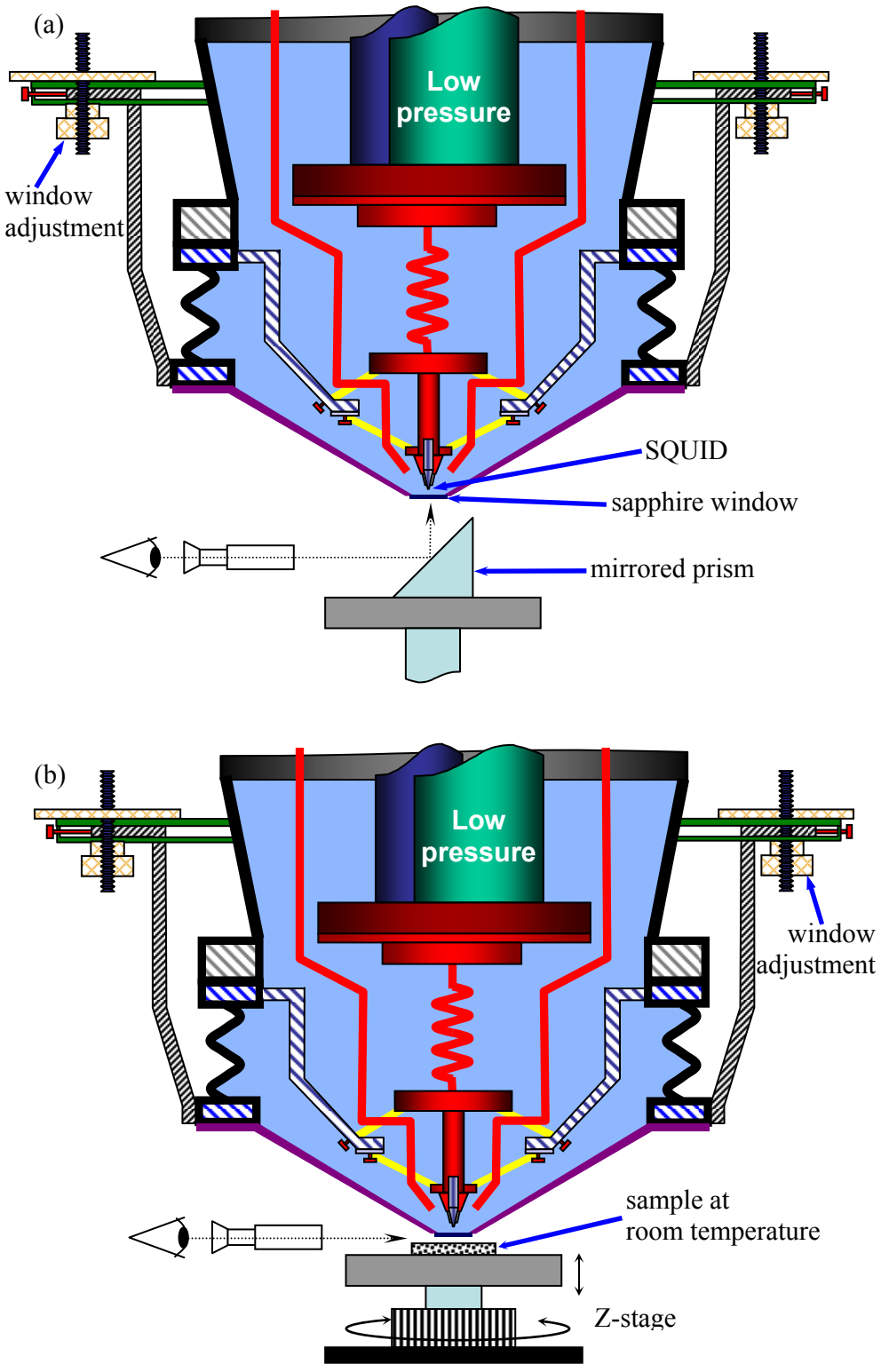

Fig. 6.23. (a) Using a mirrored prism and an optical microscope I guided the sapphire window close to the SQUID. (b) After mounting a sample I used the manual *z*-stage to position the sample very close to the sapphire.

height adjustment knobs to raise the window as close as possible to the SQUID without touching it.

After the window is in place and I am satisfied with the SQUID *IV*, I connect the pulse generator to the SQUID current bias line. The output from the SQUID is connected to the Picosecond Pulse Labs 5840 microwave amplifier which in turn is connected to the Agilent 53132A universal counter. Finally, the Agilent 33120A function generator is connected through a 10 kΩ resistor to the single turn loop on the SQUID chip. Once all the lines are connected I can then start the microscope scanning software and hardware.

In order to scan a sample the sample has to be mounted to the *z*-axis translation stage and positioned close to the sapphire window. I use the optical microscope to gauge the distance between the sample and SQUID window [see Fig. 6.23(b)]. Great care must be exercised to avoid breaking the window. It is very important to check that there is enough space between the sample and the window over the entire *xy*-scanning range. Also, in order to avoid introducing an artificial gradient in the measured flux while scanning the sample, the horizontal plane of the sample should be parallel with the translation stage. I checked the alignment using the optical microscope and look out for any obstructions on the sample or the translation stages that need to be removed.

The region of interest to scan is then determined and I enter the scanning parameters into the scanning software. I can then manually position the translation stages to the initial position and start a scan. After each line scan a flux versus delay time image is displayed and updated in real time on the computer monitor. Upon completion of the scan the data is saved for latter processing and examination. A typical scan of *e.g*. a

microstrip line (see Chapter 9) covers an area of 8 mm by 51 mm and takes about 4.5 hours, with about 1200 pixels.

6.7.3 Microscope service and maintenance

Over the last two years (2007-2009) there were periods when I ran the microscope continuously for months without losing vacuum or experiencing large temperature drift. Invariably, however, the system would eventually need to be taken down for repair or maintenance. Prior to shutting down the cryocooler, the sapphire window should be moved several millimeters away from the SQUID tip so that thermal expansion or jostling of the system does not lead to a disaster. As a matter of fact, this can be called the first rule of scanning SQUID microscopy. Care of the sapphire window is the most important thing to consider if you want to use the microscope for long periods of time.

Another precaution to take prior to shutting down is to totally disconnect all electrical cables from the microscope. This minimized the chance of blowing out the SQUID junctions from static discharge. To protect the exposed leads, I placed 50 Ω SMA electrical terminators on all the connectors leading to the SQUID. After the cryocooler is turned off, it takes about 24 hours to warm to room temperature.

I leave the vacuum pump operating in order to prevent condensation from forming in or on the outside of the vacuum chamber or on the sapphire window. When the temperature of the cooling water leaving the cryocooler compressor matches the temperature of the water leaving the compressor, I turn off the water chiller. When the cold finger and second stage have reached room temperature the vacuum pump can be turned off, and the system vented through the vacuum line.

Disassembly of the microscope is done in the reverse order of its assembly. I begin by removing the fiberglass cone with its thin window. In order to remove the cold finger and pulse tube system, the Kevlar vibration isolation system must be disconnected. Next, the cryocooler is unbolted from the vacuum chamber and lifted straight up and out of the vacuum chamber along with the cold finger and SQUID tip. As a word of warning, the basic cold head weighs 14 kg and must be lifted (preferably by two people) straight up and out of the vacuum chamber. Great care must be exercised in order to avoid damaging the SQUID tip and radiation shields during removal or insertion of the cryocooler. Until a design exits that allows for easier access to the microscope, removal or insertion of the cryocooler should be performed as infrequently as possible so as to minimize the risk of damage to the cryocooler.

Maintenance on the pulse-tube crycooler is rather straightforward. The cold head generally requires maintenance only after an obvious increase in the base temperature. Since there are no moving parts, there should not be wear to the cold head while operating. Recommended routine maintenance on the compressor is specified for every 15,000 hours [29]. This consists of replacing the charcoal absorber, a simple 30 minute procedure. Additionally, I would recommend recording on a daily basis several key operating parameters concerning the cryocooler compressor and water chiller; including the low and high pressure readings on the compressor, and the temperature, pressure, and flow rate of the water chiller. The importance of the water chiller is simple - the cryocooler cannot work without chilled water cooling the cryocooler compressor. Finally, I note that anyone using the system should carefully read the Cryomech PT405 cryogenic

refrigerator installation, operation and routine maintenance manual. It is a well written and descriptive manual and is highly recommended [29].

6.8 Summary

I began this chapter with an overview to the microscope. I next discussed in detail the main components. This included the helium cryocooler, vacuum system and cold finger. I then gave a detailed description of the cold finger, starting with the fabrication of the SQUID chip on the sapphire rod. This was followed by a description of how I assembled the cold finger. I next gave a step-by-step discussion of how to assemble the microscope and described how I thermally anchored the cold finger. I then discussed details of the thermal radiation shielding and discussed the wiring from the room temperature electronics to the SQUID tip. I next explained how to align the window relative to the SQUID and how the window is raised up to the SQUID tip. This was followed by a discussion of how to mount the sample and position it near the sapphire window. Finally, I concluded this chapter with a discussion on the operation and maintenance of the microscope and cryocooler.

Chapter 7: Measurement of the SQUID's Response to a Rapidly Varying Flux Signal

7.1 Statement of the Problem

In this chapter I discuss a series of experiments that I performed to test the pulsed SQUID sampling technique that I described in section 5.3. These experiments were done with a hysteretic niobium dc SQUID in a liquid helium (LHe) dewar. This work allowed me to test the temporal resolution of the SQUID for flux detection and develop the electronics that I incorporated into the microscope.

The experiments involved sending bias current pulses to a hysteretic dc SQUID and measuring its voltage response while applying a sinusoidal magnetic flux. Depending on the amplitude of the current pulse and the magnetic flux through the SQUID, the probability of the SQUID switching to the voltage state will vary.

7.2 Large Bandwidth Dip Probe Design and Construction

7.2.1 Dip Probe Design and Construction

For these experiments, I constructed a large bandwidth "dip probe". The dip probe allowed for a fast and convenient means to measure and characterize the SQUID while it was in a thermally stable environment. The dip probe was constructed using a metallic electronic project box connected to a 1 m long thin-walled stainless steel tube (see Fig. 7.1). The thickness of the tube wall was 0.02 in; stainless steel was chosen for its rigidity and poor thermal conductance. I attached an aluminum mount/sample box to one end of the probe. The maximum size of the holder was dictated by the inner diameter of the neck

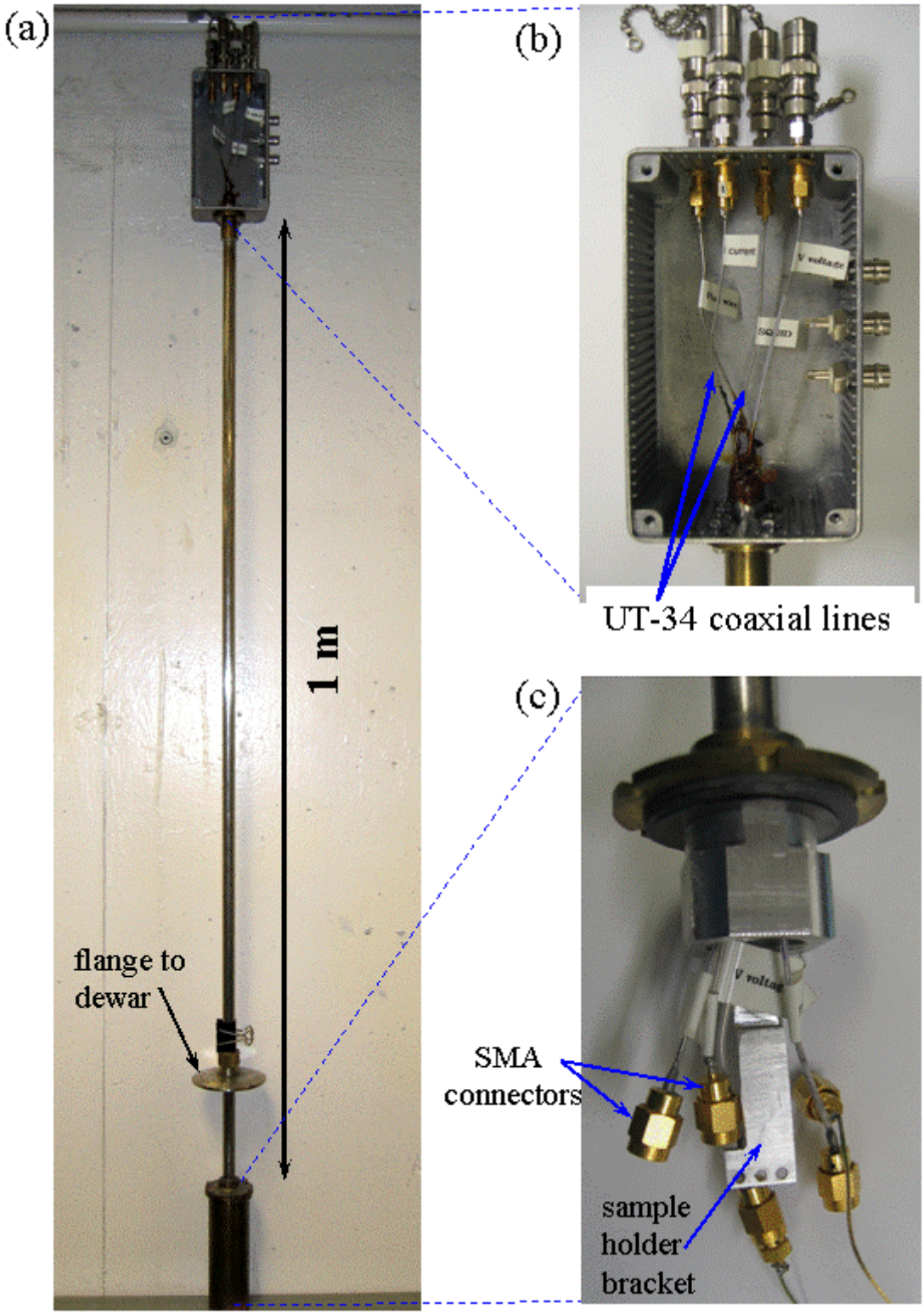

Fig. 7.1. (a) Photograph of dip probe used in liquid helium dewar to test the SQUID. (b) Close-up of top of dip probe showing semirigid coaxial cables and SMA connectors. (c) Bottom of dip probe showing SMA connectors and SQUID mount.

of the LHe dewar, which was 2 in. All the components used for the sample holder and holder bracket were made from non-magnetic materials. The sample holder could be enclosed in a hollow brass cylinder that had an interior lined with 0.06 in thick lead [see Fig. 7.1(a)] which is superconducting at 4.2 K. This was done to shield the SQUID from fluctuating magnetic fields in the laboratory.

Since I was using a pulsed SQUID sampling technique, I constructed a dip probe using coaxial transmission lines with greater than 1 GHz bandwidth. Coaxial transmission lines are readily available in a variety of materials and diameters. I chose UT-34-SS semi-rigid cable; this is a relatively small diameter 50 Ω coaxial cable from Micro-Coax [1] [see Figs. 7.1(b) and 7.1(c)]. This coax is rated to have a bandwidth of dc to 154 GHz. It has an outer diameter of 0.034 in and inner conductor diameter of 0.008 in. The outer conductor is 304-stainless steel, and the dielectric material is (0.026 in diameter) polytetrafluoroethylene (PTFE, or Teflon). The inner conductor is a silver-plated copper-weld steel (SPCW); the silver plating is done to minimize the attenuation of a signal along the inner conductor. I chose this stainless steel coaxial line because it has a low thermal conductivity. The capacitance per meter for the cable is 95.1 pF/m and the insertion loss at 1 GHz is 3.67 dB/m. Semi-rigid transmission lines are relatively flexible and easy to work with; in the case of UT-34-SS the minimum bending radius is 2.54 mm.

In order to maintain 50 Ω impedance at the connections to the cable, I soldered 50 Ω Sub-Miniature Adapter (SMA) connectors at each end of the coaxial lines [2]. The bandwidth for the SMA connector is 18 GHz and for an SMA to-BNC converter the bandwidth is 4 GHz [see Figs. 7.1(b) and 7.1(c)]. While this is much less than the 154

GHz bandwidth for my coaxial line, it had little impact on my measurements because the pulse generator I used had a minimum pulse width of 400 ps. Each coaxial line was insulated with Teflon tubing and shielded by housing them inside the dip probe's stainless steel tubing, described above [see Fig. 7.1(b)].

At the top of the dip probe, I hard soldered a brass flange to the stainless steel tube. I then attached a connector box to the brass flange using six 4-40 stainless steel screws. I sealed the top of the stainless steel tube with silicone sealant to stop moisture and air from going down the tube when the probe was in liquid helium. At the other end of the stainless steel tube the sample bracket was attached to a brass threaded tube which in turn was attached to the stainless steel tube. This brass threaded tube is 1" long, and hard soldered to the stainless steel tube. The sample box was then screwed on to the sample bracket.

7.2.2 Sample Holder

The SQUID chip was mounted in a package [see Fig. 7.2(a)] that contained a 25 mm x 25 mm x 10 mm SQUID chip holder made from Delrin on which was mounted a 25 mm x 25 mm circuit board. I soldered four SMA board connectors to the circuit board. For my measurements only three coaxial lines were needed. One coaxial line was for the SQUID bias current pulses, the second was for measuring the voltage response, and the third was for applying magnetic flux to the SQUID (see Fig. 7.2(a)). Using GE varnish, I attached the SQUID chip directly to the Delrin holder through a hole in the circuit board. The final step was to use wire bonds to connect the circuit board to the SQUID contact pads; I used approximately 2 mm-long Au wire bonds.

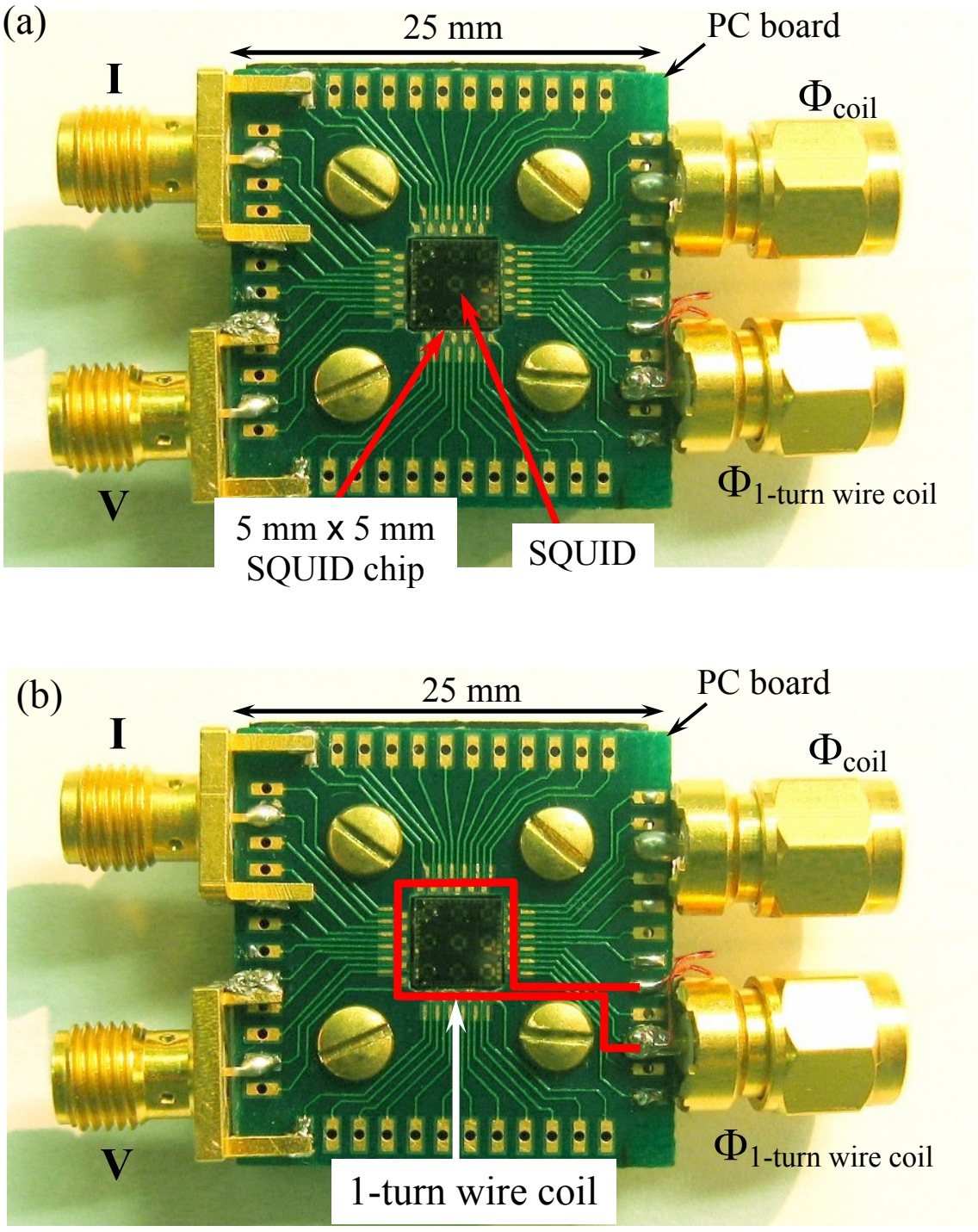

Fig. 7.2. (a) Sample package with SQUID chip mounted in center of package. The circuit board is 25 mm x 25 mm with a 5 mm x 5 mm square center hole for the SQUID chip. The SMA connectors on the left are the bias current (top) and voltage response (bottom). Whereas, the connectors on the right are the on-chip single-turn coil (top) and copper wire (bottom) for applying external magnetic flux to the SQUID. (b) Outline of 1-turn wire coil formed by Cu wire under circuit board.

The sample holder was then bolted to the sample holder bracket and the SMA connectors connected to their respective points on the sample holder.

If everything worked properly, I had two choices for applying flux to the SQUID: an on-chip one-turn coil or a thin copper wire that ran in a channel machined into the Delrin mount. For these experiments, it turned out that the one-turn coil was not functional, due either to design or fabrication failure, so I used the copper wire to apply flux. Figure 7.2 (b) shows an outline where the Cu wire traces around the SQUID chip below the circuit board.

Prior to connecting the SMA connectors to the SQUID sample package, I placed 50 Ω terminating resistors to the room temperature lines at the top of the connector box; this was done to protect the SQUID from electrostatic discharge. After the sample package was connected, the dip probe could be inserted into the LHe dewar. I did this slowly so as to save liquid helium, to allow for the sample to reach thermal equilibrium, and to minimize thermal stress.

7.3 SQUID and Pulse Signal Characterization

Figure 7.3 shows a photograph of the Hypres SQUID I used for the measurements, device HS_1. This was a different device, with a somewhat different design, than the SQUID I used for microscopy. This SQUID had smaller junctions and a washer design with an on-chip single-turn coil along the inside of the washer hole. The outside washer is a 30 μm x 30 μm square loop and the center hole is 10 μm x 10 μm (see Fig. 7.3). For this device, I found that the critical current modulated between 55 μA and 87 μA. As I noted above, the 1-turn coil was not functional and I instead used a thin copper wire for the flux line.

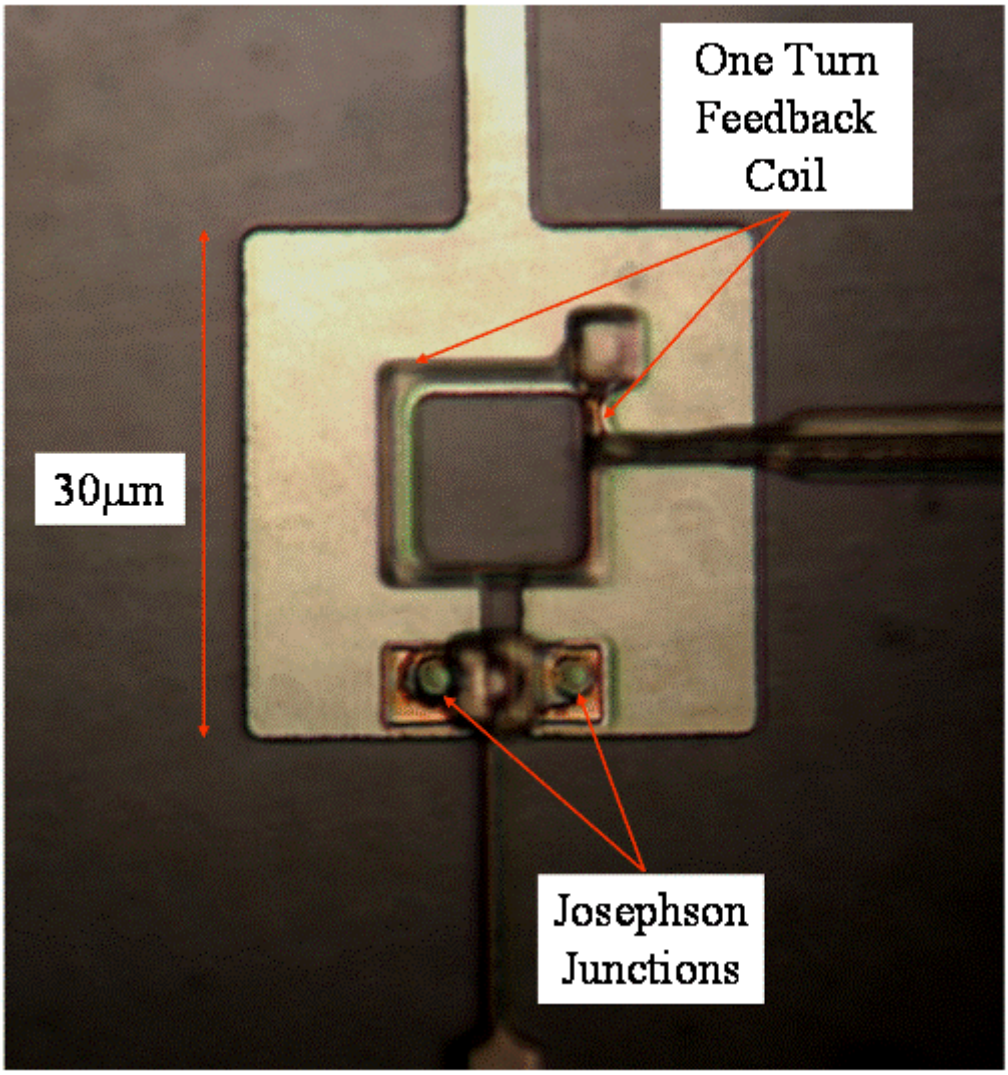

Fig. 7.3. Photograph of hysteretic niobium SQUID (device HSQ_1) used for 4 K measurements in the dip probe. The SQUID washer is a 30 μm x 30 μm square loop with a 10 μm x 10 μm square hole in the center. The Josephson junctions are 3 μm x 3 μm and there is no shunt resistor. The SQUID inductance is about 15 pH and $\beta \approx 1$.

Figure 7.4 shows the pulsed sampling measurement circuit that I used to test the SQUID. For these early experiments, I used a Stanford Research Systems DG535 pulse generator to send fixed amplitude current pulses with a 10 ns pulse width to the SQUID [3]. The bias current pulse amplitude and the dc flux were set such that, in the absence of any signal flux, the SQUID showed a voltage pulse for approximately 50% of the current

pulses (see Fig. 7.5); If the bias current pulse amplitude is set too low or too high, the SQUID will either never show a voltage pulse, or show continuous pulsing. When the SQUID does switch, the amplitude of the raw SQUID output voltage pulse is approximately 2 mV. I fed the output pulse into a Picosecond Pulse Labs high frequency amplifier [4] (model 5840B) with a gain of 200 to boost the output to about 0.5 V (see Fig. 7.5). I sent the output of this amplifier to an Agilent 53132A universal counter [5] that counted the number of voltage pulses above a 0.3 V threshold in a given time. With a current pulse repetition rate of 1 MHz and a counting interval of 1 to 20 ms, this yields maximum counts of 1000 to 20,000.

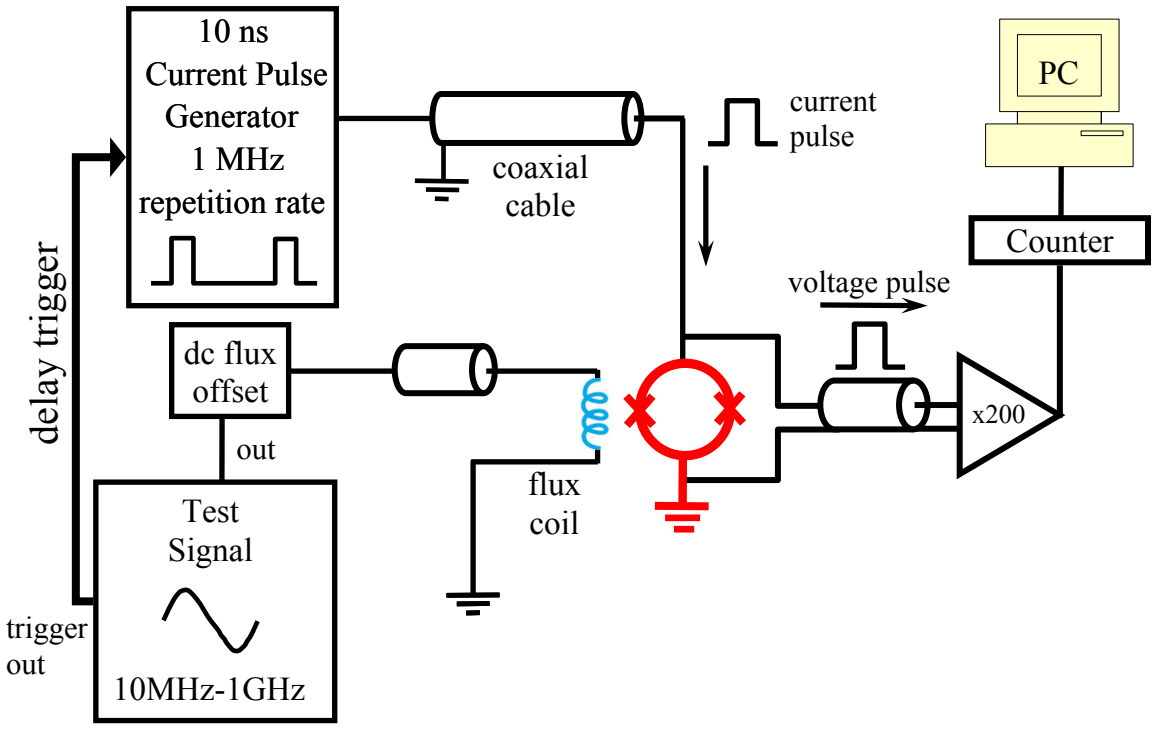

Fig. 7.4. Schematic of the experimental setup. The test signal (a 10 MHz–1 GHz sine wave) is provided by a microwave generator connected to the flux line. A controllable dc offset is coupled into the same line as the flux signal. The SQUID current pulse generator sends 10 ns pulses to the SQUID at a 1 MHz rate. A counter detects the number of voltage pulses from the SQUID in a given time interval (1 to 20 ms).

With the current pulse height set near the midpoint of the SQUID's critical current range, the voltage pulses can be turned on and off by adjusting the flux applied to the SQUID. I used a function generator to supply a computer-controlled dc current of between -50 mA to +50 mA to the flux line. From the periodicity of the $I_c(\Phi)$ curve, I found that 82.5 mA in the flux line generated one quantum of flux $\Phi_0=(h/2e)$ in the SQUID, which means that the mutual inductance between the SQUID and the flux line was 25 pH. For our 10 μm x 10 μm SQUID loop, and given the area of the SQUID and the 100 Ω current-limiting resistor, this corresponds to a coil transfer function of 0.84 μT/V.

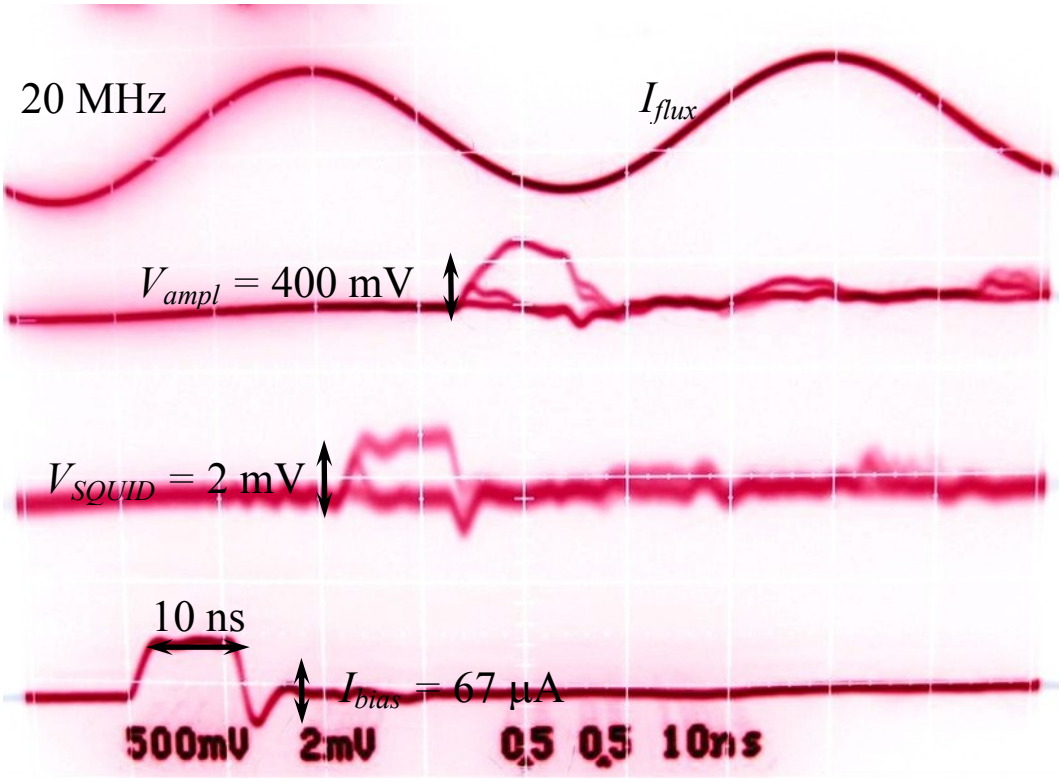

Fig. 7.5. Oscilloscope trace showing (from bottom to top) 10 ns bias current pulse of amplitude 67 μA, 2 mV SQUID voltage response (superimposed on non-switching voltage response), 400 mV amplified SQUID voltage, 20 MHz test signal sent to flux line.

7.4 Detection of Microwave Frequency Magnetic Fields using Pulsed SQUIDs

To see if the SQUID could measure a fast, time-dependent flux, I sent an oscillating test signal to the flux line (see Fig. 7.4). I externally triggered the bias current pulse from this test signal. By adjusting the delay of the bias current pulse relative to the test signal, the SQUID responds to the signal at different delay times. To measure the test-signal flux as a function of time, I fixed the bias current at an optimum location (in the middle of its range); then, for a given delay between the signal and the bias pulse, I swept the dc flux level to see the SQUID switching voltage turn on or off. I then recorded the number of counts in a 1 to 20 ms time interval at each flux value. I then incremented the delay by one pulse width (10 ns) and accumulated counts as I again swept the dc flux. By repeating this process I generated a 2D histogram of the number of switching events as a function of both flux and delay time. For each value of the delay, I then found the interpolated value of the flux for which the counts were 50% of full scale. This technique was first used by Matthews and Kwon [6,7] and the result is a map of the flux from the test signal as a function of time.

Figure 7.6 shows an example of a flux waveform $\Phi(t)$ obtained by this process. In this case a 10 MHz sine wave with an amplitude of 20 $m\Phi_0$ was used as the signal. Since I sampled with 10 ns current pulses, and set the delay to increment in 10 ns steps, this gives 10 samples per period. This false color plot shows the number of counts for each delay and flux value. Blue corresponds to no counts, red to the maximum number of counts, 10^4 in this case, and white corresponds to 50% or 5000 counts. The solid circles mark the

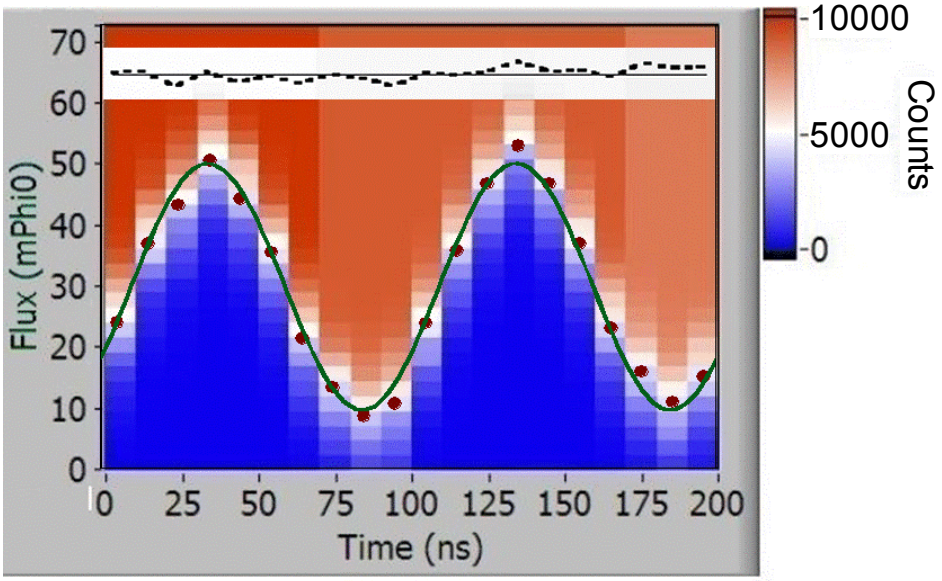

Fig. 7.6. False color plot showing the number of counts for each delay (sampled every 10 ns) and flux value for a 10 MHz test signal. Blue corresponds to no counts, red to the maximum number of counts (10000). Solid circles mark the interpolated 50% count rate, solid green line is the best fit to 10 MHz sine wave. The current pulse width was 10 ns with a repetition rate of 1 MHz. The inset shows the residual difference between the fit and the measured data.

interpolated 50% count rate, the solid line is the best fit of a 10 MHz sine wave to these points. The residual is shown as a dashed line, with the zero shifted by 65 $m\Phi_0$ for clarity.

Figure 7.7 shows results for a 100 MHz sine wave flux signal. Here I set the delay to increment in 1 ns steps, which again let me sample the test signal 10 times per period. Note however, that this was 10 times shorter than the current pulse itself. The plot in Fig. 7.7 shows the resulting number of counts for each delay and flux value. Blue corresponds to no counts and red to the maximum number of counts, which was again 10^4. The solid circles mark the interpolated 50% count rate, the solid line is the best fit of a 100 MHz sine wave to these points. Again, the measured 50% points are well fit by a sinusoidal curve.

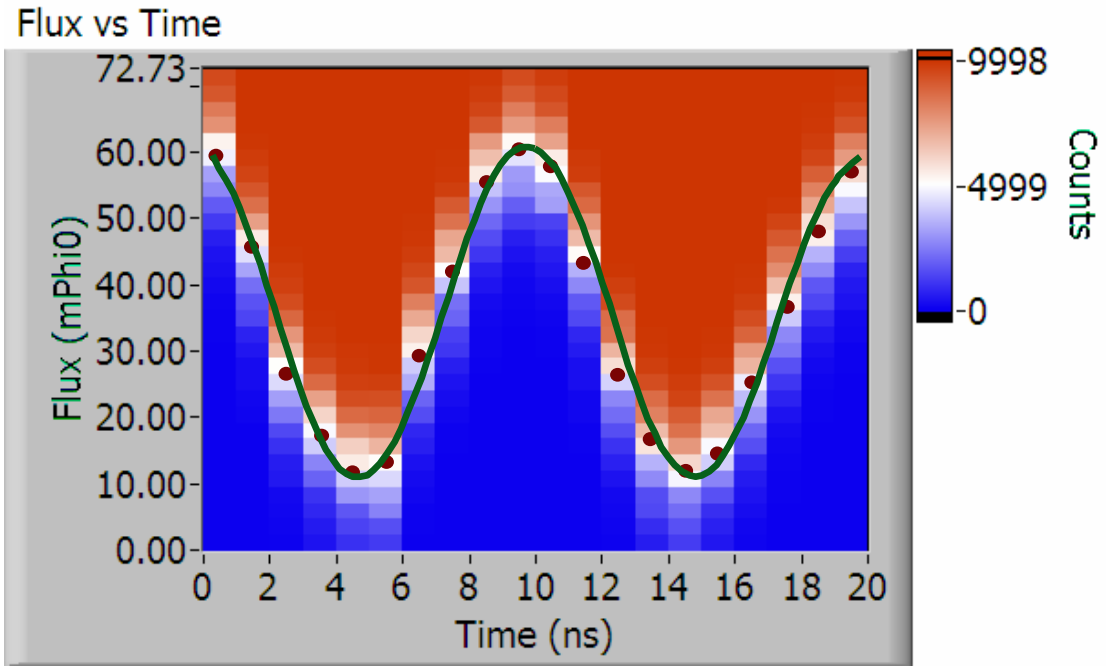

Fig. 7.7. False color plot showing the number of counts for each delay (sampled every 1 ns) and flux value for a 100 MHz test signal. Blue corresponds to no counts, red to the maximum number of counts (10000). Solid green line is the best fit to 100 MHz sine wave. The current pulse width was 10 ns with a repetition rate of 1 MHz.

Finally, Fig. 7.8 shows the results of an experiment in which the signal-under-test was a 1 GHz sine wave. Although the current pulse width remains at 10 ns, in this case the time delay with respect to the test signal is shifted by increments of only 10 ps, rather than 10 ns. Despite the fact that the period (1 ns) of the applied signal is ten times shorter than the pulse width (10 ns), we still measure a well-defined sine wave at 1 GHz. This strongly supports the idea that the effective pulse width is considerably shorter than 10 ns. Investigation of periodic signals other than sine waves would be necessary to confirm this.

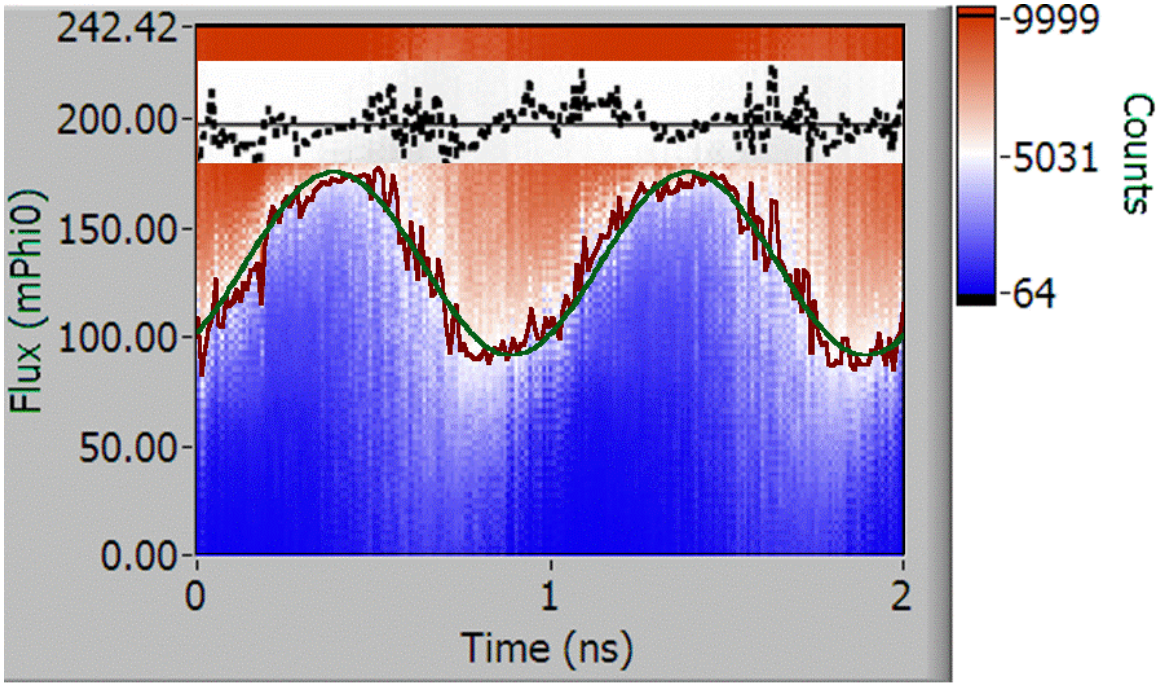

Fig. 7.8. False color plot showing the number of counts for each delay (sampled every 10 ps) and flux value. Black corresponds to no counts, white to the maximum number of counts (10000). Solid circles mark the interpolated 50% count rate, the solid line is the best fit to a 1 GHz sine wave. The residual is shown as a dotted line, with the zero shifted by 200 mΦ_0 for clarity. The current pulse width was 10 ns.

Finally, we note that the residual plotted in Fig. 7.8 shows a somewhat higher noise level than that found in Fig. 7.6 or Fig. 7.7. This may be due to external noise, since we operate in an unshielded environment, or to drift or excess low-frequency noise. However, none of these noise sources would be expected to vary with the source frequency. Thus it appears that the extra noise is due to the application of the relatively high frequency test signal to the SQUID.

7.5 Noise

Figure 7.9 shows a line cut through the intensity plot of Fig. 7.6 at a 50 ns delay time when the test signal is near the middle of its range. We can estimate the magnetic

flux noise from the spread of this switching histogram. For a normal distribution we would expect the single-shot uncertainty σ_Φ in the flux to be half of the range between the 16% and 84% marks (i.e. $\pm 2\sigma$ will encompass 2/3 of the data points, as indicated by solid lines in Fig. 7.9). Averaging over all possible delay times, we obtain an uncertainty in the flux of $\sigma_\Phi = 7.6\ m\Phi_0$. A pulse width of 10 ns corresponds to a bandwidth of 100 MHz, which indicates an equivalent rms white flux noise level of $S_\Phi^{1/2} \cong 7.6\times10^{-7}\ \Phi_0 / \sqrt{Hz}$, where S_Φ is the power spectral density of the flux noise.

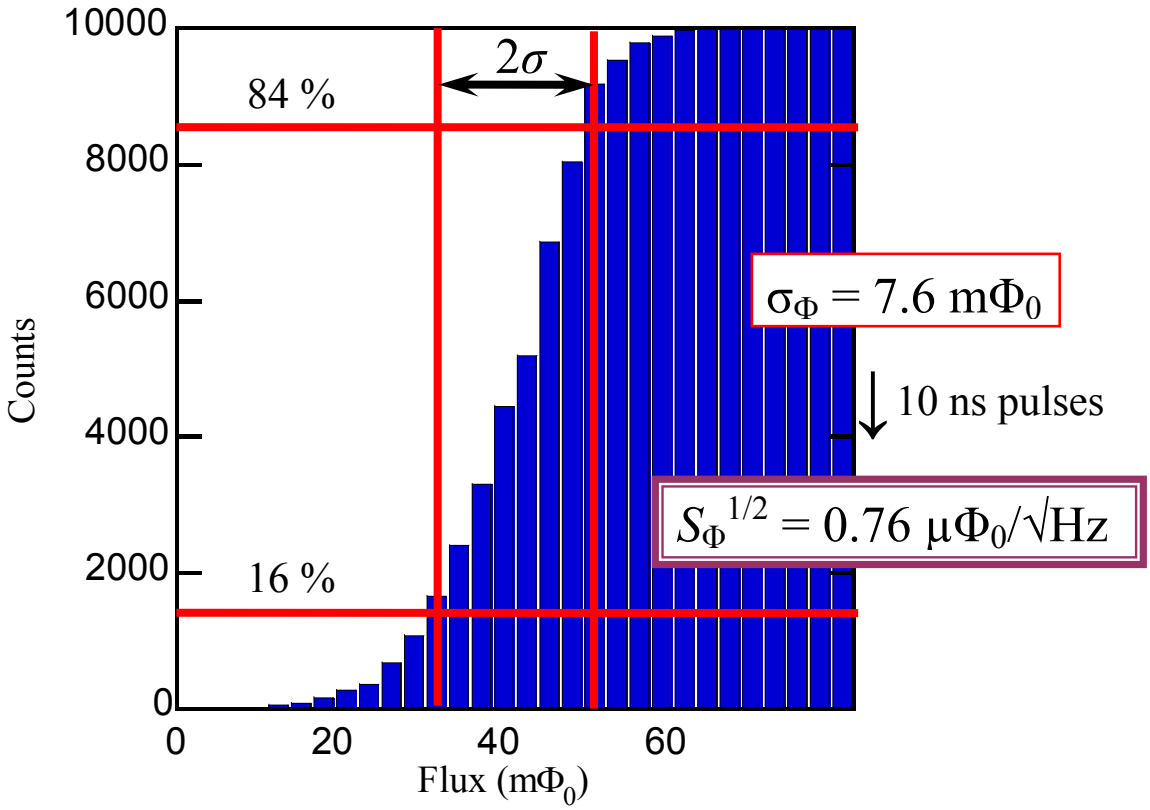

Fig. 7.9. Histogram showing a line cut through the intensity plot of Fig. 7.6 at 50 ns delay time. We can estimate the magnetic flux noise from the spread of the histogram. For a normal distribution we would expect the single-shot uncertainty in the flux to be half of the range between the 16% and 84% marks, indicated by solid lines.

We can calculate an expected S_Φ for comparison. For a loop with inductance L at temperature T, the rms Johnson current noise σ_I obeys:

$$\frac{k_B T}{2} \approx \frac{1}{2} L \sigma_I^2 \tag{7.1}$$

Thus

$$\sigma_\Phi \approx \sqrt{k_B T L}. \tag{7.2}$$

With L = 25 pH and T = 4.2 K, we obtain $\sigma_\Phi = 20 m\Phi_0$. To find the spectral density of the noise, we define the cut-off frequency to be the junction plasma frequency, f_p, given by

$$f_p = \sqrt{\frac{I_0}{2\pi \Phi_0 C}}. \tag{7.3}$$

For the SQUID (HSQ_2) we used, I_0 = 45 μA is the average junction critical current, and the average junction capacitance C = 0.3 pF. From Eq. (7.3) we find f_p = 100 GHz, and $S_\Phi^{1/2} = 6 \times 10^{-8}\, \Phi_0 / \sqrt{Hz}$, about an order of magnitude smaller than our measurement. Of course the SQUID is not just an inductor, but has non-linear elements (the junctions) and this would be expected to modify this estimate.

Another possible explanation for this discrepancy is that although the current pulses are nominally 10 ns long, the effective pulse may be shorter when it reaches the SQUID. In particular, the switching could be taking place very soon after the current pulse is applied due to ringing at the leading edge of the pulse. This would also explain how we could observe a 1 GHz wave with a 10 ns pulse! From the measured flux noise, $\sigma_\Phi = 7.6 m\Phi_0$, and the estimated spectral noise flux density,

$S_\Phi^{1/2} = 6\times10^{-8}\,\Phi_0/\sqrt{Hz}$, we can estimate an effective pulse width of 65 ps or a limiting bandwidth of 15.3 GHz.

To examine the noise at low frequencies, I repeated the experiment with the test signal turned off. As expected, we just see noise (see Fig. 7.10). The level of the noise is about $10 = m\,\Phi_0/\sqrt{Hz}$ when the measurement is made this way. This is much higher than the limiting flux noise present in the SQUID (of order $1\,\mu\Phi_0/\sqrt{Hz}$ or less) because we are sampling very slowly compared to the bandwidth of the SQUID. Additionally, 1/*f*-noise or drift is also evident below 0.1 Hz.

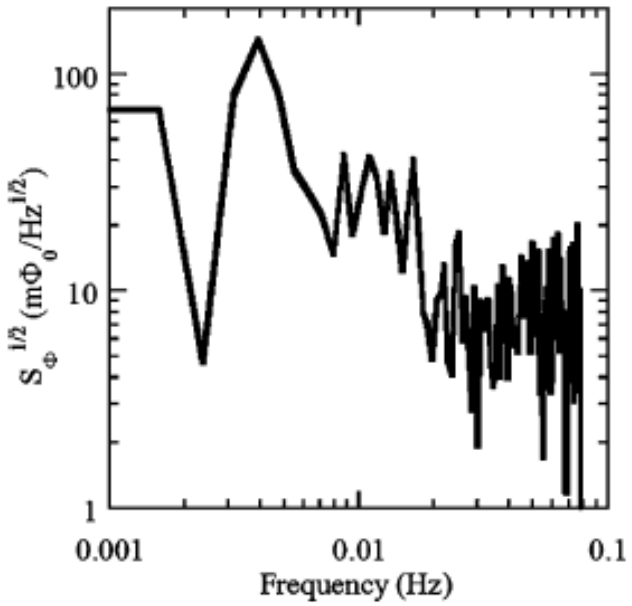

Fig. 7.10. Flux noise power density for a scan with no test signal. The total scan time is several minutes and the noise spectrum is dominated by low frequency 1/*f*-type noise.

7.6 Summary

In this chapter I described how I used a hysteretic dc SQUID-based technique for sampling small high-frequency periodic magnetic fields up to about 1 GHz. Although I was able to observe 1 GHz signals with 10 ns long pulses, in order to reliably extend the

technique to 1 GHz or higher, reliable generation of shorter pulses would probably lead to improvement in the high-frequency performance. In Chapter 9, I describe SQUID imaging experiments where I used a faster pulse generator for imaging magnetic fields with frequencies exceeding 2 GHz.

Chapter 8: Electromagnetic Wave Propagation along Transmission Lines

In this thesis I use a microstrip line as a test platform for carrying microwaves that I then image with the microscope. Transmission lines are structures designed to guide or direct the transmission of electromagnetic waves or electrical power from one place to another. I use them for imaging because they produce calculable and non-trivial field patterns at high frequencies.

Transmission line theory bridges the gap between basic circuit theory and field analysis. The key difference between the basic circuit theory and field analysis is the size of the system compared to the wavelength. Circuit theory generally assumes that the physical dimensions of a network are smaller than the electrical wavelength. In contrast, transmission lines are typically a considerable fraction of a wavelength to many wavelengths in size. Thus, transmission lines can be treated as distributed networks, where the voltages and currents can vary both in magnitude and phase along the length of the transmission line. Transmission line theory can also be used to understand wave properties such as reflections at discontinuities, standing versus travelling waves, phase and group velocity as well as the characteristics of various guiding structures.

Early microwave systems used waveguides and coaxial transmission lines to guide waves. Waveguides in use today are capable of handling high power and are low-loss, but they are bulky and expensive. Coaxial transmission lines have a very high-bandwidth and are convenient for connecting electronic and microwave equipment, but are difficult to fabricate into compact microwave structures. Planar transmission lines,

such as a microstrip line, are compact, and can be easily integrated with other electronics devices, such as diodes and transistors, to form a microwave integrated circuit.

In the next three sections I examine wave propagation on transmission lines. I then discuss the B-fields that would be produced above a planar transmission line. It is these B-fields which my system will be able to image.

8.1 Waves on Transmission Lines

To understand the propagation of waves on a transmission line I analyze the system as a distributed circuit. For simplicity I will ignore any losses along the line. In this section, I derive the transmission line equations and examine the current and voltage variations along its length.

Figure 8.1 shows a circuit model for a small length in a uniform two-conductor transmission line [1]. For the differential line length *dz*, I define the distributed inductance $\mathscr{L}$ per unit length, and the distributed capacitance $\mathscr{C}$ per unit length, *i.e.* length *dz* has inductance $L\,dz$ and capacitance $C dz$. The voltage change across the length *dz* is given by

$$\Delta V = V(z+\Delta z) - V(z) = \frac{\partial V}{\partial z} dz = -\left(L\, dz\right)\frac{\partial I}{\partial t}. \tag{8.1}$$

A similar argument can be made for the change in current along the differential length of line *dz*. The current changes because some current is shunted across the distributed capacitance (see Fig. 8.1). The current change along this length is given by:

$$\Delta I = I(z+\Delta z) - I(z) = \frac{\partial I}{\partial z} dz = -\left(C dz\right)\frac{\partial V}{\partial t} \tag{8.2}$$

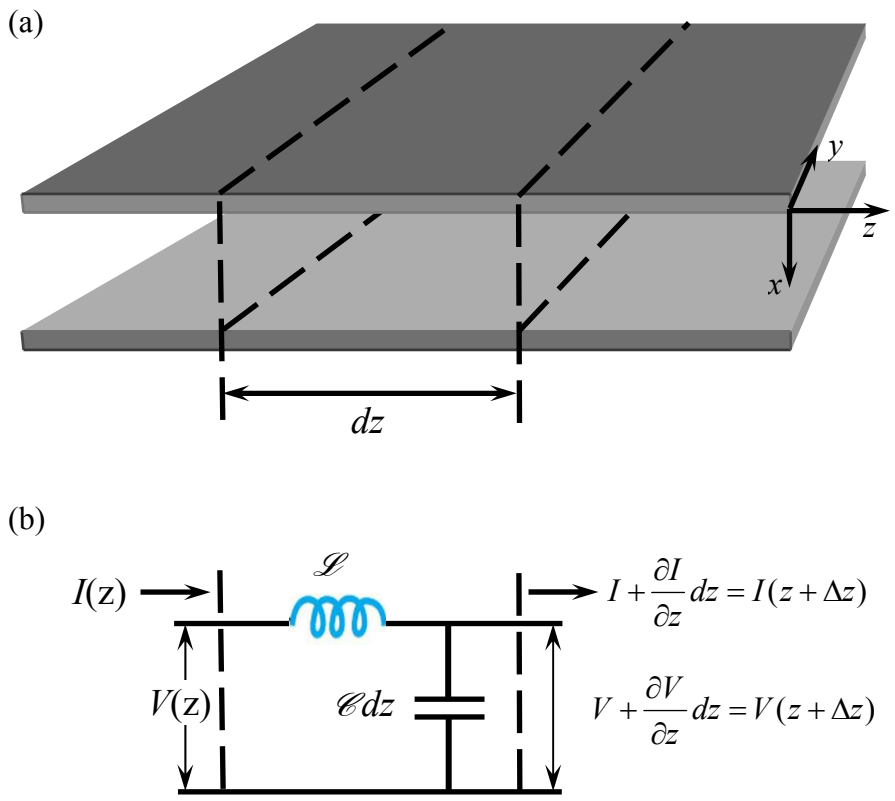

Fig. 8.1. (a) Physical model section of a two-conductor transmission line and (b) the equivalent circuit for a differential length.

From Eq. (8.1) and Eq. (8.2) we obtain:

$$\frac{\partial V}{\partial z} = -\mathsf{L}\frac{\partial I}{\partial t} \tag{8.3}$$

and

$$\frac{\partial I}{\partial z} = -\mathsf{C}\frac{\partial V}{\partial t}. \tag{8.4}$$

The above two equations are known as the Telegrapher's equations [1] and are the fundamental differential equations for the analysis of a uniform lossless transmission line. Equations (8.3) and (8.4) can be combined to form a wave equation for either the current or voltage. Taking the partial derivative of Eq. (8.3) with respect to distance and the partial derivative of Eq. (8.4) with respect to time one finds

$$\frac{\partial^2 V}{\partial z^2} = -L\,\frac{\partial^2 I}{\partial z \partial t} \tag{8.5}$$

$$\frac{\partial^2 I}{\partial t \partial z} = -C\frac{\partial^2 V}{\partial t^2}. \tag{8.6}$$

The mixed partial derivatives are the same regardless of the order they are taken. Equation 8.6 can then be substituted into Eq. (8.5) and one finds:

$$\frac{\partial^2 V}{\partial z^2} = LC\frac{\partial^2 V}{\partial t^2} = \frac{1}{v^2}\frac{\partial^2 V}{\partial t^2} \tag{8.7}$$

where

$$v = \frac{1}{\sqrt{LC}}. \tag{8.8}$$

Equation 8.7 is just the 1-*D* wave equation for a wave with propagation speed *v*. A similar wave equation can be obtained for the current:

$$\frac{\partial^2 I}{\partial z^2} = LC\frac{\partial^2 I}{\partial t^2} = \frac{1}{v^2}\frac{\partial^2 I}{\partial t^2}. \tag{8.9}$$

The voltage wave equation 8.7 has the general solution:

$$V(z,t) = V_1\left(t - \frac{z}{v}\right) + V_2\left(t + \frac{z}{v}\right) \tag{8.10}$$

where V_1 and V_2 are arbitrary functions. The function $V_1(t - z/v)$ represents a wave travelling in the $+z$ direction with velocity *v*. Similarly, $V_2(t + z/v)$ represents a wave moving in the $-z$ direction with velocity *v*.

Substituting Eq. (8.10) into the first of the telegrapher's equations Eq. (8.3), we obtain the current on the line in terms of the functions V_1 and V_2:

$$-L\,\frac{\partial I}{\partial t} = -\frac{1}{v}V_1'\left(t - \frac{z}{v}\right) + \frac{1}{v}V_2'\left(t + \frac{z}{v}\right). \tag{8.11}$$

If this expression is integrated with respect to t, then the current is found to obey

$$I(z) = \frac{1}{L\,v}\left[V_1\left(t - \frac{z}{v}\right) - \frac{1}{v}V_2\left(t + \frac{z}{v}\right)\right] + f(z) \tag{8.12}$$

where *f*(z) is a constant of integration that is not important for the solution and can be dropped. Equation (8.12) can then be written as:

$$I(z) = \frac{1}{Z_0}\left[V_1\left(t - \frac{z}{v}\right) - \frac{1}{v}V_2\left(t + \frac{z}{v}\right)\right] \tag{8.13}$$

where

$$Z_0 = Lv = \sqrt{\frac{L}{C}}\ . \tag{8.14}$$

The constant Z_0 is called the "characteristic impedance" of the line, and is the ratio of the voltage to current for a single travelling wave at any given point and instant.

An alternative approach to solving the equations is to assume a wave of frequency ω; Eqs. (8.3) and (8.4) then simplify to

$$\frac{\partial V}{\partial z} = -j\omega L\, I(z) \tag{8.15}$$

and

$$\frac{\partial I}{\partial z} = -j\omega C V(z). \tag{8.16}$$

The above two equations can be combined to give a one-dimensional wave equation for $V(z)$ or $I(z)$:

$$\frac{\partial^2 V}{\partial z^2} - \gamma^2 V(z) = 0 \tag{8.17}$$

and

$$\frac{\partial^2 I}{\partial z^2} - \gamma^2 I(z) = 0 \tag{8.18}$$

where

$$\gamma = \alpha + j\beta = j\omega\sqrt{L\,C} \tag{8.19}$$

is a complex propagation constant. The propagation constant is frequency dependent and since we have here assumed a lossless line $\alpha = 0$ and $\beta = \omega\sqrt{L\,C}$.

Travelling wave solutions to Eqs. (8.17) and (8.18) can be expressed as

$$V(z) = V_0^+ e^{-\gamma z} + V_0^- e^{+\gamma z} \tag{8.20}$$

and

$$I(z) = I_0^+ e^{-\gamma z} + I_0^- e^{+\gamma z}. \tag{8.21}$$

The $e^{-\gamma z}$ term represents a wave propagating in the $+z$ direction, and the $e^{\gamma z}$ term represents a wave propagating in the $-z$ direction. Applying Eq. (815) to Eq. (8.20) gives the current in terms of the voltage on the line,

$$I(z) = \frac{\gamma}{j\omega L}\left[V_0^+ e^{-\gamma z} - V_0^- e^{+\gamma z}\right]. \tag{8.22}$$

The characteristic impedance Z_0 of the line can be found from Eqs. (8.21) and (8.22), and one finds:

$$Z_0 = \frac{j\omega L}{\gamma} = \sqrt{\frac{L}{C}} \tag{8.23}$$

In this way the current and voltage on the line are related as

$$\frac{V_0^+}{I_0^+} = Z_0 = \frac{-V_0^-}{I_0^-}. \tag{8.24}$$

I note that the characteristic impedance of a transmission line depends on $\mathscr{L}$ and $\mathscr{C}$, which in turn are geometry dependent. Thus for different transmission line configurations the characteristic impedance will be different.

The general solutions for the voltage and current at frequency ω on a lossless transmission line can be summarized as follows:

$$V(z) = V_0^+ e^{-j\beta z} + V_0^- e^{+j\beta z}, \tag{8.25}$$

$$I(z) = \frac{V_0^+}{Z_0} e^{-j\beta z} - \frac{V_0^-}{Z_0} e^{+j\beta z}. \tag{8.26}$$

The characteristic impedance, wavelength and phase velocity for the transmission line are

$$Z_0 = \sqrt{\frac{L}{C}}, \tag{8.27}$$

$$\lambda = \frac{2\pi}{\beta} = \frac{2\pi}{\omega\sqrt{LC}}, \tag{8.28}$$

and

$$v_p = \frac{\omega}{\beta} = \frac{1}{\sqrt{LC}}, \tag{8.29}$$

respectively.

8.1.1 The Terminated Lossless Transmission Line

Transmission lines are used to connect various electrical components together. If the impedance of the components is not the same as the characteristic impedance Z_0 of the line, then reflections will be produced. Figure 8.2 shows the simplest case, a transmission line terminated by an arbitrary load impedance Z_L.

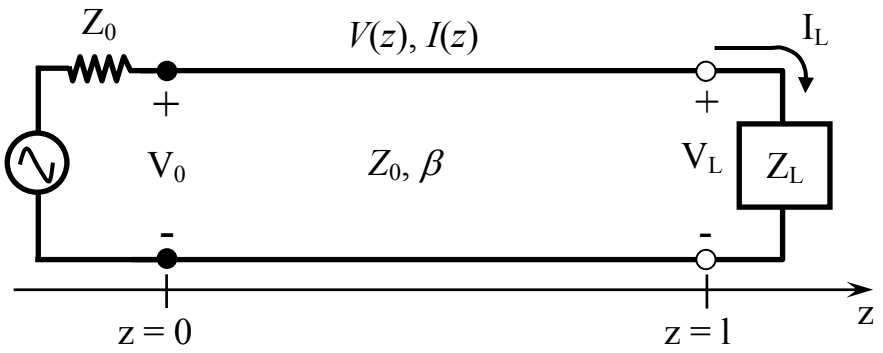

Fig. 8.2. Transmission line terminated with an arbitrary load impedance Z_L.

If an incident wave is generated from a source at $z = 0$ that is matched to the line (it has source impedance Z_0), and the line is terminated by an arbitrary load Z_L where $Z_L \neq Z_0$, then [2]

$$Z_L = \frac{V(l)}{I(l)} = \left(\frac{V_0^+ + V_0^-}{V_0^+ - V_0^-} \right) Z_0 \tag{8.30}$$

where V_0^+ is the voltage amplitude of the incident wave, and V_0^- is the amplitude of the reflected wave. We can define the voltage reflection coefficient, Γ [2] as:

$$\Gamma = \frac{V_0^-}{V_0^+}. \tag{8.31a}$$

and using Eq. 8.30, we find:

$$\Gamma = \frac{Z_L - Z_0}{Z_L + Z_0}. \tag{8.31b}$$

Notice that $\Gamma = 0$ when $Z_L = Z_0$ (matched line), as expected.

The voltage and current on the transmission line can now be written in terms of the reflection coefficient as

$$V(z) = V_0^+ \left[e^{-j\beta z} + \Gamma e^{+j\beta z} \right], \tag{8.32}$$

$$I(z) = \frac{V_0^+}{Z_0}\left[e^{-j\beta z} - \Gamma e^{+j\beta z}\right]. \tag{8.33}$$

The time-averaged power flow along the transmission line is given by [2]

$$P_{avg} = \frac{1}{2}\frac{\left|V_0^+\right|^2}{Z_0}\left(1 - \left|\Gamma^2\right|\right), \tag{8.34}$$

This last result shows that the time averaged power flow at point along the transmission line is constant. Also notice that if $|\Gamma| = 0$, *i.e.* no reflection, and then the power flow down the line is a maximum, while if $|\Gamma| = 1$ then all the power is reflected and there is no net power flow.

Equations 8.32 and 8.33 show that the voltage and current vary with position along the transmission line, and thus the impedance looking down the transmission line varies with position. Indeed, the input impedance at a distance $z = l$ from the load (i.e. at $z = 0$) is

$$Z_{in} = \frac{V(0)}{I(0)} = \frac{1+\Gamma e^{-2j\beta l}}{1-\Gamma e^{-2j\beta l}} Z_0. \tag{8.35}$$

This expression can also be calculated for arbitrary load impedance Z_L at l; one finds,

$$Z_{in} = Z_0\left(\frac{Z_L + jZ_0 \tan\beta l}{Z_0 + jZ_L \tan\beta l}\right). \tag{8.36}$$

This result gives the input impedance of a length of a length l transmission line that is terminated on the other end with load impedance Z_L.

I note three special cases for terminated transmission lines which frequently appear. If $Z_L = Z_0$, then $Z_{in} = Z_0$. If instead the line is terminated by a short circuit, $Z_L = 0$, then the input impedance is

$$Z_{in} = jZ_0 \tan \beta l. \tag{8.37}$$

Finally a transmission line terminated by an open circuit, $Z_L = \infty$, will have an input impedance

$$Z_{in} = -jZ_0 \cot \beta l. \tag{8.38}$$

In both cases the input impedance is purely imaginary for any length *l*. Of course this analysis neglects loss in the transmission line, which would introduce a real part.

8.2 Field Analysis of Transmission Lines

A version of the Telegrapher equations in terms of the electric field $\vec{\mathbf{E}}$ and magnetic field $\vec{\mathbf{B}}$ can also be derived directly from Maxwell's equations. This is a useful approach for my thesis work because the SQUID measures the B-field rather than *I* or *V*.

For simplicity, I consider a coaxial transmission line that extends along the *z*-axis. The inner conductor has radius $\rho = a$ and the inner wall of the outer conductor has radius $\rho = b$ (see Fig. 8.3). A transverse electromagnetic wave along a perfectly conducting coaxial line is characterized by $E_z = H_z = 0$, where E_z and H_z are the electric and magnetic field components in the z-direction, respectively. For a wave of frequency ω Maxwell's equations inside the coaxial line can be written

$$\nabla \times \vec{E} = -j\omega\mu\vec{H}, \tag{8.39}$$

and

$$\nabla \times \vec{H} = j\omega\varepsilon\vec{E}, \tag{8.40}$$

where ε is the dielectric constant and μ is the permeability of the material in the space between the inner and outer conductor. Expanding Maxwell's equations using the above

conditions gives the following equations for the electric and magnetic fields inside a coaxial line [2]:

$$-\hat{\rho}\frac{\partial E_\phi}{\partial z}+\hat{\phi}\frac{\partial E_\rho}{\partial z}+\hat{z}\frac{\partial}{\partial \rho}\left(\rho E_\phi\right)=-j\omega\mu\left(\hat{\rho}H_\rho+\hat{\phi}H_\phi\right), \tag{8.41}$$

and

$$-\hat{\rho}\frac{\partial H_\phi}{\partial z}+\hat{\phi}\frac{\partial H_\rho}{\partial z}+\hat{z}\frac{\partial}{\partial \rho}\left(\rho H_\phi\right)=j\omega\varepsilon\left(\hat{\rho}E_\rho+\hat{\phi}E_\phi\right). \tag{8.42}$$

Further consideration of equations 8.41 and 8.42 reveals I have assumed azimuthal symmetry and dropped terms containing $\partial/\partial\phi$. The azimuthal components of the electric and magnetic fields have the following forms [2]:

$$E_\phi=\frac{f(z)}{\rho}\text{ and }H_\phi=\frac{g(z)}{\rho}, \tag{8.43}$$

because E_z and H_z must vanish.

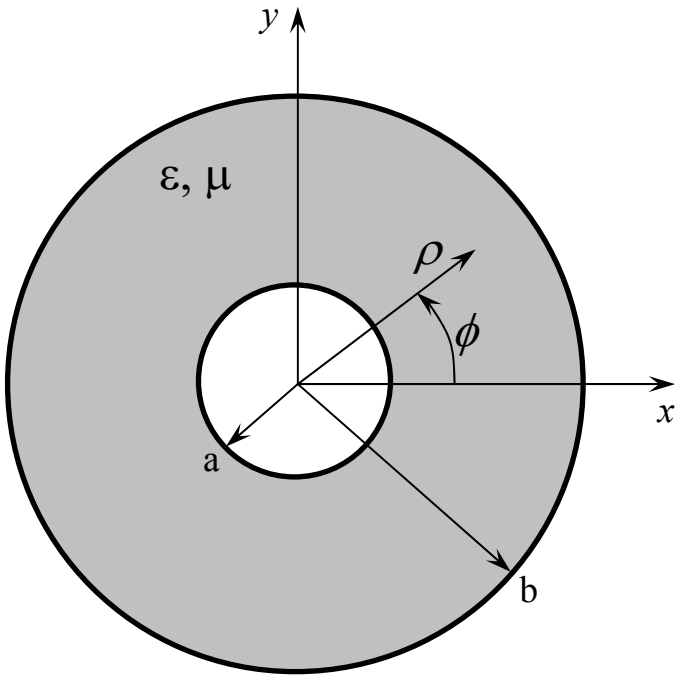

Fig. 8.3. Cross-sectional geometry of a coaxial line.

Applying the boundary conditions, $E_\phi = 0$ and $H_\rho = 0$ at $\rho = a$ and $\rho = b$ to Eqs. 8.43, we find $E_\varphi(z) = 0$ and $H_\rho(z) = 0$, and the two Maxwell equations reduce to

$$\frac{\partial E_\rho}{\partial z} = -j\omega\mu H_\phi, \tag{8.44}$$

$$\frac{\partial H_\phi}{\partial z} = -j\omega\varepsilon E_\rho. \tag{8.45}$$

Taking the derivative of the second equation with respect to z and substituting into the first yields a wave equation for E_ρ:

$$\frac{\partial^2 E_\rho}{\partial z^2} + \omega^2\mu\varepsilon E_\rho = 0, \tag{8.46}$$

From this, we find the propagation constant $\gamma = \sqrt{-\omega^2\mu\varepsilon} = \alpha + j\beta$. If we assume a lossless medium, this reduces to $\alpha = 0$ and $\beta = \omega\sqrt{\mu\varepsilon} = \omega\sqrt{LC}$. The characteristic impedance for the coaxial transmission line is then found to be:

$$Z_0 = \frac{E_\rho \ln(b/a)}{2\pi H_\phi} = \sqrt{\frac{\mu}{\varepsilon}}\frac{\ln(b/a)}{2\pi}. \tag{8.47}$$

8.3 Microstrip Transmission Lines

In the previous example, $\vec{\mathbf{E}}$ and $\vec{\mathbf{H}}$ fields are contained within the coaxial transmission line and would not be measureable with a SQUID microscope located outside the outer conductor of the coaxial line. Whereas, a microstrip line is a type of planar transmission line that is widely used in integrated circuits. The geometry of a microstrip line is shown in Fig. 8.4(a). The top conductor of width w is on top of a dielectric of thickness d that has relative dielectric constant ε_r. The bottom of the microstrip line, beneath the dielectric, is a ground plane. Figure 8.4 shows a qualitative

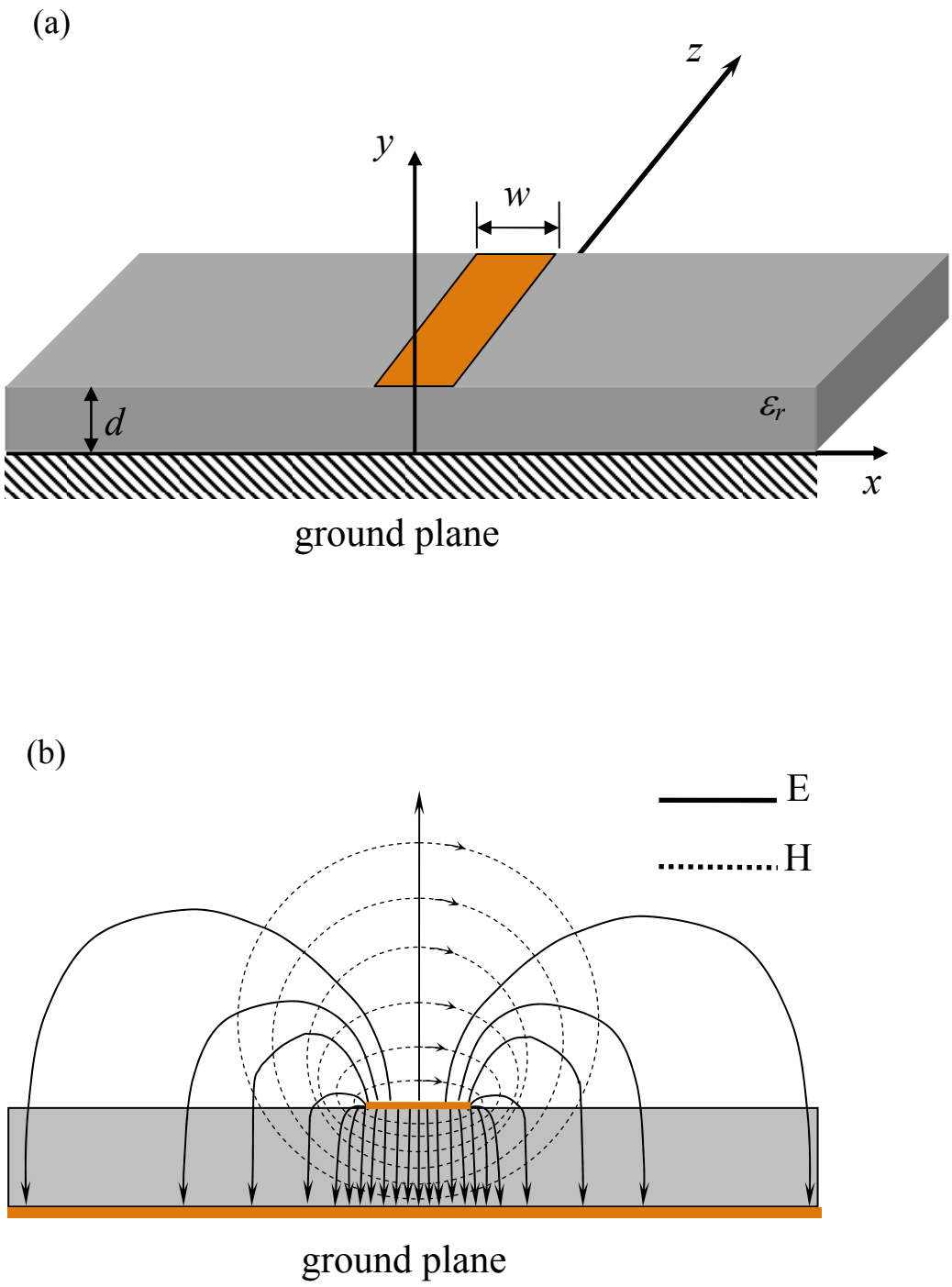

Fig. 8.4. (a) Geometry of microstrip transmission line. (b) Schematic cross-sectional view of electric and magnetic field lines near a microstrip line [2].

sketch of the electric and magnetic field lines produced when an electromagnetic wave is propagating down this line.

If the dielectric were not present, the microstrip line could be modelled as a two-wire line consisting of two conductors of width w with the top wire separated by $2d$ from its image in the ground plane. In this case, we would have a TEM transmission line, with $v_p = c$ and $\beta = k_0$. However in a typical microstrip the dielectric does not fill the region above the top conductor. This seriously complicates the analysis of the microstrip. Unlike the coaxial line, where all the field lines are enclosed within a homogeneous dielectric region, the microstrip has some of its field lines in vacuum and some in the dielectric region, concentrated between the top and bottom conductors.

At low frequencies, typically below a few GHz for practical microstrip lines, the dielectric substrate is electrically thin ($d << \lambda$), and the line can support a quasi-TEM mode of propagation. Analytical techniques can be used to determine the fields of a microstrip line [3] and one finds that the exact fields of a microstrip line are a hybrid TE-TM wave [3]. Nevertheless, good approximations for the phase velocity, propagation constant and characteristic impedance have been obtained from static and quasi-static calculations [4,5]. In these approximations one finds the phase velocity is:

$$v_p = \frac{c}{\sqrt{\varepsilon_e}}, \tag{8.48}$$

$$\beta = k_0\sqrt{\varepsilon_e}, \tag{8.49}$$

where ε_e is the effective dielectric constant of the microstrip line and satisfies the relation $1 < \varepsilon_e < \varepsilon_r$.

A useful approximation for the effective dielectric constant of a microstrip line is given by [4,5]:

$$\varepsilon_e = \frac{\varepsilon_r + 1}{2} + \frac{\varepsilon_r - 1}{2}\left(\frac{1}{\sqrt{1+\frac{12d}{w}}}\right). \tag{8.50}$$

Bahl and Gupta found the following design formula for the line impedance by curve fitting to rigorous quasi-static numerical calculations [4,5],

$$Z_0 = \begin{cases} \dfrac{60}{\sqrt{\varepsilon_e}} \ln\left(\dfrac{8d}{w} + \dfrac{w}{4d}\right) & for\ w/d \le 1 \\ \dfrac{120\pi}{\sqrt{\varepsilon_e}\left[\dfrac{w}{d} + 1.393 + 0.667\ln\left(\dfrac{w}{d} + 1.444\right)\right]} & for\ w/d \ge 1. \end{cases} \tag{8.51}$$

Thus, given the dimensions of the microstrip line, from the above formula the characteristic impedance can be calculated. With the impedance known, one can then use the usual transmission line equations to find the current and voltage along the line.

8.4 Calculating Magnetic Field from Current Density

I use my scanning SQUID microscope mainly to image magnetic fields from microwave signals flowing along planar electronic structures. Given a time-dependent current density $\vec{\mathbf{J}}(\vec{\mathbf{r}}', t')$, the magnetic field $\vec{\mathbf{B}}(\vec{\mathbf{r}}, t)$ at point $\vec{\mathbf{r}}$ and time t can be found from the generalized Biot-Savart law [6]:

$$\vec{\mathbf{B}}(\vec{\mathbf{r}}, t) = \frac{\mu_0}{4\pi}\int d^3\vec{r}' \left\{\left[\vec{\mathbf{J}}(\vec{\mathbf{r}}', t_r)\right]_{ret} \times \frac{\hat{\mathbf{R}}}{R^2} + \left[\frac{\partial \vec{\mathbf{J}}(\vec{\mathbf{r}}', t_r)}{\partial t_{tr}}\right]_{ret} \times \frac{\hat{\mathbf{R}}}{cR}\right\}, \tag{8.52}$$

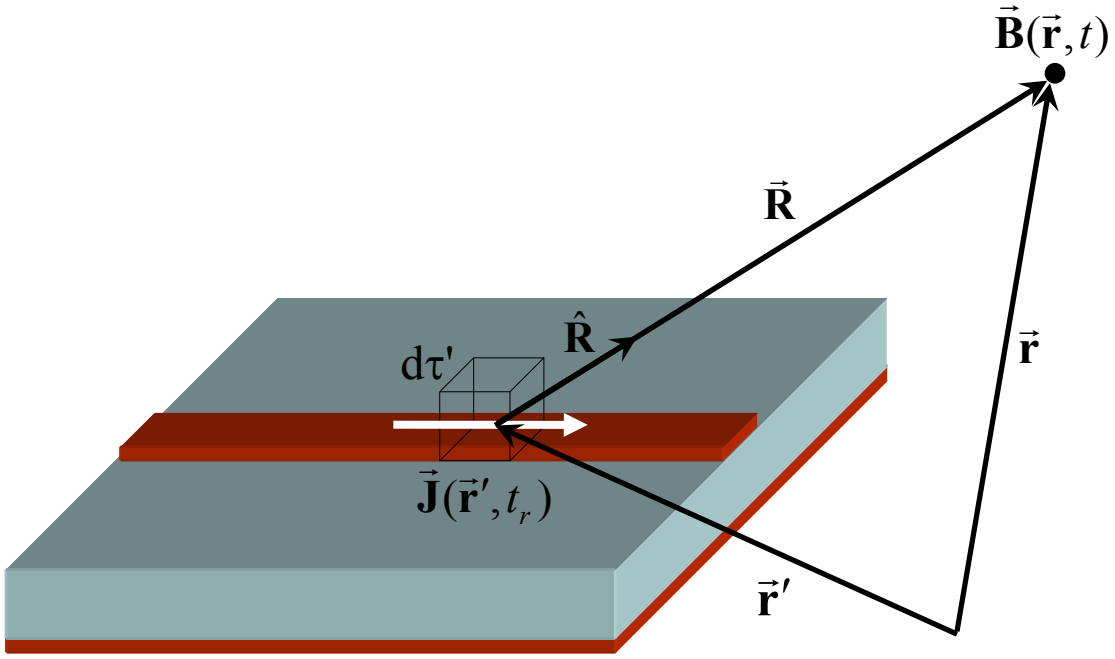

Fig. 8.5. Sketch of current density $\vec{\mathbf{J}}(\vec{\mathbf{r}}',t_r)$ in two-dimensional geometry showing volume element dτ, where $\vec{\mathbf{R}}$ is the distance from the source point $\vec{\mathbf{r}}'$ to the field point $\vec{\mathbf{r}}$.

where, $R=\left|\vec{\mathbf{r}}-\vec{\mathbf{r}}'\right|$, $\vec{\mathbf{R}}=\vec{\mathbf{r}}-\vec{\mathbf{r}}'$, $\hat{\mathbf{R}}=\vec{\mathbf{R}}/R$, and $\mu_0 = 4\pi\times10^{-7}$ T·μ/A is the permeability of free space (see Fig. 8.5). The pair of brackets, $\left[\ \right]_{ret}$, in Eq. (8.52) implies the quantity within is to be evaluated at the retarded time, $t_r = t - R/c$ with c being the speed of light. If the current density is time independent, the expression reduces to the familiar static result, *i.e.* the Biot-Savart Law. The magnetic field from a planar structure, such as a microstrip line, is generated by a two-dimensional current density $\vec{\mathbf{J}}(x',y',t')$ confined to a very thin non-magnetic conducting sheet of thickness d, and $z \gg d$, where z is the distance (along the z-axis) between the current path and the sensor (see Fig. 8.5).

From Eq. (8.52), the components of the magnetic field for a planar structure can then be written as

$$\vec{B}_x(x,y,z,t) \approx zd\,\frac{\mu_0}{4\pi}\iint\left\{\frac{J_y(x',y',0,t_{tr})}{\left((x-x')^2+(y-y')^2+z^2\right)^{3/2}}+\right.$$
$$\left.\frac{1}{c\sqrt{(x-x')^2+(y-y')^2+z^2}}\frac{\partial J_y(x',y',0,t_{tr})}{\partial t}\right\}dx'dy', \tag{8.53}$$

$$\vec{B}_y(x,y,z,t) \approx -zd\,\frac{\mu_0}{4\pi}\iint\left\{\frac{J_x(x',y',0,t_{tr})}{\left((x-x')^2+(y-y')^2+z^2\right)^{3/2}}+\right.$$
$$\left.\frac{1}{c\sqrt{(x-x')^2+(y-y')^2+z^2}}\frac{\partial J_x(x',y',0,t_{tr})}{\partial t}\right\}dx'dy', \tag{8.54}$$

and:

$$\vec{B}_z(x,y,z,t) \approx d\,\frac{\mu_0}{4\pi}\iint\left\{\frac{J_x(x',y',0,t_{tr})\cdot(y-y')-J_y(x',y',0,t_{tr})\cdot(x-x')}{\left((x-x')^2+(y-y')^2+z^2\right)^{3/2}}+\right.$$
$$\left.\frac{1}{c\sqrt{(x-x')^2+(y-y')^2+z^2}}\frac{\partial\left(J_x(x',y',0,t_{tr})\cdot(y-y')-J_y(x',y',0,t_{tr})\cdot(x-x')\right)}{\partial t}\right\} \tag{8.54}$$

where $J_x(x',y',0,t_r)$ and $J_y(x',y',0,t_r)$ are the x and y components of the current density, respectively. I note the approximation arises because I have assumed the current is confined to a thin non-magnetic conducting sheet of thickness $d \ll z$.

If we expand the retarded current density:

$$\left[\mathbf{J}\right] = \mathbf{J}\left(\mathbf{r}, t-\frac{R}{c}\right) = \mathbf{J}(\mathbf{r},t) - \frac{R}{c}\dot{\mathbf{J}}(\mathbf{r},t) + \frac{1}{2}\left(\frac{R}{c}\right)^2\ddot{\mathbf{J}}(\mathbf{r},t) + \cdots, \tag{8.55}$$

and substitute this into Eq. (8.52) we obtain a correction to the Biot-Savart law and can write:

$$\mathbf{B} = \frac{\mu_0}{4\pi}\int\left(\mathbf{J}(\mathbf{r},t) - \frac{1}{2}\left(\frac{R}{c}\right)^2\ddot{\mathbf{J}}(\mathbf{r},t) + \cdots\right)\times\frac{\hat{\mathbf{R}}}{R^2}\,d^3\vec{r}'. \tag{8.56}$$

If we express the characteristic time T for changes in J, such that $\ddot{\mathbf{J}} \sim J/T^2$, then the dominant correction to the Biot-Savart law is of the order $\left(R/cT\right)^2$. So long as the current changes by a small amount in the time it takes light to travel from the source to the field point (sensor) this correction is very small. Take, for example, a signal at frequency 1 GHz and the distance above the current density is 200 μm the 2nd-order correction $\left|\ddot{\mathbf{J}}\right|/\left|\vec{\mathbf{J}}\right| \approx 4\times10^{-7}$ Thus up to second order in the small parameter $\left(R/cT\right)^2$ the Biot-Savart law gives a very good approximation in the near-field quasi-static regime where my microscope operates..

In particular, my SQUID microscope measures the *z*-component of the magnetic field, i.e., the field in the direction normal to the *xy*-plane. Thus, in order to simulate the measured magnetic field, I could use Eq. (8.54) to calculate the magnetic field assuming 2-dimensional current density in the *xy* scanning plane. In practice, instead of calculating the current density in a planar electronic structure in order to use Eq. (8.54), I used CAD electromagnetic software (see Chapter 9) to simulate the magnetic fields generated by microwave signals flowing in microstrip lines.

8.5 Summary

In this chapter, I discussed the basic phenomenon of wave propagation along a transmission line using circuit theory and Maxwell's equations. A transmission line can be thought of as a distributed network where the voltage and current can vary in magnitude and phase along the length of the line. The Telegrapher's equations were derived and the general solutions for voltage and current on a lossless transmission line were presented. I also used field analysis of a coaxial line to find the Telegrapher's

equations as well as the characteristic impedance of a coaxial line. Next, I discussed the microstrip line and how the surrounding B-fields it produces can be approximately calculated.

Chapter 9: Magnetic Field Image of Test Circuits

9.1 Instrumentation and Experimental Arrangement

Figure 9.1 shows a schematic diagram of my experimental set-up for obtaining images of rapidly varying magnetic fields. An Agilent E4426B microwave signal generator sends a repetitive test signal to the sample and the reference signal from this generator acts as the master clock. The signal generator also generates a delay trigger to an Avtech AVPP-1-B pulse generator. Each time a trigger signal is detected, the pulse generator sends a rectangular current pulse with 400 ps duration to the SQUID. The experiment also has a function generator that sends a dc current to the one-turn coil that couples a static flux offset to the SQUID. The voltage response from the SQUID is amplified, sent to an Agilent 53132A counter, and the counts (voltage above threshold) are recorded by a computer. The computer also drives the *xy*-scanning table, which moves the sample in a raster pattern under the SQUID, and controls the flux offset, amplitude of the current pulse, and signal generator.

In traditional flux-locked loop SQUID electronics [1], the bias current for the SQUID is set at a fixed value. In my experiment, fixed amplitude 400 ps current pulses are sent to the SQUID. The bias current pulse amplitude and the dc flux are set such that, in the absence of any signal flux, the SQUID produces a voltage pulse for 50% of the current pulses. This corresponds to the current pulse amplitude being set equal to the SQUID's critical current at the given dc flux offset. If the bias current pulse amplitude is set too low or too high, the SQUID will either never show a voltage pulse, or always

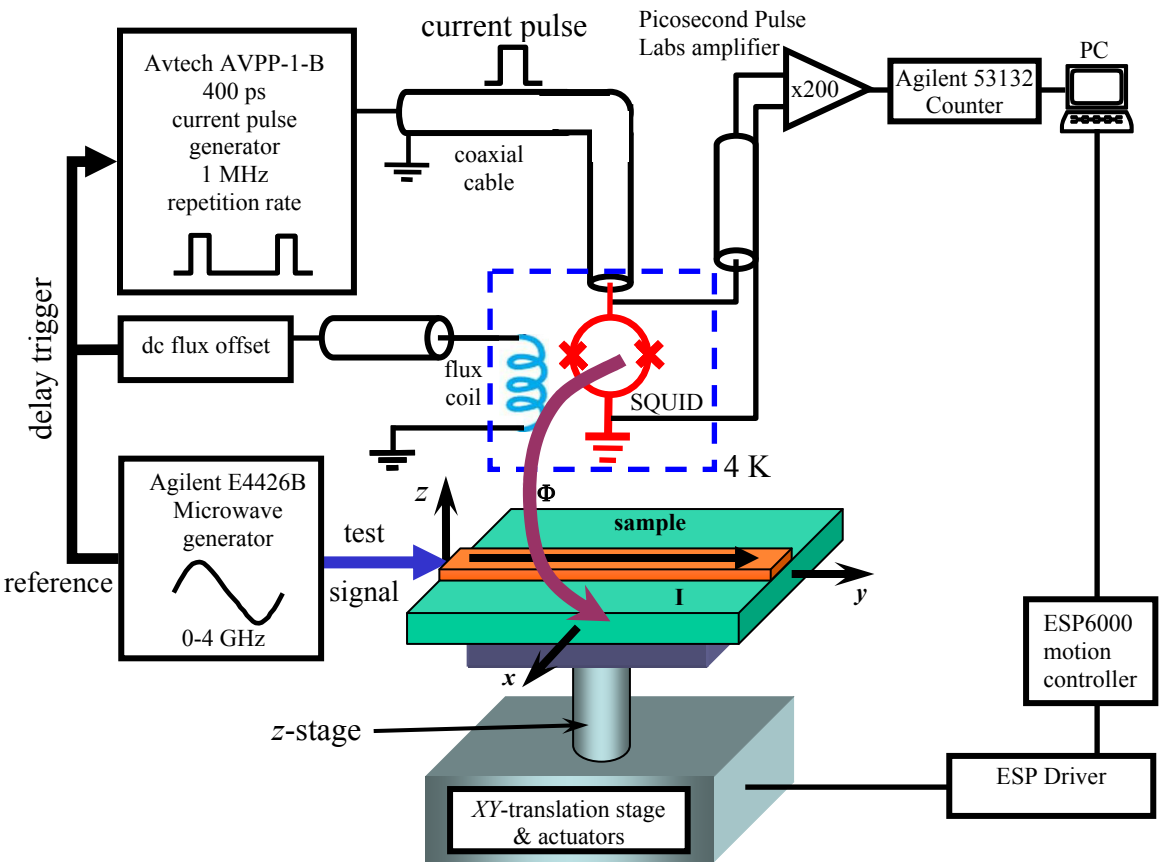

Fig. 9.1. Experimental arrangement for high-bandwidth SQUID microscope measurement. The signal under-test (a GHz sine wave) is provided by a microwave generator connected to the sample. A controllable dc offset flux is coupled to the SQUID via a one-turn on-chip loop. The SQUID current source is a 400 ps pulse generator. A counter detects the number of voltage pulses from the SQUID in a given time interval (1 to 20 ms).

switch with each current pulse, so some care must be taken in setting up the pulse generator. The amplitude of the raw voltage output of the SQUID pulse is approximately 2.8 mV, but this is fed into a Picosecond Pulse Labs high frequency amplifier with a gain of 200 that boosts the output to almost 0.5 V. The resulting pulses are fed to an Agilent 53132 counter that records the number of voltage pulses above a 150 mV threshold in a given time (typically between 1 and 20 ms). I set the pulse repetition rate to a maximum

of 1 MHz that in turn yields a maximum of 1000 to 20,000 counts for 1 to 20 ms counting interval.

With the bias current set near the midpoint of the SQUID's critical current range, the voltage pulses can be turned on and off by adjusting the flux applied to the SQUID. To set the flux bias point, I use a function generator to supply a computer-controlled dc current of between -100 μA to 100 μA to the flux modulation coil. For the results in this chapter, I used device HSQ_2 (see Table 4.1). From the periodicity of the $I_c(\Phi_a)$ curve (see Fig. 9.2), I found that 82.5 μA generated one quantum of flux (*h/2e*) in the SQUID. This implies that the mutual inductance between the coil and SQUID is $M \approx 25\,pH$. For my SQUID loop area of 300 μm^2 (see Fig. 4.3), and given the 100 Ω current-limiting source resistor in the function generator, this corresponds to a transfer function of 2.5 μT at the SQUID per volt at the function generator.

9.2 Magnetic Field Images of a Magnetic Dipole

To test the imaging capabilities of the SQUID microscope, I made a magnetic dipole out of semi-rigid coaxial cable [2] (see Fig. 9.4). The cable has an outer diameter of 2.17 mm and the diameter of the inner conductor is 0.5 mm. The outer conductor and inner conductor are both made of copper. To make the dipole, I exposed the inner conductor at one end of the cable and then bent it around and soldered it to the outer conductor. This formed a small loop, about 2 mm by 2.1 mm high at the end of the coaxial line. Figure 9.4 shows the final arrangement in which the coaxial transmission line is bent at 90° and placed into a groove in the bottom of a Delrin block. Only the loop at the end of the coaxial line is exposed above the Delrin block.

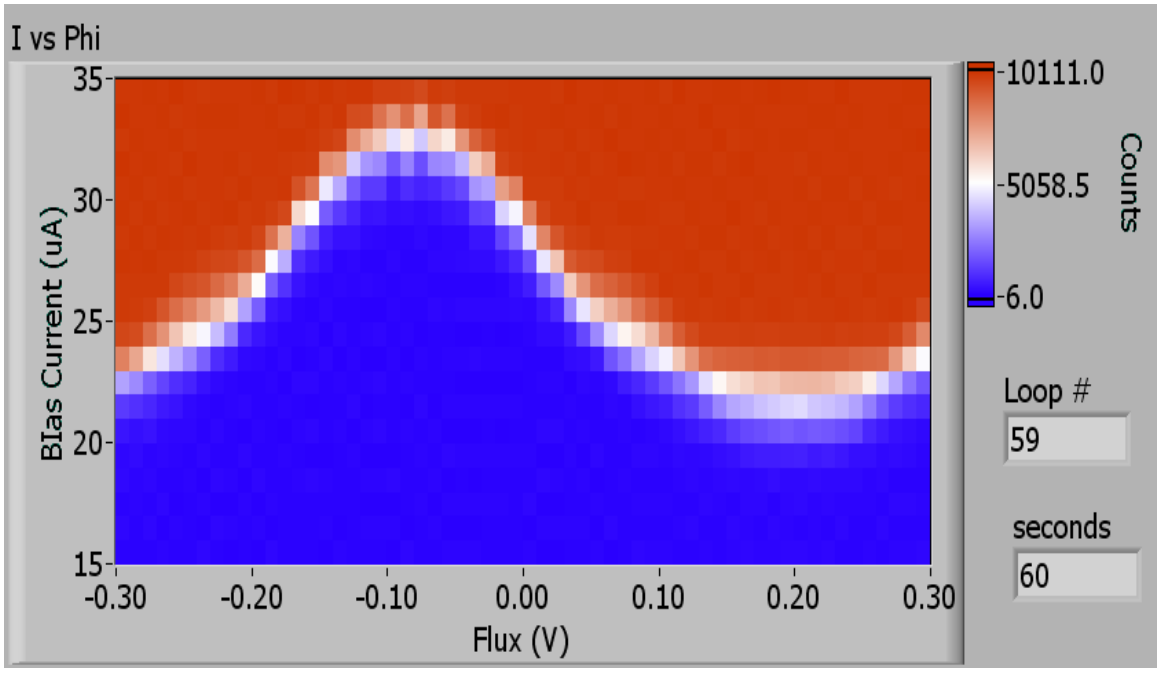

Fig. 9.2. False-color plot showing measured number of switching events versus current (*y-axis*) and flux (*x-axis*).

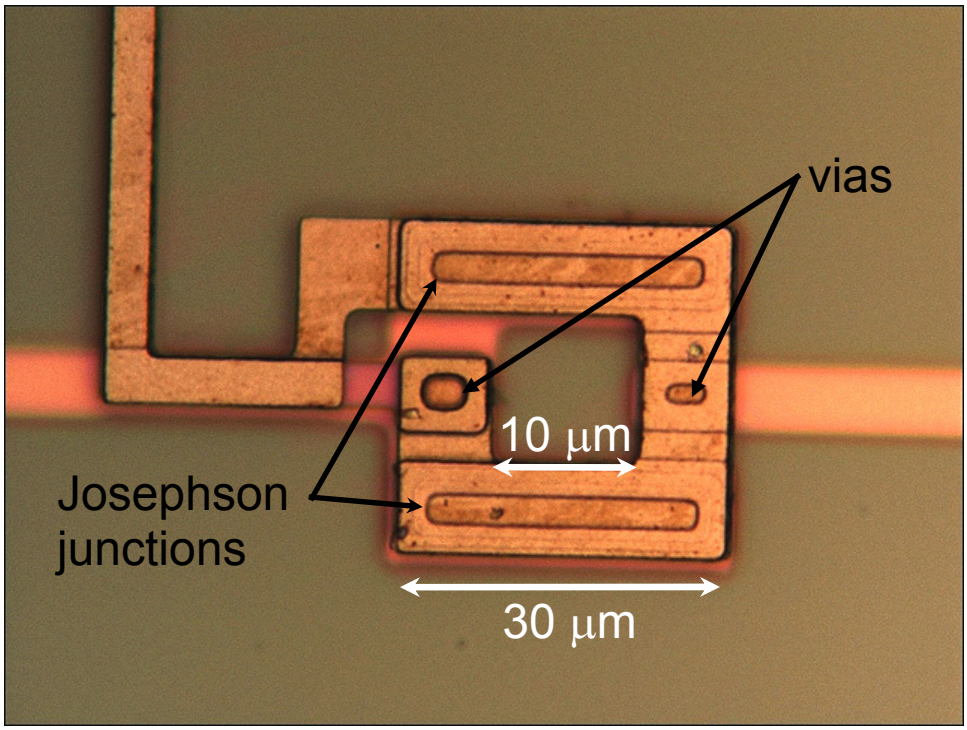

Fig. 9.3. Close-up of SQUID (Device HSQ_2) with junctions at the top and bottom of the square washer.

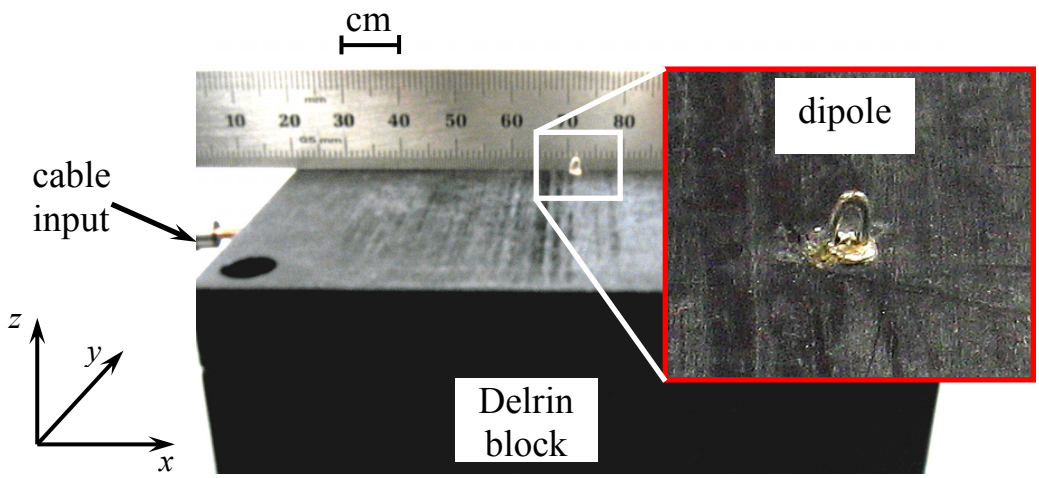

Fig. 9.4. Photograph of magnetic dipole sample and Delrin sample block on *xyz*-stage. The dipole is made from semi-rigid coaxial transmission line with the inner conductor bent into a loop and soldered onto the outer conductor. The loop is approximately 2 mm wide by 2.1 mm tall. The diameter of the inner conductor wire is 0.5 mm.

The loop was then placed on the *xyz*-stage and raised to within 150 μm of the 25 μm thick sapphire window.

Figures 9.5 shows an image of the background dc magnetic field over the dipole using the SQUID HSQ_2 described in section 4.2. No current was applied to the dipole for this image. For each pixel I used a 50 ns pulse width and a 20 ms count time and the SQUID was about $z = 700$ μm above the loop. The area scanned was 8 mm by 8 mm with 0.5 mm steps for 289 pixels. The acquisition time per pixel was 10 sec resulting in a total image acquisition time of 48 minutes. The dipole was positioned parallel to the *x*-axis with its center at approximately $x = 15$ mm and $y = 42$ mm. I note that the image shows a background field of about -7 μT in the z-direction and a gradient of $\partial B/\partial y \simeq -200\,nT/mm$.

Figures 9.6 shows the corresponding dc magnetic field image taken with a dc current of 4 mA applied to the loop. A 50 ns pulse width was

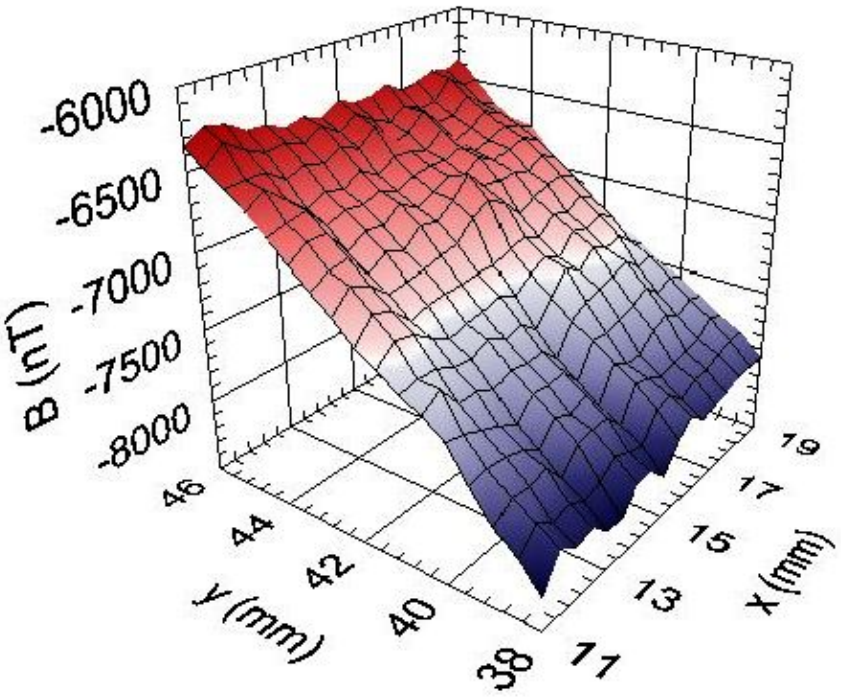

Fig. 9.5. Background magnetic field image over the dipole shown in Fig. 9.4. No current was applied to the dipole.

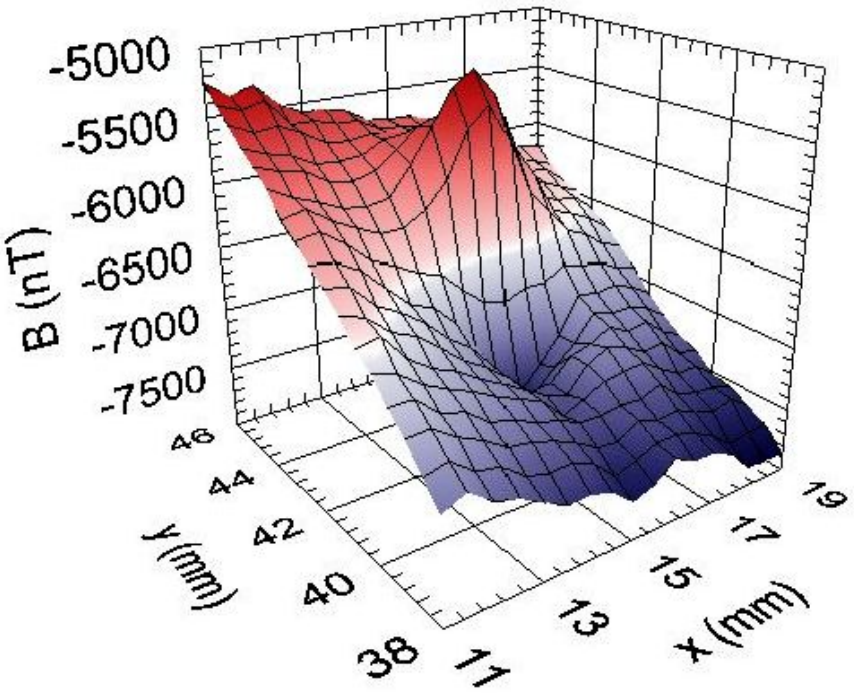

Fig. 9.6. A dc magnetic field image of the loop shown in Fig. 9.4 taken with a 4 mA dc current applied to the loop.

used along with a 20 ms count time. As with Fig. 9.5, the area scanned over the dipole was 8 mm × 8 mm with 0.5 mm steps for 289 pixels and the acquisition time per pixel was 10 sec. The dipole loop was positioned parallel to the *x*-axis with its center at approximately $x = 15$ mm and $y = 42$ mm. As expected for the field from a loop with this orientation, the image shows a clear maximum (positive) and minimum (negative) lobes of the field that is about ±1.15 μT and positioned along the *y*-direction above and below the "zero-field" point where the coil is centered. As with Fig. 9.5, there is a background field of about -7 μT in the z-direction and a gradient of about $\partial B / \partial y \simeq -200\, nT / nm$.

Figure 9.7 shows a top down view of the magnetic field from the dipole. Here I have subtracted Fig. 9.5 from Fig. 9.6 in order to remove the background field shown in Fig. 9.5. As expected, we see a positive and negative lobe characteristic of the *z*-component of magnetic field from a dipole. White corresponds to zero field while red and blue regions correspond to ±500 nT. Note that the separation between the lobes is approximately 2 mm, and this corresponds roughly to the distance from the loop.

Figure 9.8(a-j) shows ten magnetic field images of the loop taken with a 0.8 mA applied current of frequency $f = 100$ MHz at successive delay time increments of 0.1 ns. For these images, I used a 10 ns pulse width and a 20 ms count time with the SQUID about 1.25 mm above the loop. I scanned an area of 31 mm × 10 mm using 1.0 mm steps for 121 pixels. The acquisition time per pixel was 10 sec resulting in a total time-elapsed image acquisition time of 20.2 minutes for each image. As expected, two lobes are present that form a maximum and minimum that oscillate (±400 nT) at 100 MHz.

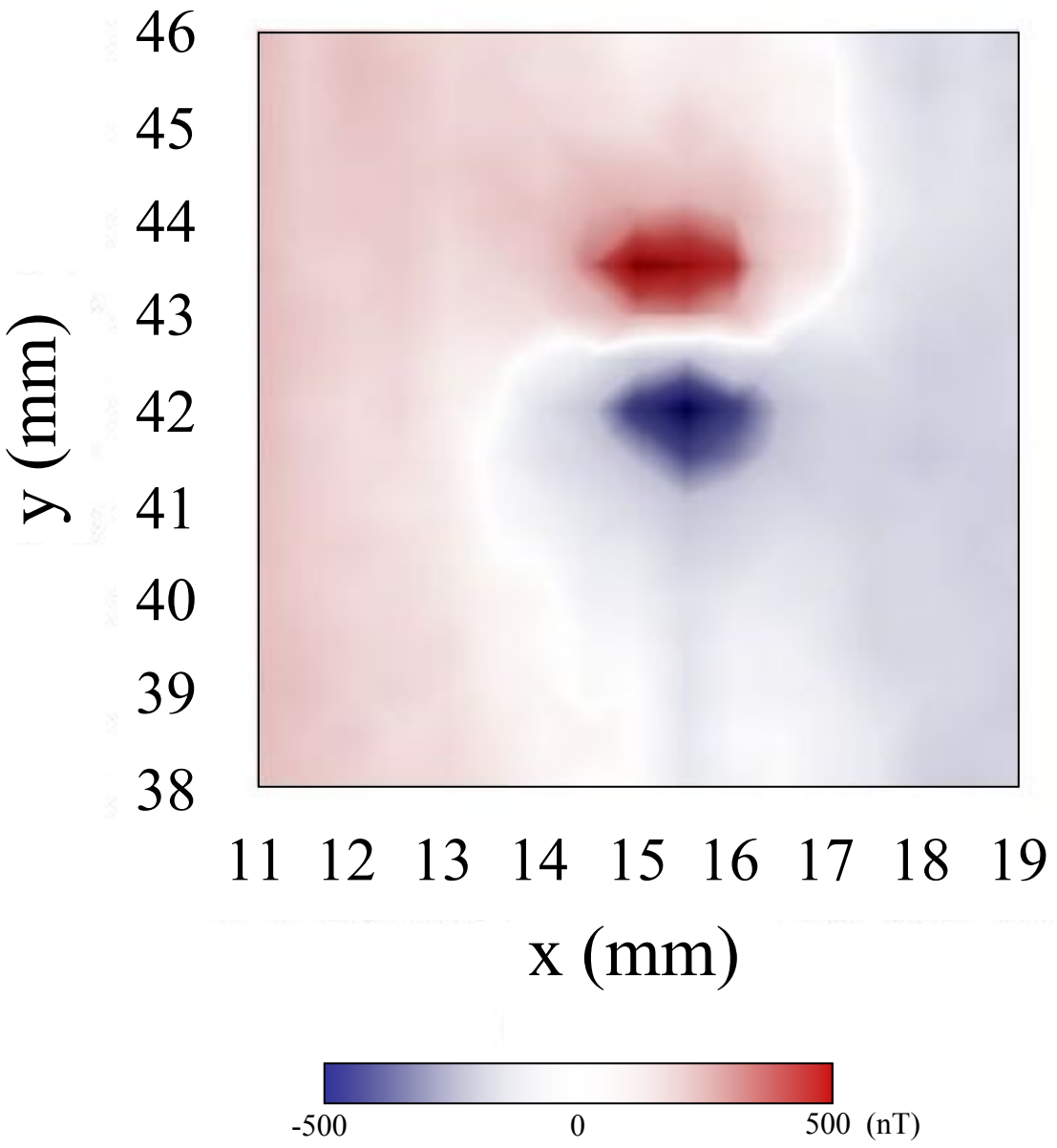

Fig. 9.7. Magnetic field difference image of dipole found by subtracting in Fig. 9.5 from Fig. 9.6. White corresponds to zero field while red and blue regions correspond to ±500 nT.

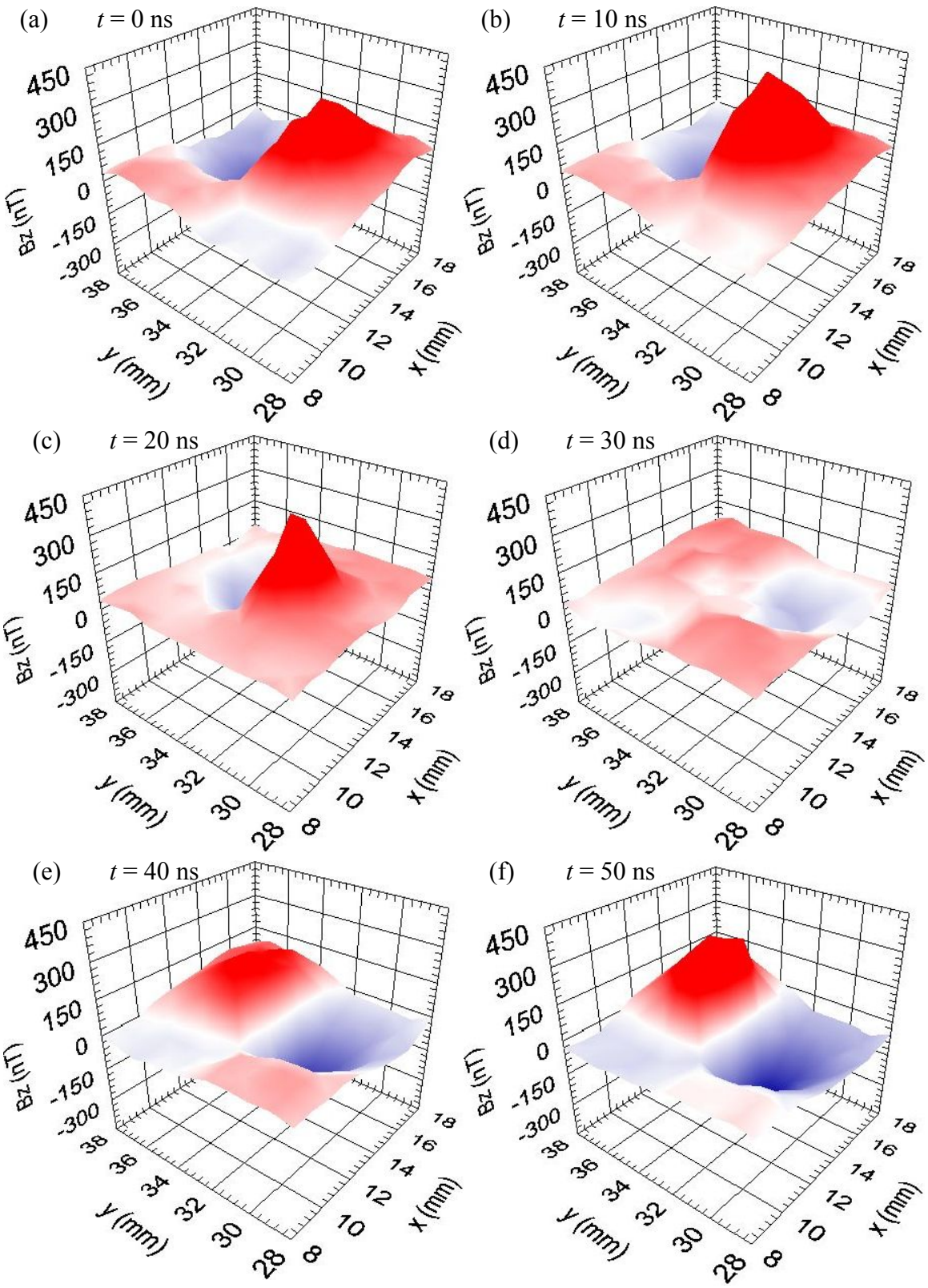

Fig. 9.8. (a-f) Magnetic field images of a dipole at t = 0, 10 ns, … , 50 ns. The frequency of the applied current signal was f = 100 MHz, the current amplitude was 800 μA.

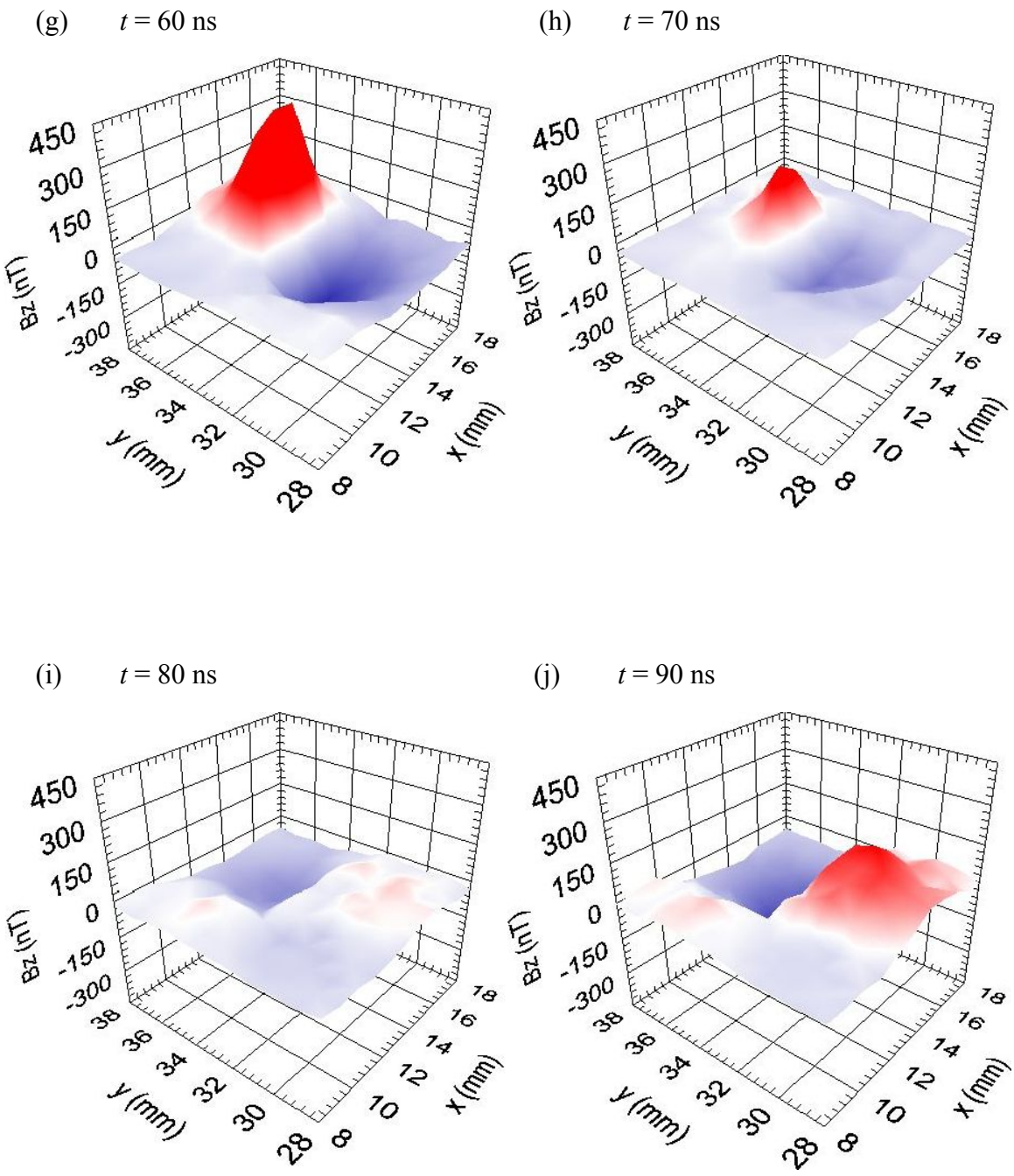

Fig. 9.8. (g-j) Magnetic field image of a dipole imaged at times 60 ns, 70 ns, 80 ns and 90 ns. The frequency of the applied current is f = 100 MHz, and the current amplitude was 800 μA.

Figure 9.9(a-j) shows the corresponding top down view of the ten magnetic field images shown in Fig. 9.8(a-j). White corresponds to zero field while red and blue regions correspond to ±400 nT. With a SQUID-dipole separation of about 1.25 mm this level of field corresponds to a current of about 2 mA in the loop, which is about a factor of 2.5 more than I applied. The field depends strongly on the separation, so this could be due to the distance z being somewhat smaller than 1.25 mm.

Figure 9.10 shows ten magnetic field images of the loop taken with a -21 dBm (400 μA) applied microwave signal of frequency f = 1 GHz at successive delay time increments of 0.1 ns. A 400 ps pulse width was used along with a 20 ms count time. The area scanned over the dipole was 10 mm × 10 mm with 0.5 mm steps for 441 pixels. The acquisition time per pixel was 10 sec resulting in a total time-elapsed image acquisition time of 1.22 hours. As expected, there is a field maximum and minimum (±400 nT) that oscillate about the zero field point of x = 14 mm and y = 33 mm.

Figure 9.11 shows the corresponding top down view of magnetic field images shown in Fig. 9.10(a-j). White corresponds to zero field while red and blue regions correspond to ±500 nT with a SQUID-dipole separation of about 550 μm. Again we see that the maximum and minimum oscillate as expected at 1 GHz about the zero field point of x = 13 mm and y = 33 mm. In fact, Figs 9.10-9.11 appear clearer than the images at lower frequency. This is partly due to my increased understanding of how to operate the system that I gained for these later images. In any case, these images clearly demonstrate that the system could image up to at least 1 GHz.

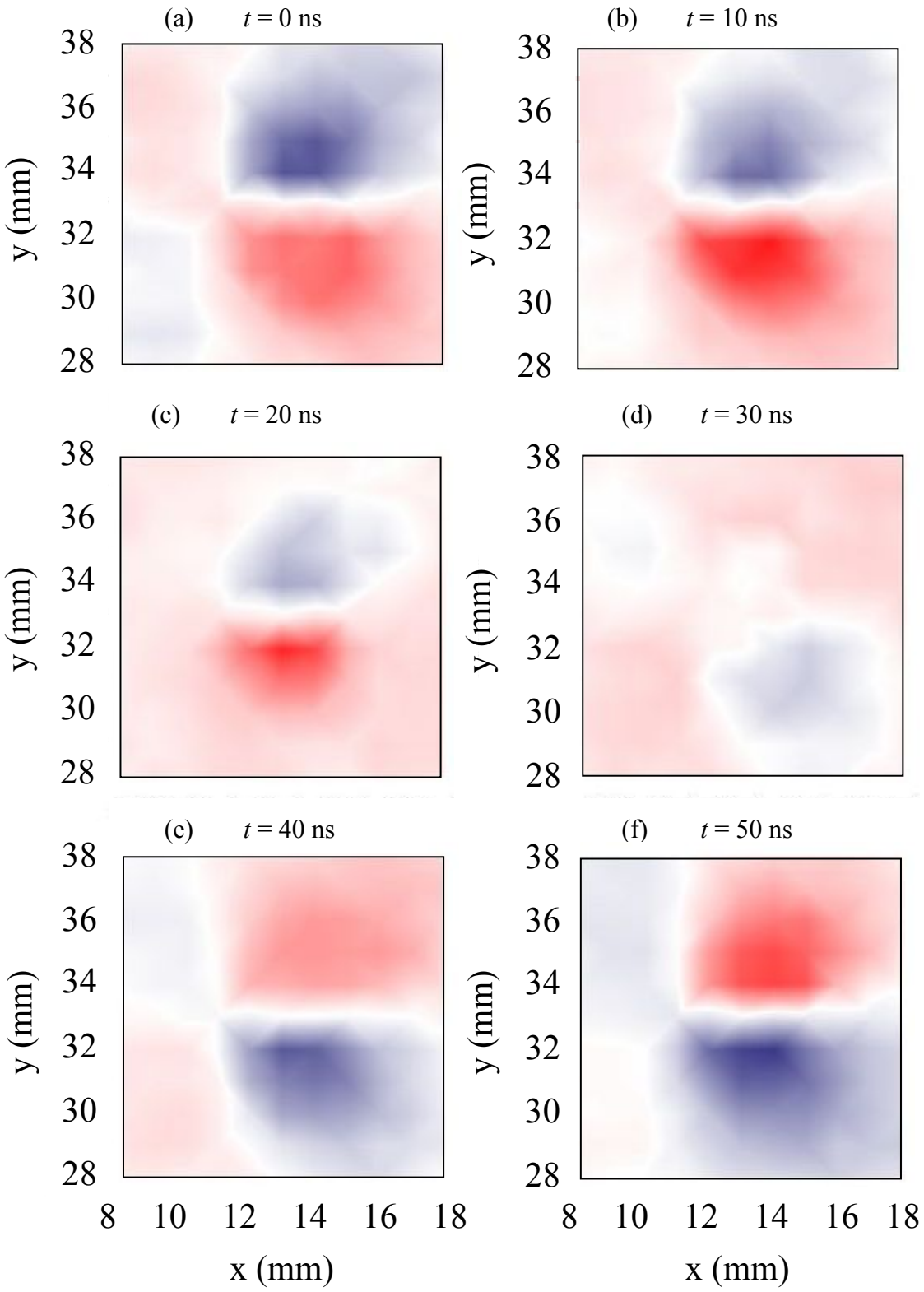

Fig. 9.9. (a-f) Top down view of magnetic field images shown in Fig. 9.8(a-f). The frequency of the applied current signal was f = 100 MHz, the current amplitude was 800 μA. Imaged at successive delay times of t = 0, 10 ns, … , 50 ns.

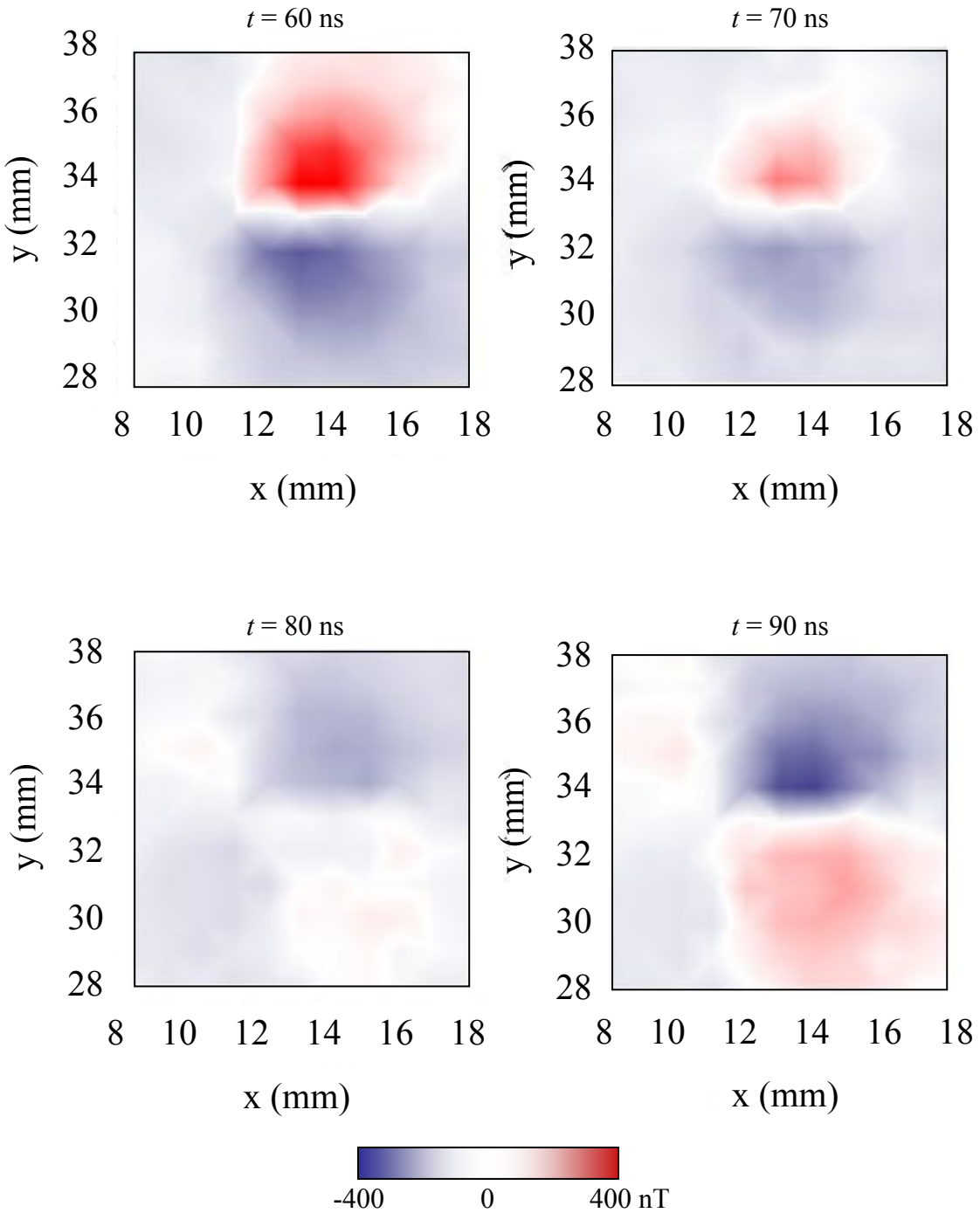

Fig. 9.9. (g-j) Top down view of magnetic field image of a dipole shown in Fig. 9.8(g-j). Imaged at times 60 ns, 70 ns, 80 ns and 90 ns. The frequency of the applied current is f = 100 MHz, and the current amplitude was 800 μA.

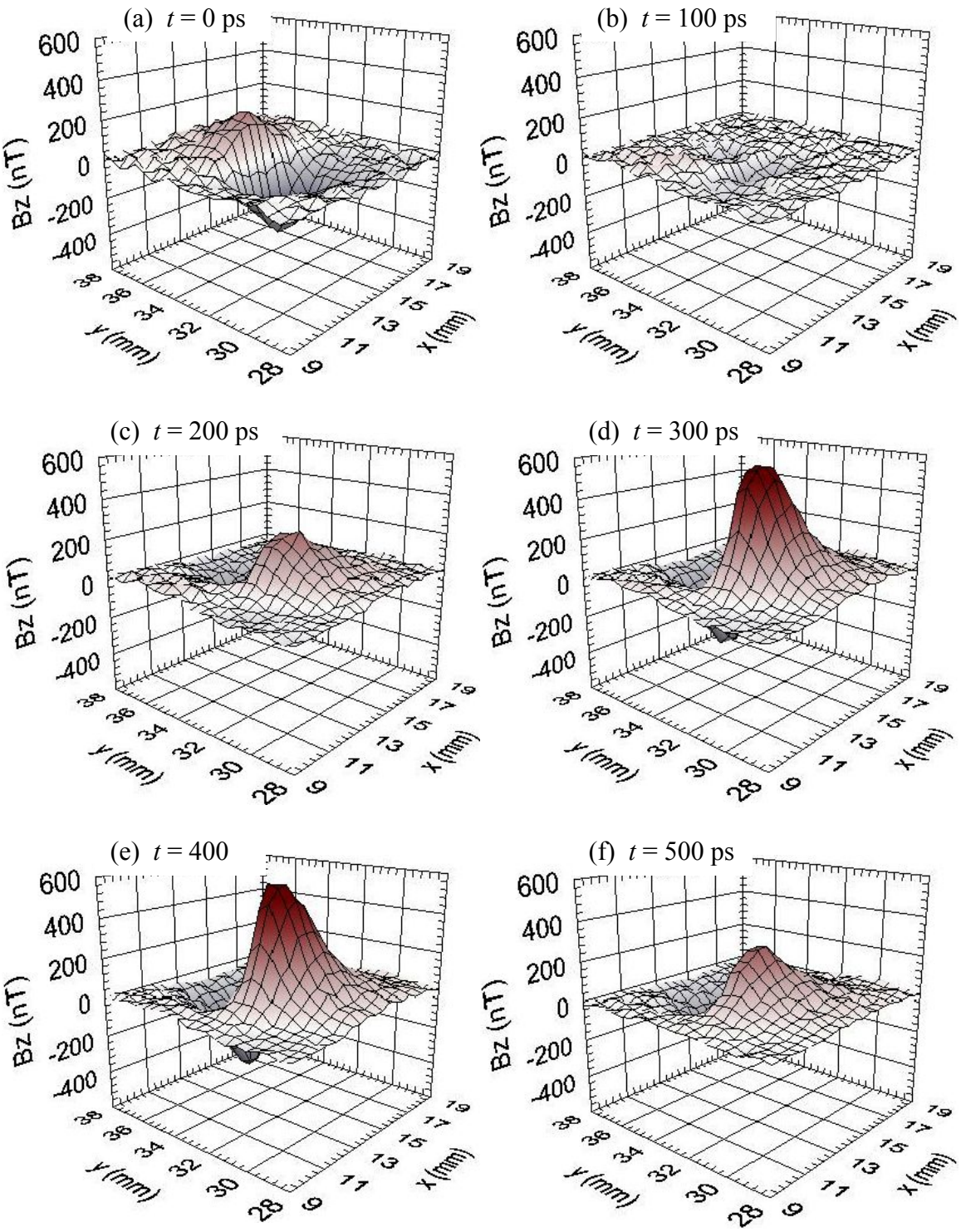

Fig. 9.10. (a-f) Magnetic field image of the dipole shown Fig. 9.4 imaged at successive times separated by 0.1 ns intervals. The frequency of the applied microwave signal was $f = 1$ GHz and the current amplitude was 400 μA.

(g) t = 600 ps

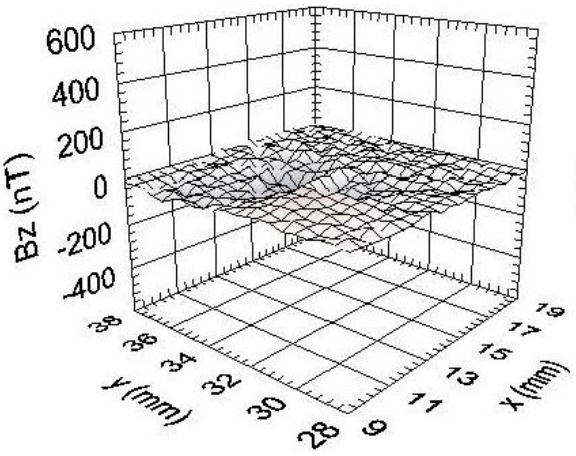

(h) t = 700 ps

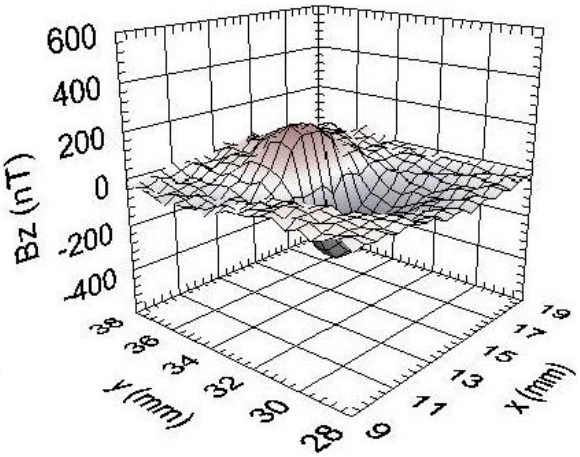

(i) t = 800 ps

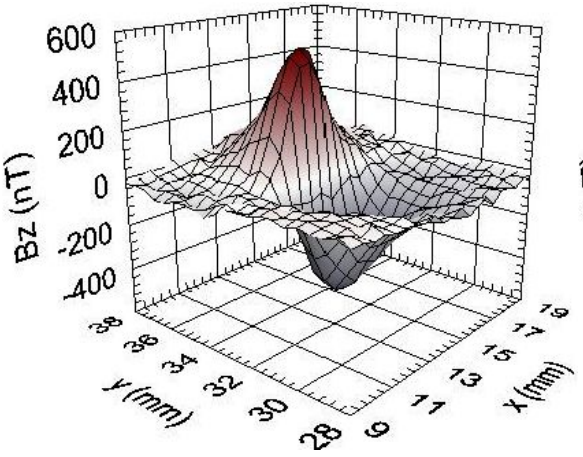

(j) t = 900 ps

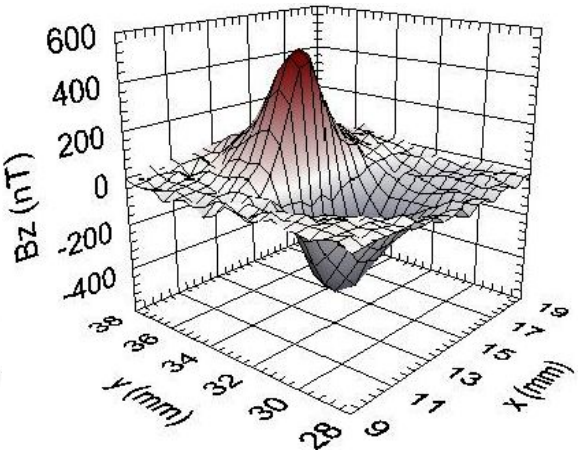

Fig. 9.10. (g-j) Magnetic field image of dipole shown in Fig. 9.4. The frequency of the applied microwave signal was f = 1 GHz and the current amplitude was 400 μA.

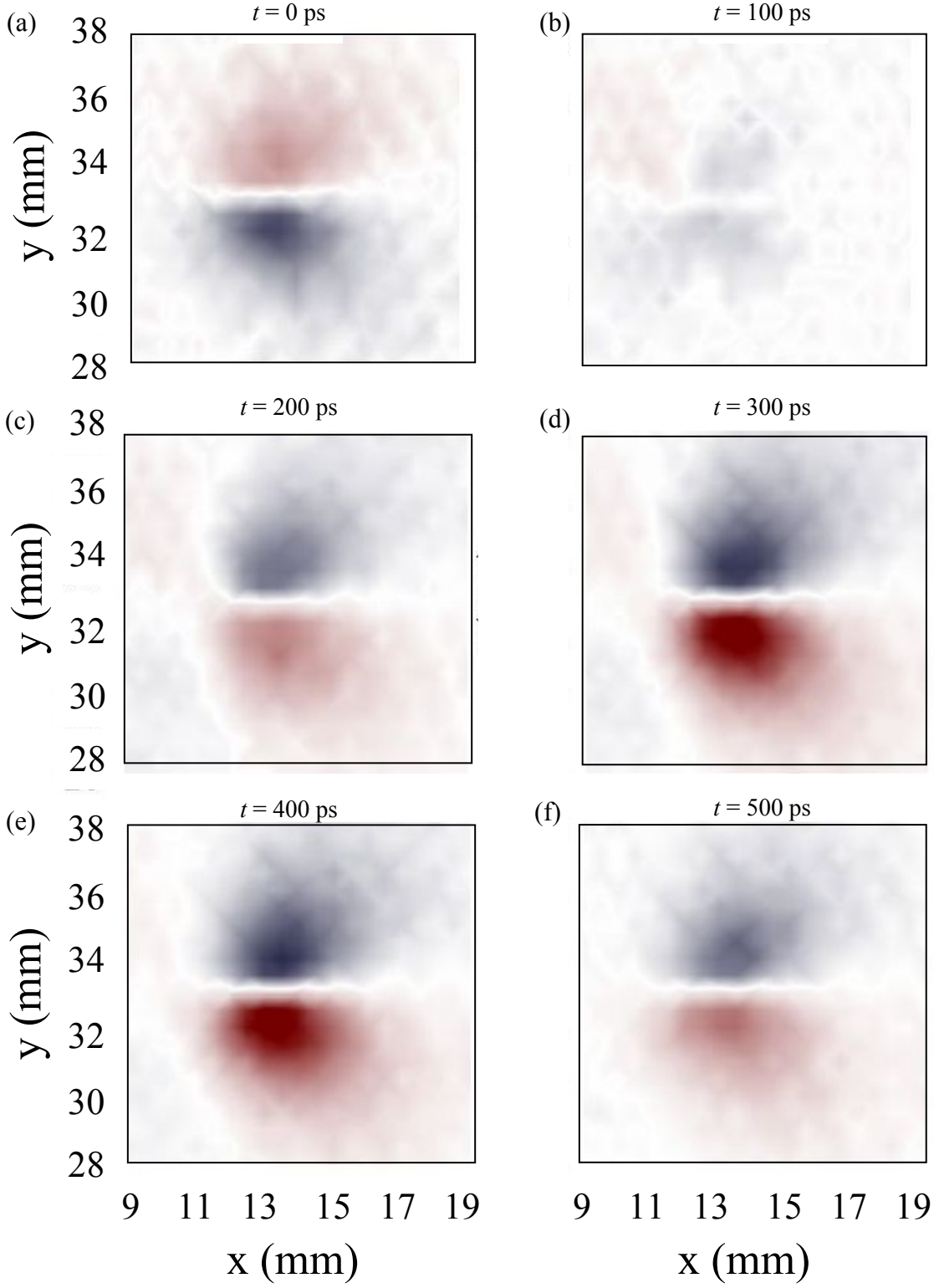

Fig. 9.11. (a-f) Top down view of magnetic field images shown in Fig. 9.10(a-f). The frequency of the applied current signal was f = 1 GHz, the current amplitude was 400 μA. Imaged at successive delay times of t = 0, 100 ps, … , 500 ps.

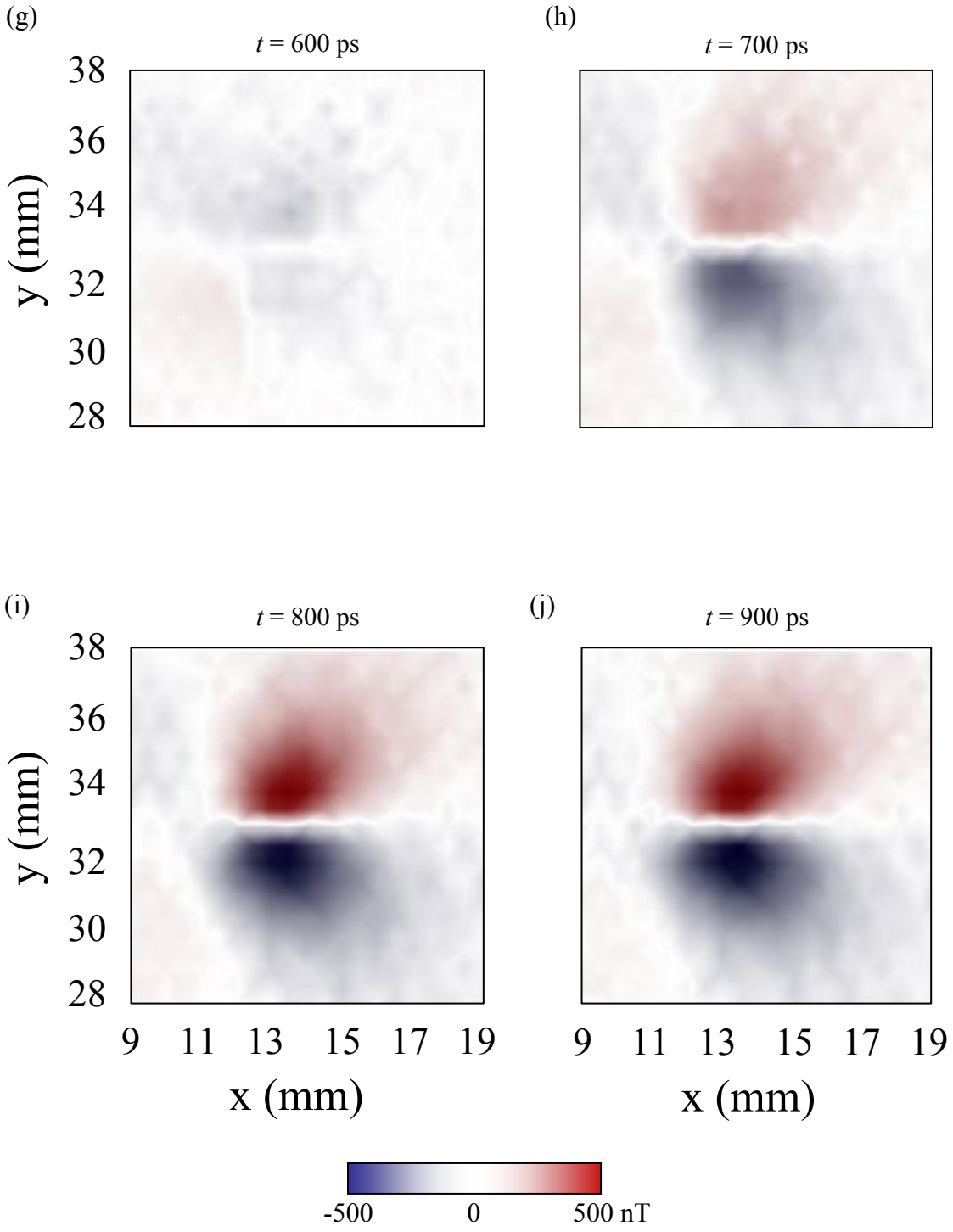

Fig. 9.11. (g-j) Top down view of magnetic field images shown in Fig. 9.10(g-j). The frequency of the applied current signal was f = 1 GHz, the current amplitude was 400 μA. Imaged at successive delay times of t = 600, 700, 800, 900 ps.

9.3 Magnetic Field Images of a Microstrip Transmission Line

To further test the system, I scanned a section of a 200 μm wide stripline (see Fig. 9.12) carrying a microwave signal. The dielectric substrate material for the microstrip is FR-4 Duroid with a dielectric constant of $\varepsilon_r \approx 4.4$. The backside of the FR-4 laminate is covered by a 43 μm thick copper ground plane and the board's overall thickness is 1.75 mm. I calculated the characteristic impedance of the microstrip line to be 140 Ω [3]. Each end of the microstrip line has a 50 Ω SMA connector and I applied a microwave sine wave signal to one end and terminated the other end with either a 50 Ω termination or a 139 Ω terminator.

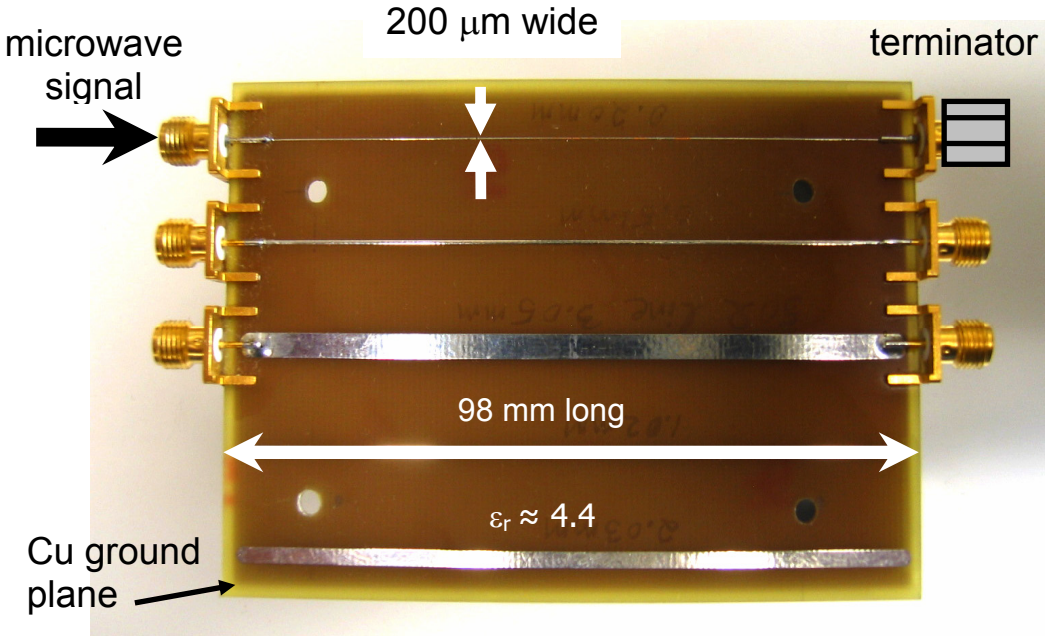

Fig. 9.12. Photograph of sample with three microstrip transmission lines. The lines are 200 μm, 500 μm, and 3.05 mm wide. The board is 98 mm long by 60 mm wide, and the dielectric material is FR-4 Duroid which has a relative permittivity of $\varepsilon_r \approx 4.4$. I used the 200 μm line for the data shown in Figs. 9.13-9.30.

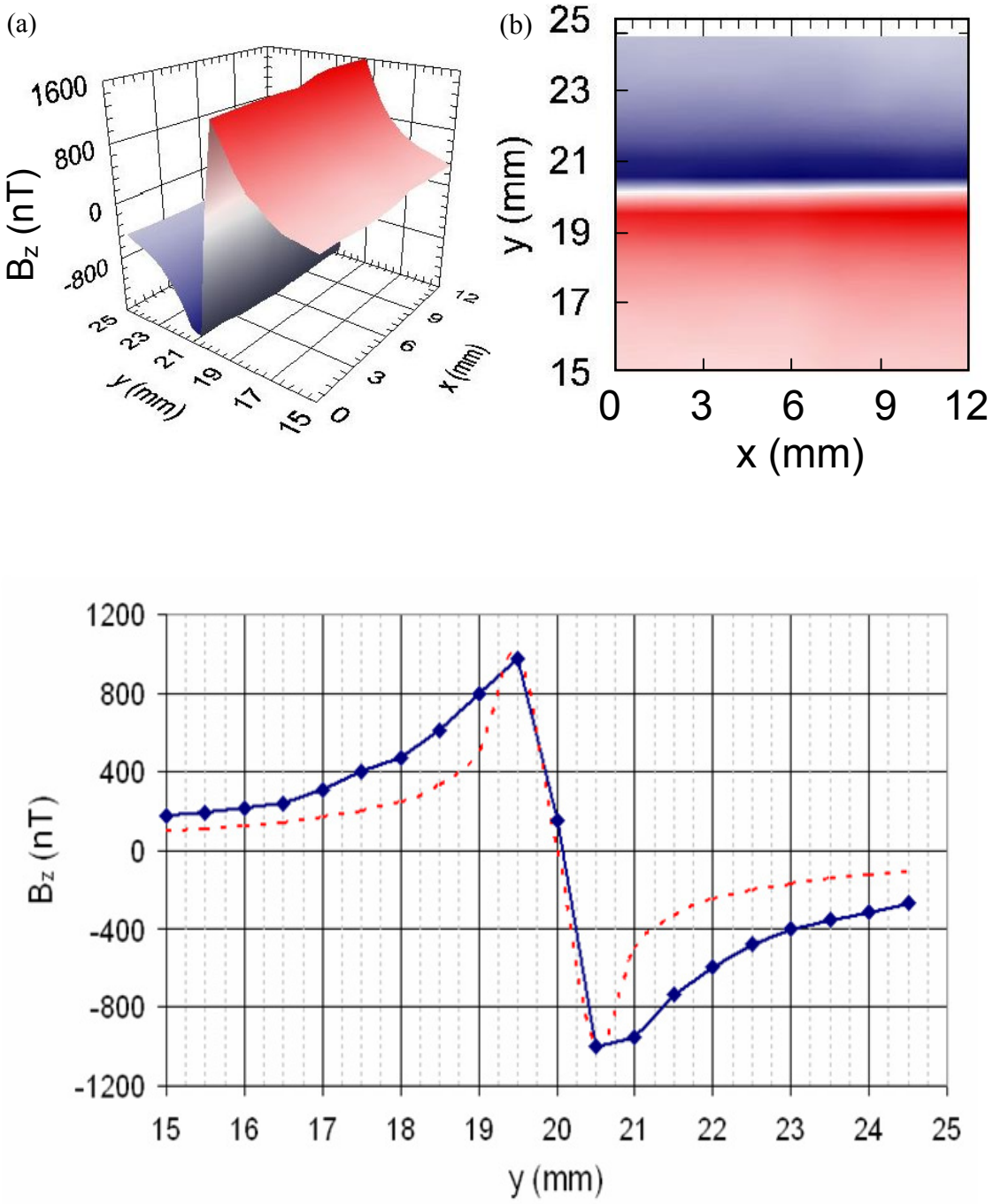

Fig. 9.13. (a) dc magnetic field image of the 200 μm-wide microstrip shown in Fig. 9.9. Background has been subtracted. The area scanned was 13 mm × 10 mm and the current amplitude is 10 mA. The SQUID was about 500 μm above the surface. (b) Top down view of microstrip line. (c) Line cut at x = 0 mm. The dashed red curve is the expected dependence of the B_z on y for a wire with negligible width.

Figure 9.13(a) shows a magnetic field image (B_z) of the 200 μm microstrip line shown in Fig. 9.12 taken with a 10 mA applied dc signal. The dc background magnetic field was subtracted from this image. An 8 ns pulse width was used along with a 20 ms count time and the SQUID was about z = 500 μm above the sample. The area scanned over the microstrip line was 13 mm x 10 mm with 0.5 mm steps for 441 pixels. The acquisition time per pixel was 10 sec resulting in a total time-elapsed image acquisition time of 73.5 minutes. The microstrip was positioned parallel to the x-axis with its center at approximately y = 20 mm. I found that the field maximum and minimum (±1.0 μT) are located at about y = 19.5 mm and y = 20.5 mm, *i.e.* ± 0.5 mm to either side of the center of the microstrip line [see Fig. 9.13(c)]. Figure 9.13(b) shows a top down view of B_z. The B_z = 0 field line is directly over the microstrip at about y = 20 mm. As expected the maximum/minimum of the magnetic field is at $\pm d$ where d = 500 μm is the distance between the plane of the microstrip line and the SQUID. From Fig. 9.13(c) we can also see that the measured field differs significantly from that due to a wire with negligible width. This difference is likely due to the actual 200 μm width of the line and the finite size of the SQUID.

Figures 9.14 to 9.30 show images of the field from the 200 μm wide microstrip line when I applied microwaves with frequency of 100 MHz up to 3.5 GHz. I present both 3D and 2D plots to provide a clearer view of the data. Beginning with 500 MHz and above one can see a wave propagating down the microstrip line at speed $c' \approx c/2$.

Figure 9.14 shows ten magnetic field images of the microstrip line taken with a -13 dBm (1 mA) applied microwave signal of frequency f = 100 MHz at successive delay time increments of 10 ns. A 10 ns pulse width was used along with a 20 ms count time.

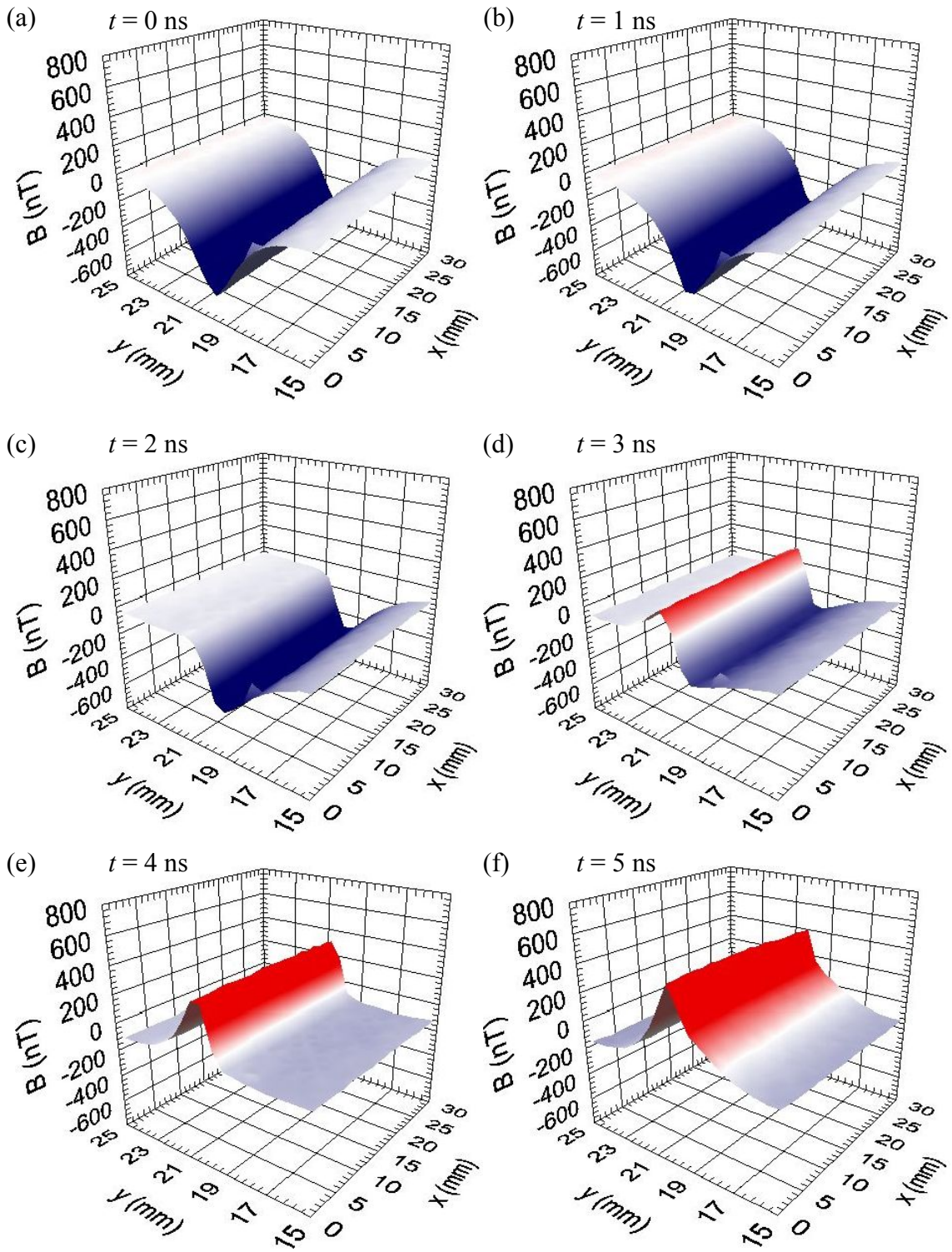

Fig. 9.14. (a-f) Measured $B_z(x,y,t)$ for delay time t = 0 ns to 5 ns for a microwave signal of frequency f = 100 MHz applied to the end of the 200 μm wide microstrip line shown in Fig. 9.12. The microstip line was terminated by a 50 Ω termination in this case. The SQUID was 625 μm above the surface. Note x-axis is compressed as compared to y-axis

(g) t = 6 ns (h) t = 7 ns

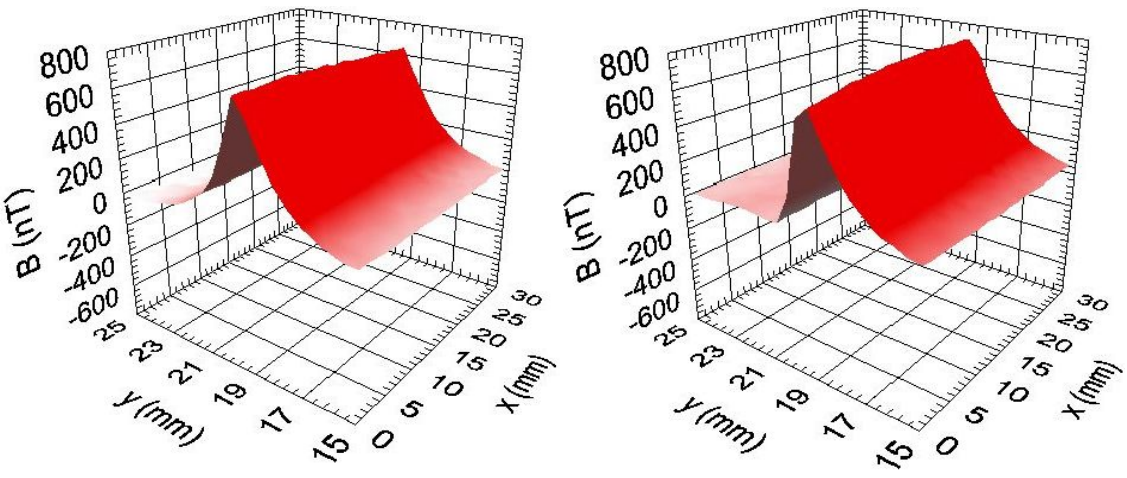

(i) t = 8 ns (j) t = 9 ns

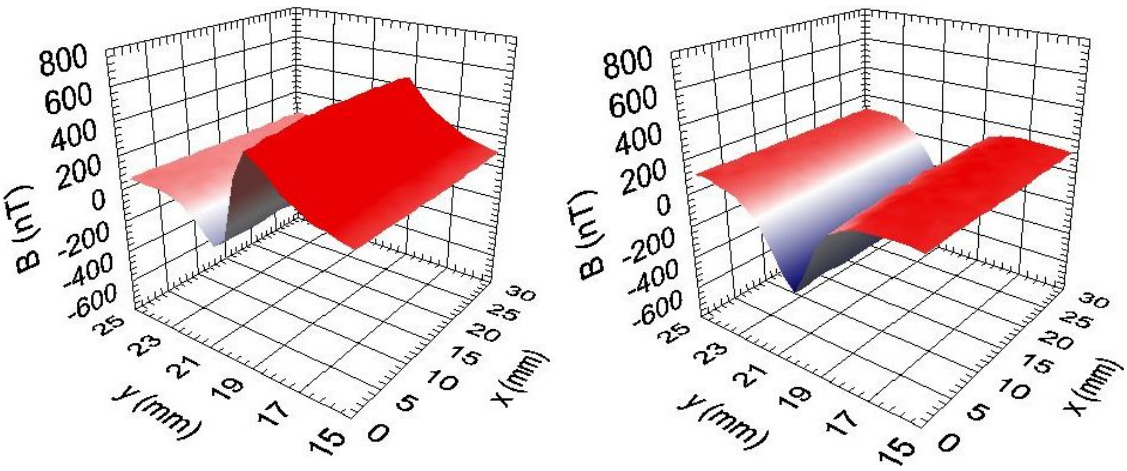

Fig. 9.14. (g-j) Measured $B_z(x,y,t)$ for delay time t = 6 ns to 9 ns for a microwave signal of frequency f = 100 MHz applied to the end of the 200 μm wide microstrip line shown in Fig. 9.12. The microstip line was terminated by a 50 Ω termination in this case.

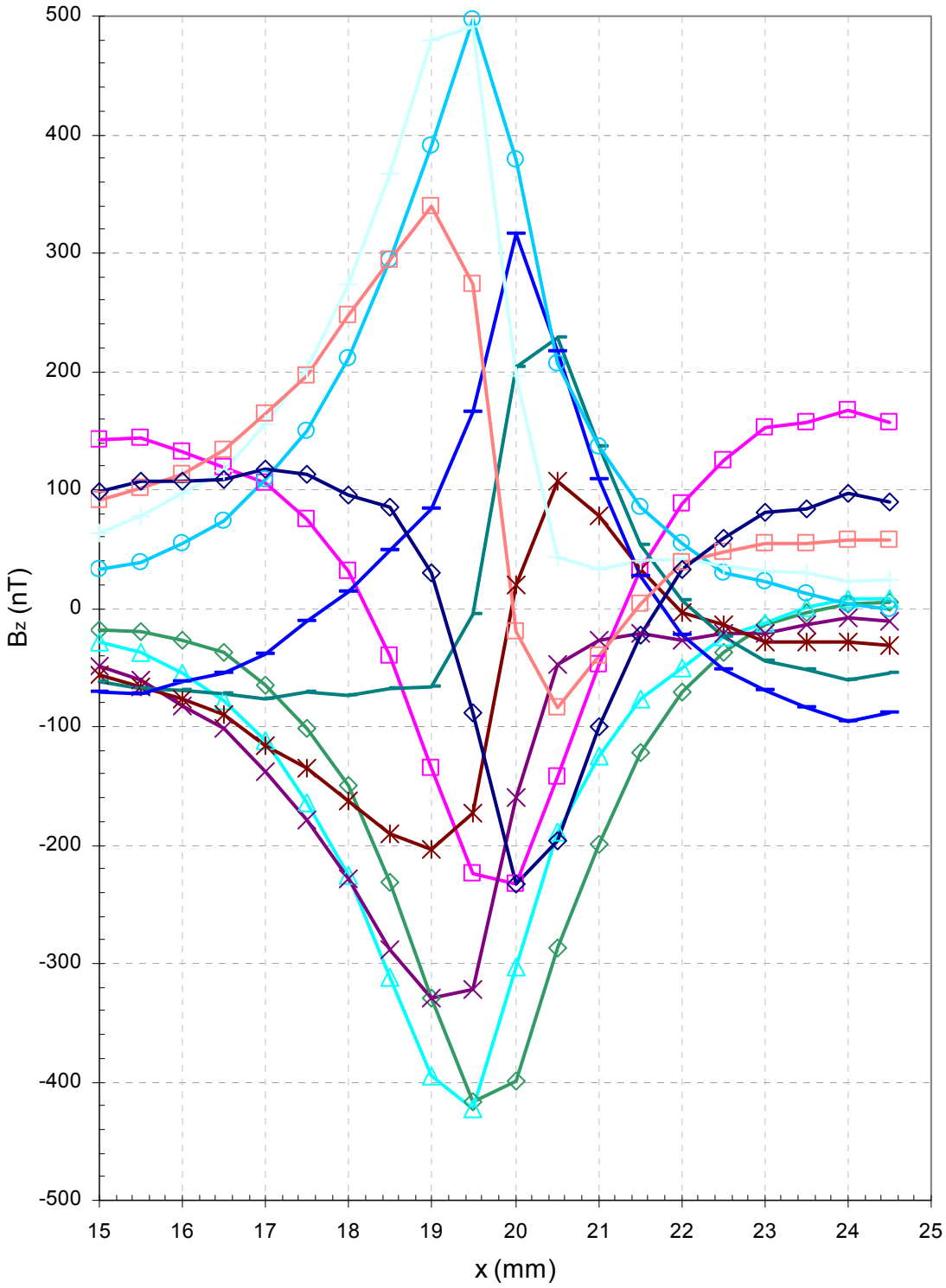

Fig. 9.15. Line scan across the *y*-axis at x = 10.5 mm in Fig. 9.19 for the 100 MHz applied current. Plot legend: 0 ns, 1 ns, 2 ns, 3 ns, 4 ns, 5 ns, 6 ns, 7 ns, 8 ns, 9 ns, 10 ns.

The area scanned over the microstrip was 10 mm (0.5 mm steps) x 31 mm (1.5 mm steps) for 441 pixels. The acquisition time per pixel was 10 sec resulting in a total time-elapsed image acquisition time of 74 minutes. The microstrip was parallel to the *x*-axis and centered at y = 20 mm. The maximum and minimum oscillate (±700 nT) about the zero field point and the SQUID was 625 μm above the microstrip line. Note that in this 3D image (and later ones) the *x*-axis is compressed as compared to the *y*-axis.

Figure 9.15 shows individual line scans taken across the *x*-axis at y = 10.5 mm in Fig. 9.14. Both Figs. 9.14 and 9.15 show a field pattern that is unlike what one sees at dc. In fact it appears that the y-component of the magnetic field is being detected in addition to the *z*-component; the y-component peaks directly over the wire much like the data at t = 5 to 7 ns.

Figure 9.16 shows ten magnetic field images of the microstrip line taken with an applied microwave power of -7 dBm at f = 250 MHz for successive delay time increments of 4 ns. I used a 8 ns pulse width and a 20 ms count time. The area scanned was 10 mm (0.5 mm steps) x 31 mm (1.5 mm steps) for 441 pixels. Note here the *x* and *y* axes are flipped with respect to the earlier figures so the microstrip line is parallel to the *y*-axis. The acquisition time per pixel was 10 sec resulting in a total time-elapsed image acquisition time of 73.5 minutes or 7.35 minutes per frame. The maximum and minimum oscillate by ±250 nT. As was the case for Fig. 9.15, Fig. 9.16 also shows evidence of other magnetic field components (B_x) in addition to B_z..

Figure 9.17 shows individual line scans taken across the *x*-axis at y = 10.5 mm in Fig. 9.16. The microstrip here was parallel to the *y*-axis and centered at x = 20 mm. From the line scans it is evident that more than the z-component of the field is being detected.

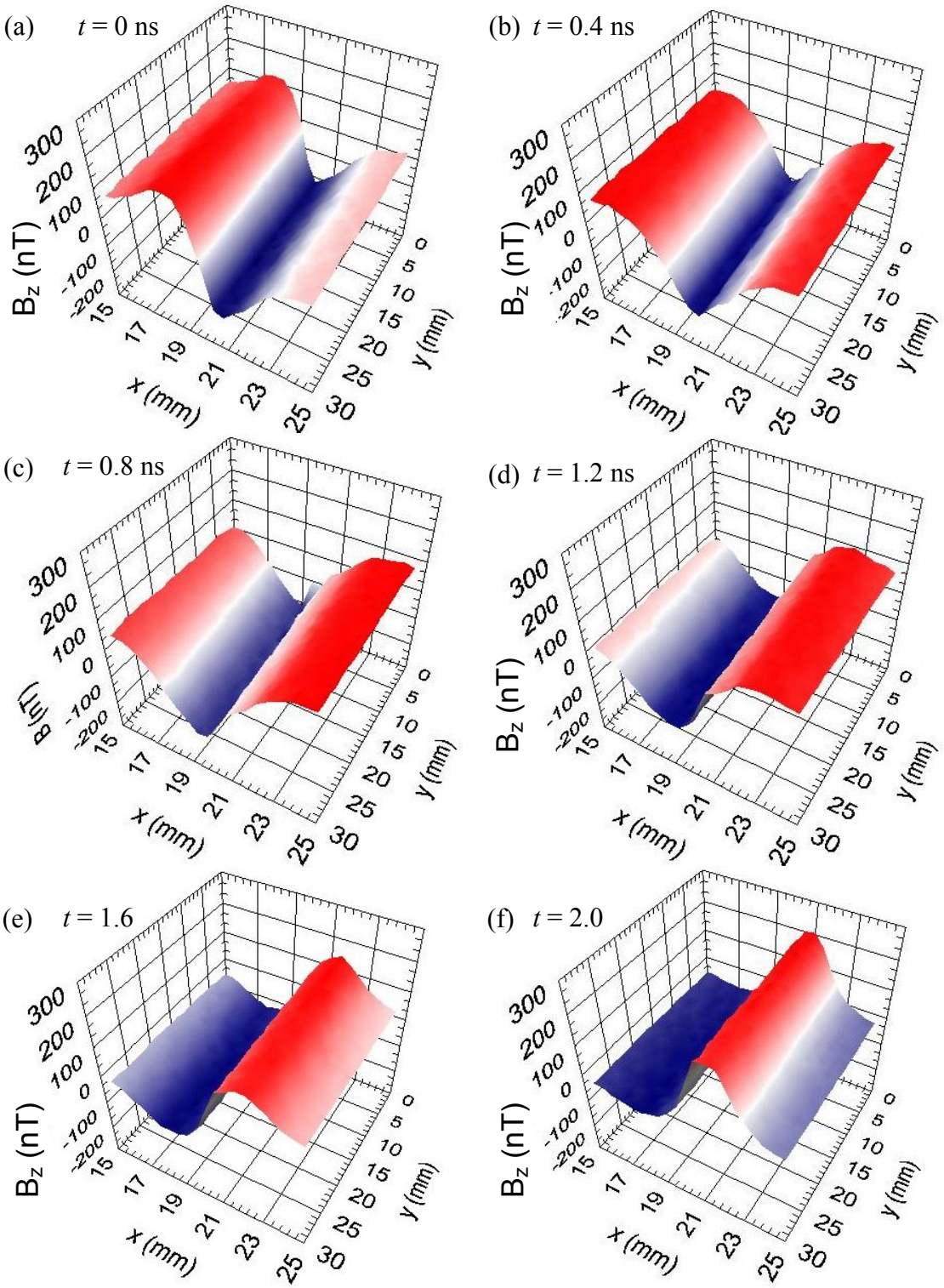

Fig. 9.16. (a-f) Measured $B_z(x,y,t)$ for delay time t = 0 ns to 2.0 ns for a microwave signal of frequency f = 250 MHz applied to the end of the 200 μm wide microstrip line shown in Fig. 9.12. The microstip line was terminated by a 50 Ω termination in this case. The SQUID was 500 μm above the strip.

(g) t = 2.4 ns (h) t = 2.8 ns

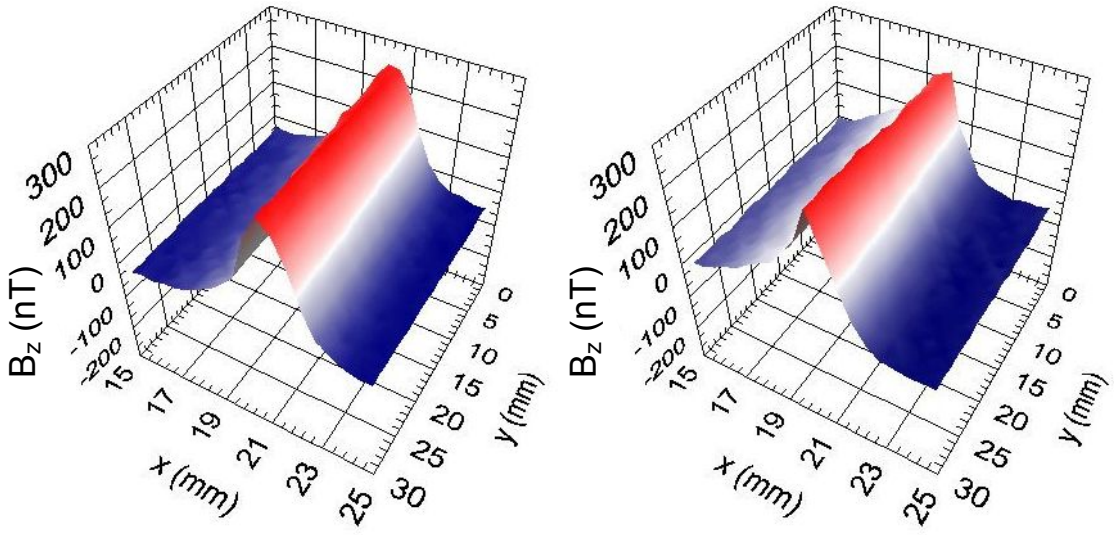

(i) t = 3.2 ns (j) t = 3.6 ns

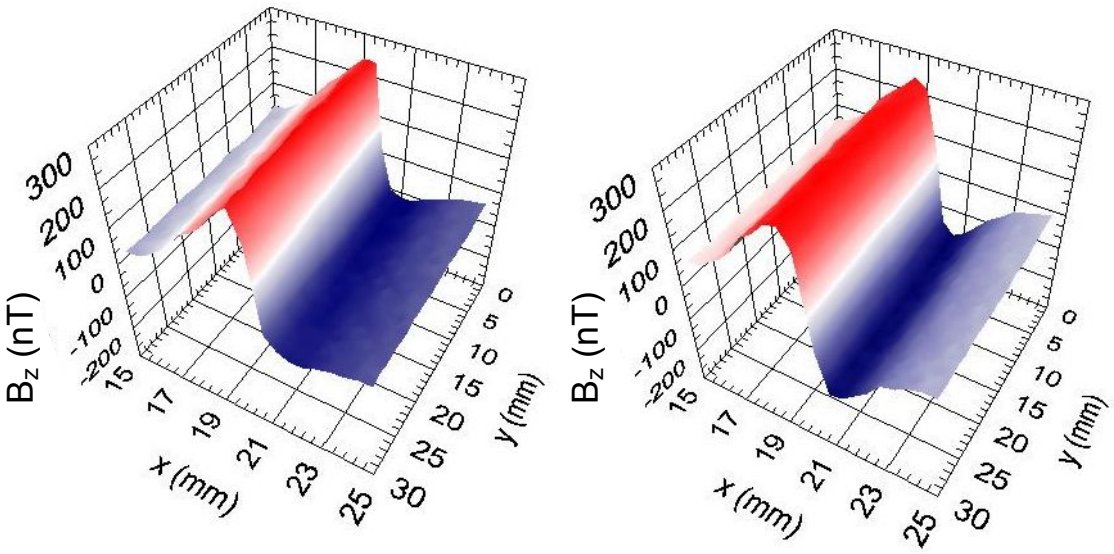

Fig. 9.16. (g-j) Measured *B(x,y,t)* for delay time t = 2.4 ns to 3.6 ns for a microwave signal of frequency f = 250 MHz. The microwaves were applied to the end of the 200 μm wide microstrip line shown in Fig. 9.12. The microstip line was terminated by a 50 Ω termination in this case.

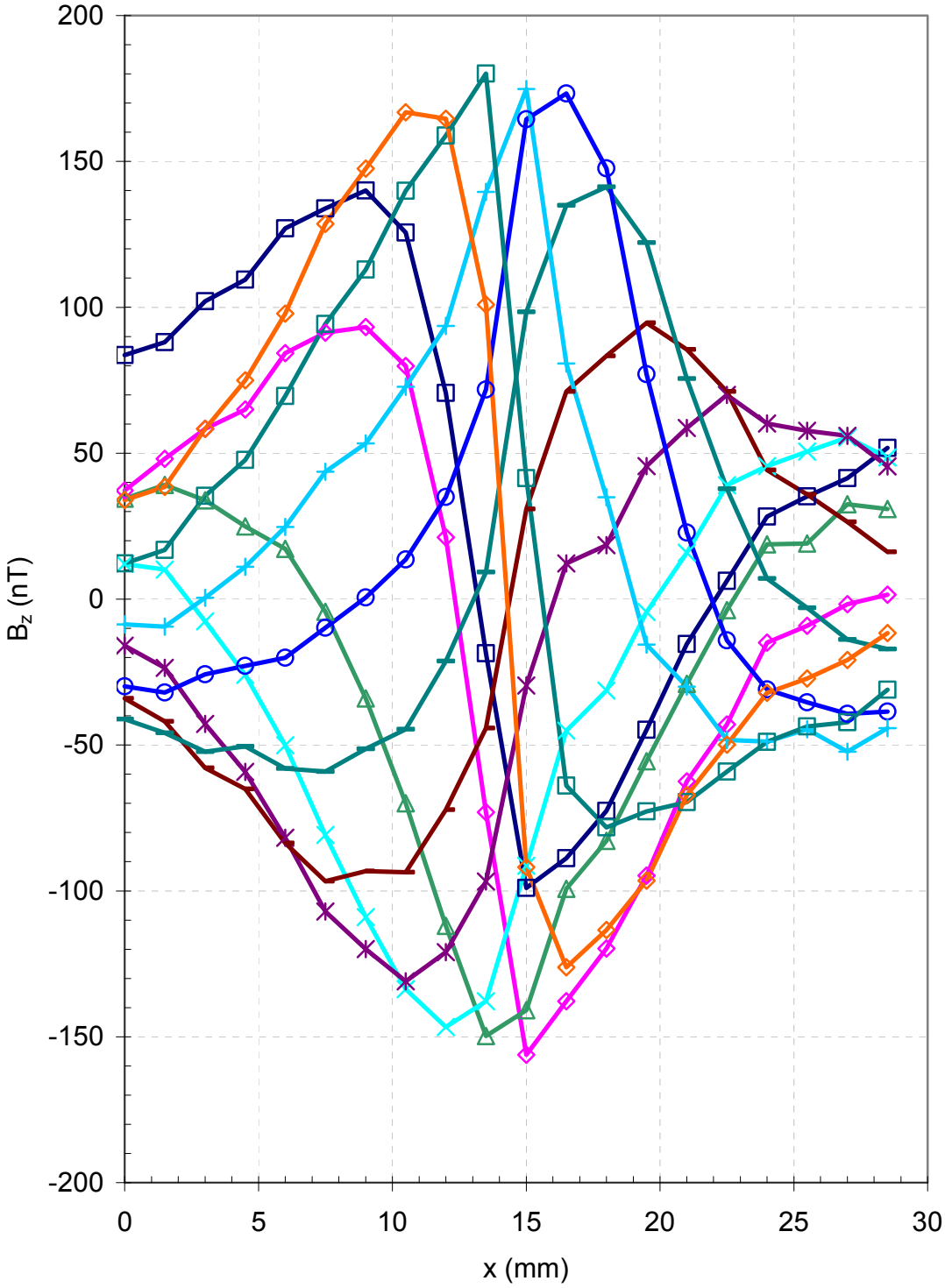

Fig. 9.17. Line scan across the *x*-axis at y = 10.5 mm in the 250 MHz data shown in Fig. 9.16. Plot legend: 0 ns, 0.4 ns, 0.8 ns, 1.2 ns, 1.6 ns, 2.0 ns, 2.4 ns, 2.8 ns, 3.2 ns, 3.6 ns, 4.0 ns.

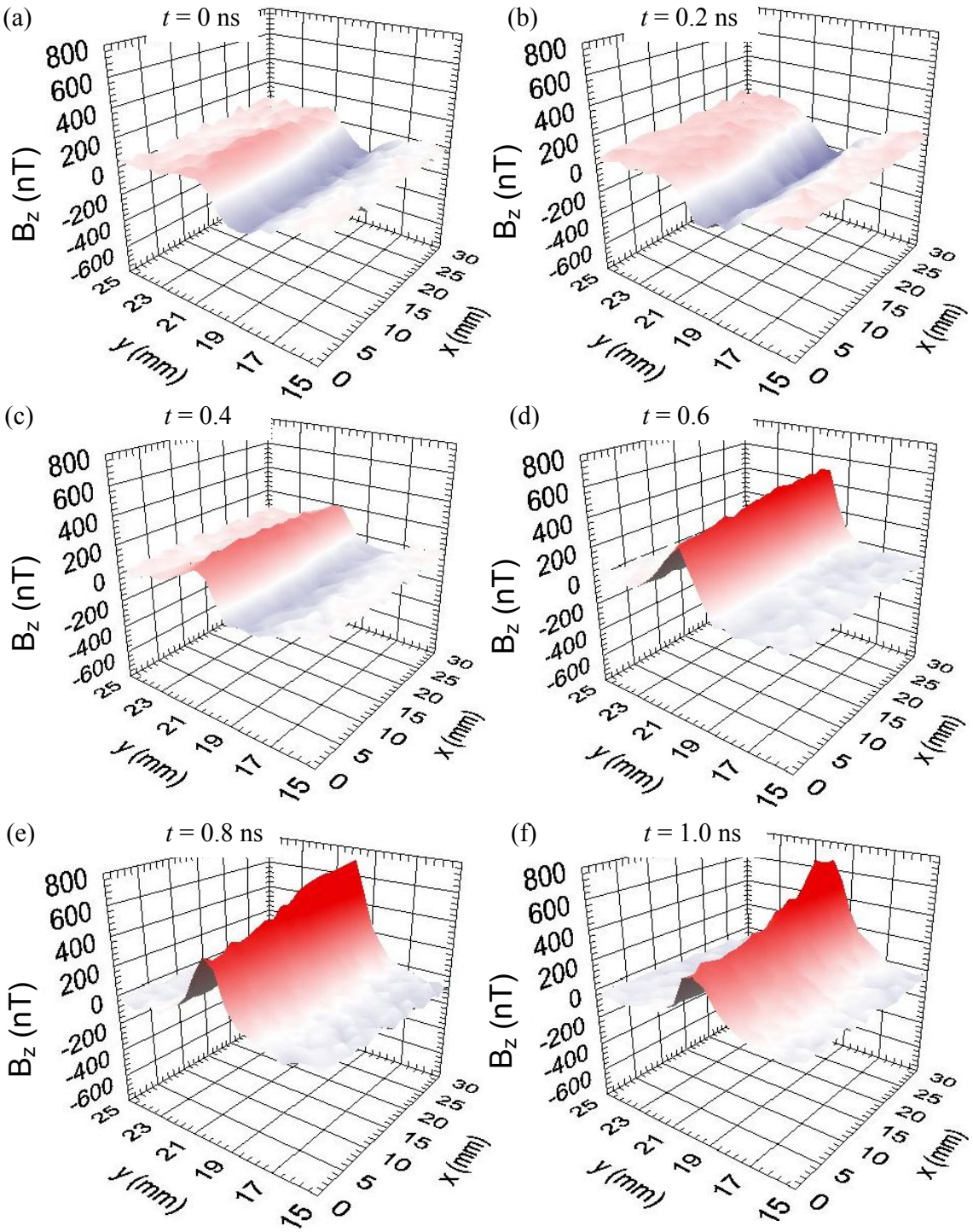

Fig. 9.18. (a-f) Measured $B_z(x,y,t)$ for delay time t = 0 ns to 1.0 ns for a microwave signal of frequency f = 500 MHz applied to the end of the 200 μm wide microstrip line shown in Fig. 9.12. The microstip line was terminated by a 50 Ω termination in this case. The SQUID was 600 μm above the surface.

(g) t = 1.2 ns (h) t = 1.4 ns

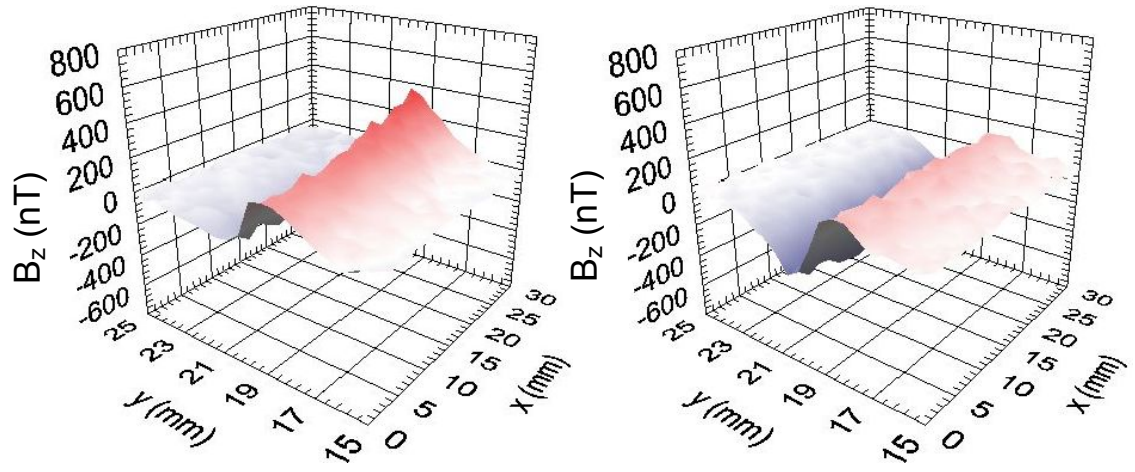

(i) t = 1.6 ns (j) t = 1.8 ns

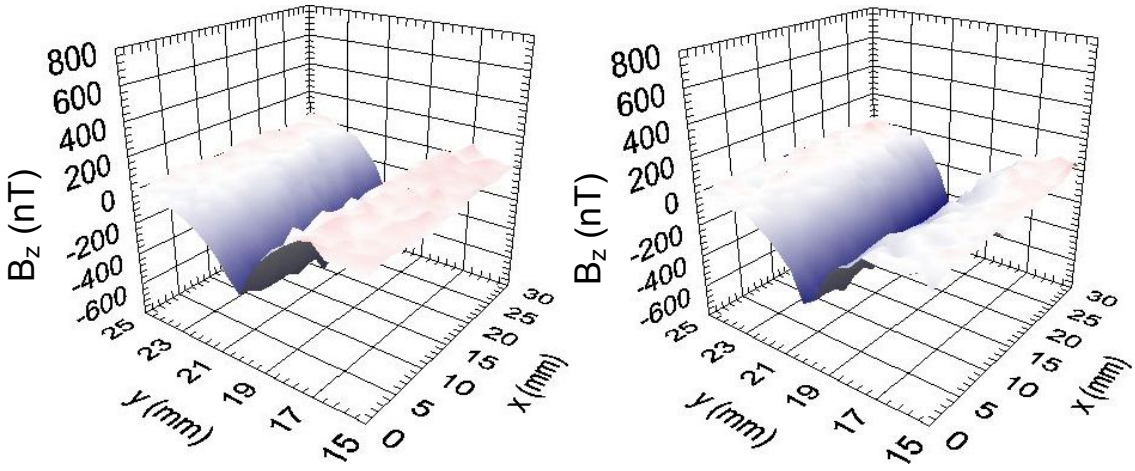

Fig. 9.18. (g-j) Measured $B_z(x,y,t)$ for delay time t = 1.2 ns to 1.8 ns for a microwave signal of frequency f = 500 MHz. The microwaves were applied to the end of the 200 μm wide microstrip line shown in Fig. 9.12. The microstip line was terminated by a 50 Ω termination in this case.

Notice that the orange line (*i.e*. 4 ns line) has much of the shape expected for the line, but the data at 3.2 ns peaks over the wire, much like the B_x-component.

Figure 9.18 shows a similar set of ten magnetic field images of the microstrip line taken with a 334 μA of applied microwave signal at frequency f = 500 MHz for successive delay time increments of 2 ns. I used a 10 ns pulse width along with a 20 ms count time. Again, the area scanned over the microstrip was 31 mm (1.5 mm steps) x 10 mm (0.5 mm steps) for 441 pixels and its acquisition time per pixel was 10 sec. Unlike the previous image at 100 MHz, here we are just starting to see some variation along x (down the line) as expected for a travelling wave.

Figure 9.19 shows the corresponding individual line scans taken across the x-axis at y = 10.5 mm in Fig. 9.16 for the 500 MHz data. Again for Figs. 9.18 and 9.19, it looks as if the z-component and the y-component (transverse component) of magnetic field are being detected.

Figure 9.20 shows images of $B_z(x,y,t)$ for an applied microwave signal of frequency f = 1.0 GHz for successive time increments of 100 ps. In this case the line was terminated with a 50 Ω load. For these images I used a power of -21 dBm (I = 148 μA), a 400 ps pulse width and a 20 ms count time. The area scanned was 51 mm (1.0 mm steps) x 6 mm (0.25 mm steps) for a total of 1275 pixels. The acquisition time per pixel was 12 sec resulting in a total time-elapsed image acquisition time of 4.25 hours or approximately 0.43 hours per frame. Red indicates that the magnetic field is pointing up from the microstrip line, blue indicates the field is pointing below the strip line, and white indicates that the field is approximately zero. The SQUID-microstrip separation is about

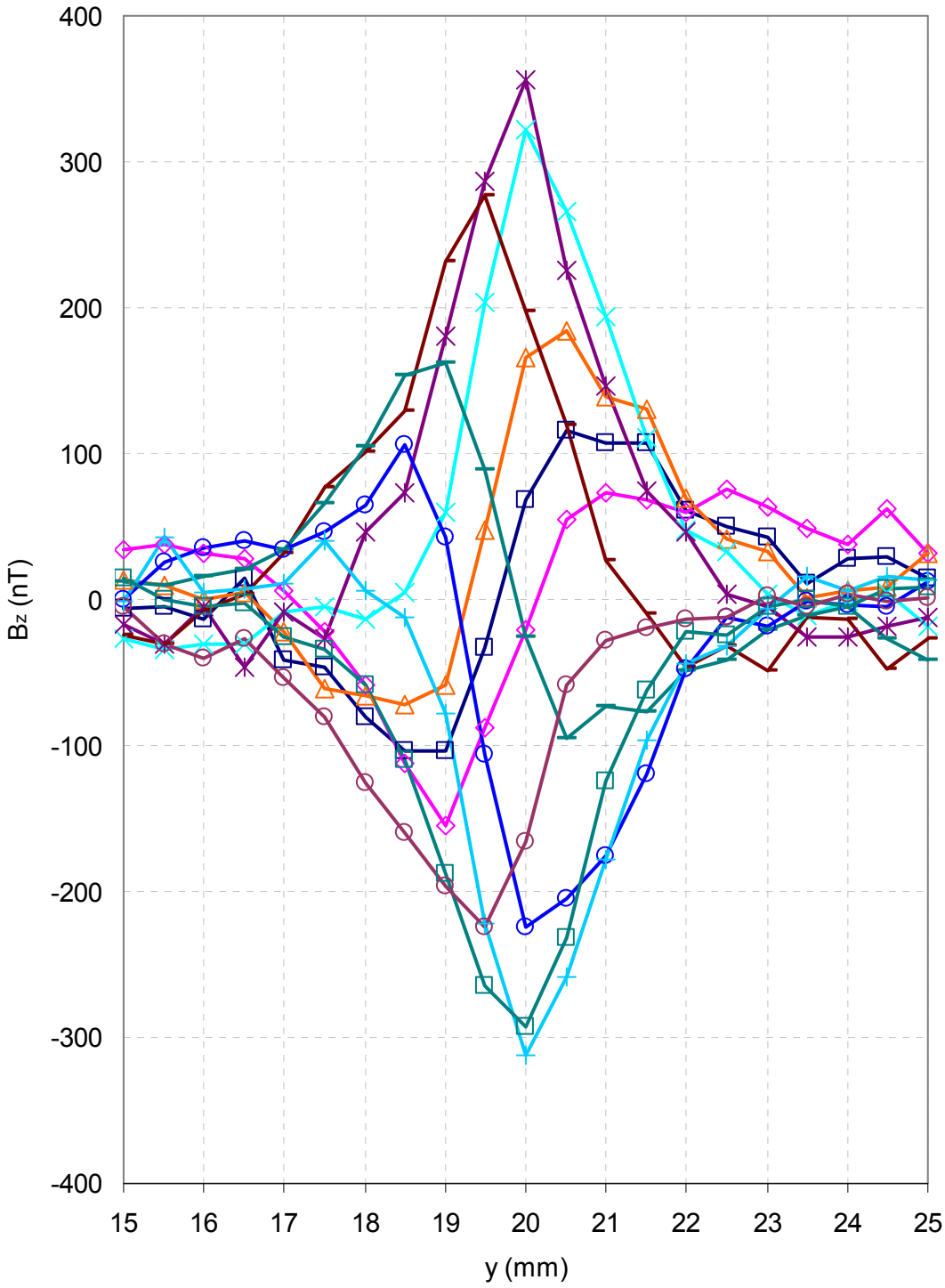

Fig. 9.19. Line scan across the *x*-axis at y = 10.5 mm for the 500 MHz data shown in Fig. 9.18. Plot legend: 0 ns, 0.2 ns, 0.4 ns, 0.6 ns, 0.8 ns, 1.0 ns, 1.2 ns, 1.4 ns, 1.6 ns, 1.8 ns, 2.0 ns.

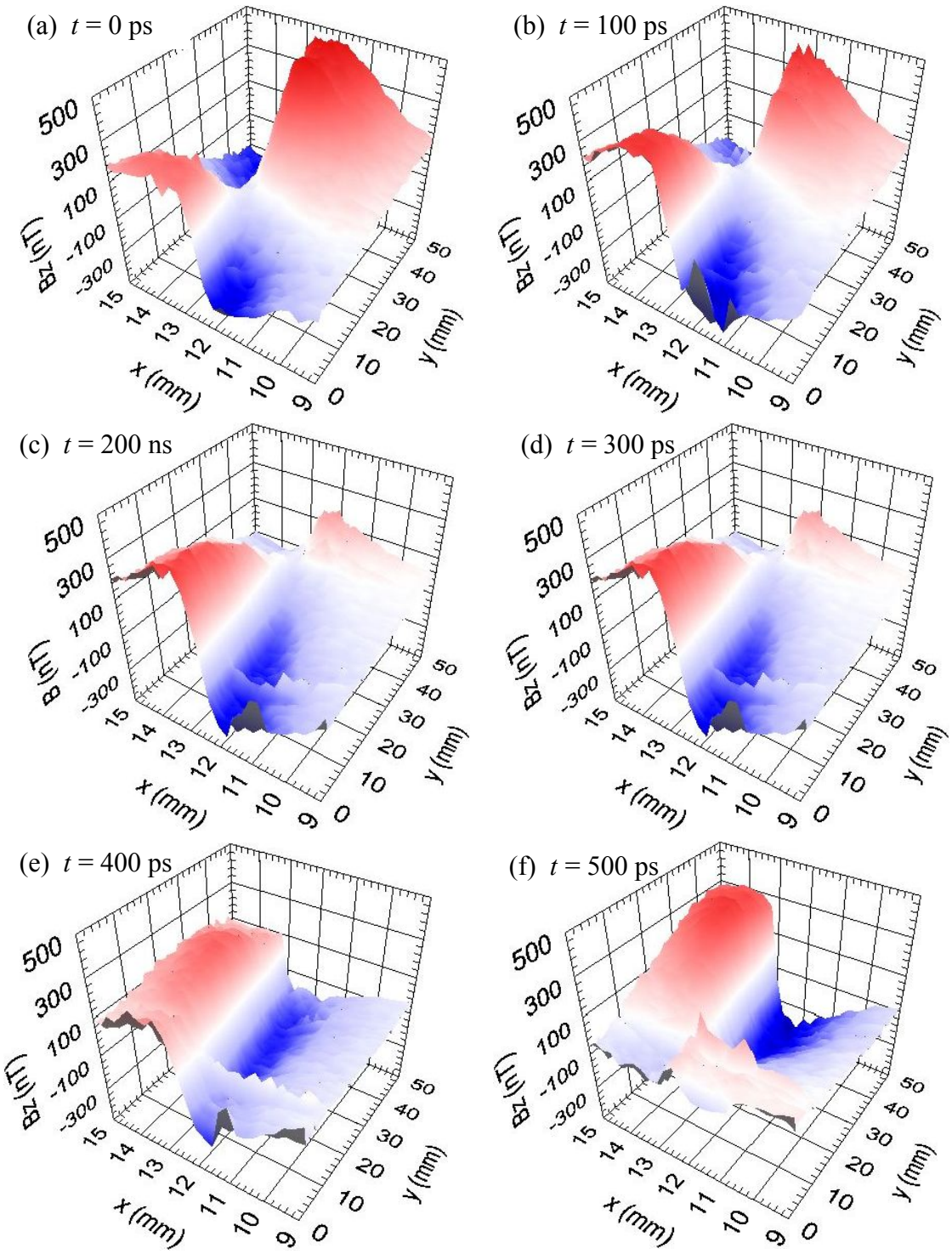

Fig. 9.20. (a-f) Measured $B_z(x,y,t)$ for delay time t = 100 ps to 600 ps for a microwave signal of -21 dBm and frequency f = 1 GHz. Signal applied to the end of the 200 μm wide at $x \approx 12$ mm. The microstip line was terminated by a 50 Ω termination and the SQUID was 500 μm above the surface of the microstrip line. White corresponds to zero field while red and blue regions correspond to ±500 nT. Note y-axis scale compressed compared to x-axis.

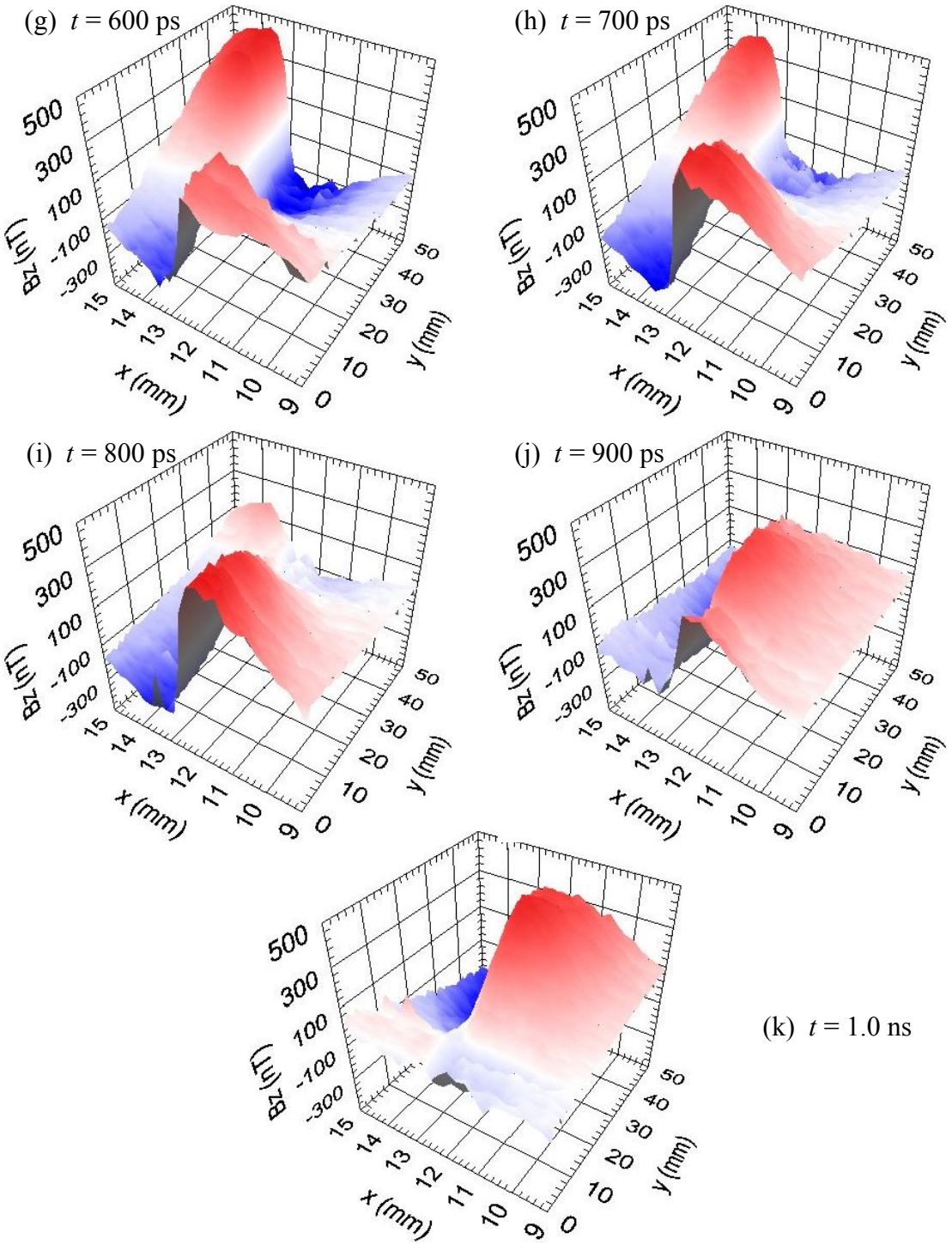

Fig. 9.20. (g-k) Measured $B_z(x,y,t)$ for delay time t = 700 ps to 1.0 ns for a microwave signal of frequency f = 1 GHz applied to the end of the 200 μm wide microstrip line shown in Fig. 9.4. The microstip line was terminated by a 50 Ω termination and the SQUID was 500 μm above the surface of the microstrip line. White corresponds to zero field while red and blue regions correspond to ±500 nT. Note y-axis scale compressed compared to x-axis.

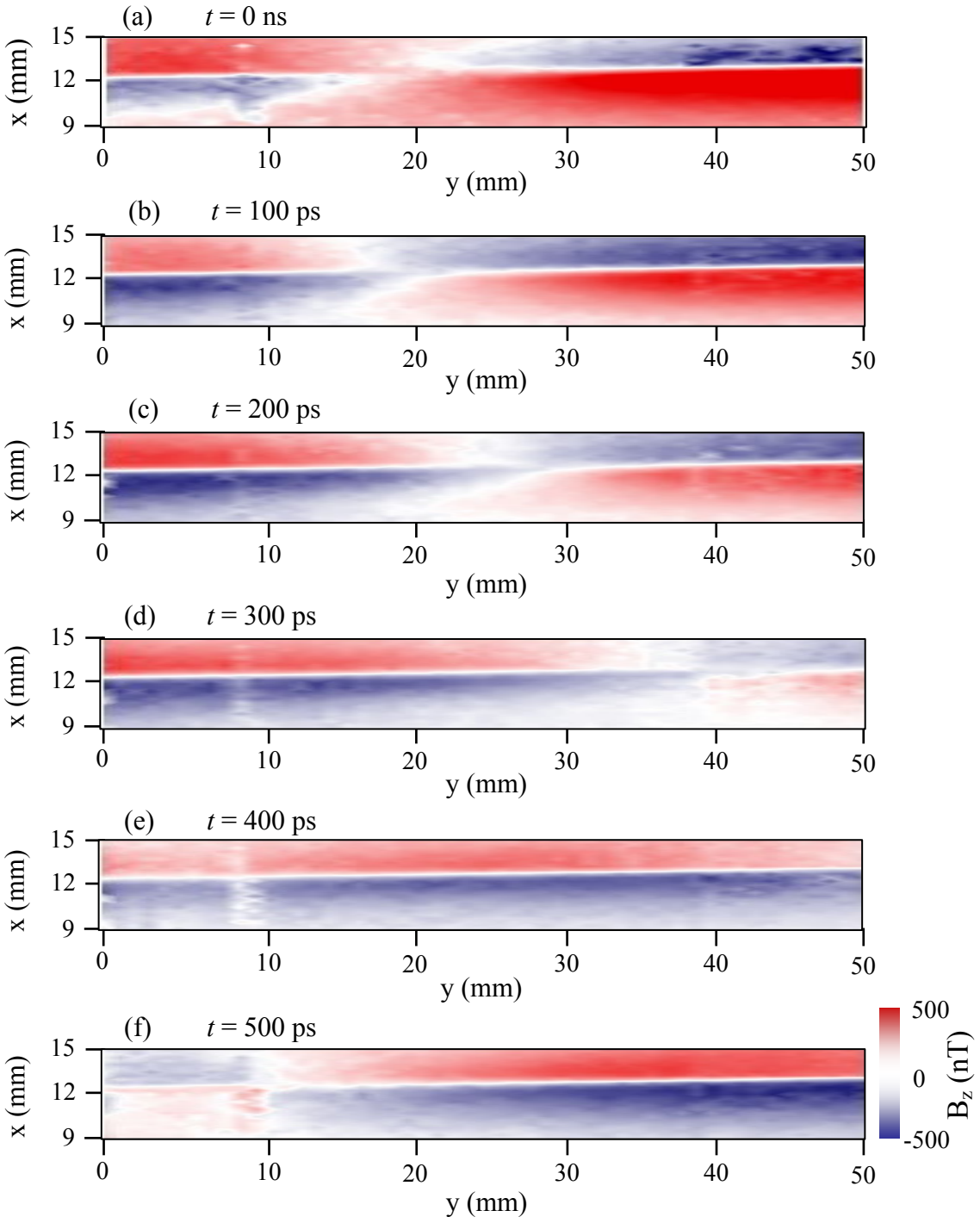

Fig. 9.21. (a-f) Top down view of magnetic field $B_z(x,y,t)$ data shown in Fig. 9.20. Frequency $f = 1$ GHz. Signal applied from left side at $x \approx 12$ mm and line terminated with 50 Ω load. The SQUID was 500 μm above the surface of the microstrip line. White corresponds to zero field while red and blue regions correspond to ±500 nT. Note x and y axes are to the same scale.

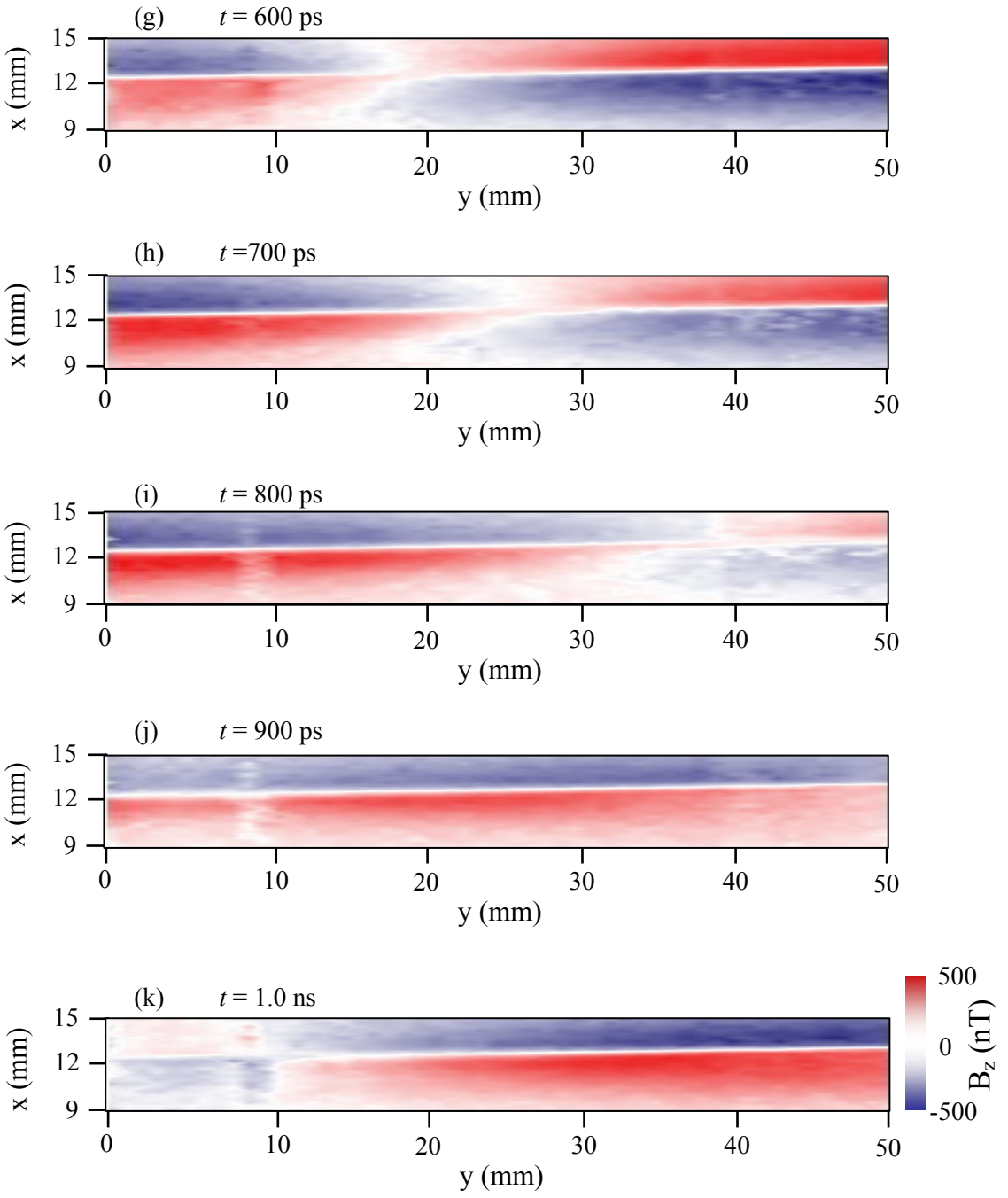

Fig. 9.21. (g-k) Top down view of magnetic field $B_z(x,y,t)$ data shown in Fig. 9.20. Frequency $f = 1$ GHz. Signal applied from left side at $x \approx 12$ mm and line terminated with 50 Ω load. The SQUID was 500 μm above the surface of the microstrip line. White corresponds to zero field while red and blue regions correspond to ±500 nT. Note x and y axes are to the same scale.

500 μm. The microstrip was parallel to the *y*-axis and centered at x = 12 mm. The maximum and minimum oscillate by ±500 nT about zero field.

Figure 9.21(a-k) shows the same data as in Fig. 9.20(a-k) except presented in top-down view. From this view, we can clearly see a wave propagates from the left side of the microstrip line towards the right. Red indicates that the magnetic field is pointing up out of the page whereas blue indicates that the field is pointing into the page. From Fig. 9.21(a-f) a half-wavelength travels about 62 mm in 500 ps resulting in a speed of $c' \simeq 1.3\times10^{8} m/s$, a wavelength of $\lambda' = 130\,mm$, and a frequency of $f' \simeq 1 GHz$. Assuming a dielectric constant of ε_r = 4.4 for the microstrip line I expect a signal speed of $c' = 1.43\times10^{8} m/s$ and a wavelength of $\lambda' = 143\,mm$ for a signal frequency of f = 1.0 GHz.

Figure 9.22(a-t) shows images of $B_z(x,y,t)$ for an applied microwave signal of frequency f = 1.5 GHz for successive time increments of 33 ps (note that these 3D plots are compressed along the *x*-axis). For these images I used a power of -27 dBm (I = 200 μA), a 400 ps pulse width, a 20 ms count time and the line was terminated with 139 Ω (matched). The area scanned was 51 mm (0.5 mm steps) × 8 mm (0.2 mm steps) for a total of 4141 pixels. The acquisition time per pixel was 12 sec resulting in a total time-elapsed image acquisition time of 11.5 hours or approximately 1.2 hours per frame. The height above the microstrip line was 250 μm. These images show much more apparent noise or "rippling," indicating the signal to noise ratio has degraded under application of the 1.5 GHz field.

Figure 9.23(a-t) shows the same magnetic field data as shown in Fig. 9.22(a-t) except presented in top-down view. From this view, we again see a wave that propagates from the left side of the microstrip line towards the right. Although "ripples" are clearly

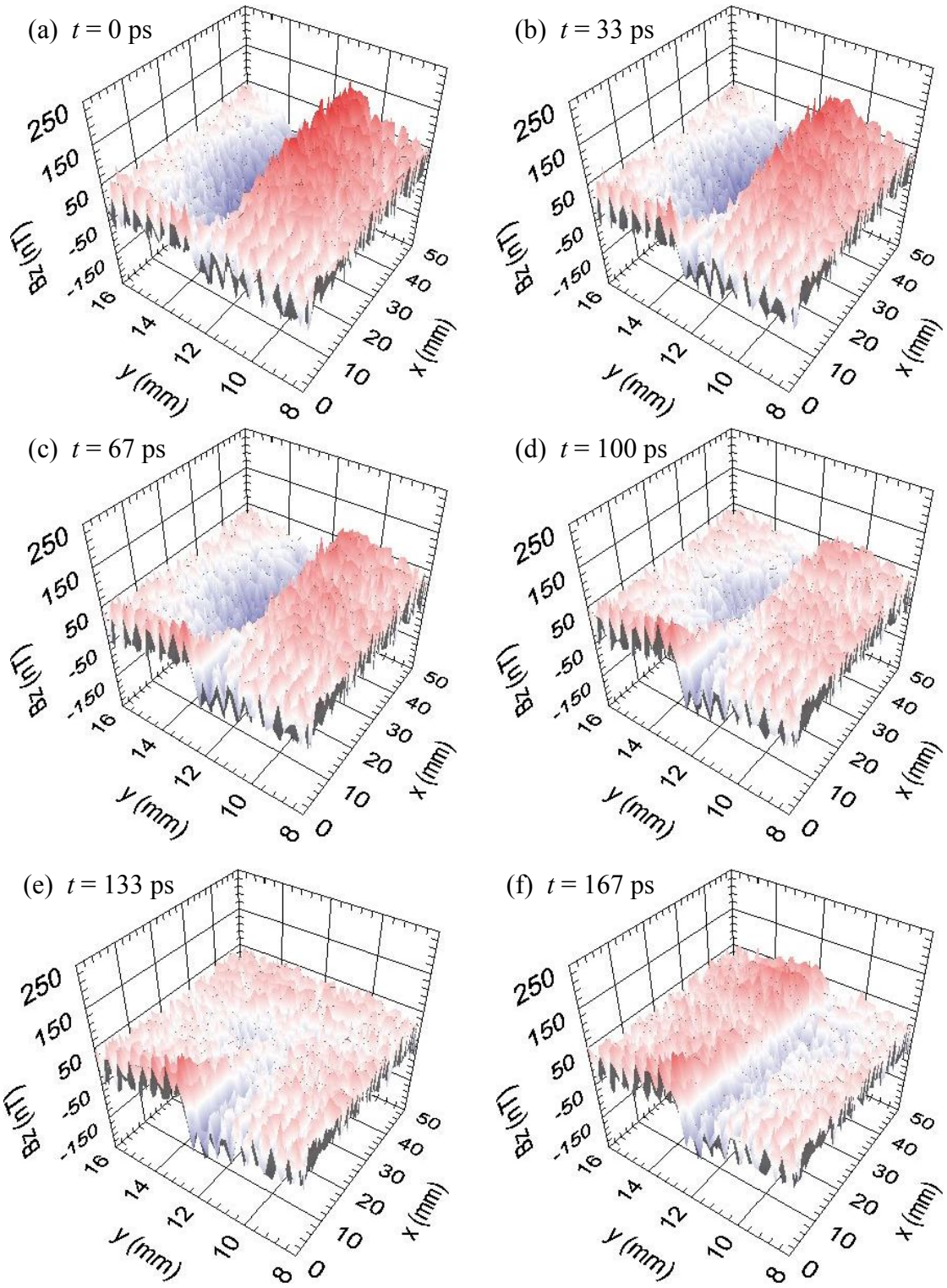

Fig. 9.22. (a-f) Measured $B_z(x,y,t)$ for delay times of t = 0 ps to 167 ps for a microwave signal of frequency f = 1.5 GHz applied to the end of the 200 μm wide microstrip line shown in Fig. 9.9. The microstip line was terminated by a 139 Ω termination in this case. The SQUID height above microstrip line was about 250 μm.

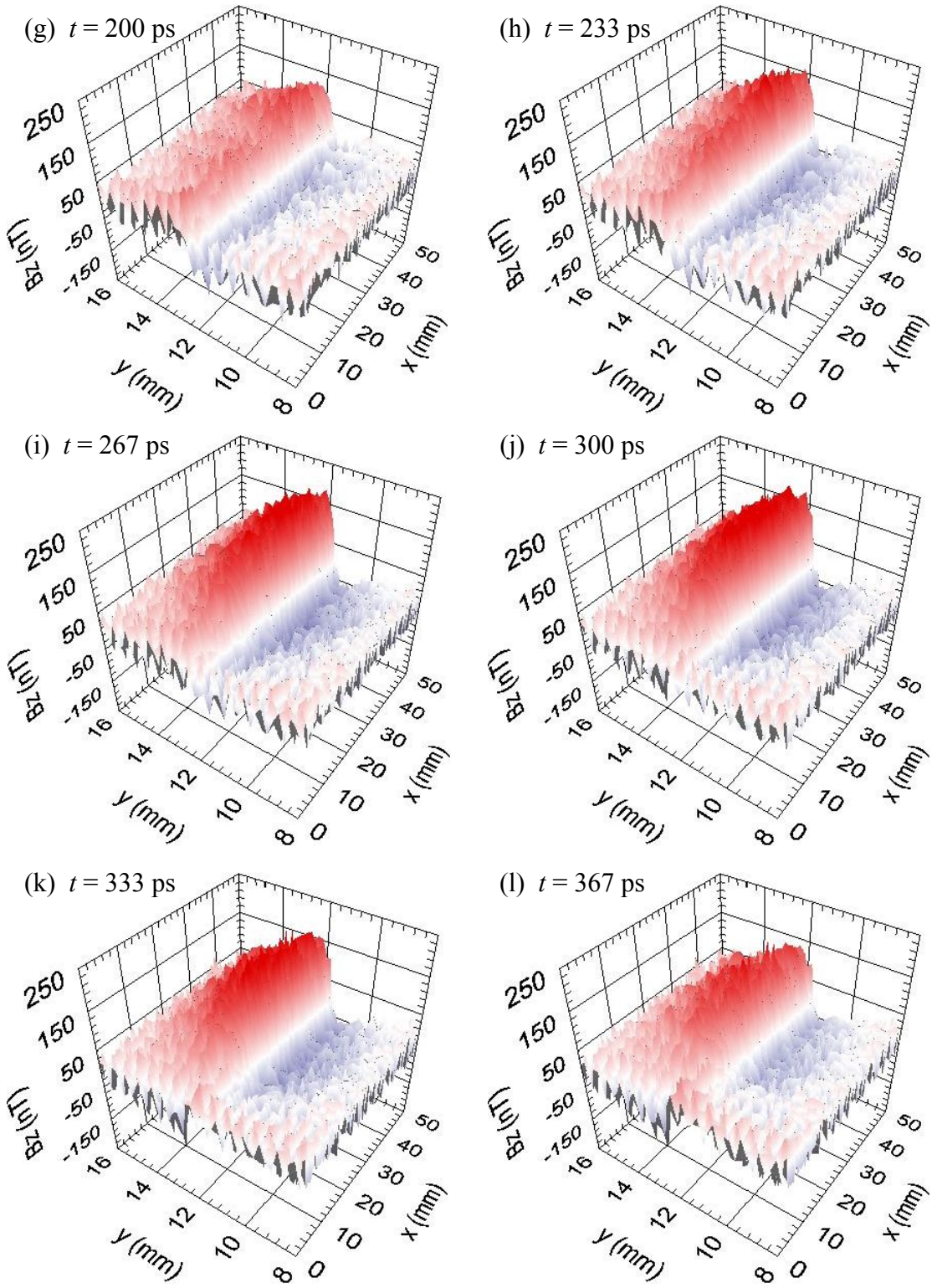

Fig. 9.22. (g-l) Measured $B_z(x,y,t)$ for delay times of t = 200 ps to 367 ps for a microwave signal of frequency f = 1.5 GHz applied to the end of the 200 μm wide microstrip line shown in Fig. 9.4. The microstip line was terminated by a 139 Ω termination in this case. The SQUID height above microstrip line was about 250 μm.

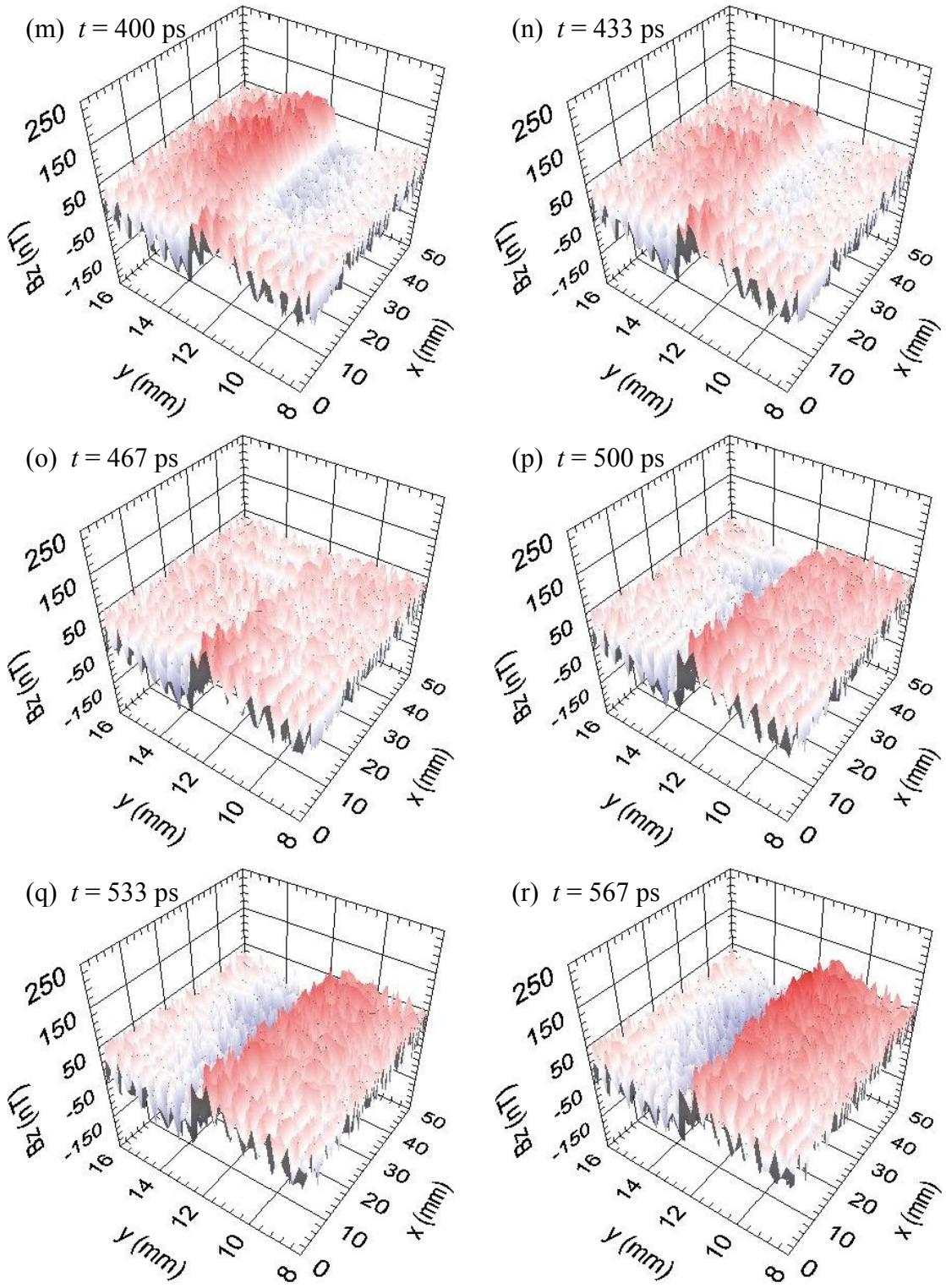

Fig. 9.22. (m-r) Measured $B_z(x,y,t)$ for delay times of t = 400 ps to 567 ps for a microwave signal of frequency f = 1.5 GHz applied to the end of the 200 μm wide microstrip line shown in Fig. 9.4. The microstip line was terminated by a 139 Ω termination in this case. The SQUID height above microstrip line was about 250 μm.

(s) t = 600 ps (t) t = 633 ps

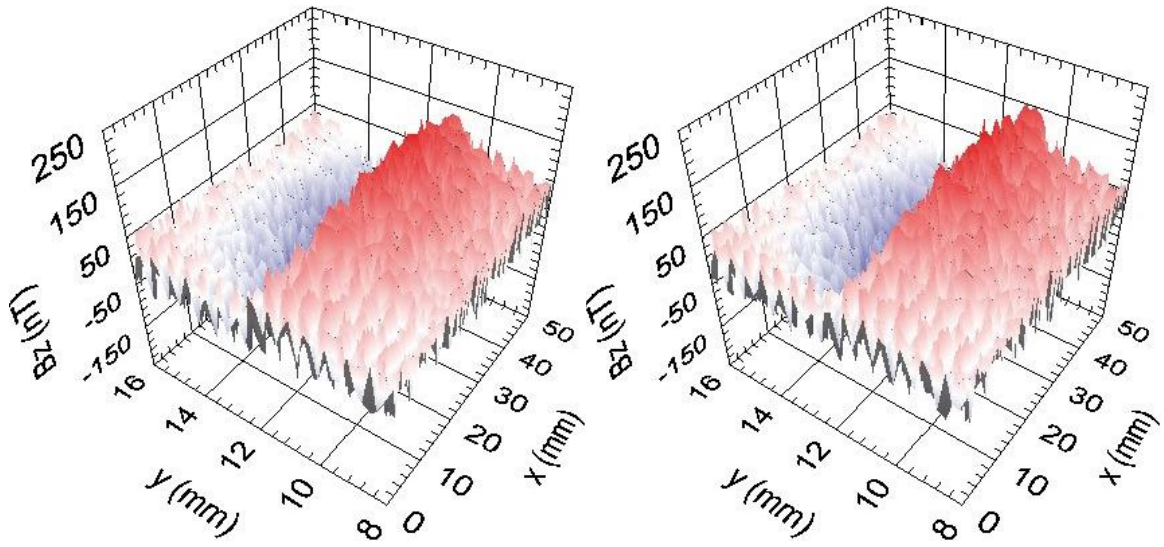

Fig. 9.22. (s-t) Measured $B_z(x,y,t)$ for delay times of t = 600 ps to 667 ps for a microwave signal of frequency f = 1.5 GHz applied to the end of the 200 μm wide microstrip line shown in Fig. 9.4. The microstip line was terminated by a 139 Ω termination in this case. The SQUID height above microstrip line was about 250 μm. Note x-axis scale compressed compared to y-axis.

seen in these images, never the less the wave shows relatively little distortion. Red indicates that the magnetic field is pointing up out of the page whereas blue indicates that the field is pointing into the page. The maximum and minimum oscillate (±200 nT) about zero field. From Fig. 9.23(a-l) a half-wavelength travels about 48 mm in 367 ps resulting in a speed of $c' \simeq 1.3\times10^8$ m/s, a wavelength of $\lambda' = 96$ mm, and a frequency of $f' = 1.4$ GHz. As I noted above, for a dielectric constant of ε_r = 4.4 for the microstrip line one expects $c' \simeq 1.4\times10^8$ m/s and a wavelength of $\lambda' = 95.3$ mm for a signal frequency of f = 1.5 GHz.

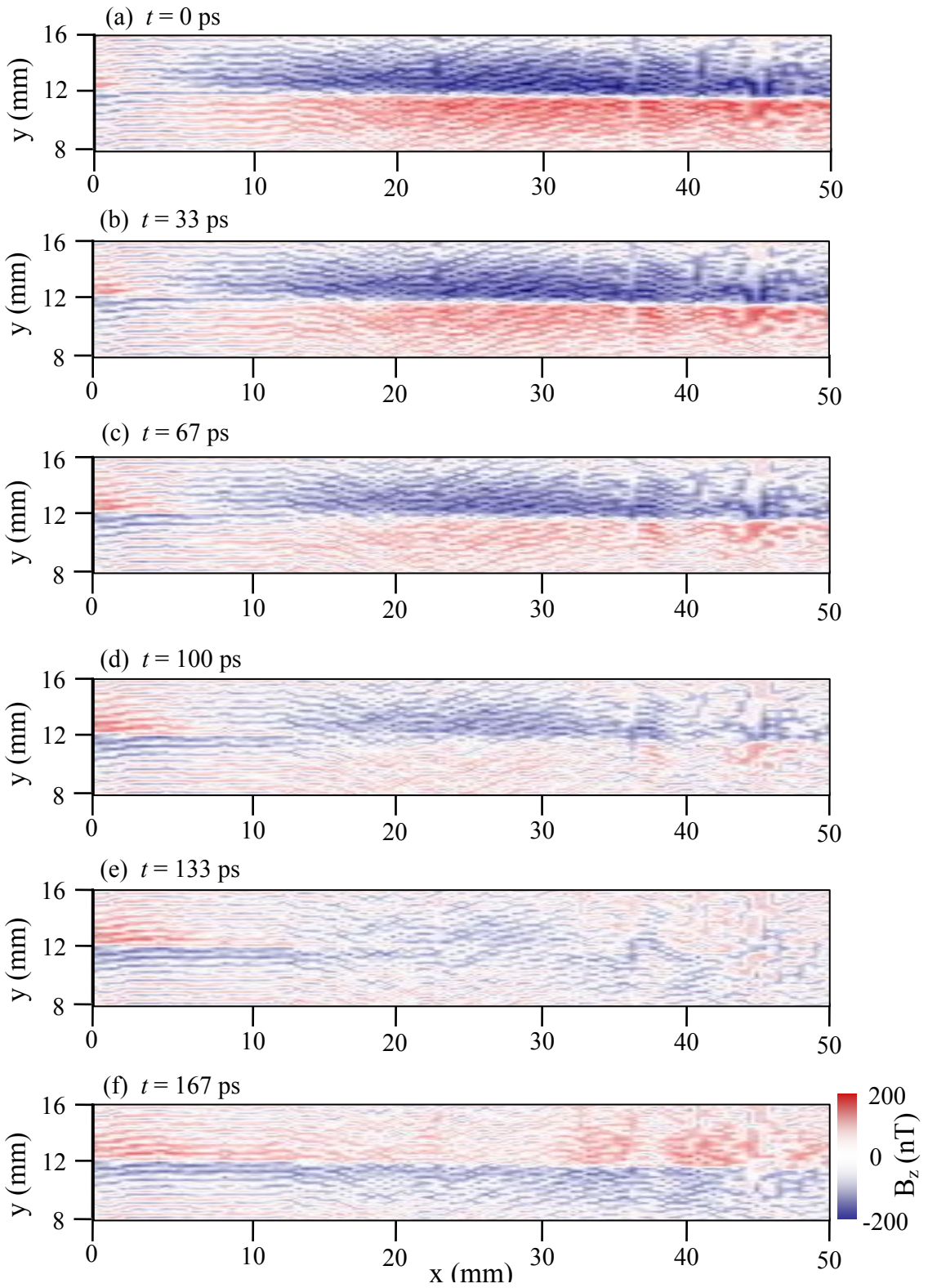

Fig. 9.23. (a-f) Top down view of magnetic field $B_z(x,y,t)$ above the microstrip line for f = 1.5 GHz microwaves. The SQUID height above the microstrip line was about 250 μm.

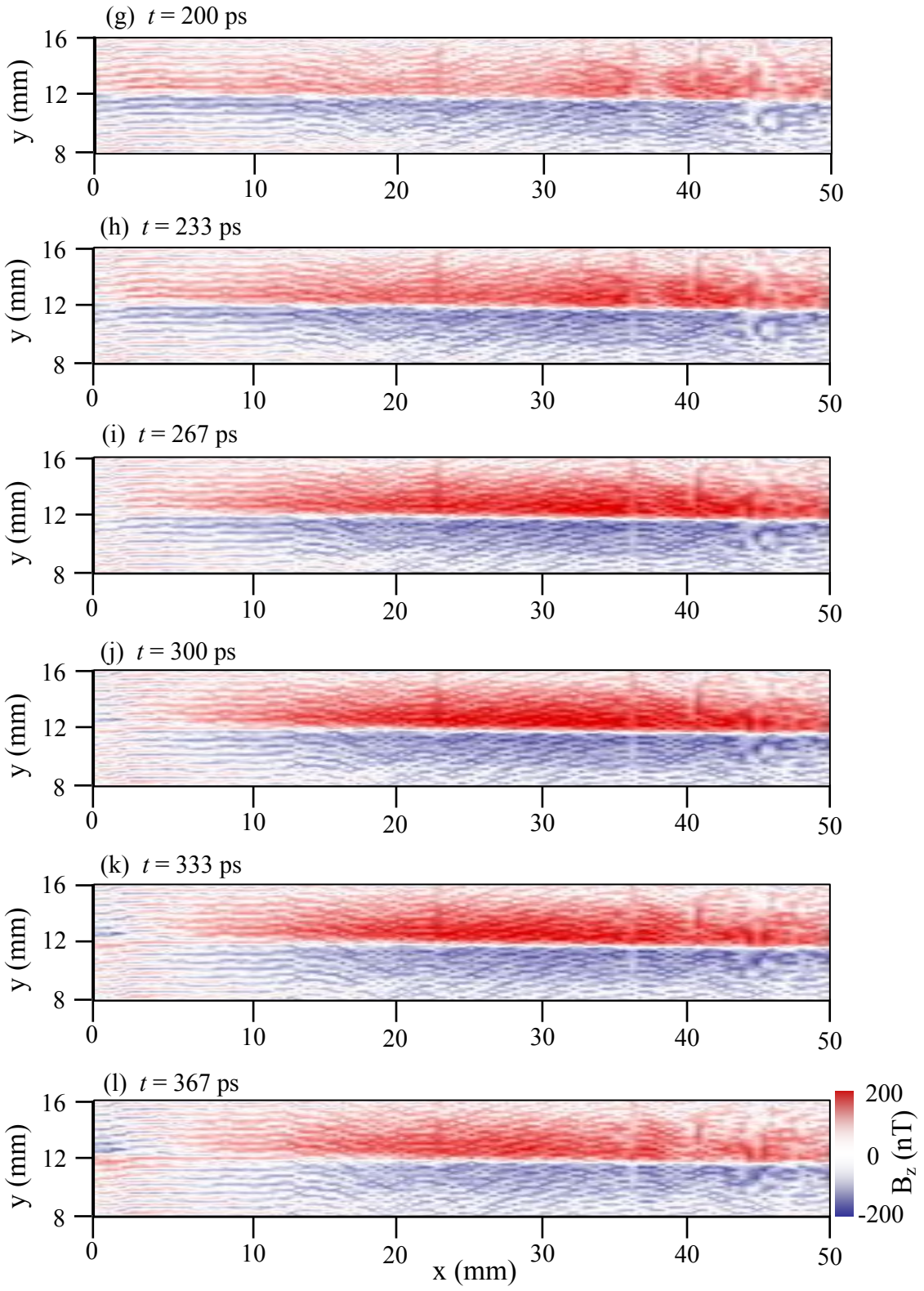

Fig. 9.23. (g-l) Top down view of magnetic field $B_z(x,y,t)$ microstrip line for f = 1.5 GHz microwaves. The SQUID height above the microstrip line was about 250 μm.

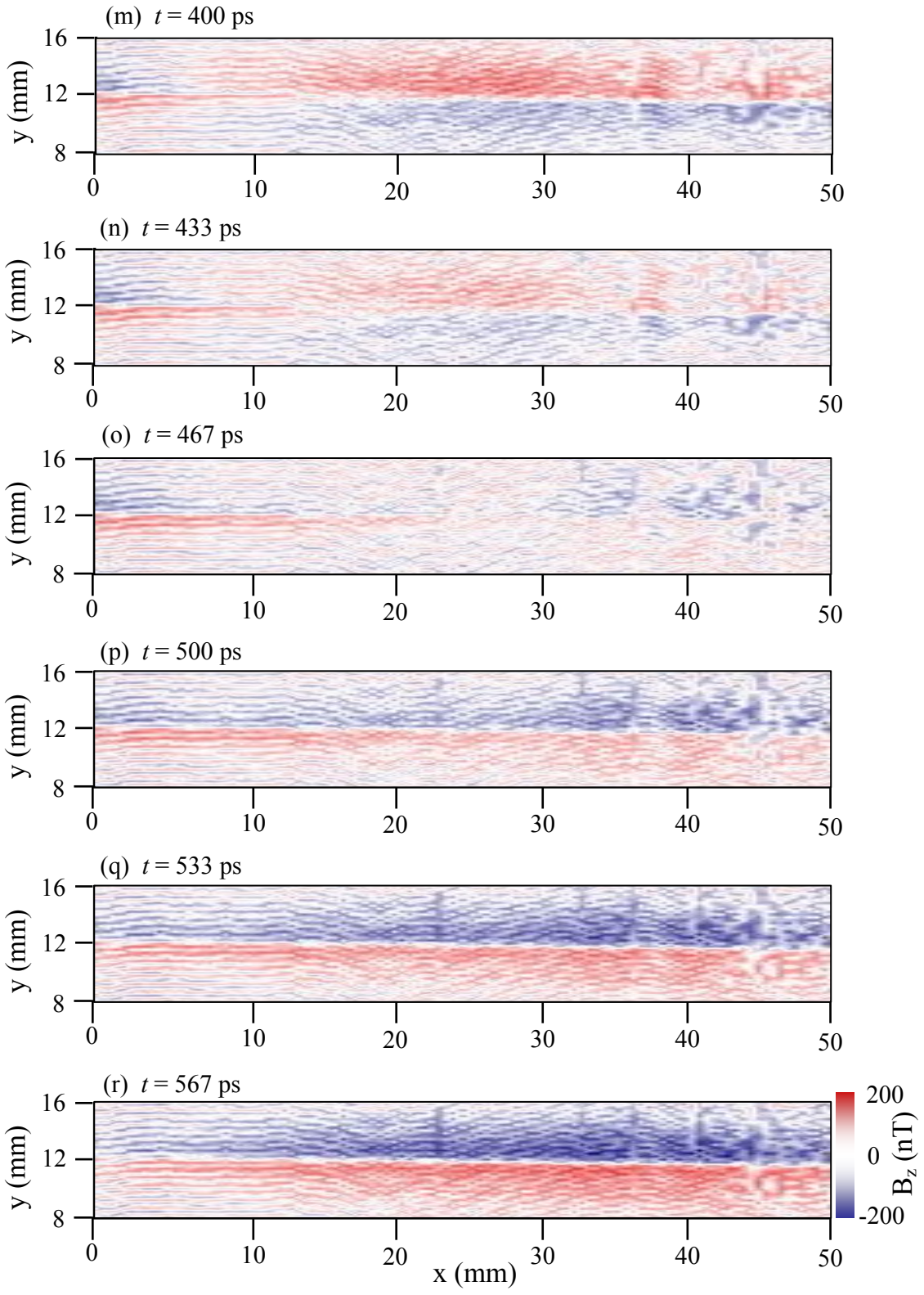

Fig. 9.23. (m-r) Top down view of magnetic field $B_z(x,y,t)$ microstrip line. Frequency f = 1.5 GHz. The SQUID height above microstrip line was about 250 μm.

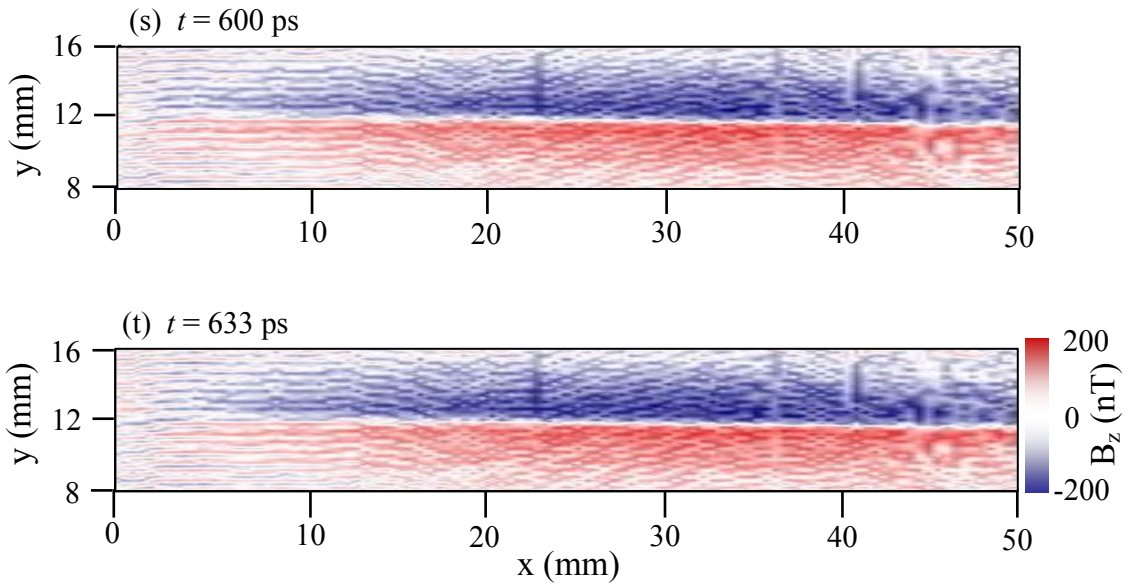

Fig. 9.23. (s-t) Top down view of magnetic field $B_z(x,y,t)$ data shown in Fig. 9.22 for f = 1.5 GHz. The SQUID height above the microstrip line was about 250 μm. Red indicates magnetic field pointing up while blue indicates field pointing down and white is zero-field. Note x and y axes are to the same scale.

Figure 9.24(a-j) shows a corresponding set of images of $B_z(x,y,t)$ for an applied -21 dBm microwave signal of f = 2 GHz at successive time increments of 50 ps. Here I used a 400 ps pulse width and a 20 ms count time and the line was terminated with a 139 Ω (matched) load. The area scanned was 51 mm (0.5 mm steps) x 8 mm (0.2 mm steps) for 4141 pixels and acquisition time per pixel was 10 sec. The SQUID was 300 μm above the surface of the microstrip line. From the above images I estimate the wave travels about 48 mm in 367 ps, again yielding $c' \simeq 1.3\times10^8$ m/s.

Figure 9.25(a-j) shows the same magnetic field data as shown in Fig. 9.24(a-j) except presented in top-down view. The wave propagates from the left side of the microstrip line towards the right. Red indicates that the magnetic field

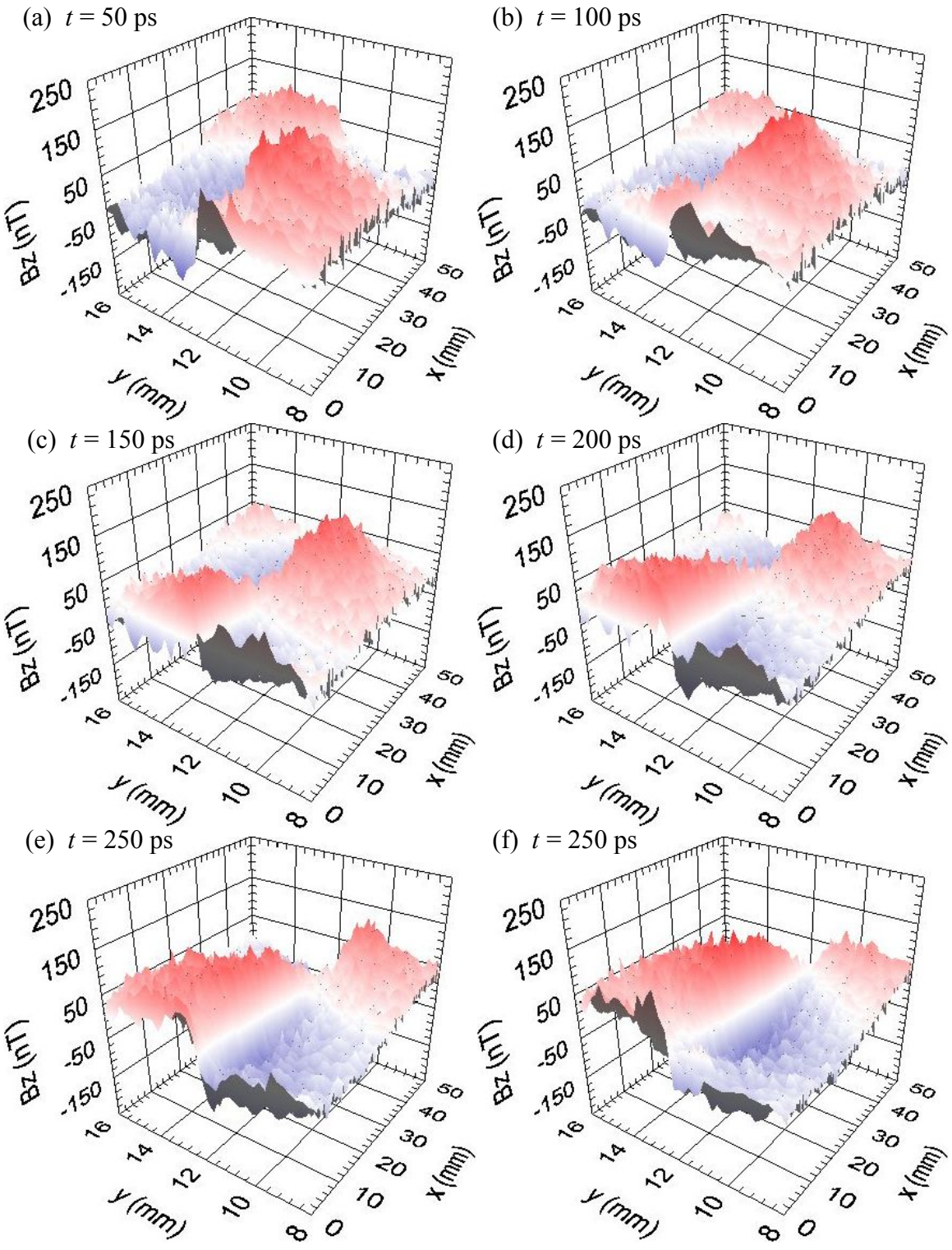

Fig. 9.24. (a-f) Measured $B_z(x,y,t)$ for 50 ps timesteps when microwaves at f = 2 GHz were applied to the 200 μm wide microstrip line that was terminated by 139 Ω. For delay time t = 50 ps to 300 ps. The SQUID was 300 μm above the surface of the microstrip line. Note x-axis scale compressed compared to y-axis.

(g) t = 350 ps

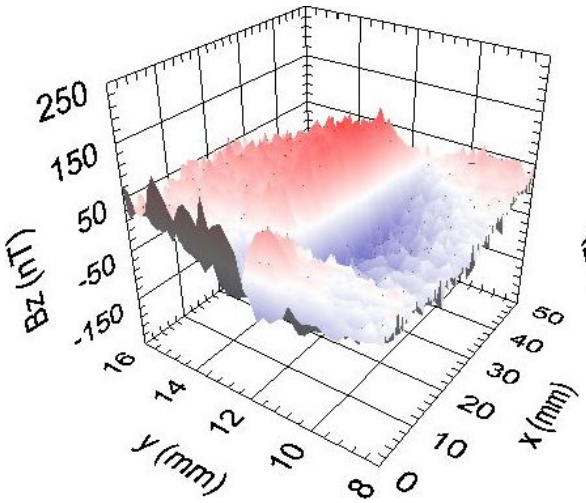

(h) t = 400 ps

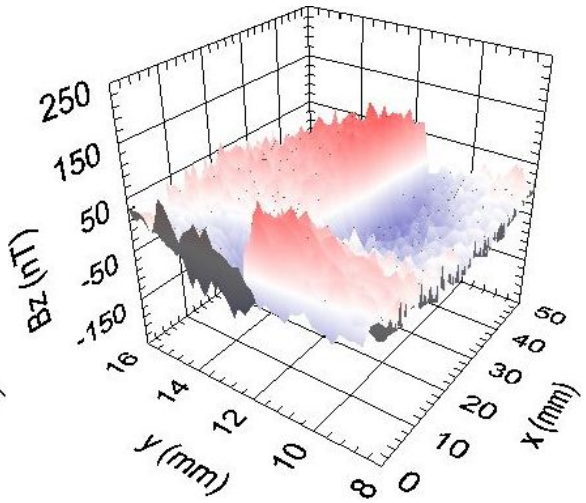

(i) t = 450 ps

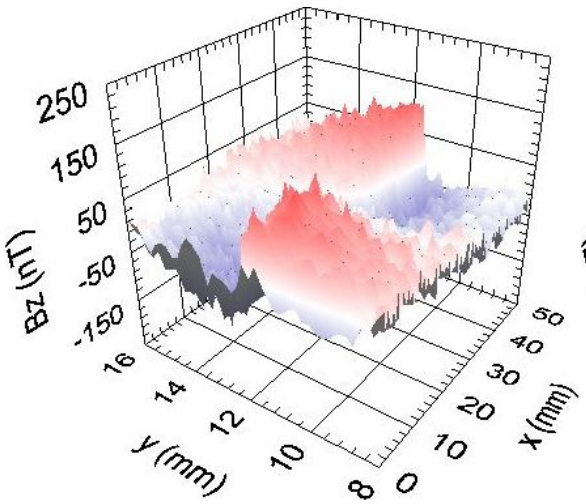

(j) t = 500 ps

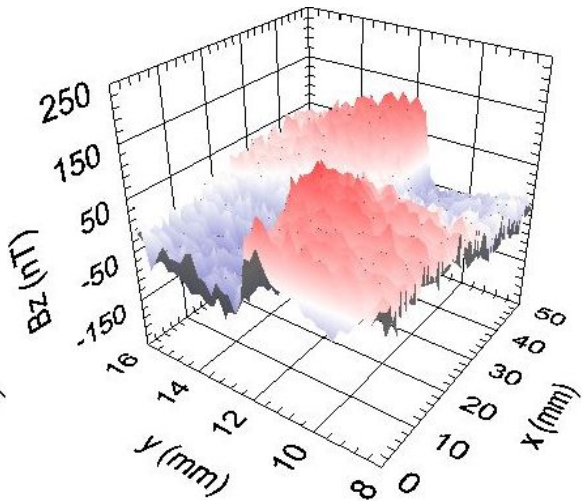

Fig. 9.24. (g-j) Measured $B_z(x,y,t)$ when microwaves at f = 2 GHz were applied to the 200 μm wide microstrip line that was terminated by 139 Ω. (g-j) Successive images are for delay times of t = 350 ps to 500 ps. Note x-axis scale compressed compared to y-axis.

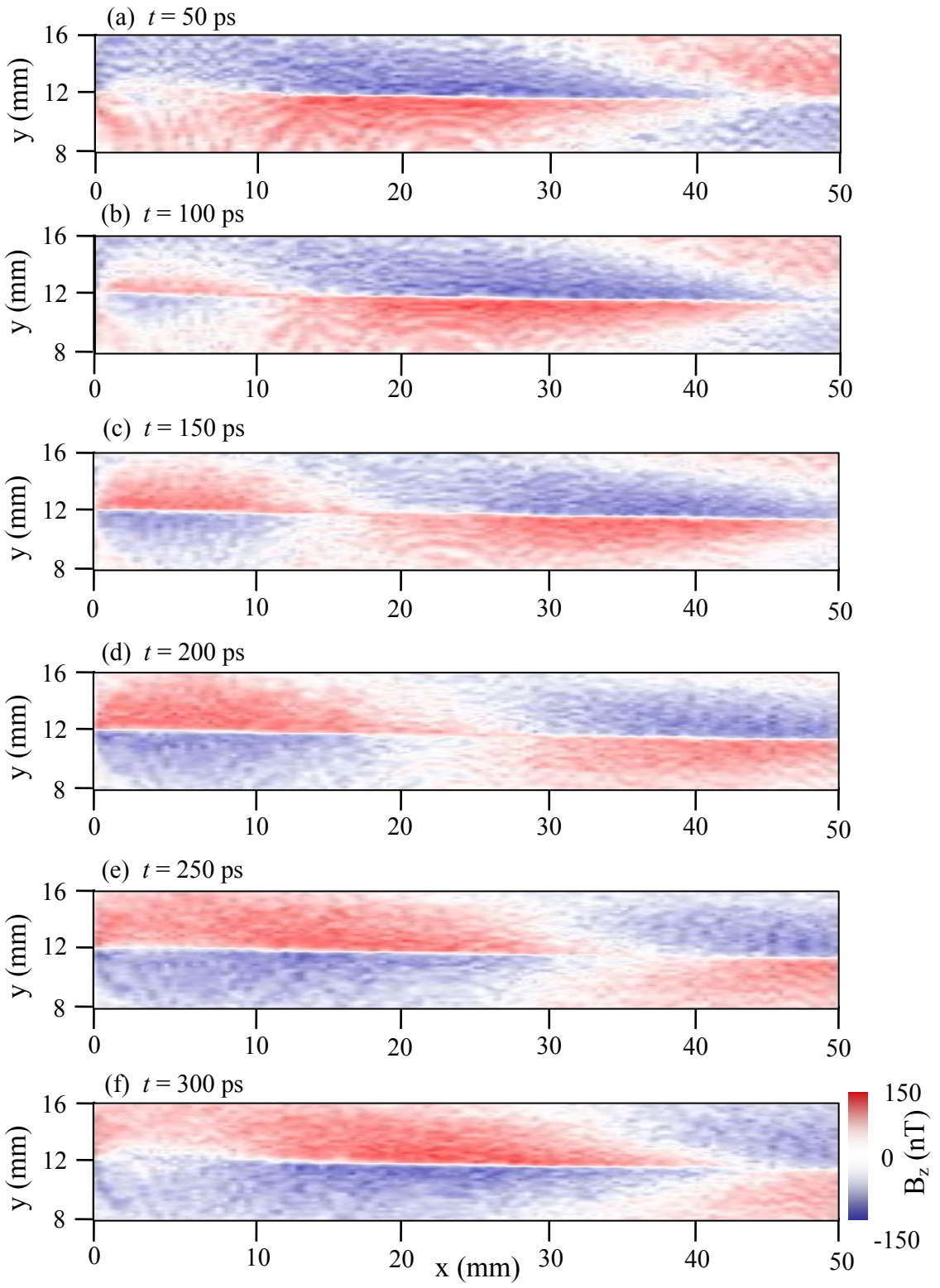

Fig. 9.25. (a-f) Top down view of magnetic field $B_z(x,y,t)$ on microstrip line with 2 GHz microwave current applied. The SQUID was 300 μm above microstrip line. Red indicates field pointing up and blue indicates field pointing down.

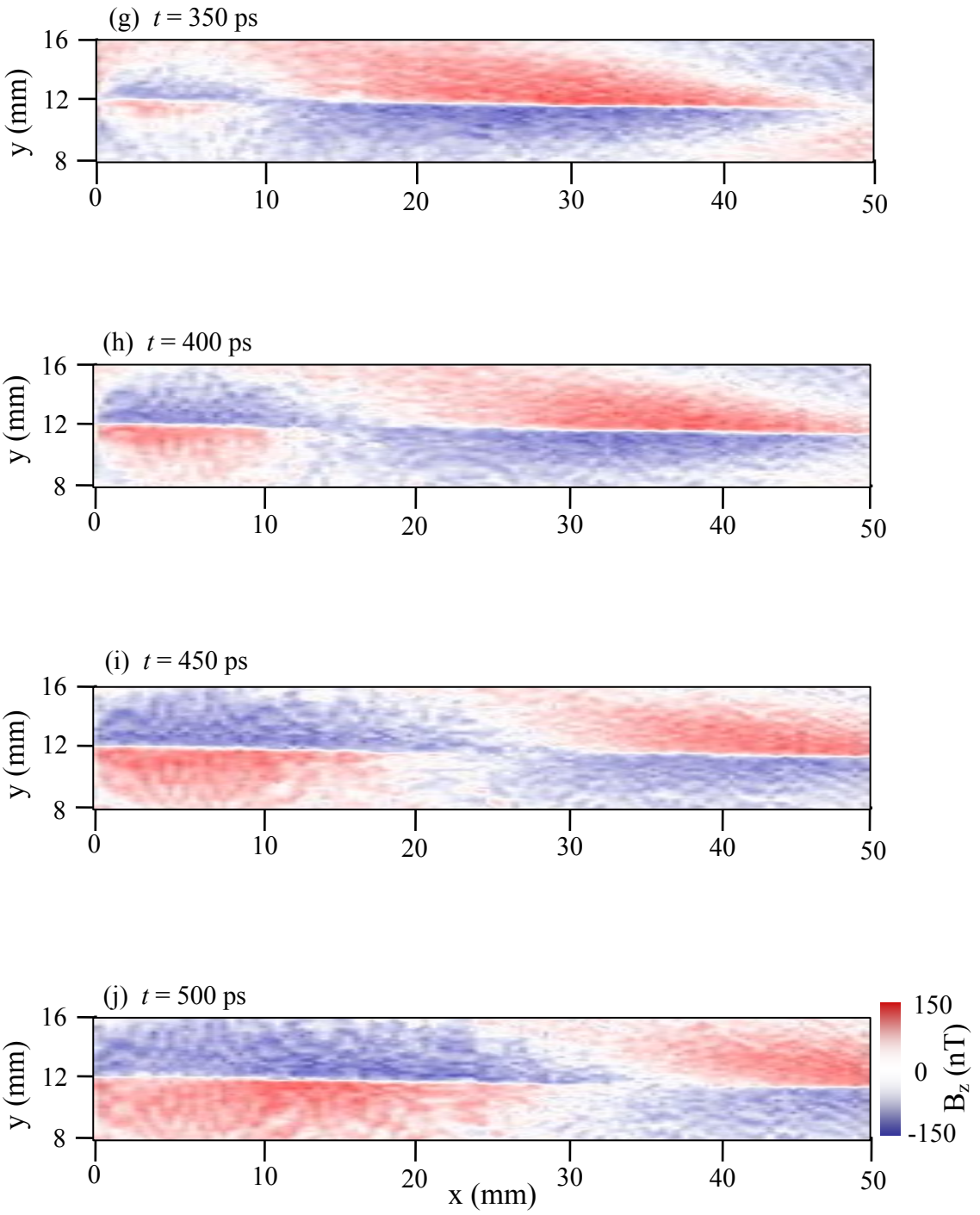

Fig. 9.25. (g-j) Top down view of magnetic field $B_z(x,y,t)$ microstrip line for 2 GHz applied microwave. The SQUID was 300 μm above the surface of the microstrip line. Red indicates field pointing up while blue indicates field pointing down. Note x and y axes are to the same scale.

is pointing up out of the page whereas blue indicates that the field is pointing into the page. The SQUID was 300 μm above the surface of the microstrip line. Again from these images I estimated the propagation speed, wavelength and frequency of the signal. From Fig. 9.25(a-d) a half-wavelength travels about 31 mm in 200 ps resulting in a speed of $c' \simeq 1.55 \times 10^8 m/s$, a wavelength of $\lambda' = 62\,mm,$ and a frequency of $f' = 2.6\,GHz.$ For the expected signal speed of $c' \simeq 1.43 \times 10^8$ m/s the expected wavelength is $\lambda' = 71.5$ mm for a signal frequency of $f = 2.5$ GHz.

I note that these 2 GHz images do not look as one would expect. There is a prominent distortion of the wave compared to the data at 1.5 GHz. Two possible causes for such distortion or artifacts are rf electric or magnetic fields that couple to the SQUID sensor or wiring respectively. First, at sufficiently high frequencies, voltages in the microstrip can capacitively induce significant currents in a SQUID, which then can be detected [4,5]. This coupling can lead to undesirable electric-field induced artifacts in the SQUID microscope image [4,5]. For example, suppose a microwave voltage V_m from a sample is capacitively coupled (with capacitance C_c) to the current bias leads of a SQUID. This coupling will induce a high-frequency current $(V_m / i\omega C_c)$ and thus the total current I flowing through the SQUID will be a superposition of the bias current I_b and the induced current $I = I_b + I_{mw} \sin(\omega_{mw} t)$, where $I_{mw} \simeq i\omega C_c V$ is the induced microwave current and ω_{mw} is the microwave frequency. In this case if we measure the switching current of the SQUID, we will see a term that scales with the voltage on the line, in addition to any flux signal.

The other possible cause for the artifacts in the magnetic field images is the result of the wires to the SQUID intercepting the transverse component of the B-field and

generating an EMF which causes the SQUID to switch sooner. This effect would depend on the geometry of the SQUID wiring with respect to the transmission line. It is not presently clear which of these mechanisms is the cause of the distortion, or if there is some other cause.

Figure 9.26(a-t) shows images of $B_z(x,y,t)$ above the microstrip when a microwave signal of frequency f = 2.5 GHz and -27 dBm (200 μA) was applied. I used a 400 ps pulse width along with a 20 ms count time and the line was terminated with a 139 Ω (matched) load. The area scanned was again 51 mm (0.5 mm steps) x 8 mm (.2 mm steps) for 4141 pixels and the acquisition time per pixel was 10 sec. Although a propagating wave is visible, the level of noise is very high.

Figure 9.27(a-t) shows the same $B_z(x,y,t)$ data as in Fig. 9.26(a-t), except presented in top-down view. The microwave signal was applied from the left side at about x = 12 mm. The wave propagates from the left side of the microstrip line towards the right. The maximum and minimum oscillate (±150 nT) about the zero field point. From the images, the "noise" is seen to be a more or less regular set of ripples or interference pattern, rather than random uncorrelated spikes. From Fig. 9.27(a-j) a half-wavelength travels about 27 mm in 180 ps, resulting in a speed of $c' \simeq 1.5\times10^8$ m/s, a wavelength of $\lambda' = 54\,\text{mm}$, and a frequency of $f' = 2.8\,\text{GHz}$. For the expected signal speed of $c' \simeq 1.43\times10^8$ m/s and frequency of 2.5 GHz, the wavelength would be $\lambda' = 71.5\,\text{mm}$.

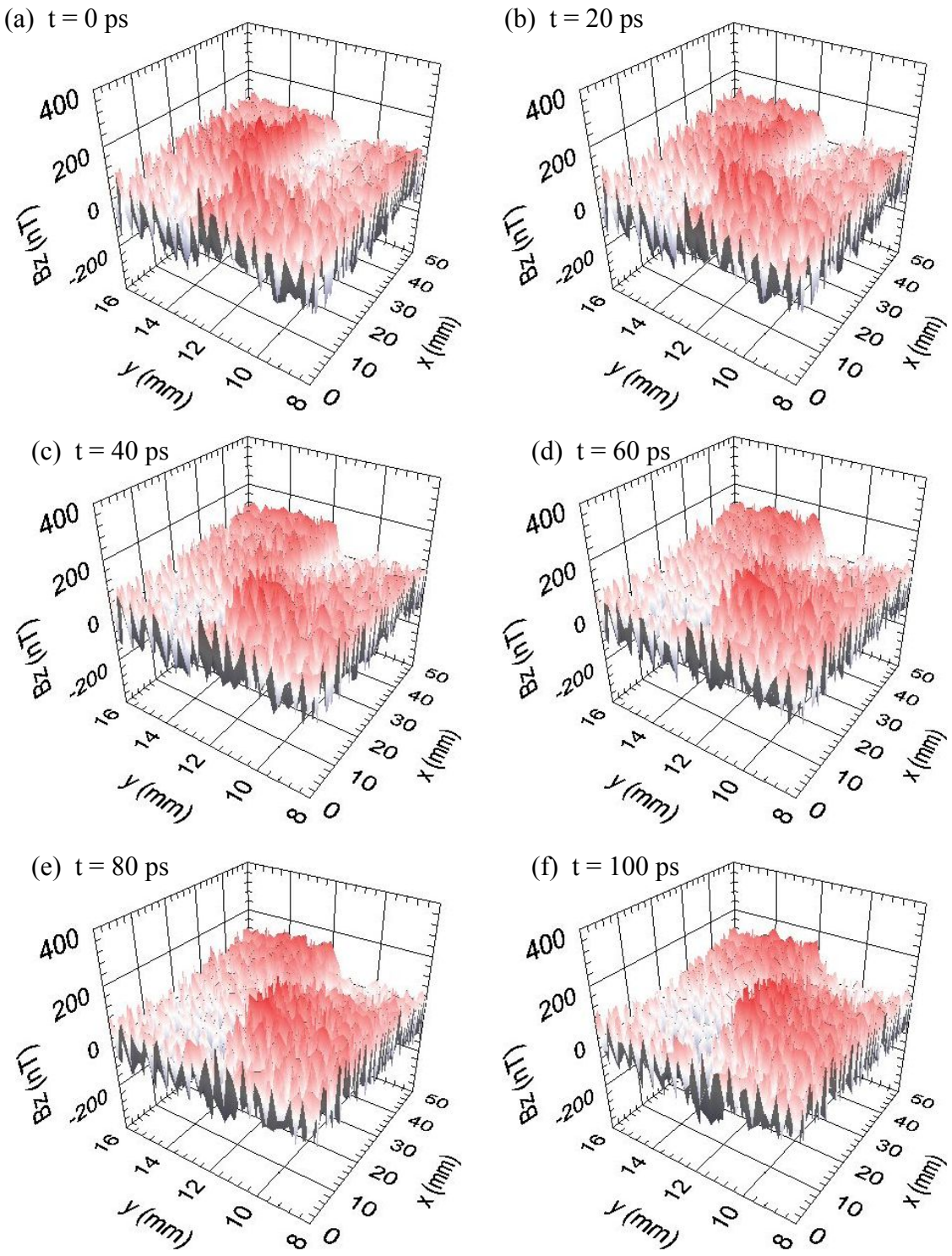

Fig. 9.26. (a-f) Measured $B_z(x,y,t)$ for 20 ps timesteps when microwaves at $f = 2.5$ GHz were applied to the 200 μm wide microstrip line that was terminated with 139 Ω. Successive images are for delay times of $t = 0$ ps to 100 ps. Note x-axis scale compressed compared to y-axis.

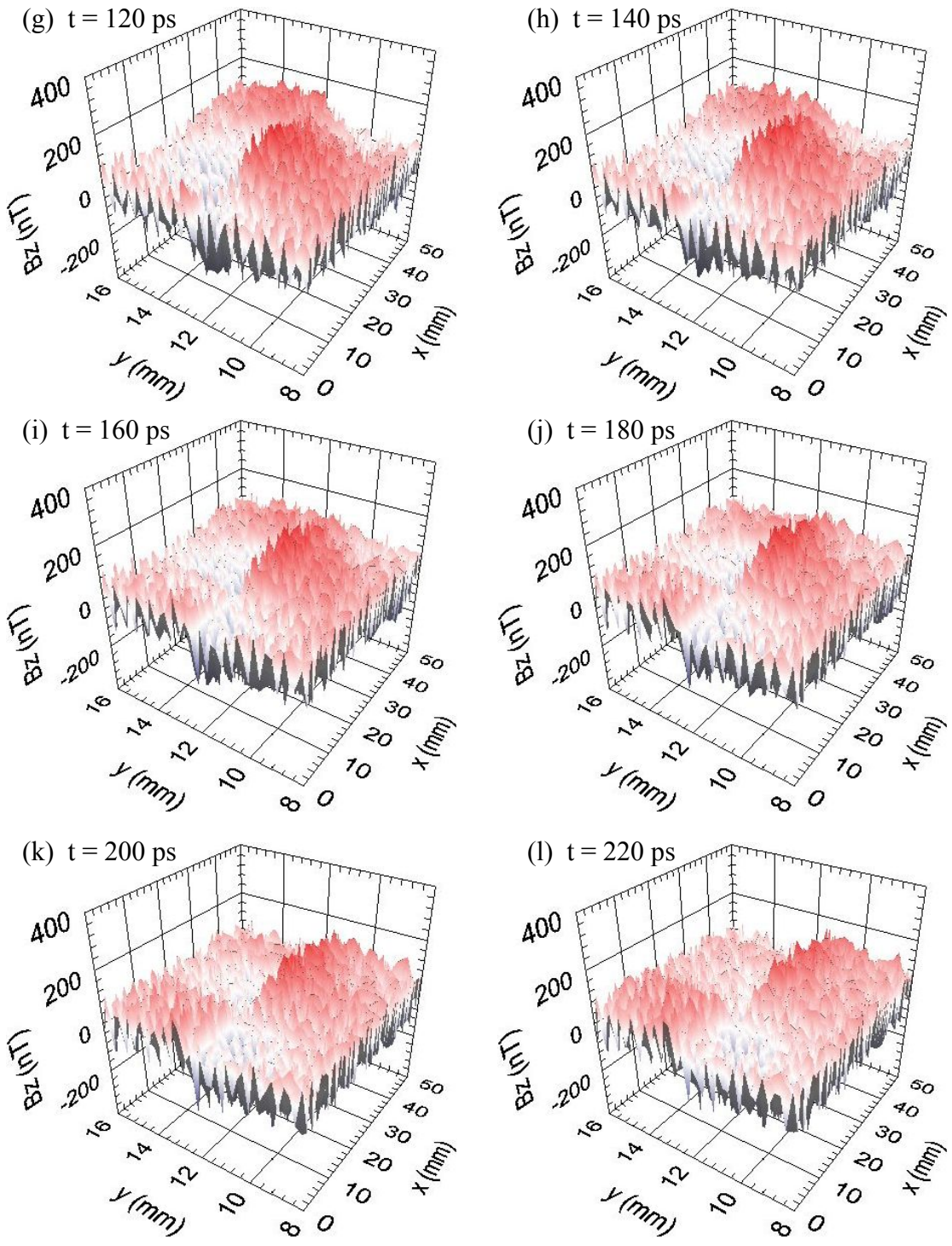

Fig. 9.26. (g-l) Measured $B_z(x,y,t)$ when microwaves at $f = 2.5$ GHz were applied to the 200 μm wide microstrip line that was terminated with 139 Ω. Successive images are for delay times of $t = 120$ ps to 220 ps. Note x-axis scale compressed compared to y-axis.

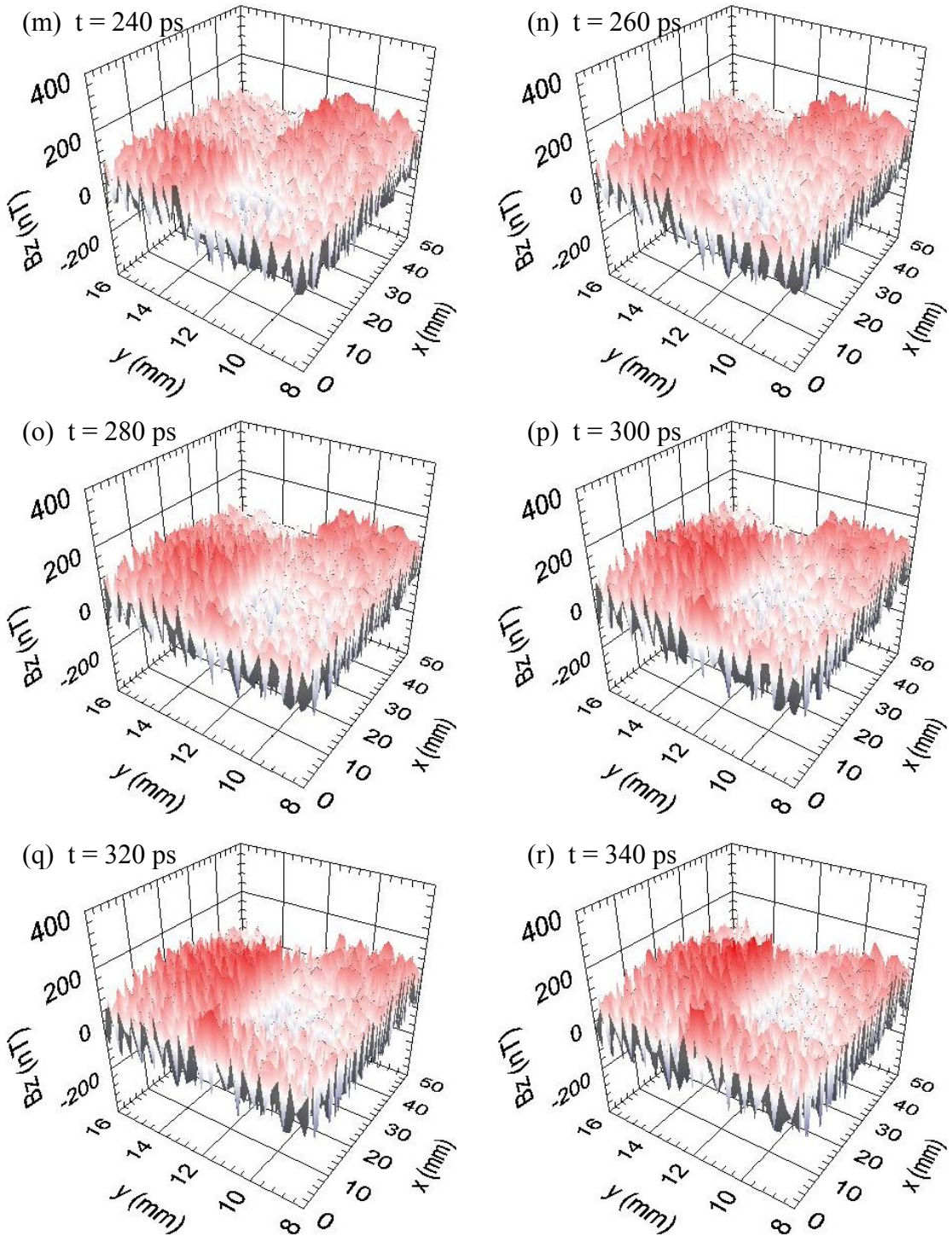

Fig. 9.26. (m-r) Measured $B_z(x,y,t)$ when microwaves at $f = 2.5$ GHz were applied to the 200 μm wide microstrip line that was terminated with 139 Ω. Successive images are for delay times $t = 240$ ps to 340 ps. Note x-axis scale compressed compared to y-axis.

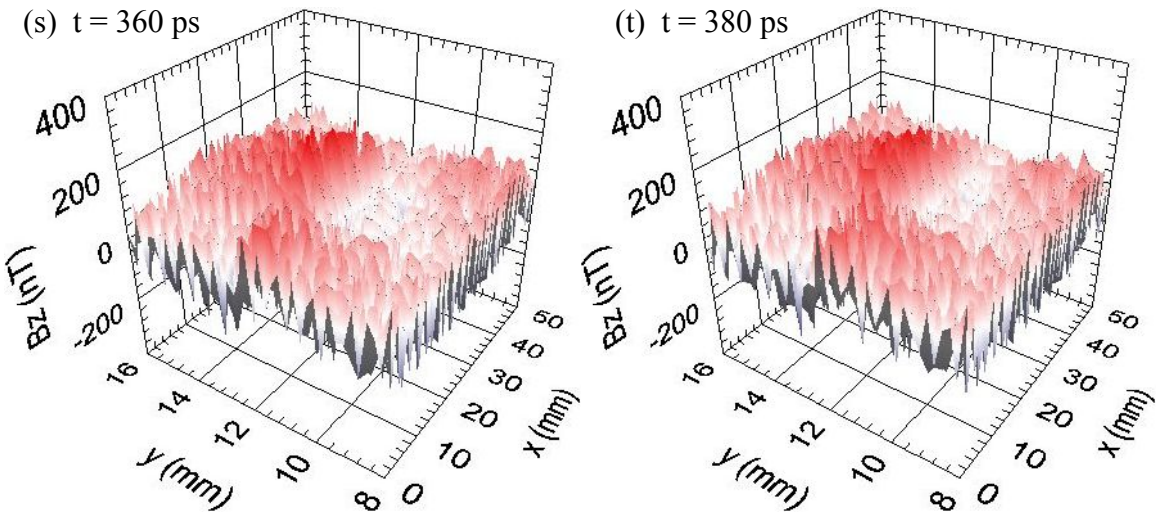

Fig. 9.26. (s-t) Measured $B_z(x,y,t)$ when microwaves at f = 2.5 GHz were applied to the 200 μm wide microstrip line that was terminated with 139 Ω. Images are for successive delay times of t = 360 ps to 380 ps. Note x-axis scale compressed compared to y-axis.

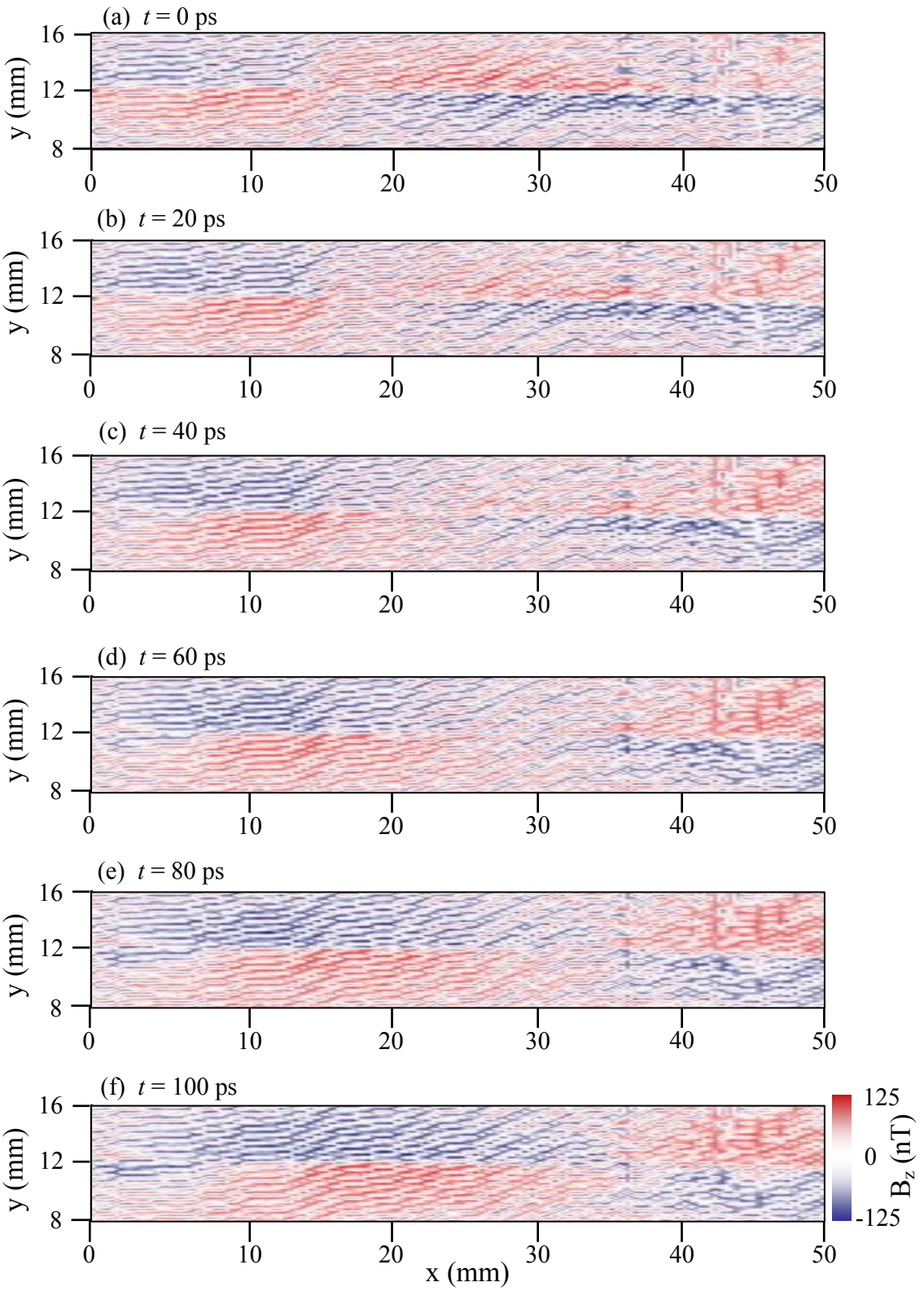

Fig. 9.27. (a-f) Top down view of magnetic field $B_z(x,y,t)$ above microstrip line. Frequency f = 2.5 GHz. Red and blue indicate±150 nT while white indicates zero field.

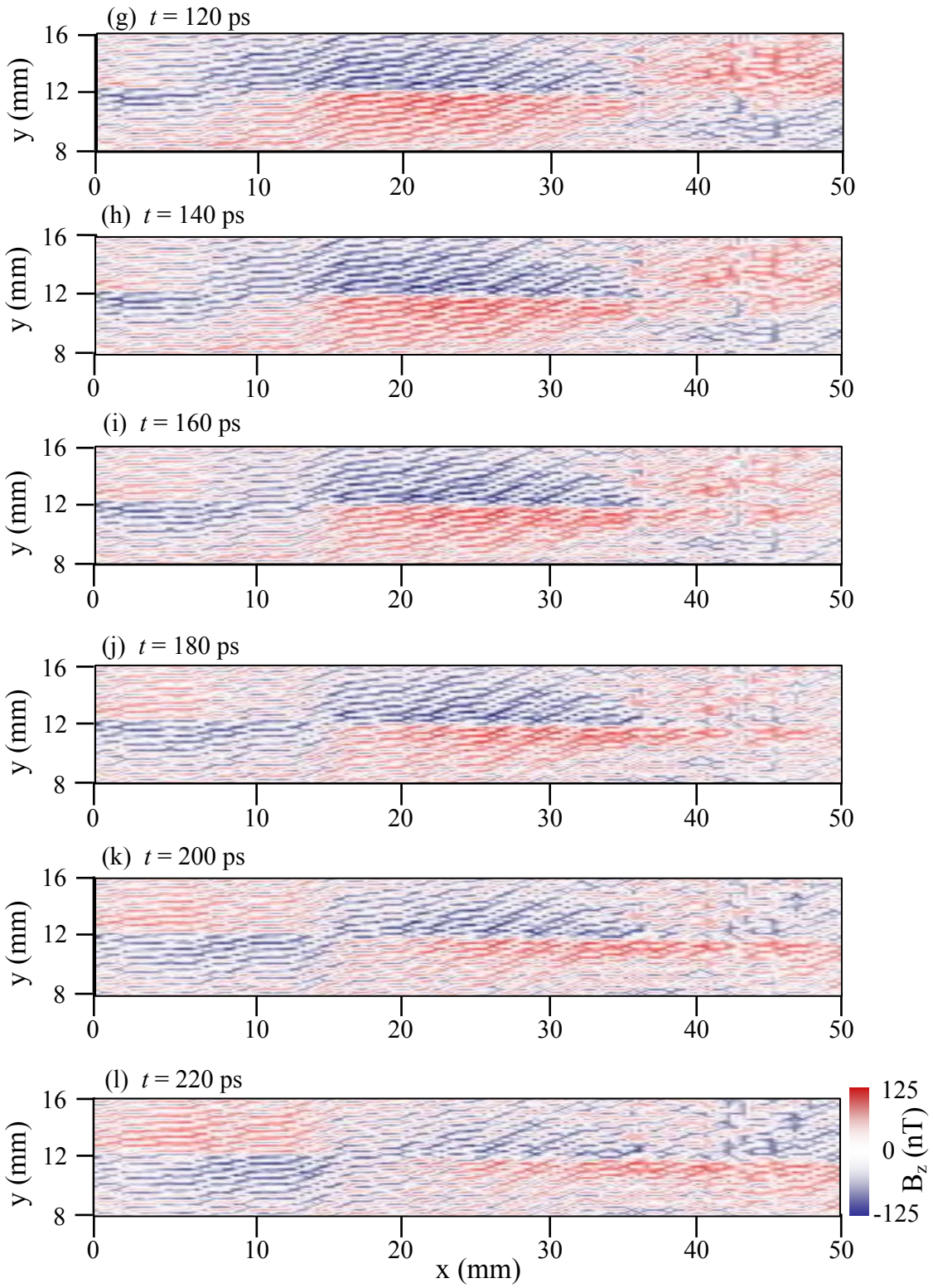

Fig. 9.27. (g-l) Top down view of magnetic field $B_z(x,y,t)$ microstrip line. Frequency f = 2.5 GHz. Red and blue indicate±150 nT while white indicates zero field. Note x and y axes are to the same scale.

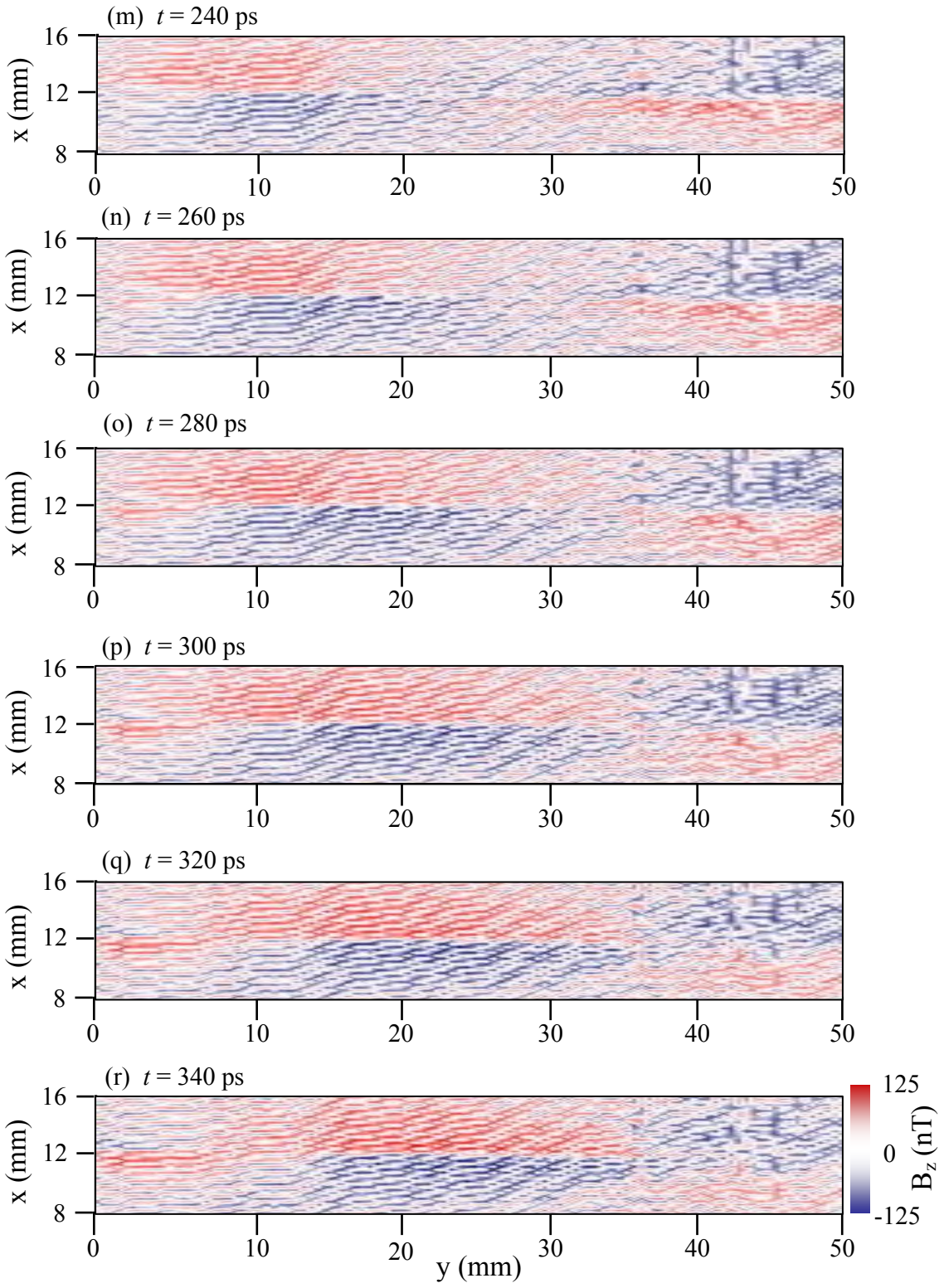

Fig. 9.27. (m-r) Top down view of magnetic field $B_z(x,y,t)$ microstrip line. Frequency f = 2.5 GHz. Red and blue indicate ±150 nT while white indicates zero field. Note x and y axes are to the same scale.

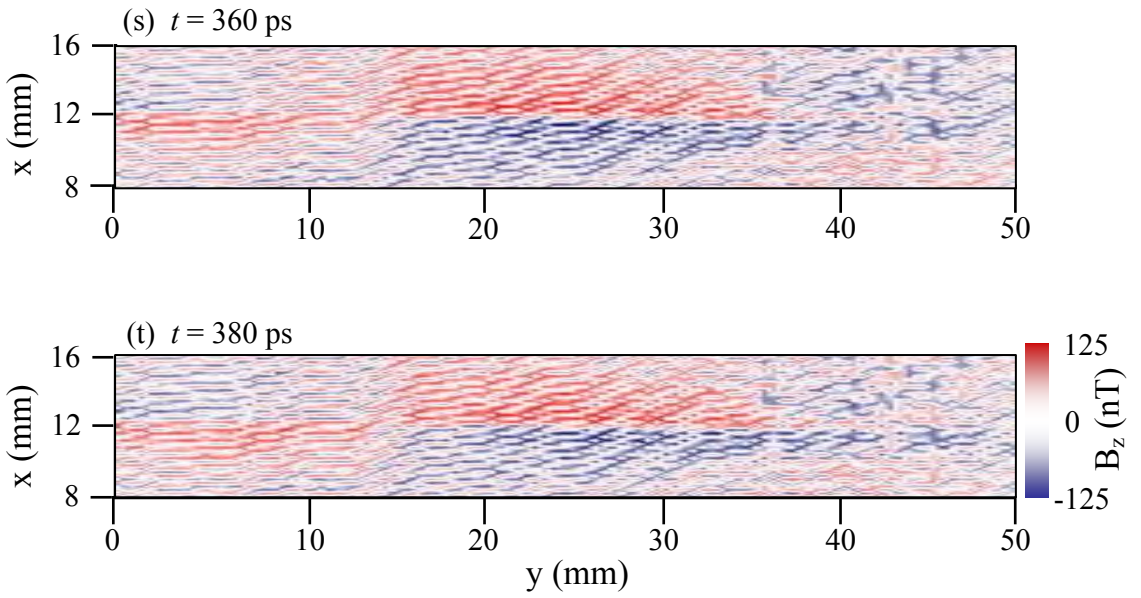

Fig. 9.27. (s-t) Top down view of magnetic field $B_z(x,y,t)$ microstrip line. Frequency f = 2.5 GHz. Red and blue indicate±150 nT while white indicates zero field. Note x and y axes are to the same scale.

Figure 9.28(a-k) shows images of $B_z(x,y,t)$ with the line terminated with a 139 Ω resistor when I applied a microwave signal of frequency f = 3 GHz at -33 dBm. Again, I used a 400 ps pulse width and a 20 ms count time. The area scanned was 51 mm (0.5 mm steps) x 8 mm (.2 mm steps) for 4141 pixels, and the acquisition time per pixel was 11 sec.

Figure 9.29(a-k) shows the same magnetic field $B_z(x,y,t)$ over the microstrip line as shown in Fig. 9.28(a-k) except presented in top-down view. A wave is visible propagating from the left to the right. The signal is distorted and just barely visible above the large noise. Finally, although the noise was more substantial for these images, I could still estimate the propagation speed, wavelength and frequency of the signal. From Fig. 9.29(a-h) a half-wavelength travels about 23 mm in 150 ps resulting in a speed of $c' \simeq 1.5\times10^{8} m/s$, a wavelength of $\lambda' = 46\,mm,$ and a frequency of $f' = 3.3\,GHz.$

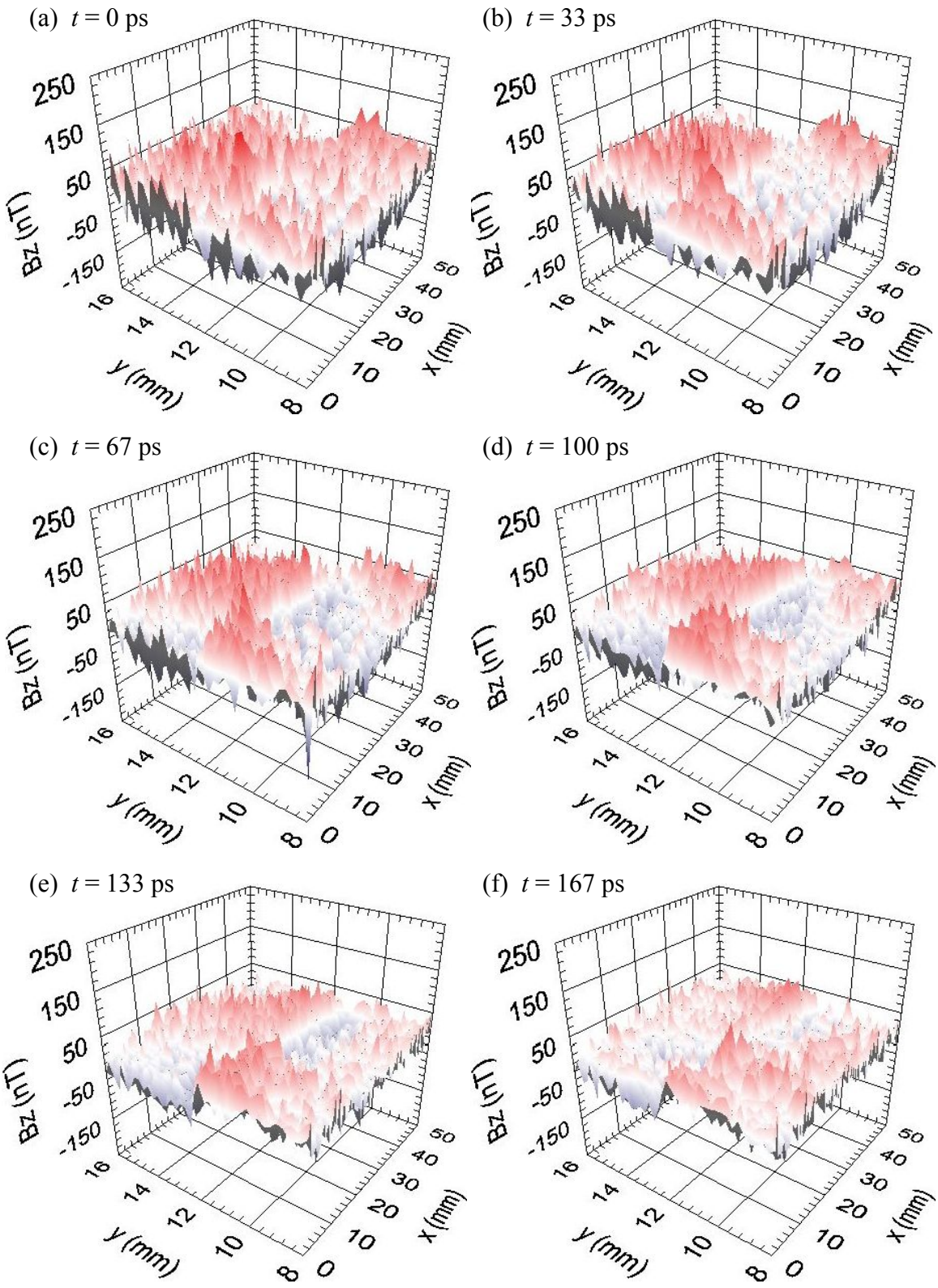

Fig. 9.28. (a-f) Measured $B_z(x,y,t)$ for 20 ps timesteps when microwaves at f = 3 GHz were applied to the 200 μm wide microstrip line that was terminated by 139 Ω. Images are for successive delay times of t = 0 ps to 160 ps.

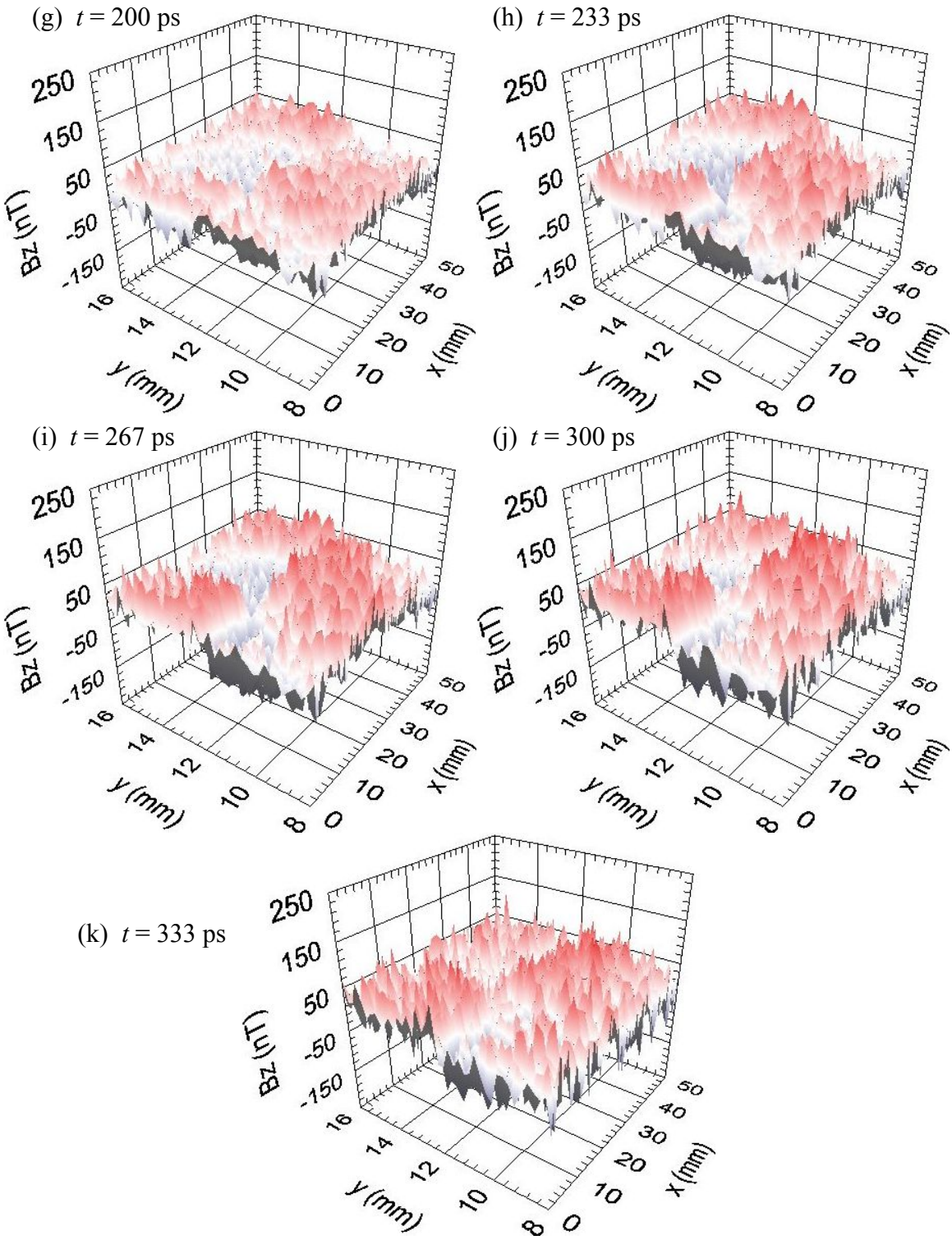

Fig. 9.28. (g-k) Measured $B_z(x,y)$ when microwaves at $f = 3$ GHz were applied to the 200 μm wide microstrip line that was terminated by 139 Ω. Images are for successive delay times of $t = 200$ ps to 333 ps. Note x-axis scale compressed compared to y-axis.

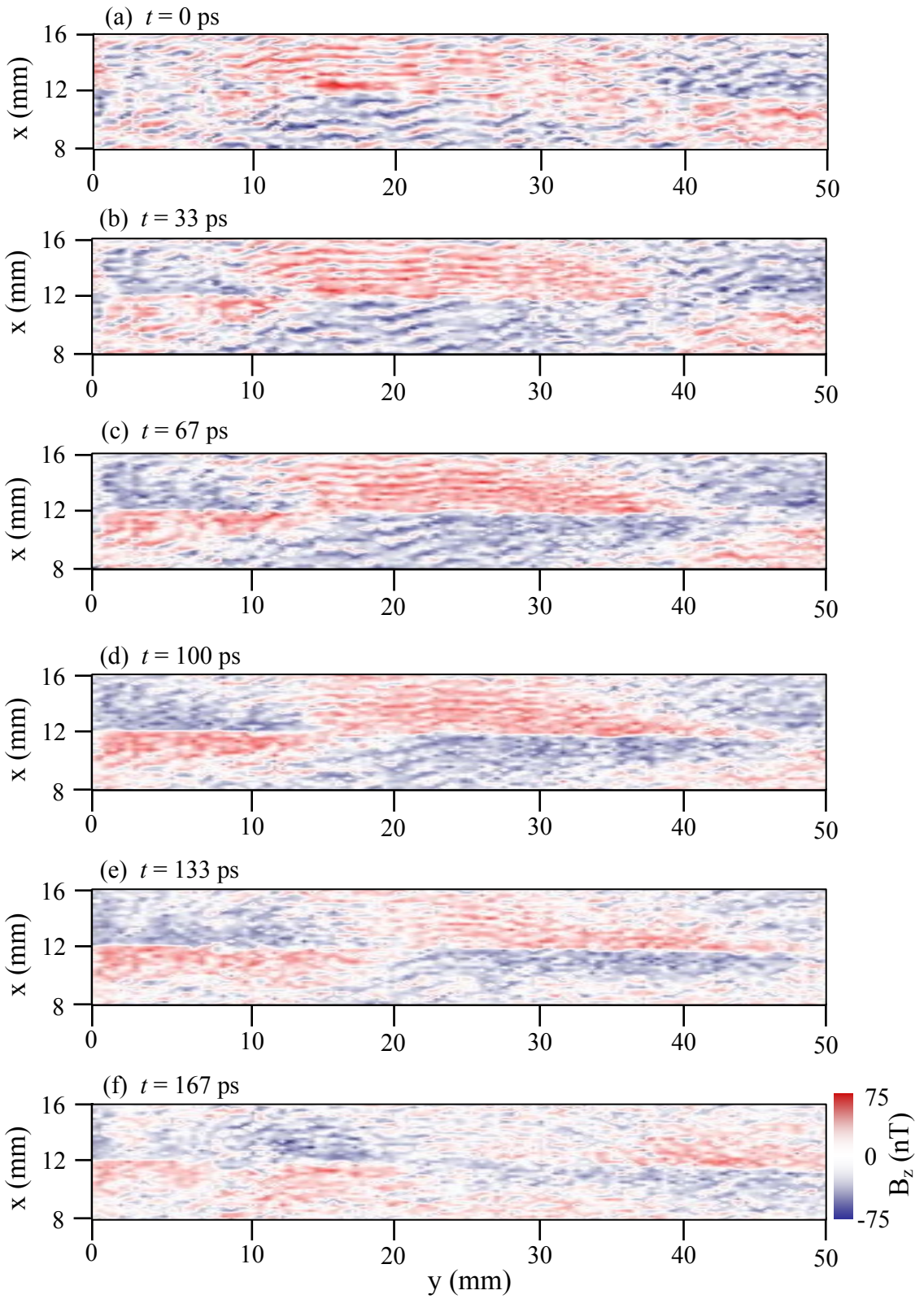

Fig. 9.29. (a-f) Top down view of magnetic field $B_z(x,y,t)$ microstrip line. Frequency $f = 3$ GHz. Note x and y axes are to the same scale.

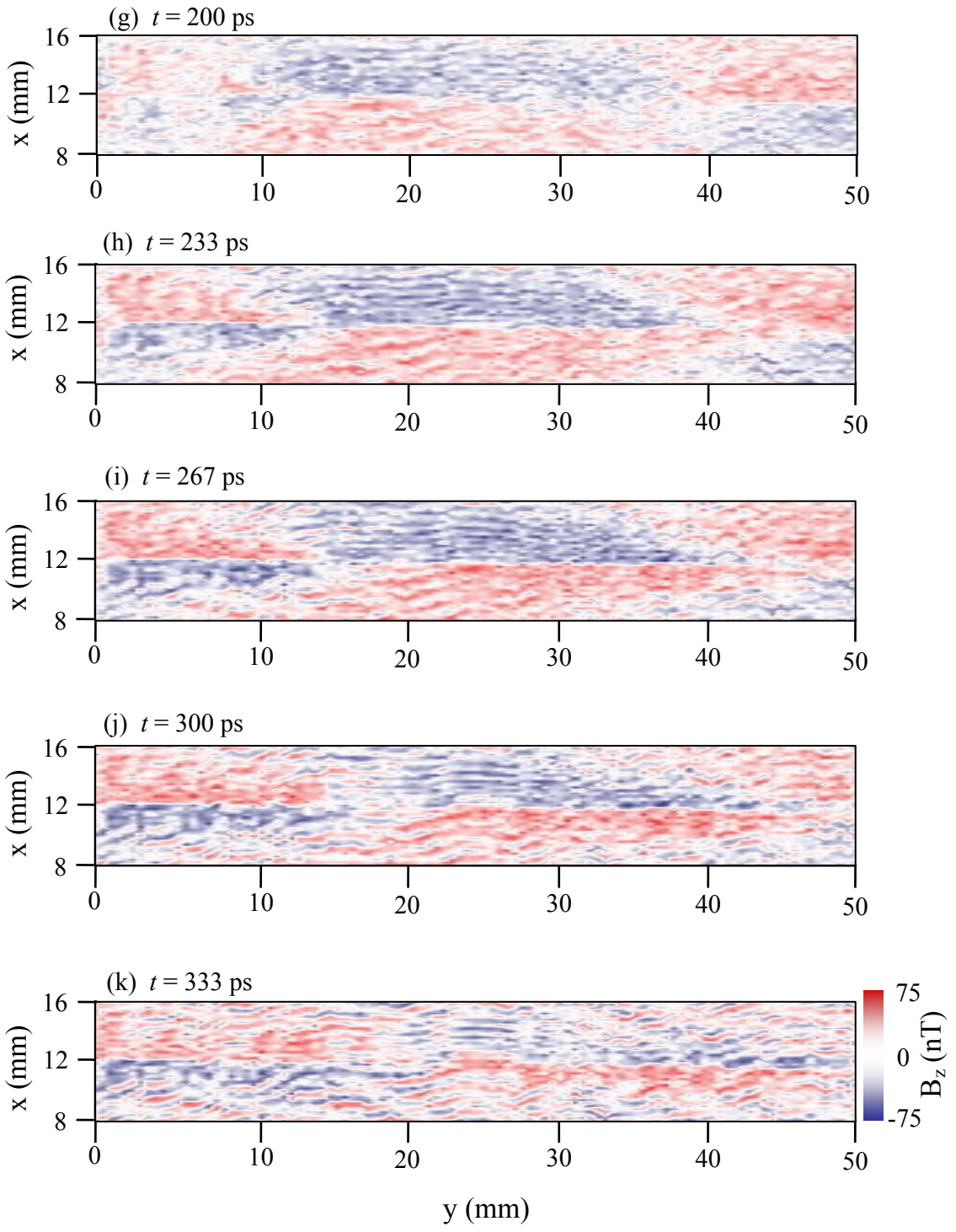

Fig. 9.29. (g-k) Top down view of magnetic field $B_z(x,y,t)$ microstrip line. Frequency f = 3 GHz. Note x and y axes are to the same scale.

For the expected $c' \simeq 1.43 \times 10^8$ m/s the wavelength would be $\lambda' = 47.7$ mm for a signal frequency of f = 3.0 GHz.

Finally, in Fig. 9.30(a-f) I show images of $B_z(x,y,t)$ with the line terminated with a 139 Ω resistor when I applied a microwave signal of frequency f = 3.5 GHz at -33 dBm and imaged at successive delay time increments of 25 ps. A 400 ps pulse width was used along with a 20 ms count time. Again, the area scanned was 51 mm (0.5 mm steps) x 8 mm (0.2 mm steps) for 4141 pixels and the acquisition time per pixel was 11 sec. At this frequency the signal is not visible. I tried 4 GHz as well, with a similar null result.

From Figs. 9.13 to 9.30 we can thus conclude that the system works at some level up to about 2 or 3 GHz, although significant distortion is present. A brief analysis of these results is presented in section 9.6, and a comparison with simulations is presented in Chapter 10.

9.4 Magnetic Field Images of a Microstrip Transmission Line with gap

I also used the microscope to image magnetic fields in a line with an open circuit fault. Open circuits are one of the main types of defects in chips, and they are difficult to locate using conventional techniques including standard low-frequency SQUID microscopy. The idea was to image the fields produced when there was a high frequency standing wave in the system, and see if I could identify the location of break by its effect on the wave.

For this experiment, I prepared a 167 μm wide gap in a 200 μm wide microstrip transmission line (see Fig. 9.31). To image the sample, I applied a 1 GHz sine wave (-27 dBm) to the connector on the left-hand side of the transmission line in Fig. 9.31(a). Figure 9.32(a-j) shows the resulting magnetic field $B_z(x,y,t)$ data at successive time

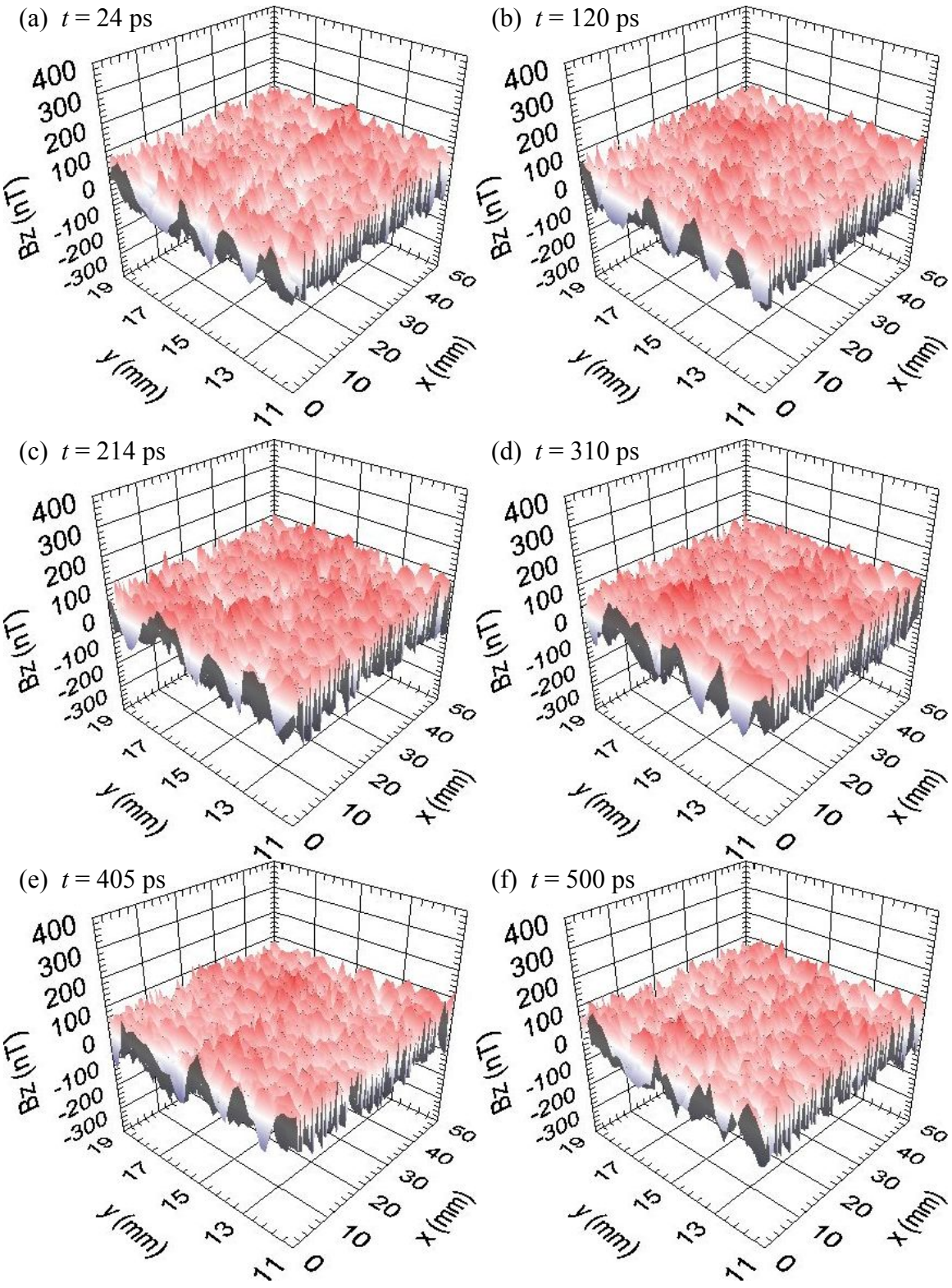

Fig. 9.30. (a-f) Measured $B_z(x,y,t)$ for 24 ps timesteps when microwaves at $f = 3.5$ GHz were applied to the 200 μm wide microstrip line that was terminated by 139 Ω. The signal is no longer detectable; just noise is evident.

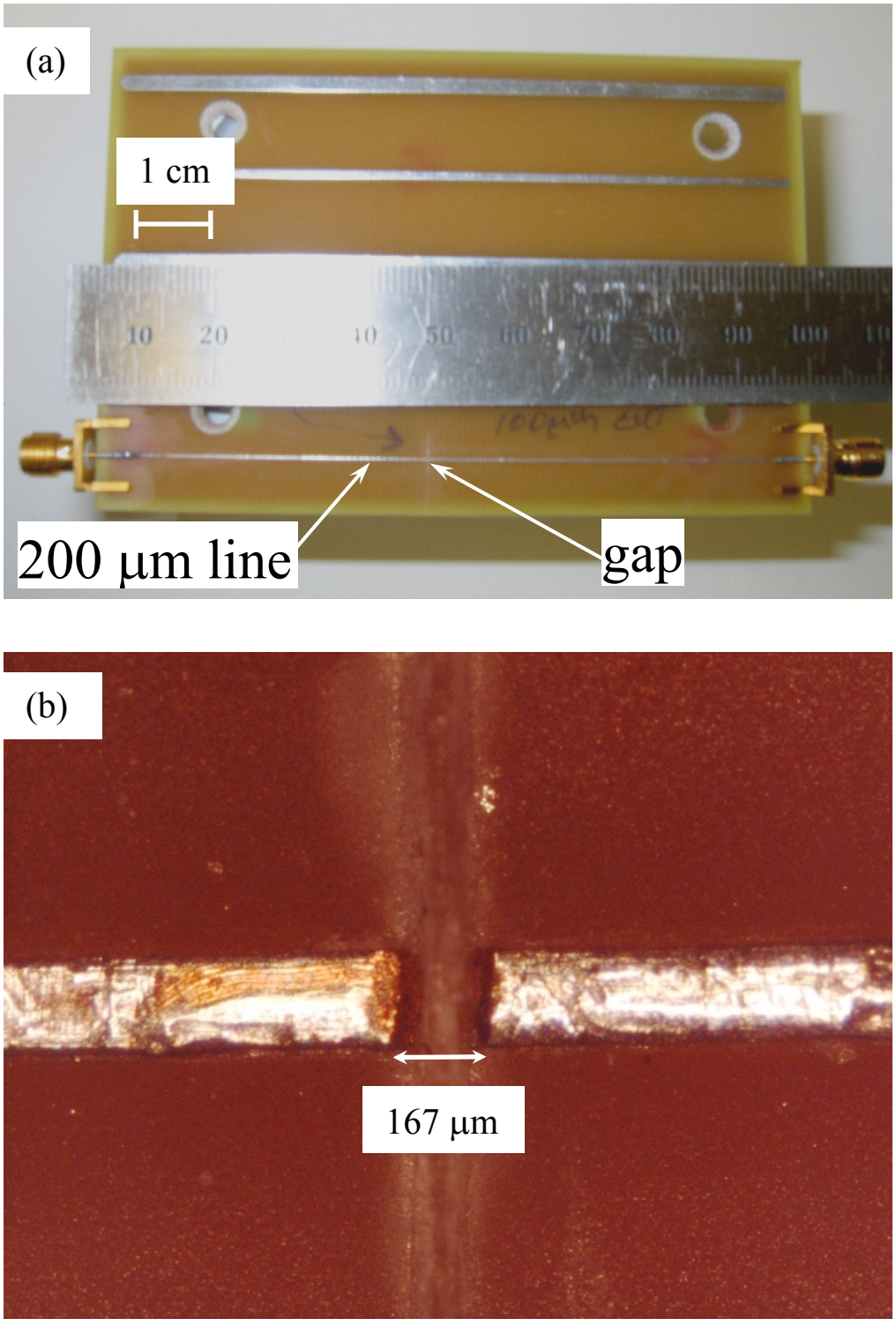

Fig. 9.31. (a) Photograph of 200 µm wide microstrip transmission line. The board is 98 mm long by 60 mm wide, and the dielectric material is FR-4 Duroid which has a relative permeability of $\varepsilon_r \approx 4.4$. I used the 200 µm line for the data shown in Figs. 9.21-9.22. (b) Enlarged view of the gap shows the 167 µm open cut in the microstrip line.

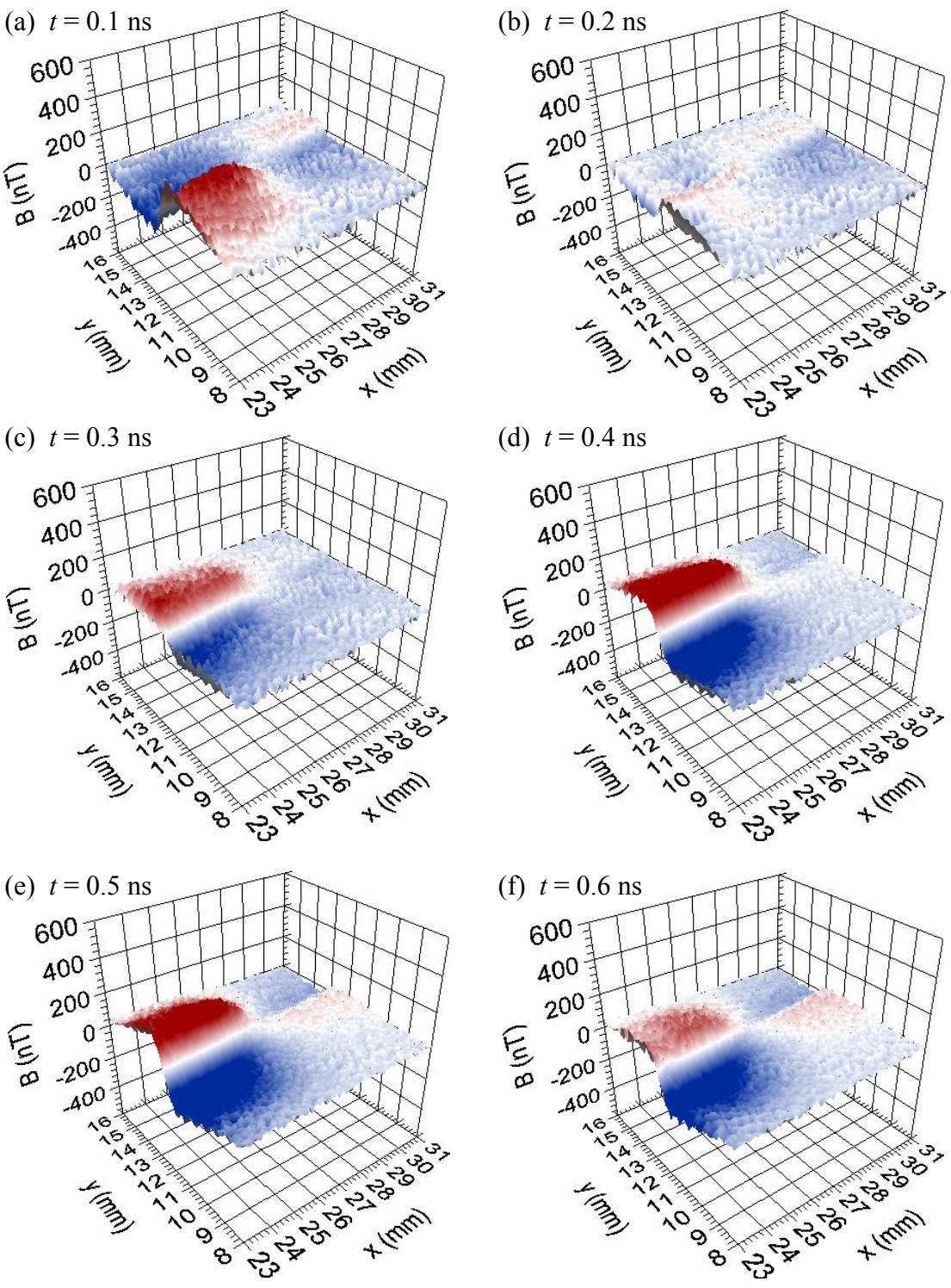

Fig. 9.32. (a-f) Measured $B_z(x,y,t)$ for t = 0.1 ns to 0.6 ns in the region near the open in the 200 μm microstrip line shown in Fig. 9.31(b). The applied signal is f = 1 GHz (-27 dBm) and the open is at approximately x = 27 mm and y = 12.5 mm.

(g) $t = 0.7$ ns

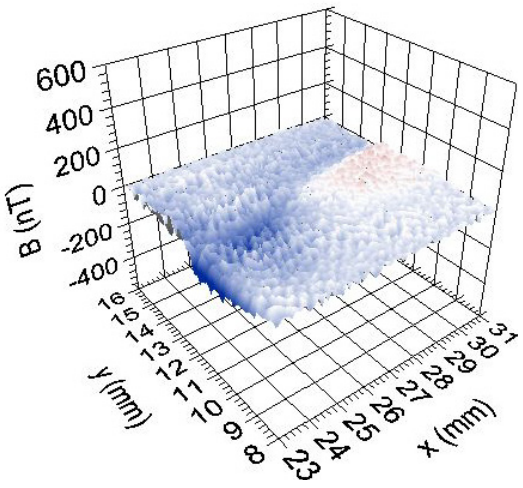

(h) $t = 0.8$ ns

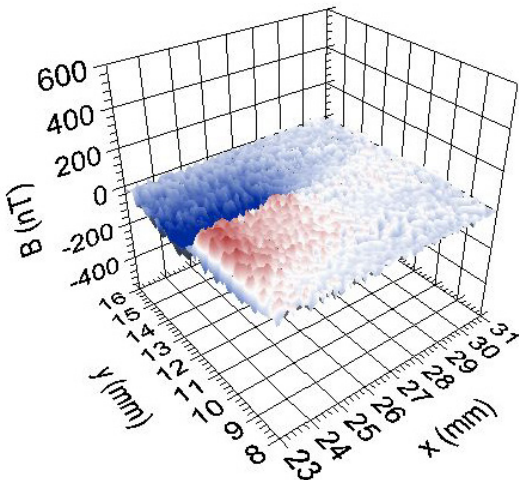

(i) $t = 0.9$ ns

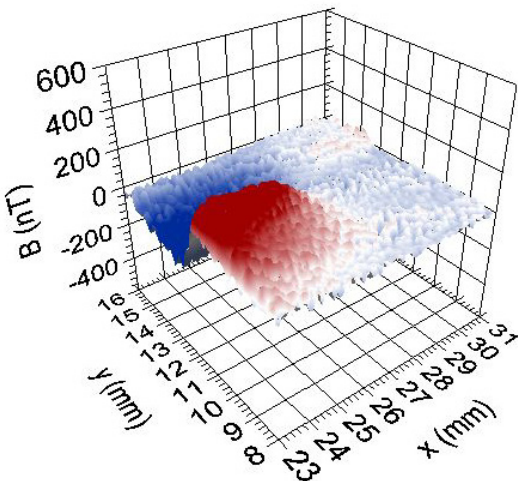

(j) $t = 1.0$ ns

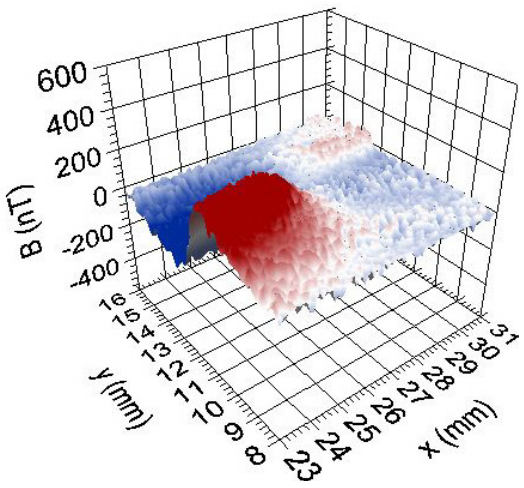

Fig. 9.32. (g-k) Measured $B_z(x,y,t)$ at $t = 0.7$ ns to 1.0 ns in the region near the open in the 200 μm microstrip line shown in Fig. 9.31(b). The applied signal is $f = 1$ GHz (-27 dBm) and the open is at approximately $x = 27$ mm and $y = 12.5$ mm.

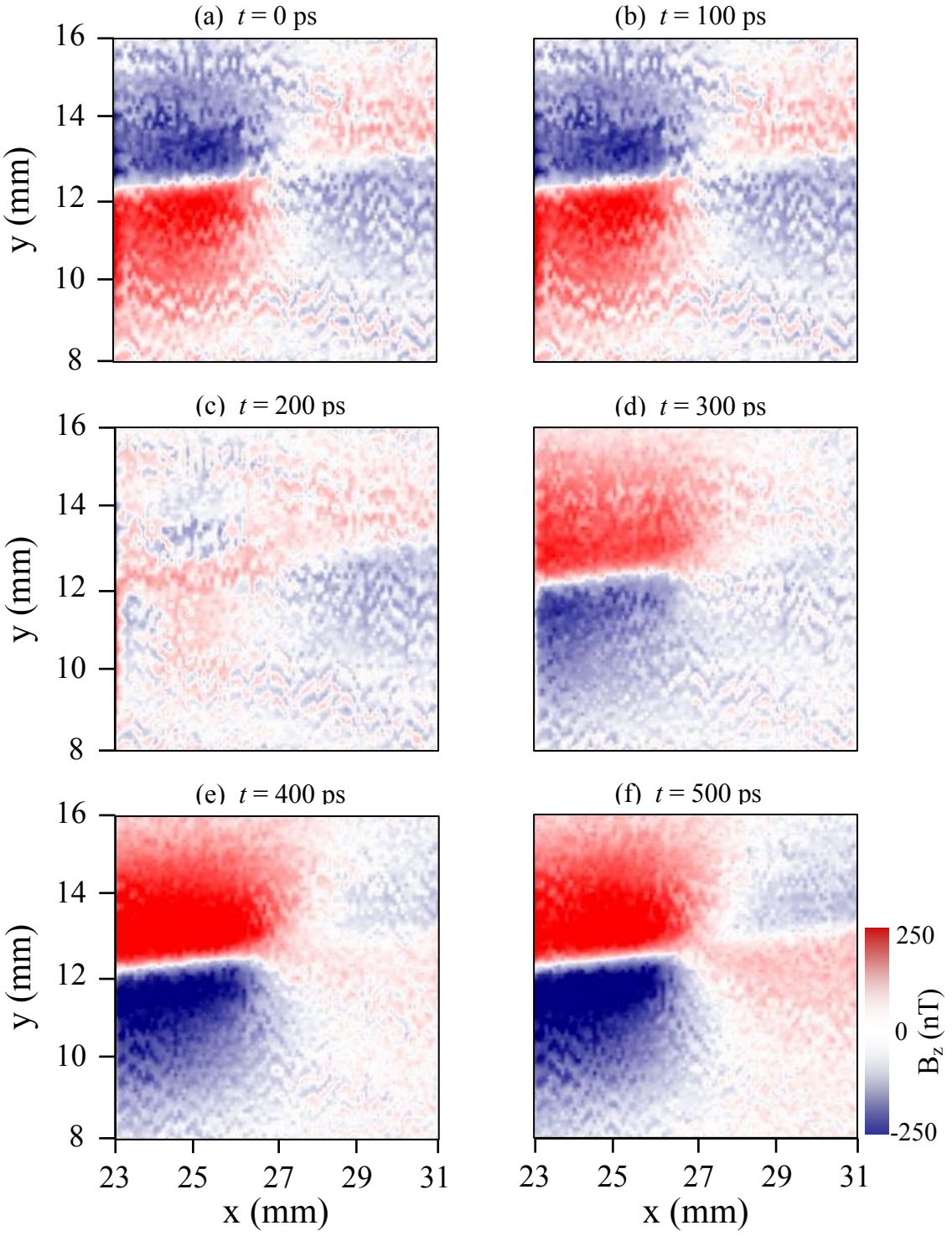

Fig. 9.33. (a-f) Top view of measured $B_z(x,y,t)$ for t = 0.1 ns to 0.6 ns in the region near the open in the 200 μm microstrip line shown in Fig. 9.31(b). The at approximately x = 27 mm and y = 12.5 mm. Microwaves of -27 dBm at frequency f = 1 GHz are applied to the left side of the microstrip line.

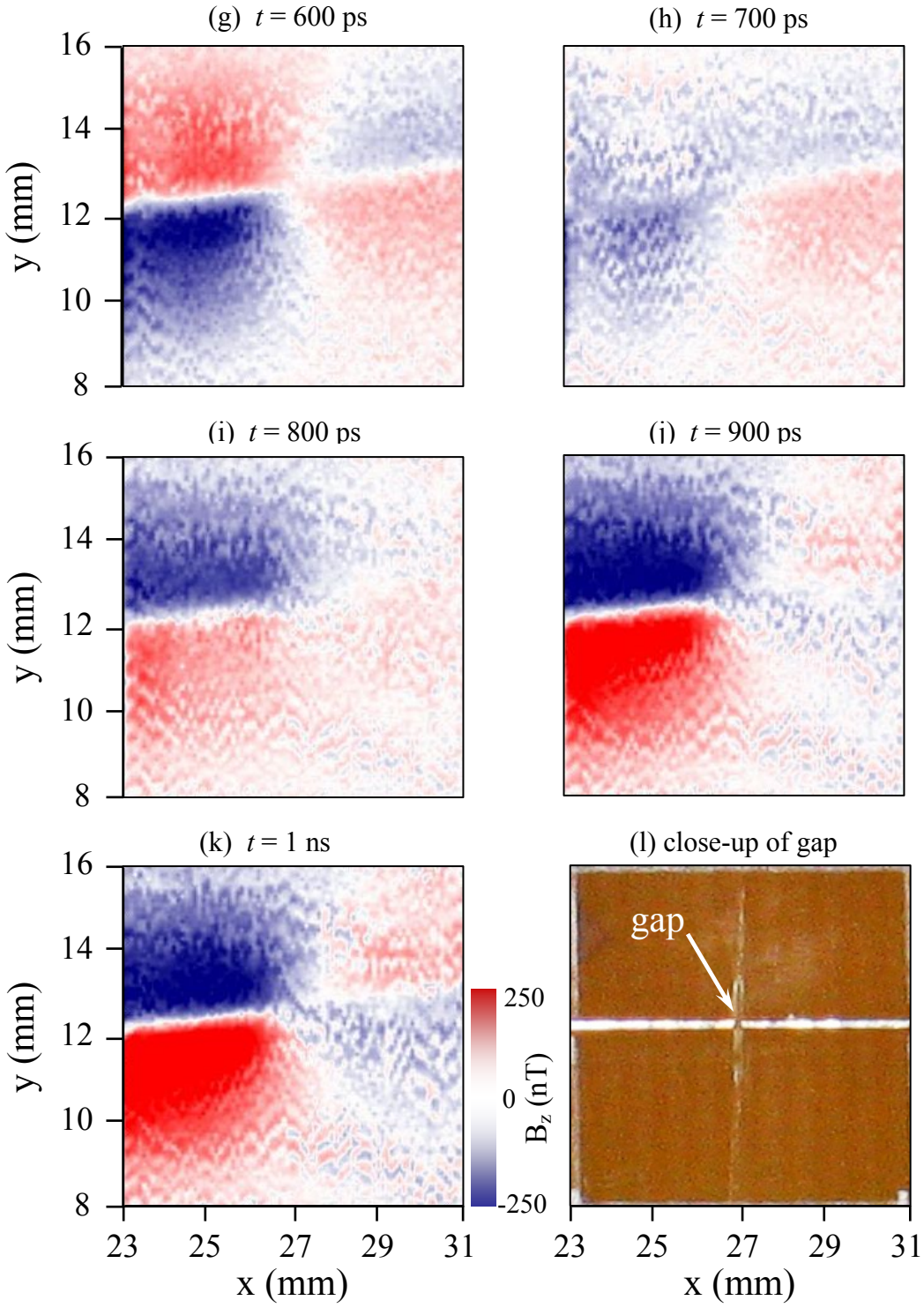

Fig. 9.33. (g-k) False color image of measured $B_z(x,y,t)$ for t = 0.6 ns to 1.0 ns in the region near the open in the 200 μm microstrip line shown in Fig. 9.31(b). (l) Photograph showing 8 mm by 8 mm area centered at 167 μm wide break in microstrip line.

intervals of 0.1 ns. For this image I scanned an 8 mm (0.1 mm steps) × 8 mm (0.1 mm steps) area of the transmission line with the open approximately in the middle of the image, *i.e.* at $(x,y) = (27 \text{ mm}, 12.5 \text{ mm})$.

Examination of the images shows that a relatively strong magnetic field signal is only present for $x \leqslant 27$ mm, *i.e.* up to about the location of the break. The SQUID was about 550 μm above the sample. There is also visible a weak signal propagating further along the line, probably due to capacitive coupling across the break. Such a pattern could clearly be used to locate an open in a line and this provides proof of principle that the system could be used to locate an open in failure analysis. Of course we don't need the full set of time dependent images to see this pattern; all we would need would be a single frame, which took about 20 min to complete.

In order to see the location of the open fault more easily, Fig. 9.33(a-k) shows a corresponding top-down view of the previous magnetic field $B_z(x,y,t)$ data at time intervals of 100 ps. Again, the images clearly show that a relatively strong magnetic field signal is only present for $x \leqslant 27$ mm, *i.e.* up to about the location of the break. Indeed, these raw images suggest that the location of the break is within about 500 μm of $(x,y) = (27 \text{ mm}, 12.5 \text{ mm})$. Furthermore, this level of smearing is what we would expect from the SQUID-sample separation of 500 μm. The implication is that by reducing the height to 50 μm we could localize the break to within 50 μm, and then other failure analysis tools could be employed to identify the root cause of the open circuit. A careful analysis of the image would certainly yield a more accurate estimate. Alternatively, one could next apply a 1 GHz sine wave from the other end of the line and perhaps use a difference analysis to further localize the break.

9.5 Magnetic Field Images Compared with Simulation

In order to better understand the magnetic field distribution that I measured in some of the samples, I tried modelling the microstrip line using FEKO [6], a commercial program for simulating time-varying electromagnetic fields. The name is an acronym from the German name: "FEldberechnung bei Körpern beliebiger Oberfläche", which translates into *field computations involving bodies of arbitrary shape*. FEKO is based on the Method of Moment (MoM) integral formulation of Maxwell's equations [7]. It incorporates MoM using a linear triangular mesh for metallic structures. It supports several hybrid methods, such as Finite Element Method (FEM)/(MoM), where a FEM region is bounded with an integral equation-based condition to ensure full coupling between the FEM and MoM solution areas of the problem [8-11].

The method of moments technique is applicable to problems involving currents on metallic and dielectric structures and radiation in free space. It is a full wave solution of Maxwell's integral equations in the frequency domain [12]. One of the chief advantages of the MoM is that it is a "source method" as opposed to a "field technique", *i.e*. only the structure of interest is discretized, and not free space. Further, boundary conditions do not have to be set and memory requirements scale proportional to the size of the geometry in the problem and the solution frequency. A special extension included in FEKO's MoM formulation allows the use of planar Green's functions for the modeling of multilayered dielectric media, *e.g*. substrates for microstrip transmission lines. The planar Green's function technique uses 2D infinite planes with finite thickness for each layer of the dielectric. The advantage of this approach is that the conducting surfaces and wires in the dielectric layers have to be discretized, but not the dielectric planes

themselves, hence reducing the computational overhead of the problem. Further details about computational electromagnetics and the MOM/FEM technique can be found in references [12-14].

I first chose to model the uniform unbroken microstripline sample shown in Fig. 9.12. for frequency of 1 GHz. The simulation was performed on a Dell Dimension 4600i personal computer with an Intel Pentium 4 3.2 GHz CPU running XP Professional. FEKO generated 8752 triangles and 12039 edges and the computation required 1.1 Gbytes of memory and 15.1 hours to complete. Figure 9.34(b) shows the result of the simulation of $B_z(x,y,t)$. The size of the image is 6 mm x 51 mm, the time delay is t = 0.5 ns and z = 200 μm above the strip line. For an applied current of 500 μA, FEKO calculates the magnetic field intensity with a range of ±0.4 A/m which (assuming vacuum permeability) coincides with a magnetic field of ±500 nT.

For comparison, Fig. 9.34(a) shows a 6 mm x 51 mm top down view of the magnetic field I measured at time delay 0.5 ns while applying a current 500 μA of 1 GHz to the line. This is just Fig. 9.21 with a different color scale and the y-axis compressed compared to the x-axis. The microstrip line was terminated by a 50 Ω termination in this case. The scale of the Fig. 9.34(a) is similar to Fig. 9.21 where the magnetic field has a range of ±500 nT. The simulation captures the basic features such as magnetic field amplitude, and the general shape of the node of the wave propagation located at (x,y) = 12.5 mm, 25 mm. What the simulation does not capture is the noise and asymmetry in the magnetic field pattern that is evident in Fig. 9.34(a).

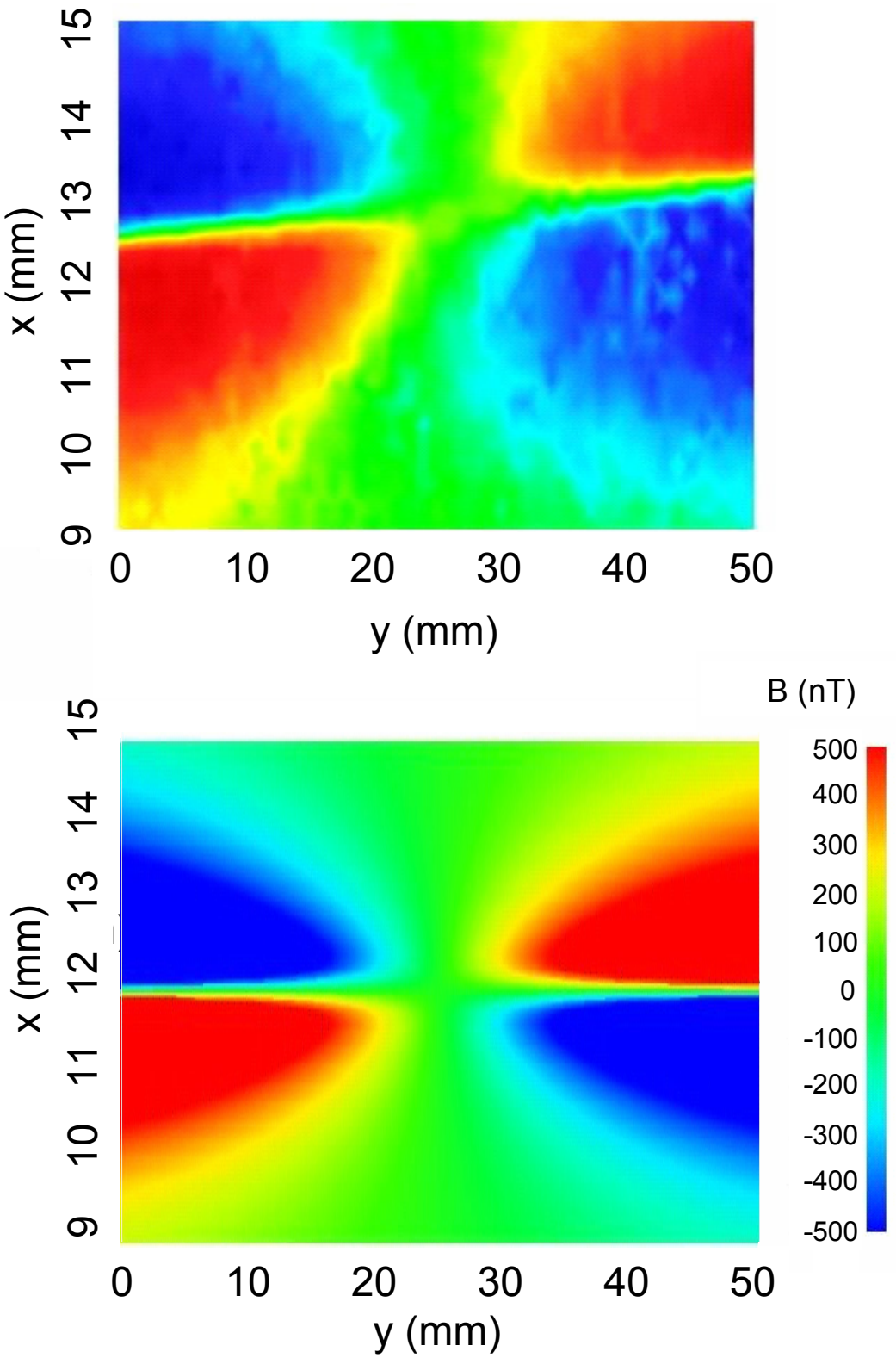

Fig. 9.34. (a) Measured $B_z(x,y,t)$ 200 μm above microstrip line at frequency f = 1 GHz and at time delay 0.5 ns (same as Fig. 9.21). (b) Corresponding magnetic field from FEKO simulation.

I next used FEKO to simulate the propagation of a 1 GHz microwave on a microstrip line with a gap with the same dimensions as the one I used to test the microscope (see Fig. 9.31). I assumed an applied current of 250 μA. FEKO generated 8736 triangles and 12014 edges for the model. The computation required 1.1 Gbytes of memory and 15.8 hours to complete. Figure 9.35(b) shows the resulting calculated magnetic field 200 μm above the microstrip line at a time delay t = 0.5 ns. FEKO calculates the magnetic field intensity with a range of ±0.2 A/m which corresponds to a magnetic field of ±250 nT.

For comparison Figure 9.35(a) shows a 8 mm x 8 mm top down view of the magnetic field I measured above the microstrip line with a 167 mm wide gap for an applied power of -27 dBm. This is just a version of Fig. 9.32(e) at time delay t = 0.5 ns for a microwave signal of 1 GHz. The microwaves are applied from the left end at approximately x = 23 mm and y = 12.5 mm.

The simulation shown in Fig. 9.35(b) captures several important features seen in the data. In particular the model confirms that the gap in the microstrip is located where the propagation of the microwave signal ends at x = 12.5 mm and y = 27 mm. The maximum and minimum oscillate (±250 nT) about the zero point and so is in reasonable agreement with Fig. 9.35(a). Additionally, the simulation indicates a weak signal propagating further along the line, again probably due to capacitive coupling across the gap. On the other hand the simulation produced a symmetrical distribution of field, while the data shows some distortion in the shape of the field pattern near the node. Again, this suggests that the microscope is detecting something in addition to B_z.

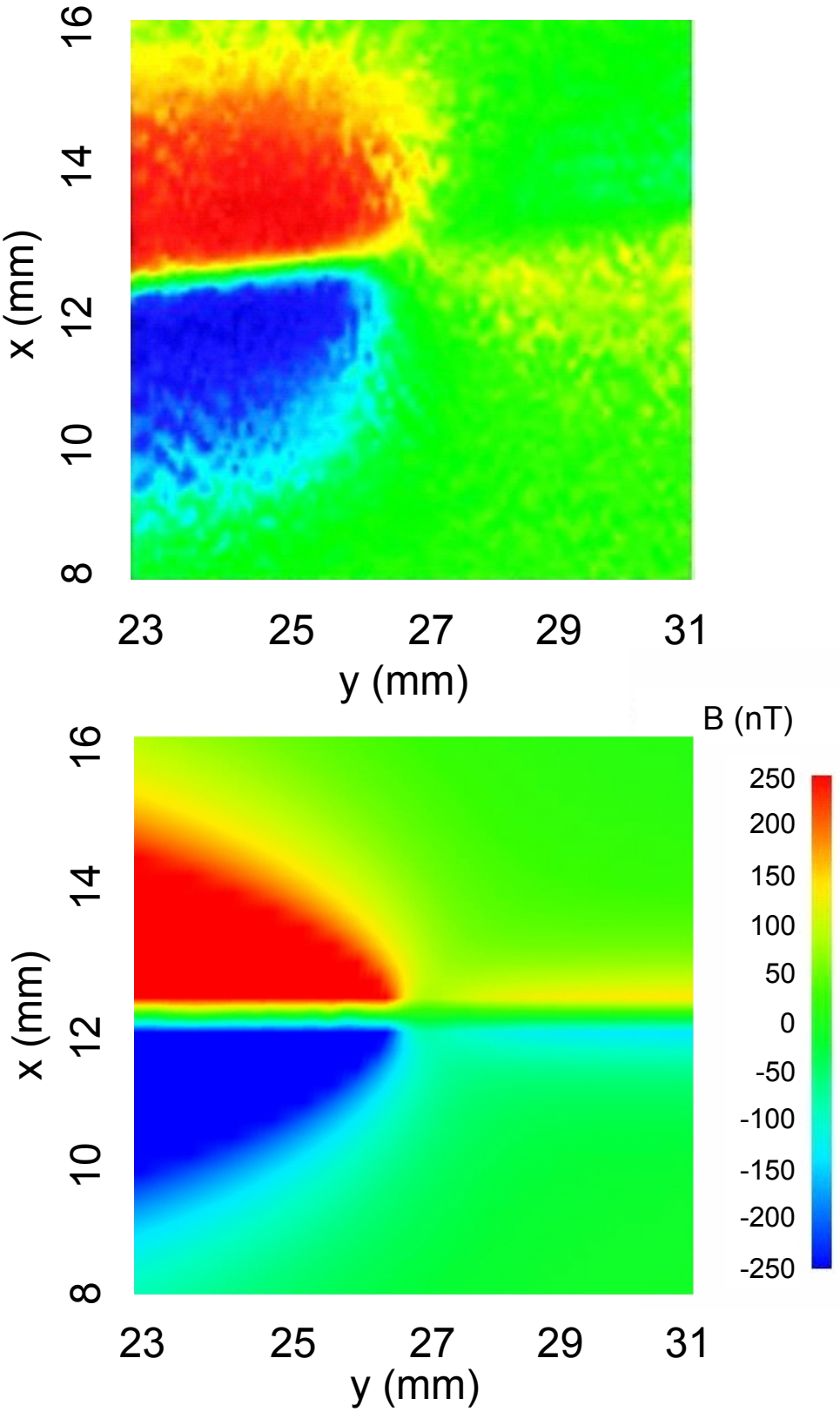

Fig. 9.35. (a) Measured magnetic field $B_z(x,y,t)$ 200 μm above open in microstrip line [same as Fig. 9.33(f)]. (b) Corresponding FEKO simulation of 200 μm wide microstrip line with 167 μm wide cut.

I note that the voltage is a maximum at the gap (antinode), so effects from coupling to the line voltage would be largest there.

9.6 Noise and Measured Bandwidth of the Microscope

From the data described in section 9.3 on the microstrip transmission line, I can estimate the bandwidth of the microscope. Just qualitatively, these results suggest that the microscope had a bandwidth of approximately 2 GHz. Of course these were particular results with pulse times of 400 ps. However, I tried other pulse lengths and these results were the best I was able to obtain.

The degradation of the images at high frequencies is quite striking. For example, Fig. 9.36 shows three 2D images of $B_z(x,y)$ of the microstrip line of Fig. 9.12 at 2 GHz, 2.5 GHz, 3 GHz, and 3.5 GHz, respectively. Red indicates the B-field pointing out of the page and blue indicates the B-field pointing into the page. Examination of Fig. 9.36 reveals a complete degradation of the image quality at 3 GHz and above due to increasingly large "noise" or "ripple".

For the data in Fig. 9.36, I used the analysis I described in section 9.1 to estimate the root-mean-square magnetic flux noise σ_Φ from the spread of the switching histogram. For the data in Fig. 9.39(a), I found $\sigma_\Phi \approx 23.1\ \mathrm{m}\Phi_0$. By averaging for $n = 2 \times 10^4$ pulses, I could reduce the uncertainty of the average flux to $\sigma_{N,\Phi} = \frac{\sigma_\Phi}{\sqrt{N}} = 163.5\ \mu\Phi_0$.

Given a total measurement time of 1 ms with this measurement scheme (using 2×10^4 shots in a 1 ms)

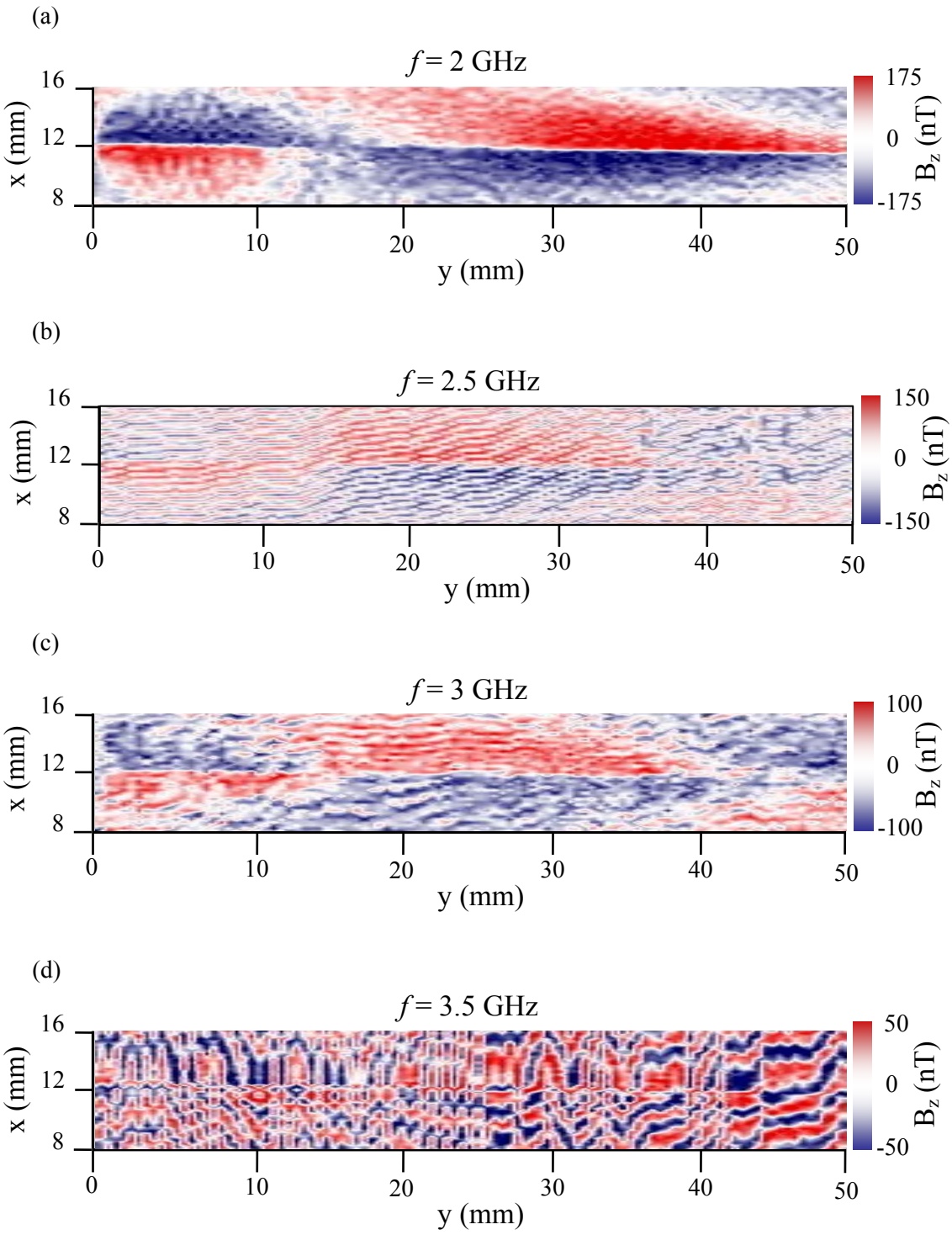

Fig. 9.36. Degradation of images above 2 GHz. (a) Top down view of magnetic field over the microstrip line with applied microwave frequency $f = 2$ GHz, (b) $f = 2.5$ GHz, (c) $f = 3$ GHz, and (d) $f = 3.5$ GHz.

and the equivalent root flux noise power spectral density is:

$$\sqrt{S_\Phi} \cong \frac{\sigma_{N,\Phi}}{\sqrt{f_{BW}^{meas}}} = \frac{1.6\,\mu\Phi_0}{\sqrt{Hz}}. \tag{9.1}$$

With a SQUID area of 300 μm^2 the single-shot uncertainty in the magnetic field is $\sigma_B \approx$ 77.1 nT. Similarly for a 1 ms measurement time the uncertainty in the average magnetic field found from 2x10^4 shots is $\sigma_{N,B} = \frac{\sigma_B}{\sqrt{N}} = 0.55nT$ and the equivalent root magnetic field power spectral density is:

$$\sqrt{S_B} \cong \frac{\sigma_{N,B}}{\sqrt{f_{BW}^{meas}}} = \frac{43.5\,pT}{\sqrt{Hz}}. \tag{9.2}$$

The impact of this noise is not negligible, especially when trying to detect high frequency signals. As can be seen by comparing Fig. 9.36(a) to Fig. 9.36(c), there is a lot of additional noise in the image at 3 GHz. When the frequency is further increased up to 3.5 GHz, there is only noise in the image [see Fig. 9.36(d)]. Figure 9.37(a) shows the single shot noise in these pictures versus frequency.

By comparing the measured peak magnetic field $B_z^{\max}$ to the actual field applied to the SQUID versus frequency, I can also extract the bandwidth of my system. Here I assume the applied field is equivalent to the magnetic field from the current flowing in a wire. Figure 9.37(b) shows the ratio of measured to applied field versus frequency ranging from dc to 4 GHz. A -3 dB or 50% degradation in amplitude is evident by 2 GHz; *i.e*. the bandwidth of the system is about 2 GHz. In chapter 10, I show that these results are in rough agreement with simulations of the SQUID dynamics.

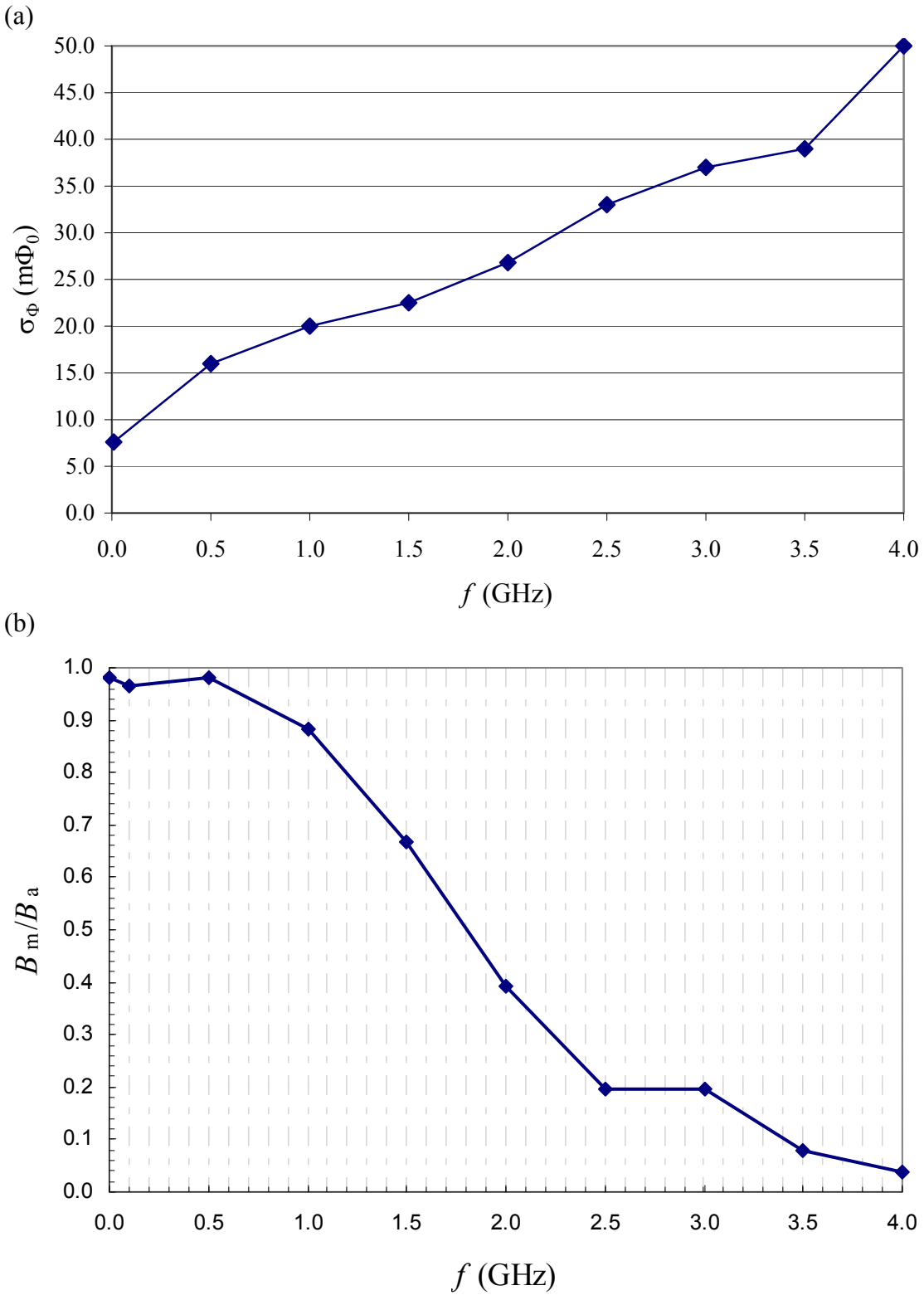

Fig. 9.37. (a) Single shot noise in Fig. 9.39(a-d) versus frequency. (b) The ratio of measured magnetic field $B_z(x,y,t)$ to applied field versus frequency. A -3 dB or 50% reduction in magnetic field occurs by approximately 2 GHz.

9.7 Summary

In this chapter, I described a SQUID microscope for imaging small high-frequency periodic magnetic fields up to about 3 GHz with a single-shot noise level of about 80 nT. I measured the *B*-field at distances down to about 200 μm, using a 4 K cryocooled scanning SQUID microscope, thereby demonstrating that the sampling method can be used in a practical scanning SQUID system. I tested the microscope by imaging three samples: a magnetic dipole, a microstrip transmission line and a microstrip line with a gap. The images of the microstrip line with an open gap demonstrated that it may be possible to use the microscope as a tool to find the location of open faults in electronic circuits. Once the fault is localized to a small region, standard failure analysis tools could be used to analyze the physical nature of the fault. Finally, I estimated the bandwidth of the SQUID microscope using the magnetic field data taken over the microstrip line at frequencies from dc to 4 GHz. I qualitatively estimated the bandwidth of the microscope to be in the 2-3 GHz range. Alternatively, I compared the ratio of measured magnetic field $B_z(x,y,t)$ to the applied field versus frequency and found a bandwidth of about 2 GHz.

Chapter 10: Conclusions and Suggestions for Improvements to the Microscope

As discussed in chapter 9, I found that I could image waves at frequencies up to about 2 GHz. In this chapter I put this into perspective by reviewing the time constants relevant to the microscope in order to estimate the bandwidth of my system. I then present a numerical approach to modeling the microscope and extract an estimate for the bandwidth. I next compare the simulation with my measurements of the flux versus frequency. Finally, I comment on the limits of pulsed SQUID sampling technique and conclude by offering some possible design improvements for the microscope for future reference.

10.1 Ultimate Bandwidth of SQUID Microscopy

As I discussed in chapter 4, there are several time constants in the system. They are τ_{RC}, τ_P, τ_J, τ_C, where:

$$\tau_{RC} = RC \,, \tag{10.1}$$

is the ring down time of the SQUID,

$$\tau_P = \sqrt{\frac{\pi hC}{2eI_0}} \tag{10.2}$$

the period of the plasma oscillation (for an unbiased junction),

$$\tau_J = \frac{\Phi_0}{2\pi I_0 R}, \tag{10.3}$$

is the period of the Josephson oscillation at voltage I_0R, and

$$\tau_C = \frac{2\Delta C}{eI_0}, \tag{10.4}$$

is the switching time, i.e. the time it takes the junction to charge up to the gap energy. Recall also that τ_{RC}, τ_J and the Stewart-McCumber hysteresis parameter β_C are related by

$$\beta_C = \frac{\tau_{RC}}{\tau_J} = \frac{2\pi I_C R^2 C}{\Phi_0}. \tag{10.5}$$

For a hysteretic SQUID to detect flux in a conventional manner means that the flux signal should be varying more slowly then all of the time constants. For a hysteretic SQUID one has $\beta_C > 1$, and thus $\tau_{RC} > \tau_J$. For my SQUID parameters (see Table 4.1) and assuming R = Z = 25 Ω I find $\tau_{RC} \cong 70\,\text{ps}$, $\tau_J \cong 0.6\,\text{ps}$, $\tau_P \cong 13\,\text{ps}$, and $\tau_C \cong 350\,\text{ps}$. Thus the longest time constant is τ_c and if it determined the bandwidth we would find

$$\Delta f < \frac{1}{2\pi\tau_c} = 0.45\,GHz. \tag{10.6}$$

On the other hand, τ_c is just the time it takes for the voltage signal to build up to its full value after the SQUID has escaped to the voltage state. But this description suggests in some sense that the measurement ha already taken place (when the escape occurred) and τ_c is just a waiting time for this signal to build up to the point where we detect it. Thus we expect that τ_c and Equation (10.6) do not set the bandwidth limit.

It is worth remarking that when $\beta_C = 1$, the SQUID is critically damped and $\tau_{RC} = \tau_J \left(Q = \sqrt{\beta_C} = 1\right)$ where it would be expected to have the largest bandwidth. For larger values of β_C (and thus Q) the device is under-damped and the expected bandwidth would be limited by the Q. For my SQUID, the designed junction capacitance is C = 2.8

pF. My device is unshunted, but it is wired to leads that connect to two 50 Ω coaxial lines. Assuming an impedance $Z = 25\ \Omega$ divided equally across both junctions, we obtain an RC time constant $\tau_{RC} = 71$ ps or a bandwidth of:

$$\Delta f_{RC} = \frac{1}{2\pi RC} = \frac{1}{2\pi\tau_{RC}} = \frac{10^{12}}{2\pi \times 70} \approx 2\,\text{GHz}. \tag{10.7}$$

10.2 Calculated Bandwidth of the Microscope

To check that Δf_{RC} is indeed the time constant that sets the SQUID bandwidth, I used Mathematica [2] to solve the SQUID equations (see Appendix A). The SQUID equations comprise Eqs. 3.46 and 3.48 with the additional constraint on the phase represented by Eq. 3.49. Because the SQUID equations are a system of nonlinear differential equations, an analytical solution is not feasible, and so I numerically solved them. The Mathematica function NDSolve [2] is a general purpose numerical differential solver. It can handle a wide range of ordinary differential equations (ODEs) [3,4]. In general, NDSolve finds solutions iteratively by starting at a particular value of time t, and then taking a sequence of steps, working towards covering a specified range in time from t_{min} to t_{max}. NDSolve is an adaptive routine; if the solution begins to vary rapidly in a particular region, then the routine will reduce the step size or change method so as to better keep track of the solution.

The SQUID equations are not only nonlinear but they are also stiff differential equations [5]. Stiff equations have several components varying with time t at extremely different rates. Stiffness relates to the kind of problem, the initial data, numerical method, and error tolerance demanded. Fortunately, NDSolve can automatically switch between a nonstiff and stiff solver. The stiffness switching method uses a pair of extrapolation

methods as the default. In particular, I used the implicit Backwards Differentiation Formula (BDF) and found this to be quite robust in solving the SQUID equations [5].

To verify the code was operating correctly I calculated the critical current I_C versus applied flux Φ_a by increasing the bias current and monitoring when the SQUID switches to the voltage state, I then compared these results to the method described by Tesche and Clarke [6]. The code verification program (called $I_c vs \Phi_0$ see Appendix A) used the parameters in Table 4.1 as the parameters in the numerical solution of the SQUID equations (Eqs. 3.46, 3.48, and 3.49) and the solution method of Tesche and Clarke. Following the solution of the SQUID equations the solution via the other method is calculated and then both methods are compared by plotting them together on the same plot. The Tesche and Clarke approach assumes that the bias current I_b is sufficiently low so that no voltage is produced across the SQUID. In their method, they obtain two expressions which can be expressed as a function of a single variable. Using a Newton-Raphson search routine in one variable only, I can determine the maximum supercurrent, I_c as a function of Φ_a.

Figure 10.1 shows results from the numerical solution using the method of Tesche and Clarke (blue points) overlaid on the results I found by solving the SQUID equations (red curve) for the parameters listed in Table 4.1. Voltage noise is ignored in both cases. The *y*-axis is critical current I_C and the *x*-axis is applied flux in units of the flux quantum. Notice that for applied flux $\Phi = 0$ we $I_C = 2I_0 = 41.22\ \mu A$, as expected, while at $\Phi = 0.5\Phi_0$, we have $I_c \approx 9\ \mu A$. In fact, examination of the plot shows that the two methods give identical results, as expected.

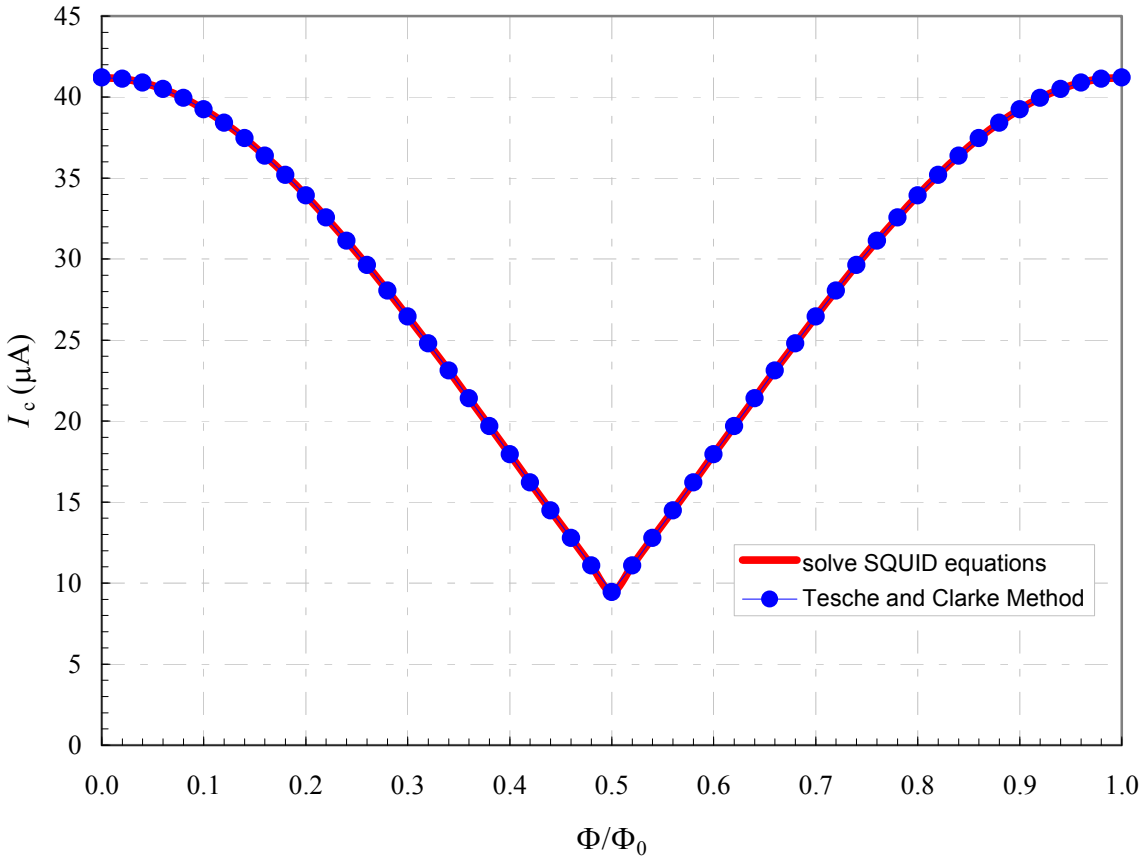

Fig. 10.1. Critical current versus applied flux. Red curve is the result of solution of SQUID equations and blue dots are results from the method due Tesche and Clarke [6].

I then used the code $I_c$vsΦ_0 as the main routine to model the microscope response across a broad frequency spectrum. Again, I used Mathematica [2] to model my scanning hysteretic SQUID microscope operation (see Appendix B). This time the problem was divided into two parts in order to simulate the way the data were taken. First, I allowed the system to evolve while applying the time-varying magnetic flux but without applying a current pulse. This allowed for the system to evolve and reach equilibrium from t = -10 ns to 0 ns. For this time period I used an implicit Runge-Kutta method of solution. Next, the current pulse was activated, again with the dc and microwave magnetic flux applied as well. This part of the simulation would last from 0 ns to 10 ns or until the system

reached equilibrium during which time I found the voltage versus time as in the actual experiment. If the device switched to the running state, this would correspond to a switching voltage or $I_0 > I_C$. The resulting simulations could then be used to construct the calculated response from the SQUID as an effective flux signal, just as in the experiment. For this second part of the simulation I used a BDF method of solution. Details of the simulation are presented in Appendix B.

To understand the bandwidth, I simulated the SQUID voltage V versus time t for applied flux of different frequencies. For these simulations I assumed an incremental flux step 5 mΦ_0, a flux bias of $\Phi = 0.25\ \Phi_0$ and ac applied flux of $0.05\ \Phi_0$. I let the system oscillate for 10 nanoseconds and then applied a current pulse of 23 μA and 400 ps duration. Figure 10.2 shows the ratio of calculated flux to applied flux ($\Phi_a = 0.05\ \Phi_0$) Φ_m/Φ_a and the x-axis is the frequency of the applied flux ranging from dc to 5 GHz in steps of 250 MHz. The response from dc to 0.5 GHz is nearly flat, with a -3 dB at about 1.5-2 GHz. This behavior is similar to the measured data (see Fig. 10.2) and roughly consistent with $1/\tau_{RC} \approx 2$ GHz.

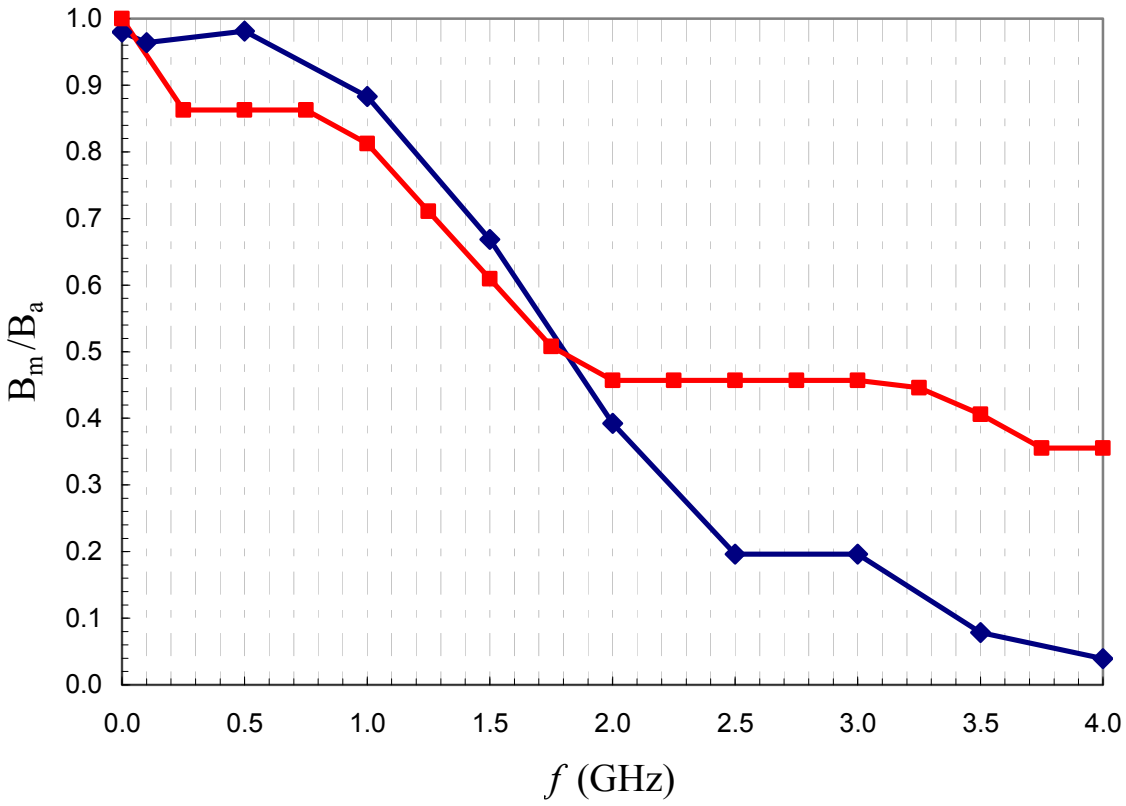

Fig. 10.2. Comparison of simulation (red squares) and measured (blue diamonds) ratio of measured flux to applied flux signal versus frequency. Applied flux $\Phi_a = 0.05\ \Phi_0$ using 250 MHz steps. Measured data are the same as in Fig. 9.37b.

10.3 Limits of the Pulsed SQUID Sampling Technique

In chapter 6, I described the pulsed synchronous sampling technique I used to measure rapidly varying signals. This technique works for repetitive flux signals because the current pulse can be synchronized to or triggered from a clock that is synchronized to the flux signal. For my SQUID, I found a bandwidth limit of about 2 GHz. To achieve this limit, the pulse generator must produce a short enough pulse. I used an AVTECH AVP-1 pulse generator with a minimum pulse width of 400 ps and a maximum pulse rate of 1 MHz. Naively, this pulse width implies a maximum bandwidth of $\Delta f = 1/2\pi\tau = 400\,\text{MHz}$. However, the nominal pulse width is not the whole story. For

example, J. Matthews and I were able to measure a 1 GHz test signal with a current pulse width of 10 ns [7]. For these measurements, we used a time delay with respect to the signal under test with increments of just 10 ps. Naively, one expects that for a pulse with a 10 ns duration, you would average over a 1 GHz signal and only see a constant value. Instead we saw a well-defined sine wave at 1 GHz [7]. The likely explanation for this discrepancy is that although the current pulses had a nominal square shape with a 10 ns long duration, the shape was distorted by the time it reached the SQUID. Since only the peak current is important, ringing or some rounding of the pulse could lead to a pulse that was effectively much shorter.

Needless to say, there are pulse generators which can produce pulse widths of 100 ps or less [8-11] so the availability of better generators is not a serious limitation to the technique.

10.4 Microscope Design Improvements

Future improvements in the microscope can take several parallel directions: 1) improving the cold-finger and design of the vibration isolation, 2) improving the speed of the data collection, 3) eliminating the field distortions evident at high frequency, and 4) extending the bandwidth beyond 2 GHz.

Improving the cold-finger and vibration isolator would address several difficulties. In general, with the current design if any significant work is required on the microscope it is best to remove the cryocooler from the vacuum chamber. In particular most of the cold-finger thermometers and wiring are surrounded by the 1st-radiation shield and getting access to this shield requires removal of the cryocooler. Given the weight of the system and the great care that must be taken to remove the cryocooler, it

would be very helpful to redesign things so that maintenance was not so challenging. Two modifications that quickly come to mind are redesigning the cold finger and Kevlar thread network so that both could be installed or removed without the need to remove the cryocooler.

A cold finger that could be inserted after the cryocooler is installed into the vacuum chamber would be ideal. One scheme would be to split the cold finger into two parts. The first part would be installed onto the cryocooler prior to the cryocooler being installed into the vacuum chamber. The second part could then be "plugged" into the first part of the cold finger. If silver paint connections failed, then the fiberglass cone could be removed and the cold-finger could just be unplugged. This would also allow greater flexibility in replacing SQUIDs or using hysteretic or non-hysteretic SQUIDs with different spatial and electrical properties. Additionally, the plug-in cold finger concept could be expanded beyond just SQUID tips to allow for other cryogenic sensors to be plugged in. For example, a single-photon bolometer, SNS mixer or a single-electron transistor (SET) [12] (an extremely sensitive electric field sensor) could replace the SQUID on the cold tip.

The Kevlar thread suspension system could also benefit from a redesign. Currently, the Kevlar threads are installed after the window and bellows assembly is installed. They are attached to the cold finger and then to the frame inside the window bellows assembly. Installing the Kevlar threads is quite time consuming and painstaking work. Each string is installed and tightened individually under an optical microscope using a mirrored prism in order to view the correct place to attach each string. Each thread is attached to the cold finger and threaded through holes in the radiation shield

before being attached to the frame in a manner similar to attaching a guitar string to a tuning post. I made my own tuning posts by drilling a transverse hole into each of the six brass screws used to secure the threads to the frame (see Fig. 6.16). I passed a thread through the hole, tied it around the screw, and then tightened or loosened each screw as needed to align the cold finger. Generally I installed the top three Kevlar threads first in order to suspend the cold finger so I didn't have to hold it up. Then I attached the last three treads. I then tightened each thread one at a time while keeping the cold finger centered in the window assembly. I cycle through each thread several times in order to finally have a centered and tightened cold finger with the tension on each string being approximately 30 lbs. In addition, one must check very carefully to ensure that none of the threads touch the heat shields. Once the threads are installed, you would need to dissemble all of them to remove the cold finger. It would be easier if you could individually tighten each string without affecting the tip alignment. I did a preliminary design for a ratchet and pawl mechanism that would reside on the frame and would allow me to tighten each string after it was installed, so some improvement is certainly conceivable.

Further, it would be helpful if these design changes were incorporated into a redesign of the window assembly. That is, the window assembly should be re-designed to allow the user to install the cold finger and work on the Kevlar suspension system while the window assembly is sitting on the lab bench. Then the entire window assembly could be installed onto the microscope. This would require a major redesign, and considerably more thought would need to be given as to how this can be done.

Finally, reducing the diameter of the sapphire rod would allow for a fiberglass cone with a sharper aspect ratio to be used. A cone with a sharper aspect ratio makes it easier to insert the microscope into electronic samples where access is limited by neighboring components.

A final issue is the relatively long time to acquire images. Currently, the main limitation is the program I use to collect data and control the *xy*-scanning stages. Labview is a command-string based instrument control software package. As such, it adds a large amount of "overhead" in terms of the time for each command string to be executed. This is particularly true for a real-time data acquisition system, such as my microscope. A faster approach would be to program the actual data collection into a buffer which could execute uninterrupted until the image or at least a line scan had completed. This would potentially decrease acquisition time from hours or less than an hour.

10.5 Summary of Work

In this thesis, I designed, developed and operated a large-bandwidth scanning SQUID microscope for spatially imaging high frequency magnetic fields. Towards this end, I presented results on a cryo-cooled 4.2 K scanning SQUID microscope. The system achieved a bandwidth of about 2 GHz and a sensitivity of about 50 nT per sample. I used a thin-film hysteretic Nb dc-SQUID with a critical current of 20.61 μA and an area of 300 μm^2. To read out the SQUID, I used a pulsed sampling technique, rather than a flux-locked loop, and this allowed me to overcome the bandwidth limitations of existing scanning SQUID microscopes. The microscope allows for non-contact images of time-varying magnetic field to be taken of room temperature samples with time steps down to 50 ps and spatial resolution ultimately limited by the size of the SQUID to about 10 μm

or the thickness of the thin sapphire window that separates the SQUID from room temperature air. In particular, I achieved a spatial resolution of about 200 μm in test images.

The pulsed current readout scheme I used involves pulsing the bias current to the SQUID while the voltage across the SQUID is monitored. Using a fixed pulse amplitude and applying a fixed dc magnetic flux allows the SQUID to measure the applied magnetic flux with a sampling time set by the pulse length of about 400 ps.

To demonstrate the imaging capabilities of the microscope I imaged magnetic fields from room temperature samples in air from 0 Hz (static fields) up to 3 GHz. Samples included a magnetic loop, microstrip transmission lines, and microstrip lines with a break in order to act as a test sample for localizing electrical opens in circuits.

Finally, I discussed the operation and modeling of the SQUID and compared this to my results for the bandwidth. I found that the simulations qualitatively agreed with my measured bandwidth of about 2 GHz and suggest further improvements in bandwidth should be possible.

Appendix A

Mathematica Code for solving SQUID equations to calculate critical current I_c versus applied flux Φ_a.

In this appendix, I describe the Mathematica notebook I used for solving the SQUID's differential equations in order to calculate the critical current I_c versus applied flux Φ_a. The SQUID equations can be found in Chapter 3. The code is based on Mathematica version 6.0. I used this code to estimate the bandwidth of my system.

```
(* Solve the dc SQUID equations as they appear in the "SQUID Handbook" by  Clarke's
(see eqs. 2.37-2.39) *)

Off[General::spell1]
Clear ["Global`*"]

(* Physical constants *)

Φ0=2.0678 10^-15;
μ0=4π 10^-7;
(* Frequency *)
f=1.0 10^9;
ω=2π f;

(* System Parameters *)
(* For a symmetric SQUID  *)

C1=2.8 10^-12;
C2=2.8 10^-12;

C0=(C1+C2 )/2;

R1 = 100.0;
R2 = 100.0;
```

I_{01}= 20.61 10^{-6};
I_{02}= 20.61 10^{-6};

$I_0=(I_{01}+I_{02})/2$;

(* SQUID Loop *)
d=10.0 10^{-6};
L_g=1.25 μ0 d;

L=L_g;

βL=(2 L I_0)/Φ0;

dcSQUID[δ01_,δ02_,v01_,v02_,Idc_,Tstart_,Tend_]:={Φ0/(2π) C_1 δ1''[t]+Φ0/(2π) 1/R_1 δ1'[t]+ I_{01}Sin[δ1[t]]==(Idc+CurrentPulse[t])/2+(Φ0/(2π L) (δ2[t]-δ1[t])-(ΦDC+Φa[t])/L),

Φ0/(2π) C_2 δ2''[t]+Φ0/(2π) 1/R_2 δ2'[t]+ I_{02} Sin [δ2[t]]==(Idc+CurrentPulse[t])/2-(Φ0/(2π L) (δ2[t]-δ1[t])-(ΦDC+Φa[t])/L),

δ1[Tstart]==δ01, δ2[Tstart]==δ02, δ1'[Tstart]==v01, δ2'[Tstart]==v02}

I_B=0.00 10^-6;

PulseStart=0.0 10^-9;
PulseWidth=400.0 10^-12;
CurrentPulse[t_]=I_B(UnitStep[PulseStart+PulseWidth-t]-UnitStep[(PulseStart-t)]);

ΦDC :=ΦRDC* Φ0
Φa[t_]:=ΦRA* Φ0 Sin[ω t]

dccurrent={};
criticalcurrent={};
Φrelative={};
δ01min={};
δ02min={};

ΦRDC=0.0;
ΦRA=0.0;

While[ΦRDC≤1.0,

```
Idc=0.0 10^-6;
△I=1.0 10^-6;
△Imin=0.001 10^-6;

δ1temp={};
δ2temp={};
v1temp={};
v2temp={};

δ01=0.0;
δ02=(2π )/Φ0  ΦDC;
v01=0.0;
v02=0.0;

Vtend=0.0;

Tstart=0.0;
Tend=5.0 10^-9;

While[△I≥△Imin,

  sol=NDSolve[dcSQUID[δ01,δ02,v01,v02,Idc,Tstart,Tend],  {δ1, δ2},{t,Tstart,
Tend},
      Method→"Automatic",AccuracyGoal→6,PrecisionGoal→6,
MaxSteps→50000000];

  δ1sol[t_] = δ1[t] /. sol[[1]];
      δ2sol[t_] =δ2[t] /. sol[[1]];

       v1sol[t_] =δ1'[t]/. sol[[1]];
       v2sol[t_] =δ2'[t] /. sol[[1]];

  a1sol[t_]=δ1''[t] /. sol[[1]];
  a2sol[t_]=δ2''[t] /. sol[[1]];

  δ01=δ1sol[Tend];
  δ02=δ2sol[Tend];
  v01=v1sol[Tend];
  v02=v2sol[Tend];
  a01=a1sol[Tend];
  a02=a2sol[Tend];

   Vtend =Φ0/(4π) (v1sol[Tend]+v2sol[Tend]);
```

```
  (* Print["Subscript[I, DC]=", Idc," ,Tend=",Tend," ,V[t]=", Vtend,   " ,Subscript[Φ,
Subscript[R, DC]]=", ΦRDC]; *)
  (* Print["δ1sol[Tend]=",δ1sol[Tend]," ,δ2sol[Tend]=",δ2sol[Tend]]; *)(*
Print["v1sol[Tend]=",v1sol[Tend]," ,v2sol[Tend]=",v2sol[Tend]]; *)
  (* Print["a1sol[Tend]=",a1sol[Tend]," ,a2sol[Tend]=",a2sol[Tend]]; *)
  (* Print[" Maximum Memory Used= ", MaxMemoryUsed[]," bytes"]; *)
  (* Print[" "]; *)

  AppendTo[δ1temp,δ01];
  AppendTo[δ2temp,δ02];
  AppendTo[v1temp,v01];
  AppendTo[v2temp,v02];

  o=Length[δ1temp];
  p=Length[δ2temp];
  q=Length[v1temp];
  r=Length[v2temp];

  If[Vtend<100.0 10^-6,
   δ1min=δ01;
   δ2min=δ02;
   v01=0.0;
   v02=0.0;

   Idc=Idc+△I,

   δ01=δ1min;
   δ02=δ2min;
   v01=0.0;
   v02=0.0;

   △I=△I/2;
   Idc=Idc-△I];

  AppendTo[δ01min,δ01];
  AppendTo[δ02min,δ02];

  aa=Length[δ01min];
  bb=Length[δ02min];

  ];

 AppendTo[dccurrent,Idc];
 AppendTo[Φrelative,ΦRDC];

  m=Length[dccurrent];
```

```
 n=Length[Φrelative];

 AppendTo[criticalcurrent,dccurrent[[m]]];
 s=Length[criticalcurrent];

 Print["I_C=   ",criticalcurrent[[s]]];
 Print[" "];

 ΦRDC=ΦRDC+0.05;
 ];
```

I_C= 0.0000412197
I_C= 0.0000407158
I_C= 0.0000392471
I_C= 0.0000369326
I_C= 0.0000339248
I_C= 0.0000303838
I_C= 0.000026450
I_C= 0.0000222627
I_C= 0.0000179463
I_C= 0.000013626
I_C= 9.44238×10^{-6}
I_C= 0.000013626
I_C= 0.000017946
I_C= 0.0000222627
I_C= 0.0000264502
I_C= 0.0000303838
I_C= 0.0000339248
I_C= 0.0000369326
I_C= 0.0000392471
I_C= 0.0000407158
I_C= 0.0000412197

dccurrent

{0.0000412197,0.0000407158,0.0000392471,0.0000369326,0.0000339248,0.0000303838,0.0000264502,0.0000222627,0.0000179463,0.000013626,9.44238×10^{-6},0.000013626,0.0000179463,0.0000222627,0.0000264502,0.0000303838,0.0000339248,0.0000369326,0.0000392471,0.0000407158,0.0000412197}

criticalcurrent

{4.12197×10^{7},4.07158×10^{7},3.92471×10^{7},3.69326×10^{7},3.39248×10^{7},3.03838×10^{7},2.64502×10^{7},2.22627×10^{7},1.79463×10^{7},1.3626×10^{7},9.44238×10^{6},1.3626×10^{7},1.79463×10^{7},2.22627×10^{7},2.64502×10^{7},3.03838×10^{7},3.39248×10^{7},3.69326×10^{7},3.92471×10^{7},4.07158×10^{7},4.12197×10^{7}}

```
criticalcurrent=(1.0 10^-6) criticalcurrent
{41.2197,40.7158,39.2471,36.9326,33.9248,30.3838,26.4502,22.2627,17.9463,13.626,9.
44238,13.626,17.9463,22.2627,26.4502,30.3838,33.9248,36.9326,39.2471,40.7158,41.21
97}
Φrelative
{0.,0.05,0.1,0.15,0.2,0.25,0.3,0.35,0.4,0.45,0.5,0.55,0.6,0.65,0.7,0.75,0.8,0.85,0.9,0.95,1.
}
L=Length[Φrelative]
21
ΦRversusIc=Table[{Φrelative[[i]],criticalcurrent[[i]]},{i,1,L}]
{{0.,41.2197},{0.05,40.7158},{0.1,39.2471},{0.15,36.9326},{0.2,33.9248},{0.25,30.38
38},{0.3,26.4502},{0.35,22.2627},{0.4,17.9463},{0.45,13.626},{0.5,9.44238},{0.55,13.
626},{0.6,17.9463},{0.65,22.2627},{0.7,26.4502},{0.75,30.3838},{0.8,33.9248},{0.85,
36.9326},{0.9,39.2471},{0.95,40.7158},{1.,41.2197}}
plt1=ListPlot[ΦRversusIc, PlotJoined→True,
PlotRange→{0.0,50},PlotStyle→{Thickness[.005],
Hue[1.00]},TextStyle→{FontFamily→"Times",FontSize→18},Frame→True,FrameLabel→
{"Φ0","I_C (μA)"},GridLines→{{0.0,0.1,0.2,0.3,0.4,0.5,0.6,0.7,0.8,0.9,1.0},Automatic}]
```

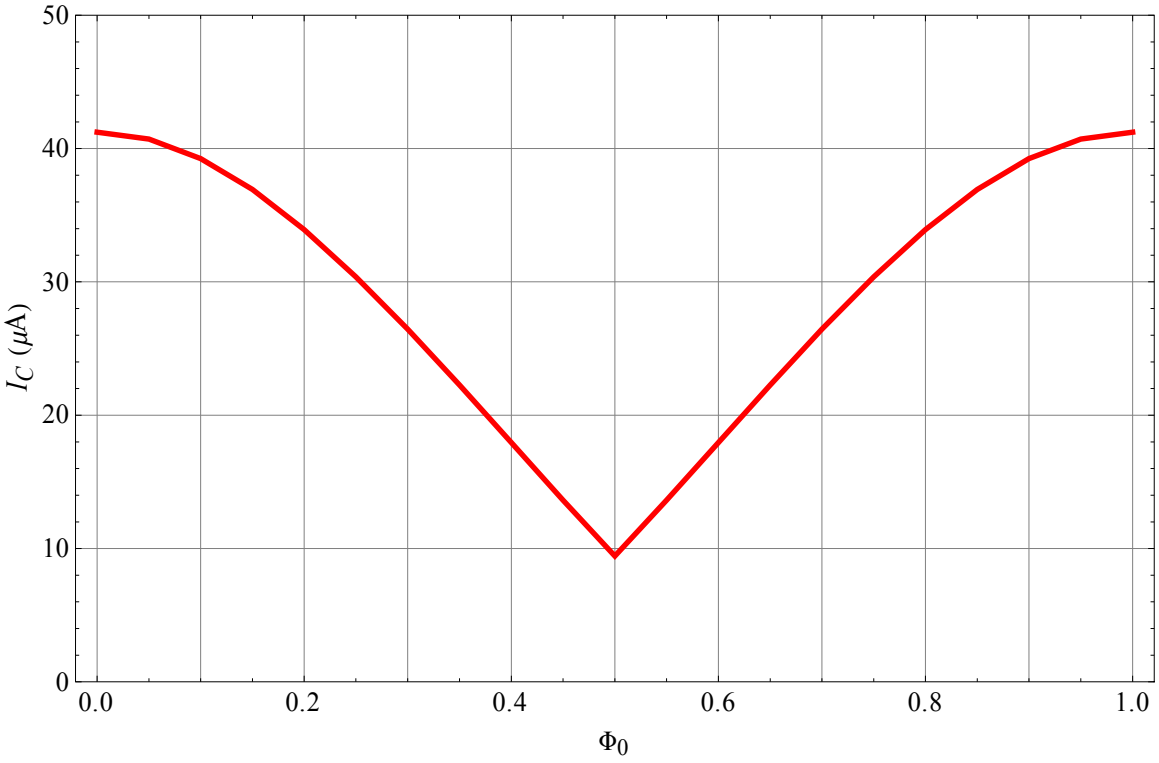


```
(* Tesche Thesis equations 3.4 and 3.5 Icversus applied flux *)

Φalist={};
δ1list={};
Iclist={};
```

```
(* Physical constants *)

Φ0=2.0678 10^-15;
μ0=4π 10^-7;
(* Frequency *)
f=1.0 10^9;
ω=2π f;

(* System Parameters *)
(* For a symmetric SQUID  *)

C1=2.8 10^-12;
C2=2.8 10^-12;

C0=(C1+C2 )/2;

R1 = 100.0;
R2 = 100.0;

I01= 20.61 10^-6;
I02= 20.61 10^-6;

I0=(I01+I02)/2;

(* SQUID Loop *)
d=10.0 10^-6;
Lg=1.25 μ0 d;

L=Lg;

βL=(2 L I0)/Φ0;


(* Equation 3.4 *)
δ2:=δ1-2 π Φa-(π βL Ic)/2+π βL Sin[δ1]
(* Equation 3.5 *)
F[Ic_,δ1_]:=Ic- Sin[δ1]- Sin[δ2]


numsol:=FindRoot[{F[Ic,δ1]==0.0,∂δ1 (F[Ic, δ1]) ==0.0},{δ1,1.5},{Ic,1.5},
MaxIterations→500,AccuracyGoal→16]

Do[numsol;AppendTo[Φalist,Φa];AppendTo[δ1list,δ1 /. numsol];AppendTo[Iclist,Ic /.
numsol],{Φa,0.0,0.5,0.05}];
```

```
numsol:=FindRoot[{F[Ic,δ1]==0.0,∂δ1 (F[Ic, δ1]) ==0.0},{δ1,0.5},{Ic,1.5},
MaxIterations→500,AccuracyGoal→16]

Do[numsol;AppendTo[Φalist,Φa];AppendTo[δ1list,δ1 /. numsol];AppendTo[Iclist,Ic /.
numsol],{Φa,0.5,1.0,0.05}];

M=Length[Iclist];
Iclist=I0 10^6 Iclist;
ΦaVersusIc=Table[{Φalist[[i]],Iclist[[i]]},{i,1,M}];
plt2=ListPlot[ΦaVersusIc,
PlotJoined→False,PlotRange→{0.0,50},FrameLabel→{"Φ0","IC
(μA)"},PlotStyle→{PointSize[0.012],
Thickness[.005],Hue[0.65]},TextStyle→{FontFamily→"Times",FontSize→18},Frame→Tr
ue,GridLines→{{0.0,0.1,0.2,0.3,0.4,0.5,0.6,0.7,0.8,0.9,1.0},Automatic}]
```

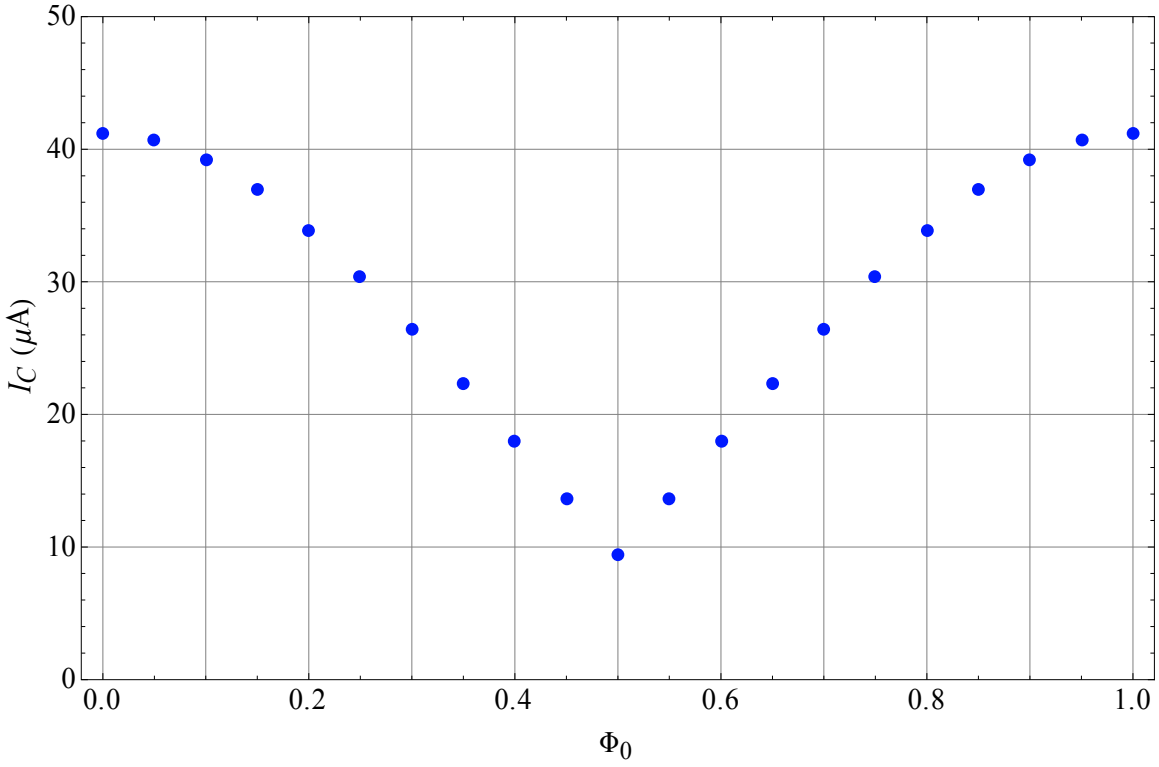


```
plt3=Show[plt1,plt2]
```

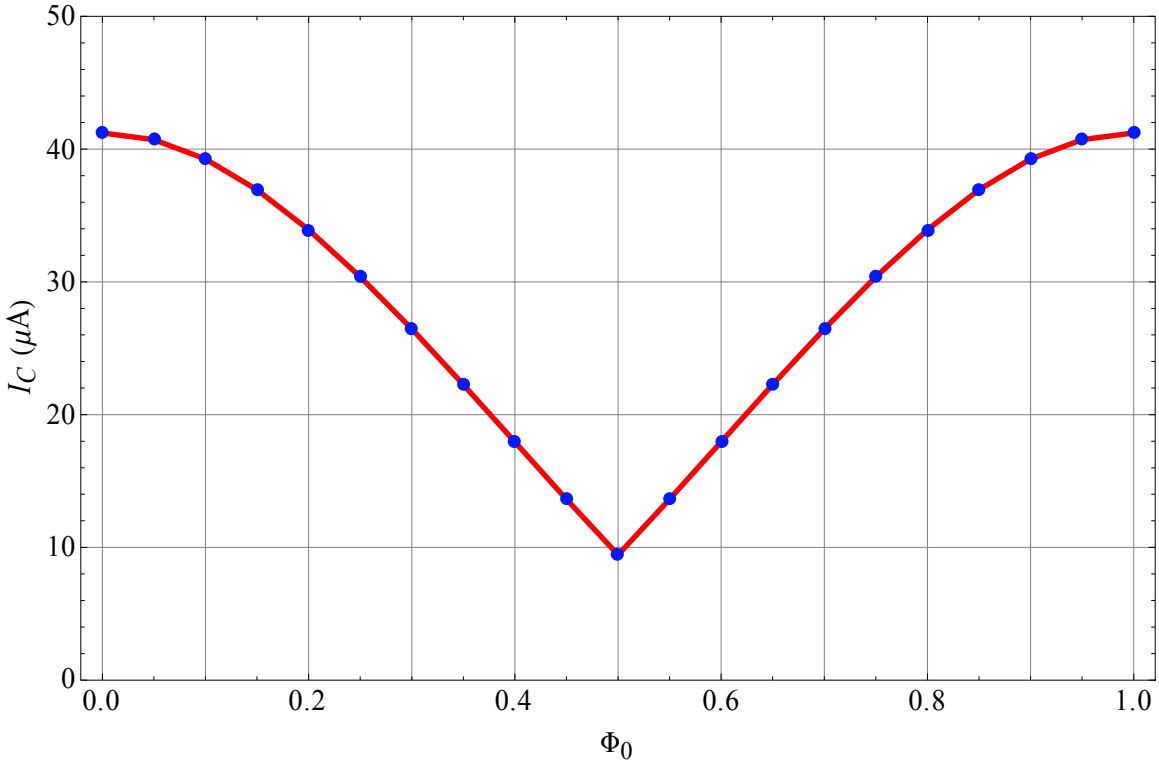

Appendix B

Mathematica Code for solving the SQUID equations to estimate the ratio of measured magnetic flux to applied flux versus frequency.

In this appendix, I provide the Mathematica notebook I used for solving the SQUID's differential equations in order to calculate the expected ratio of measured magnetic flux to applied flux Φ versus frequency. The SQUID equations can be found in Chapter 3. The code is based on Mathematica version 6.0. This code was used to estimate the expected bandwidth of my system.

```
Off[General::"spell1"]
<<"PlotLegends`"
Needs["ErrorBarPlots`"];
Needs["PlotLegends`"]
Clear["Global`*"]

Φ0=2.0678/10^15;
μ0=(4 π)/10^7;
C1=2.8/10^12;
C2=2.8/10^12;
C0=1/2 (C1+C2);
R1=150.0;
R2=150.0;
I01=20.61/10^6 ;
I02=20.61/10^6;
I0=1/2 (I1+I2);
d=10.0/10^6;
LG=1.25 μ0 d;
βL=(2 LG I0)/Φ0;
EJ=(I0 Φ0)/(2 π);


dcSQUID1[γ01_,γ02_,vγ01_,vγ02_,Torigin_,Tend1_]:={Φ0/(2π)
C1γ1''[t]+Φ0/(2π) 1/R1γ1'[t]+
I01Sin[γ1[t]]==(Idc/2)+(Φ0/(2π LG) (γ2[t]-γ1[t])-
(Φ0(Φdc+Φbias+Φa* Sin[ω t]))/LG),


 Φ0/(2π) C2 γ2''[t]+Φ0/(2π) 1/R2 γ2'[t]+ I02 Sin [ γ2[t]
]==(Idc/2)-(Φ0/(2π LG) (γ2[t]-γ1[t])-(Φ0(Φdc+Φbias+Φa*
Sin[ω t]))/LG),


 γ1[Torigin]==γ01, γ2[Torigin]==γ02, γ1'[Torigin]==vγ01,
γ2'[Torigin]==vγ02}


dcSQUID2[δ01_,δ02_,v01_,v02_,Tstart_,Tend2_]:={ Φ0/(2π) C1
δ1''[t]+Φ0/(2π) 1/R1 δ1'[t]+ I01Sin[δ1[t]]== ( 1/2 ( Idc +
CurrentPulse[t] ) ) + (Φ0/(2π LG) (δ2[t]-δ1[t])-
(Φ0(Φdc+Φbias+Φa* Sin[ω t]))/LG),
```

```
 Φ0/(2π) C2 δ2''[t]+Φ0/(2π) 1/R2 δ2'[t]+ I02  Sin[δ2[t]]== (
1/2 (Idc+CurrentPulse[t]) )-(Φ0/(2π LG) (δ2[t]-δ1[t])-
(Φ0(Φdc+Φbias+Φa* Sin[ω t]))/LG),


 δ1[Tstart]==δ01, δ2[Tstart]==δ02, δ1'[Tstart]==v01,
δ2'[Tstart]==v02}

frequencies={};
Φmaxratio={};

fstop=5.0 10^9;
Δf=250.0 10^6;
fstart=250.0 10^6;
f=fstart;

While[f≤fstop,

 Φsignal={};
 Φapplied={};

 (* Frequency of applied flux signal *)
  ω=2 π f;
 period=1/f;

 I_pulse=( 46.900097656249943 10^-6)/2;
   Idc=0;

 Φbias=0.2500;
  Φinitial=-0.060000;
 Φtemp=Φinitial;
 ΔΦ=0.005;
 Φa=0.05;

 ΔT=0.001 10^-9;

 Torigin=-5.0 10^-9;
 Tstart=0;
 Tend1=Tstart;
 Tend2=5.0 10^-9;

 Ttemp=0.0 10^-9;
 Tdstep=period/18;

 PulseWidth=400.0 10^-12;
 PulseStart=Tstart;
```

```
CurrentPulse[t_]:=I_pulse (UnitStep[PulseStart+PulseWidth-t]-
UnitStep[PulseStart-t]);

While[Ttemp≤period,

   Φdc=Φtemp;

   γ01=0.0;
   γ02=0.0;
   vγ01=0.0;
   vγ02=0.0;

  sol1=NDSolve[dcSQUID1[γ01,γ02,vγ01,vγ02,Torigin,Tend1],
{γ1, γ2},{t,Torigin, Tend1},
     Method-
>"ImplicitRungeKutta",AccuracyGoal→8,PrecisionGoal→8,MaxSte
ps→40000000];

   γ1sol[t_] = γ1[t] /. sol1[[1]];
         γ2sol[t_] =γ2[t] /. sol1[[1]];

         vγ1sol[t_] =γ1'[t]/. sol1[[1]];
         vγ2sol[t_] =γ2'[t] /. sol1[[1]];

    aγ1sol[t_]=γ1''[t] /. sol1[[1]];
     aγ2sol[t_] = γ2" [ t ]   /.   sol1[[1]];

    Vtend1 =Φ0/(4π) (vγ1sol[Tend1]+vγ2sol[Tend1]);

   (* Print["Subscript[T, origin]=",10^9 Torigin," ns","
Subscript[T, end1]=",10^9 Tend1," ns","  Subscript[T,
step]=",10^9 Ttemp," ns"]; *)
   (* Print["V[t]=",10^6 Vtend1," μV","   Subscript[Φ,
a]=", Subscript[Φ, a],"   Subscript[Φ, dc]=", Subscript[Φ,
dc]];  *)
   (* Print["γ1sol[Tend]=",γ1sol[Tend1],"
,γ2sol[Tend]=",γ2sol[Tend1]]; *)
   (* Print["vγ1sol[Tend]=",vγ1sol[Tend1],"
,vγ2sol[Tend]=",vγ2sol[Tend1]]; *)
   (* Print["aγ1sol[Tend]=",aγ1sol[Tend1],"
,aγ2sol[Tend]=",aγ2sol[Tend1]]; *)
   (* Print[" "]; *)

   δ01=γ1sol[Tend1];
   δ02=γ2sol[Tend1];
```

```
          v01=vγ1sol[Tend1];
          v02=vγ2sol[Tend1];


  sol2=NDSolve[dcSQUID2[δ01,δ02,v01,v02,Tstart,Tend2] ,
{δ1, δ2},{t,Tstart, Tend2},
     Method->"BDF",
AccuracyGoal→6,PrecisionGoal→6,MaxSteps→40000000];

           δ1sol[t_] = δ1[t] /. sol2[[1]];
           δ2sol[t_] =δ2[t] /. sol2[[1]];

           v1sol[t_] =δ1'[t]/. sol2[[1]];
            v2sol[t_]   =δ2'[t]   /.   sol2[[1]];

          a1sol[t_]=δ1''[t] /. sol2[[1]];
          a2sol[t_]=δ2''[t] /. sol2[[1]];

    Vtend[t_] =Φ0/(4π) (v1sol[t]+v2sol[t]);

   tstep=Tstart;

        Vmax=0.0 ;

   While[tstep≤Tend2,
    Vmax=Max[Vtend[tstep],Vmax];
    tstep=tstep+ΔT;
    ];

   (* Print["Subscript[T, start]=",10^9 Tstart," ns","
Subscript[T, end2]=",10^9 Tend2," ns","  Subscript[T,
step]=", 10^9 Ttemp," ns"]; *)
   (* Print["Subscript[I, pulse]=", 10^6 Subscript[I,
pulse]," μA","   Subscript[Φ, a]=", Subscript[Φ, a],"
Subscript[Φ, dc]=", Subscript[Φ, dc],"   Subscript[V,
max][t]=",10^6 Vmax," μV"]; *)
   (* Print["Pulse start=",10^9 PulseStart," ns","   Pulse
width=",10^9 PulseWidth," ns"]; *)
   (* Print["δ1sol[Tend]=",δ1sol[Tend2],"
,δ2sol[Tend]=",δ2sol[Tend2]]; *)
   (* Print["v1sol[Tend]=",v1sol[Tend2],"
,v2sol[Tend]=",v2sol[Tend2]]; *)
          (* Print["a1sol[Tend]=",a1sol[Tend2],"
,a2sol[Tend]=",a2sol[Tend2]]; *)
   (* Print[" "]; *)
   (* Print[" "]; *)
```

```
    If[Vmax≤100.0 10^-6,

     Φtemp=Φtemp+ΔΦ,

     ΦTotal=Φtemp+ΦbiasΦaSin[ω Ttemp];
   Φs=Φtemp;
   Φcirc=(L_G I_0)/(2Φ0) (Sin[δ1sol[Ttemp]]-Sin[δ2sol[Ttemp]]);

   AppendTo[Φapplied,ΦaSin[ω Ttemp]];
   AppendTo[Φsignal,Φs];

     PulseStart=PulseStart+Tdstep;
     Ttemp=Ttemp+Tdstep;
     Φtemp=Φinitial;
     ];

    ];

     Φsignalmax=Max[Φsignal];
    Φsignalmin=Min[Φsignal];

    Φappliedmax=Max[Φapplied];
    Φappliedmin=Min[Φapplied];

  Φsignalamp=Abs[(    Φsignalmax-Φsignalmin)/2];
  Φappliedamp=Abs[(    Φappliedmax-Φappliedmin)/2];

  Φratio=Abs[   Φsignalamp/ Φappliedamp];

  AppendTo[Φmaxratio,Φratio];

  mmu=MaxMemoryUsed[];

  Print["Maximum Memory Used= ",mmu ," bytes","    ,Frequency=
",10^-9 f," GHz","    ,Φmaxratio= ",Φratio];
   AppendTo[frequencies,f];

   f=f+Δf;

   ];
```
Maximum Memory Used= 40073720 bytes ,Frequency= 0.25 GHz ,Φmaxratio= 0.913884
Maximum Memory Used= 40073720 bytes ,Frequency= 0.5 GHz ,Φmaxratio= 0.913884
NDSolve::ndsz: At \[NoBreak]t\[NoBreak] == \[NoBreak]1.037037037036358`*^-9\[NoBreak], step size is effectively zero; singularity or stiff system suspected. ≫

InterpolatingFunction::dmval: Input value \[NoBreak]{1.038×10^-9}\[NoBreak] lies outside the range of data in the interpolating function. Extrapolation will be used. ≫
InterpolatingFunction::dmval: Input value \[NoBreak]{1.038×10^-9}\[NoBreak] lies outside the range of data in the interpolating function. Extrapolation will be used. ≫
InterpolatingFunction::dmval: Input value \[NoBreak]{1.039×10^-9}\[NoBreak] lies outside the range of data in the interpolating function. Extrapolation will be used. ≫
General::stop: Further output of \[NoBreak]InterpolatingFunction::dmval\[NoBreak] will be suppressed during this calculation. ≫
Maximum Memory Used= 40073720 bytes ,Frequency= 0.75 GHz ,Φmaxratio= 0.913884
Maximum Memory Used= 40073720 bytes ,Frequency= 1. GHz ,Φmaxratio= 0.913884
Maximum Memory Used= 40073720 bytes ,Frequency= 1.25 GHz ,Φmaxratio= 0.812341
Maximum Memory Used= 40073720 bytes ,Frequency= 1.5 GHz ,Φmaxratio= 0.710799
Maximum Memory Used= 40073720 bytes ,Frequency= 1.75 GHz ,Φmaxratio= 0.558485
Maximum Memory Used= 40073720 bytes ,Frequency= 2. GHz ,Φmaxratio= 0.507713
Maximum Memory Used= 40073720 bytes ,Frequency= 2.25 GHz ,Φmaxratio= 0.456942
Maximum Memory Used= 40073720 bytes ,Frequency= 2.5 GHz ,Φmaxratio= 0.456942
Maximum Memory Used= 40073720 bytes ,Frequency= 2.75 GHz ,Φmaxratio= 0.456942
Maximum Memory Used= 40073720 bytes ,Frequency= 3. GHz ,Φmaxratio= 0.507713
Maximum Memory Used= 40073720 bytes ,Frequency= 3.25 GHz ,Φmaxratio= 0.456942
Maximum Memory Used= 40073720 bytes ,Frequency= 3.5 GHz ,Φmaxratio= 0.406171
Maximum Memory Used= 40073720 bytes ,Frequency= 3.75 GHz ,Φmaxratio= 0.456942
Maximum Memory Used= 40073720 bytes ,Frequency= 4. GHz ,Φmaxratio= 0.406171
Maximum Memory Used= 40073720 bytes ,Frequency= 4.25 GHz ,Φmaxratio= 0.507713
Maximum Memory Used= 40073720 bytes ,Frequency= 4.5 GHz ,Φmaxratio= 0.456942
$Aborted

frequencies
Φmaxratio

n=Length[Φmaxratio];

m=Length[frequencies];

ΦmaxversusF=Table[{frequencies⟦i\[RightDoubleBracket]/10^9,Φmaxratio⟦i\[RightDoub

leBracket]},{i,1,n}];
plt1=ListPlot[ΦmaxversusF,Joined→True,PlotRange→All,PlotStyle→{Thickness[0.004`],
Hue[1.`],PointSize[0.012`]},BaseStyle→{FontFamily→"Times",FontSize→18},Frame→Tr
ue,FrameLabel→{"frequency (GHz)","Φmeasured/Φsignal"}]
{2.5×10^8,5.×10^8,7.5×10^8,1.×10^9,1.25×10^9,1.5×10^9,1.75×10^9,2.×10^9,2.25×10^9,2.5×10^9,2.7
5×10^9,3.×10^9,3.25×10^9,3.5×10^9,3.75×10^9,4.×10^9,4.25×10^9,4.5×10^9,4.75×10^9,5.×10^9}
{0.913884,0.913884,0.913884,0.913884,0.812341,0.710799,0.660027,0.558485,0.55848
5,0.507713,0.507713,0.507713,0.456942,0.456942,0.507713,0.456942,0.507713,0.45694
2,0.507713,0.456942}

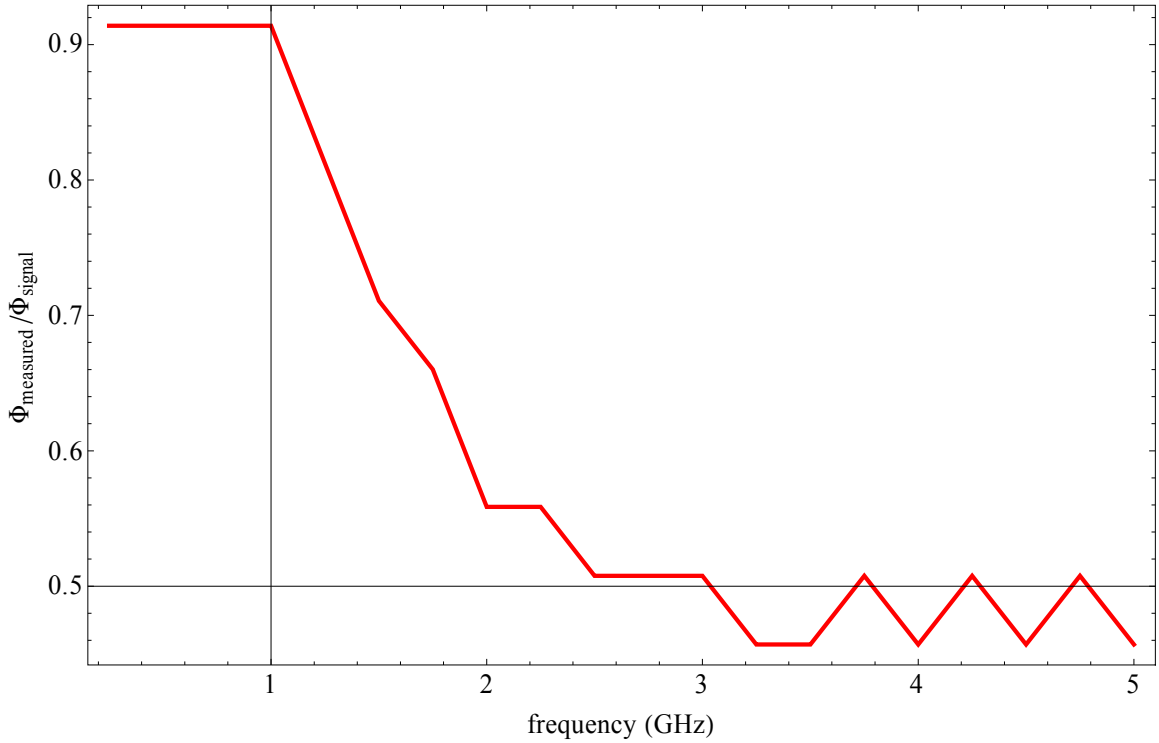

(n=Length[Φmaxratio];) (m=Length[frequencies];)

(ΦmaxversusF=Table[{frequencies⟦i\[RightDoubleBracket]/10^9,Φmaxratio⟦i\[RightDou

bleBracket]},{i,1,m}];)
(plt1=ListPlot[Φmaxversus F,Joined→True,PlotRange→All,PlotStyle→{Thickness[0.004`],
Hue[1.`],PointSize[0.012`]},BaseStyle→{FontFamily→"Times",FontSize→18},Frame→Tr
ue,FrameLabel→{"frequency (GHz)","△Φ/\!\(*SubscriptBox[\(Φ\),
\(applied\)]\)"},Epilog→Text[FontForm[" ",{"Times-Roman-Italic",12}],{0.8` 10^{9}
period,0.055`}]])

frequencies
Φmaxratio
{2.5×10^{8},5.×10^{8},7.5×10^{8},1.×10^{9},1.25×10^{9},1.5×10^{9},1.75×10^{9},2.×10^{9},2.25×10^{9},2.5×10^{9},2.7
5×10^{9},3.×10^{9},3.25×10^{9},3.5×10^{9},3.75×10^{9},4.×10^{9},4.25×10^{9},4.5×10^{9},4.75×10^{9},5.×10^{9}}
{0.913884,0.913884,0.913884,0.913884,0.812341,0.710799,0.660027,0.558485,0.55848
5,0.507713,0.507713,0.507713,0.456942,0.456942,0.507713,0.456942,0.507713,0.45694
2,0.507713,0.456942}

Bibliography

Chapter 1

[1] U. Durig, D. W. Pohl and F. Rohmer, J. Appl. Phys. **59**, 3318 (1986).

[2] R. J. Gutman, J. M. Borrego, P. Chakrabarti and Ming-Shan Wang, IEEE MTT Digest, pp 281 (1987).

[3] W. Lukosz, "Imagery with Evanescent Waves," Workshop on Unconventional Imagery, (Bellingham, WA: SPIE), Sept., pp. 73 (1984).

[4] E. A. Ash and A. Husain, Proceedings of the Fifth European Microwave Conference, Sept. pp. 213 (1975).

[5] T. Wei, X. D. Xiang, W. G. Wallace-Freedman, P. G. Schultz, Appl. Phys. Lett. **68**, 3506 (1996).

[6] E. Abbe, Archiv. Mikroskopische Anat. **9**, 413 (1873).

[7] M. Born and E. Wolf, *Principles of Optics: Electromagnetic Theory of Propagation, Interference and Diffraction of Light*, 7th edition, Cambridge University Press, New York, NY, 1999, chapter VIII.

[8] E. H. Synge, Philos. Mag. **6**, 356 (1928).

[9] I. Amato, Science **276**, 5321 (1997).

[10] G. Binnig, H. Roher, Ch. Gerber, E. Weibel. Phys. Rev. Lett. **49**, 57 (1982).

[11] C. Bohms, F. Saurenbach, P. Taschner, C. Roths and E. Kubaler, J. Phys. D, **26**, 1801 (1993).

[12] F. Giessible, Science **267**, 68 (1995).

[13] U. Durig, D. W. Pohl, F. Rohner, J. Appl. Phys. **59**, 3318 (1986).

[14] E. Betzig and J. K. Trautman, Science **257**, 189 (1992).

[15] Y. Martin and H. K. Wickramasinghe, Appl. Phys. Lett. **50**, 1455 (1987).

[16] P. C. D. Hobbs, D. W. Abraham, and H. K. Wickramasinghe, Appl. Phys. Lett. **55**, 2357 (1989).

[17] J. I. Goldstein and H. Yakowitz, eds. "Practical Scanning Electron Microscopy", Plenum, New York, 47 (1975).

[18] J. C. Geiss, C. J. Lin, D. Rugar, and A. E. Bell, Appl. Phys. Lett. **49**, 419 (1986).

[19] E. Ruska, "Advances in Optical and Electron Microscopy", Vol. 1, eds. R. Baer and V. E. Cisslett, Academic Press, New York, 116 (1966).

[20] A. Tonomura, Rev. Mod. Phys. **59**, 639 (1987).

[21] H. J. Wood, F. G. Foster, and E. A. Wood, Phys. Rev. **82**, 119, (1951).

[22] P. Kasiraj, R. M. Shelby, J. S. Best, and D. E. Horne, IEEE Trans. Magn. **MAG-22**, 837 (1986).

[23] S. Bradbury, "Basic Measurement Techniques for Light Microscopy", Royal Microscopical Society Handbook No. 23. Oxford Scientific Publications, Oxford (1991).

[24] M. Hartmann, K. Hipler, D. Koelle, F. Kober, K. Bernhardt, T. Sermet, R. Gross, and R. P. Huebener, Z. Phys. B. (Condensed Matter) **75**, 423 (1989).

[25] H. Newman and J. Culbertson, Micro. Opt. Lett. **6**, 725 (1993).

[26] A. S. Hou, F. Ho, and D. M. Bloom, Electronics Letters **28**, 2302 (1992).

[27] C. Böhm, F. Saurenbach, P. Taschner, C. Roths, and E. Kubalek, J. Phys. D. **26**, 1801 (1993).

[28] G. P. Kochanski, Phys. Rev Lett. **62**, 2285 (1989).

[29] S. J. Stranick and P. S. Weiss, Rev. Sci. Instrum. **64**, 1232 (1993).

[30] S. J. Stranick and P. S. Weiss, Rev. Sci. Instrum. **65**, 918 (1994).

[31] B. Knoll, F. Keilmann, A. Kramer, and R. Guckenberger, Appl. Phys. Lett. **70**, 2667 (1997).

[32] C. P. Vlahacos, R. C. Black, S. M. Anlage, A. Amar, and F. C. Wellstood, Appl. Phys. Lett. **69**, 3272 (1996).

[33] S. Anlage, D. E. Steinhauer, C. P. Vlahacos, B. J. Feenstra, A. S. Thanawalla, Wensheng Hu, Sudeep Dutta, and F. C. Wellstood, IEEE Trans. Appl. Supercond. **9**, 4127 (1999).

[34] R. C. Black, F. C. Wellstood, E. Dantsker, A. H. Miklich, D. T. Nemeth, D. Koelle, F. Ludwig, and J. Clarke, Appl. Phys. Lett. **66**, 99 (1995).

[35] S. E. Schwarz and C. W. Turner, IEEE Trans. Microwave Theory Tech. **MTT-34**, 463 (1986).

[36] M. J. Yoo, T. A. Fulton, H. F. Hess, R. L. Willett, L. N. Dunkleberger, R. J. Chichester, L. N. Pfeiffer, and K. W. West, Science **276**, 579 (1997).

[37] B. A. Nechay, F. Ho. A. S. Hou, and D. M. Bloom, J. Vac. Sci. Technol. Mat/June, 1369 (1995).

[38] C. C. Williams, W. P. Hough, and S. A. Rishton, Appl. Phys. Lett. **55**, 203 (1989).

[39] R. Black and F. C. Welsstood, "Measurements of Magnetism and Magnetic Properties of Matter," in J. Clarke and A. I. Braginski (eds.), *The SQUID Handbook, Vol. II: Applications of SQUIDs and SQUID systems*, *Wiley-VCH Verlag GmbH & Co*., (KGaA, Weinheim, 2006), pp. 391-440.

[40] S. Chatraphorn, E. F. Fleet, F. C. Wellstood, L. A. Knauss, and T. M. Eiles, Appl. Phys. Lett. **76**, 2304 (2000).

[41] B. J. Roth, N. G. Sepulveda, and J. P. Wilkswo, Jr., "Using a magnetometer to image a two-dimensional current distribution," J. Appl. Phys. **65**, 361 (1989).

[42] R. C. Jaklevic, J. Lambe, A. H. Silver, and J. E. Mercereau, Phys. Rev. Lett. **12**, 159 (1964).

[43] R. C. Jaklevic, J. J. Lambe, A. H. Silver, and J. E. Mercereau, Phys. Rev. Lett. **12**, 274 (1964).

[44] R. C. Jaklevic, J. Lambe, J. E. Mercereau, and A. H. Silver, Phys. Rev. **140**, 1628 (1965).

[45] D. Koelle, R. Kleiner, F. Ludwig, E. Dantsker, and J. Clarke, Rev. Mod. Phys. **71**, 631 (1999).

[46] M. B. Ketchen, W. M. Goubau, J. Clarke, and G. B. Donaldson, J. Appl. Phys. **49**, 4111 (1978).

[47] J. Clarke and R. H. Koch, Science **242**, 217 (1988).

[48] J. Clarke, Science **184**, 1235 (1974).

[49] R. C. Black, Ph.D. thesis, University of Maryland, College Park, 1995.

[50] A. Mathai, Ph.D. thesis, University of Maryland, College Park, 1995.

[51] E. F. Fleet, S. Chatraphorn, F. C. Wellstood, L. A. Knauss, and S. M. Green, Rev. Sci. Instrum. **72**, 3281 (2001).

[52] A. P. Nielsen, Ph.D. thesis, University of Maryland, College Park, 2001.

[53] S.-Y. Lee, Ph.D. thesis, University of Maryland, College Park, 2004.

[54] F. Baudenbacher, L. E. Fong, J. R. Holzer, and M. Radparvar, Appl. Phys. Lett. **82**, 3487 (2003).

[55] R. H. Koch, J. R. Rozen, P. Woltgens, T. Picunko, W. J. Goss, D. Gambrel, and D. Lathrop, "High performance superconducting quantum interference device feedback electronics," Rev. Sci. Instrum. **67**, 2968 (1996).

[56] D. Drung, C. Aßmann, J. Beyer, M. Peters, F. Ruede, and Th. Schurig, "dc SQUID Readout Electronics With Up to 100 MHz Closed-Loop Bandwidth," IEEE Trans. App. Super., Vol. **15**, 777 (2005).

[57] D. Drung, C. Hinnrichs and H.-J. Barthelmess, "Low-noise ultra-high-speed dc SQUID readout electronics," Supercond. Sci. Technol. **19**, S235–S241 (2006).

[58] S.P. Kwon, Ph.D. thesis, University of Maryland, College Park, 2005.

[59] J. Matthews, C. P. Vlahacos, S. P. Kwon, and F. C. Wellstood, IEEE Trans. Appl. Super., **15**, 688 (2005).

[60] D. Drung and M. Mück, "SQUID Electronics," in J. Clarke, A. I. Braginski (Eds.), *The SQUID Handbook, Vol. I: Fundamentals and Technology of SQUIDs and SQUID systems*, *Wiley-VCH Verlag GmbH &Co*., (KGaA, Weunheim, 2004), pp. 127-170.

Chapter 2

[1] I. K. Kominis, T. W. Kornack, J. C. Alfred and M.V. Romalis, "A subfemtotesla multichannel atomic interferometer," Nature, **422**, 596 (2003).

[2] J. R. Kirtley, M. B. Ketchen, C. C. Tsuei, J. Z. Sun, W. J. Gallagher, Lock See Yu-Jahnes, A. Gupta, K. G. Stawiasz, S. J. Wind, "Design and applications of a scanning SQUID microscope," IBM J. Res. Develop. Vol. **39** No. 6, Nov. (1995).

[3] J. R. Kirtley and J. P. Wikswo, Jr., "Scanning SQUID Microscopy," Annu. Rev. Mater. Sci. **29**, 117-148 (1999).

[4] F. C. Wellstood, Y. Gim, A. Amar, R. C. Black, and A. Mathai, "Magnetic microscopy Using SQUIDS," IEEE Trans. Appl. Supercond., **7**, pp. 3134-3138 (1997).

[5] A. Mathai, D. Song, Y. Gim, and F. C. Wellstood, "One-dimensional magnetic flux microscope based on the dc SQUID," Appl. Phys. Lett. **61**, 585-600 (1992).

[6] A. Mathai, D. Song, Y. Gim, and F. C. Wellstood, "High-resolution magnetic microscopy using a dc SQUID," IEEE Trans. Appl. Supercond. **3**, 2609-2612 (1993).

[7] R. C. Black, A. Mathai, and F. C. Wellstood, "Magnetic microscopy using a liquid nitrogen cooled YBCO SQUID," Appl. Phys. Lett. **62**, 2128-2130 (1993).

[8] E. F. Fleet, S. Chatraphorn, and F. C. Wellstood *et. al*., "HTS scanning SQUID microscope cooled by a closed-cycle refrigerator," IEEE Trans Appl. Supercond. **9**, 3704-3707 (1999).

[9] J. Vrba, K. Betts, M. B. Burbank, T. Cheung, A. A. Fife, G. Haid, P. R. Kubik, S. Lee, J. McCubbin, J. McKay, D. McKenzie, P. Spear, B. Taylor, M. Tillotson, D. Cheyne, H. Wienberg, "Whole cortex, 64 channel SQUID biomagnetic system," IEEE Trans. Appl. Super. **3**, 1878-1882 (1993).

[10] K. E. T. Knuutila, A. I. Ahonen, M. S. Hamalainen, M. J. Kajola, P. P. Laine, O. V. Lounasmaa, L. T. Parkkonen, J. T. A. Simola, and C. D. Tesche, "A 122-channel whole cortex SQUID system for measuring the brain's magnetic fields," IEEE Trans. Mag. **29**, 3315-3320 (1993).

[11] G. B. Donaldson, "The use of SQUIDs for Nondestructive Evaluation (NDE)," in H. Weinstock (ed.), *Squid Sensors, Fundamentals, Fabrication and Applications*, NATO ASI series E, (Kluwer, Dordrecht, 1996), Vol. **329**, pp. 599-628.

[12] D. Li, Y. P. Ya, W. F. Flanagan, B. D. Lichter, and J. P. Wilskwo, " Detection of hidden corrosion of aircraft aluminum alloys by magnetometry using a SQUID," Corrision **52**, 219 (1997).

[13] H. Koinuma and I. Takeuchi, "Combinatorial solid-state chemistry of inorganic materials," Nature Mater. **3**, 429 (2004).

[14] H. J. Krause and G. Donaldson, "Nondestructive Evaluation of Materials and Structures using SQUIDs," in J. Clarke, A. I. Braginski (eds.), *The SQUID Handbook, Vol. II: Applications of SQUIDs and SQUID systems*, *Wiley-VCH Verlag GmbH &Co*., (KGaA, Weinheim, 2006), pp. 441-479.

[15] B. L. T. Plourde, D. J. Van Harlingen, R. Besseling et al., "Vortex dynamics in thin superconducting strips observed by scanning SQUID microscopy," Physica C 341-348, 1023-1026 (2000).

[16] C. C. Tsuei, J. R. Kirtley, C. C. Chi, et al., "Pairing symmetry and flux quantization in a tri-crystal superconducting ring of $YBa_2Cu_3O_7$," Phys. Rev. Lett. **73**, 593 (1994).

[17] A. Mathai, Y. Gim, R. C. Black, et al., " Experimental proof of a time-reversal-invariant order parameter with π shift in $YBa_2Cu_3O_7$," Phys. Rev. Lett. **74**, 4523 (1995).

[18] S. Hsiung, K. V. Tan, A. J. Komrowski, D. J. D. Sullivan, J. Gaudestad, A. Orozco, E. Talanova, L.A. Knauss, "Failure Analysis on Resistive Opens with Scanning SQUID Microscopy," *42nd Annual International Reliability Physics Symposium*, Phoenix, (2004).

[19] J.O. Gaudestad, S.I. Woods, A. Orozco, L.A. Knauss, "Advances in magnetic microscopy for stacked-die and package-level fault isolation," Solid State Technology, December (2004).

[20] L. A. Knauss, A. Orozco, S. I. Woods, A. B. Cawthorne, "Advances in scanning SQUID microscopy for die-level and package-level fault isolation," Microelectronics Reliability, **43**, 1657-1662 (2003).

[21] Z. H. Mai, M. Palaniappan, J. M. Chin, C. E. Soh, L. A. Knauss, and E. F. Fleet, "Short failure analysis under fault isolation," *Proceedings of the 8-th IPFA*, Singapore, (2001).

[22] S. Chatraphom, E. F. Fleet, F. C. Wellstood, L. A. Knauss, and T. M. Eiles, "Scanning SQUID microscopy of integrated circuits," Appl. Phys. Lett. vol. 76, pp. 2304-2306 (2000).

[23] S. I. Woods, N. M. Lettsome, A. B. Cawthorne *et al*., "High-resolution current imaging by direct magnetic field sensing," *Proc. 29th Int. Symp. For Testing and Failure Analysis*, ASM International, Materials Park, OH, pp. 6-13 (2003).

[24] Magma C20/C30, Neocera, Inc. 10000 Virginia Manor Road, Beltsville, Maryland 20705, USA.

[25] Originally calculated as a doubling every year, Moore later refined the estimate to a period of two years.[25]. It is often incorrectly quoted as a doubling of transistors every 18 months, which David House, an Intel executive, gave that period to the increase in chip performance. The actual period is approximately 20 months.

[26] G. E. Moore, “Cramming more components onto integrated circuits”, Electronics, 38(8), April 19, 1965.

[27] G. E. Moore, “Progress in Digital Electronics,” Technical Digest, International Electron Devices Meeting, IEEE, 1975, pp. 11-13.

[28] http://download.intel.com/museum/Moores_Law/VideoTranscripts/Excepts_A_Conversation_with_Gordon_Moore.pdf

[29] Kanellos, Michael (10 February 2003). "Moore's law to roll on for another decade". cnet.

[30] C. Hawkins, and J. Soden, “Defect classes – An overdue paradigm for CMOS IC testing,” *Inter. Test Conf. (ITC)*, pp. 413-424, Oct. (1994).

[31] J. M. Soden, R. E. Anderson, C. L. Henderson, “IC Failure Analysis: Magic, Mystery, and Science,” IEEE Design & Test of Computers, July-September, (1997).

[32] J. Soden, J. Segura and C. F. Hawkins, “Electronics and failure analysis,” in *Microelectronics Failure Analysis Desk Reference*, 5th edition, (ASM International, Material Parks, Ohio 2004) pp. 90-110.

[33] R. Rodriguez-Montanes, J. Segura, V. Champac, J. Figueras, and A. Rubio, “Current vs. logic testing of gate oxide short, floating gate, and Bridging failures in CMOS,” Inter. Test Conf *(ITC)*, pp. 510-519, Oct. (1991).

[34] D. Vallet and J. Soden, “Finding fault with deep-submicron ICs,” IEEE Spectrum, Oct., **40** (1997).

[35] D. P. Vallett, “Failure analysis requirements for nanoelectronics,” IEEE Trans. on Nanoelec., **1**, 117 (2002).

[36] M. Pacheco, Z. Wang, L. Skoglund, Y. Liu, A. Medina, A. Raman, R. Dias, D. Goyal, S. Ramanathan, “Advanced fault isolation and failure analysis techniques for future package technologies,” Intel Technology Journal, **9**, 337 (2005).

[37] Jaume Segura and Charles F. Hawkins, *CMOS Electronics: How it works, How it fails*, (John Wiley & Sons, Inc., 2004).

[38] E. I. Cole Jr., P. Tangyunyong, and D. L. Barton, “Backside localization of open and shorted IC interconnections,” in Annu. Proc. – Reliability Physics Symp., 1998, pp. 129-136.

[39] K. Nikawa, T. Saiki, S. Inoune, and M. Ohtsu, “High spatial resolution OBIRCH and OBIC effects realized by near-field optical probe in the analysis of high

resistance 200 nm wide TiSi," *Proc. 24th Int. Symp. Testing and Failure Analysis*, 1998, pp. 25-29.

[40] D. Vallett, "Why Waste Time on Roadmaps When We Don't Have Cars," IEEE Trans. Dev. and Mater. Reliability, **7**(1) March, 2007.

[41] Z. Gemmill, L. Durbha, S. Jacobson, G. Gao, K. Weaver, "SEM and FIB Passive Voltage Contrast," in *Microelectronics Failure Analysis Desk Reference*, 5th edition, (ASM International, Material Parks, Ohio 2004) pp. 431-437.

[42] J. C. Tsang, J. A. Kash, and D. Vallett, " Time-Resolved Optical Characterization of Electrical Activity in Integrated Circuits," Proc. IEEE., **88**(9), Sept. 2000.

Chapter 3

[1] H.K. Onnes, "The resistance of pure mercury at helium temperatures". Commun. Phys. Lab. Univ. Leiden **12**, 120 (1911).

[2] W. Meissner and R. Ochsenfeld, "Ein neuer Effekt bei Eintritt der Supraleitfähigkeit". Naturwissenschaften **21** (44), 787–788 (1933).

[3] J. Bardeen, L. N. Cooper, and J. R. Schrieffer, "Microscopic theory of superconductivity," Phys. Rev. **106** (1), 162-164 (1957).

[4] J. Bardeen, L. N. Cooper, and J. R. Schrieffer, "Theory of superconductivity," Phys. Rev. **108** (5), 1175-1204 (1957).

[5] L. N. Cooper, "Bound electron pairs in a degenerate Fermi gas," Phys. Rev. **104**, (4) 1189-1190 (1956).

[6] R. E. Glover and M. Tinkham, Phys. Rev. **104**, 243 (1957).

[7] M. Tinkham, *Introduction to Superconductivity, 2nd ed.*, (Dover Publications Inc., Mineola, NY. 1996).

[8] V. L. Ginzburg and L. D. Landau,"On the theory of superconductivity," Zh. Eskp. Teor. Fiz. **20**, 1064-1068 (1950), (in Russian).

[9] L. P. Gor'kov, "Microscopic derivation of the Ginzburg-Landau equations in the theory of superconductivity," Sov. Phys.-JETP, **9**, 1364-1367 (1959).

[10] A. A. Abrikosov, L. P. Gor'kov, and I. E. Dzyaloshinski, *Methods of Quantum Field Theory in Statistical Physics*, (Dover Publications Inc., Mineola, NY. 1963).

[11] B. S. Deaver and W. M. Fairbank, "Experimental evidence for quantized flux in superconducting cylinders," Phys. Rev Lett. **7**, 43-46, (1961).

[12] R. Doll and M. Nabauer, "Experimental proof of magnetic flux quantization in a superconducting ring," Phys. Rev. Lett. **7**, 51-52, (1961).

[13] M. Tinkham, *Introduction to Superconductivity, 2nd ed.*, (Dover Publications Inc., Mineola, NY. 1996), Chapter 6, pp. 196-247.

[14] B. D. Josephson, "Possible new effects in superconductive tunneling," Phys. Lett., **1** (7), 251-253 (1962).

[15] P. W. Anderson, J. Rowell, "Probable observation of the Josephson superconducting tunneling effect," Phys. Rev. Lett. **10**, 230-232 (1963).

[16] R. P. Feynman and M. Sands, *The Feynman Lectures in Physics*, Vol. III, Reading , Massachusetts: Addison-Wesley, 1965, pp. 21-14.

[17] D. E. McCumber, "Effect of ac impedance on dc voltage-current characteristics of superconductor weak-link junctions," J. Appl. Phys. **39**, 3113-3118 (1968).

[18] W. C. Stewart, "Current-voltage characteristics of Josephson Junctions," Appl. Phys. Lett. **12**, 277-280 (1968).

[19] T. Van Duzer, C. W. Turner, *Principles of Superconductive Devices and Circuits,* 2nd ed., (*Prentice Hall PTR*, Upper Saddle River, NJ, 1999).

[20] Alan M. Kadin, *Introduction to Superconducting Circuits*, (John Wiley & Sons, Inc., New York, 1999).

[21] A. C. Rose-Innes and E. H. Rhoderick, *Introduction to Superconductity, 2ed.*, (Pergamon Press, Oxford, England, 1978).

[22] Terry P. Orlando and Kevin A. Delin, *Foundations of Applied Superconductivity*, (Addison-Wesley, Reading, Mass., 1991).

[23] Jaklevic, R.C., Lambe, J., Silver, A.H. and Mercereau, J.E. "Quantum interference effects in Josephson tunneling," Phys. Rev. Lett. **12**, 159-160 (1964).

[24] Zimmerman, J.E and Silver, A.H. "Macroscopic quantum interference effects through superconducting point contacts," Phys. Rev. **141**, 367-375 (1966).

[25] A. H. Silver, J. E. Zimmerman, "Quantum states and transitions in weakly connected superconducting rings," Phys. Rev. **157**, 317-341 (1967).

[26] J. Clarke, SQUID Fundamentals, H. Weinstock (ed.) *SQUID Sensors:Fundamentals, Fabrication and Applications*, (Kluwer Academic Publishers, Netherlands, 1996), pp. 1-62.

[27] R. Kleiner, D. Koelle, F. Ludwig, J. Clarke, "Superconducting Quantum Interference Devices: State of the Art and Applications," Proceedings of the IEEE*,* **92**(10), 1534 (2004).

[28] J. Clarke, A. I. Braginski (Eds.), *The SQUID Handbook, Vol. I: Fundamentals and Technology of SQUIDs and SQUID systems*, *Wiley-VCH Verlag GmbH & Co*., (KGaA, Weunheim, 2004).

[29] J. Clarke, A. I. Braginski (Eds.), *The SQUID Handbook, Vol. II: Applications of SQUIDs and SQUID systems*, *Wiley-VCH Verlag GmbH &Co*., (KGaA, Weinheim, 2006).

[30] R. L. Fagaly, "Superconducting quantum interference device instruments and applications," Rev. Sci. Instu. **77**, 101101-1 (2006).

[31] C. D. Tesche and J. Clarke, "dc SQUID:Noise and Optimization," J. Low Temp. Phys. **29**, 301 (1977).

[32] Hypres, Inc. "Niobium Integrated Circuit Fabrication: Design Rules", Revision #24, Jan. 11, 2008.

Chapter 4

[1] D. Koelle, R. Kleiner, F. Ludwig, E. Dantsker, and J. Clarke, Rev. Mod. Phys. **71**, 631 (1999).

[2] F. Baudenbacher, L. E. Fong, J. R. Holzer, and M. Radparvar, Appl. Phys. Lett. **82**, 3487 (2003).

[3] A. H. Miklich, D. Koelle, E. Dantsker, D. T. Nemeth, J. J. Kingston, R. F. Kromann, and J. Clarke, IEEE Trans. Appl. Supercond. **3**, 2434 (1993).

[4] J. M. Jaycox and M. B. Ketchen, IEEE Trans. Magn. **17**, 400 (1981).

[5] M. B. Ketchen and J. M. Jaycox, Appl. Phys. Lett. **40**, 736-738.

[6] D. E. McCumber, J. Appl. Phys. **39**, 3113-3118 (1968).

[7] W. C. Stewart*, Appl. Phys. Lett*. **12**, 277-280 (1968).

[8] P. Horowitz and W. Hill, *The Art of Electronics*, 2nd ed. (Cambridge University Press, Cambridge, Mass. 1989), Chap. 7, pg. 432.

[9] H. Nyquist, Phys. Rev. **32**, 110 (1928).

[10] J. Clarke, A. I. Braginski (Eds.), *The SQUID Handbook, Vol. I: Fundamentals and Technology of SQUIDs and SQUID systems*, *Wiley-VCH Verlag GmbH &Co*., (KGaA, Weunheim, 2004), Eq. 2.22, pg. 39.

[11] B. D. Joseph son, Phys. Lett. **1**, 251-253 (1962), Adv. Phys. **14**, 419-451 (1965).

[12] J. Clarke and R. H. Koch, Science **242**, 217 (1988).

[13] K. K. Likharev and Semenov, V. K. JETP Lett. **15**, 442-445, (1972).

[14] A. N. Vystavkin, V. N. Gubankov, L. S. Kuzmin, K. K. Likharev, V. V. Migulin, and V. K. Semenov, Phys. Rev. Appl. **9**, 79-109, (1974).

[15] M. Tinkham, *Introduction to Superconductivity* 2nd. ed. (McGraw-Hill, New York, 1996), Chap. 6, p. 225-229.

[16] V. J. de Waal, P. Schrijner, and R. Llurba, J. Low Temp. Phys. **54**, 215 (1984).

[17] C. D. Tesche and J. Clarke, J. Low Temp. Phys. **29**, 301 (1977).

[18] J. P. Bruines, V. J. de Waal, and J. E. Mooij, J. Low Temp. Phys. **46**, 383 (1982).

[19] Hypres, *HYPRES Niobium Integrated Circuit Fabrication – Design Rules* rev. 019 (Elmsford NY, 2003).

[20] J. Clarke, A. I. Braginski (Eds.), *The SQUID Handbook, Vol. I: Fundamentals and Technology of SQUIDs and SQUID systems*, *Wiley-VCH Verlag GmbH &Co*., (KGaA, Weunheim, 2004), Table A.1.1, pg. 361.

[21] D. Brandshaft and M. Stegall, *ICED – Graphics Editor for IC Design* (IC Editors Inc., Santa Clara, 1990

Chapter 5

[1] J. Clarke, "SQUID concepts and systems," in *NATO ASI series, superconducting electronics* (H. Weinstock and M. Nisenoff, eds.), (Berlin), p.11, Springer, 1989.

[2] R. H. Koch, J. R. Rozen, P. Woltgens, T. Picunko, W. J. Goss, D. Gambrel, and D. Lathrop, "High performance superconducting quantum interference device feedback electronics," *Rev. Sci. Instrum*. **67**, 2968 (1996).

[3] J. Clarke, *SQUID Fundamentals*, H. Weinstock (ed.), *SQUID Sensors: Fundamentals, Fabrication and Applications*, (Kluwer Academic Publishers, Netherlands, 1996), pp. 1-62.

[4] R. C. Black, Ph.D. thesis, University of Maryland, College Park, 1995.

[5] D. Drung, "Advanced SQUID Read-Out Electronics," in H. Weinstock (ed. *Squid Sensors, Fundamentals, Fabrication and Applications*, NATO ASI series E, (Kluwer, Dordrecht, 1996), pp. 63-116.

[6] D. Drung and M. Mück, "SQUID Electronics," in J. Clarke, A. I. Braginski (Eds.), *The SQUID Handbook, Vol. I: Fundamentals and Technology of SQUIDs and SQUID systems*, *Wiley-VCH Verlag GmbH &Co*., (KGaA, Weunheim, 2004), pp. 127-170.

[7] P. Horowitz and W. Hill, The Art of Electronics, 2nd ed. (Cambridge University Press, Cambridge, Mass. 1989), Chap. 11, pp. 775-776.

[8] K. B. Cooper, M. Steffen, R. McDermott, R. W. Simmonds, S. Oh, D. A. Hite, D. P. Pappas, and J. M. Martinis, "Observation of quantum oscillation between a Josephson phase qubit and a microscopic resonator using a fast readout," Phys. Rev. Lett. **93**, 180401-1 (2004).

[9] T. A. Palomaki, S. K. Dutta, R. M. Lewis, H. Paik, K. Mitra, B. K. Cooper, A. J. Przybysz, A. J. Dragt, J. R. Anderson, C. J. Lobb, and F. C. Wellstood, "Pulse current measurements and Rabi oscillations in a dc SQUID phase qubit," IEEE Trans. Appl. Supercond. **17**, 162 (2007).

[10] J. Matthews, C. P. Vlahacos, S. P. Kwon, and F. C. Wellstood, IEEE Trans. Appl. Super., **15**, 688 (2005).

Chapter 6

[1] R. C. Black, Ph.D. thesis, University of Maryland, College Park, 1995.

[2] S. Chatraphorn, Ph.D. thesis, University of Maryland, College Park, 2000.

[3] C. Wang and P. E. Gifford, "Performance study on a two-stage 4 K pulse tube cooler, Advances in Cryogenic Engineering," Vol. **45B** (2000).

[4] C. Wang and P. E. Gifford, "Performance characteristics of a 4 K pulse tube in current applications," Cryocoolers, **11**, 205 (2001).

[5] C. Wang and P. E. Gifford, "Development of 4 K pulse tube cryorefrigerators at Cryomech," Advances in Cryogenic Engineering, Vol. **47**, 641 (2002).

[6] Cryomech, Inc., 113 Falso Drive, Syracuse, New York 13211 USA, http://www.cryomech.com/CRYOREFRIGERATORS/PT405.htm.

[7] W. E. Gifford and R. C. Longsworth, Adv. Cryo. Eng. **3B**, 69 (1963).

[8] R. Radabaugh, Adv. Cryo. Eng. **35B**, 1191 (1990).

[9] Sapphire window, optical grade, orientation (0001), dia. 5 mm +0/-0.1 mm, thickness 25 micron, both sides optically polished, surface quality: 60/40 (S/D) Princeton Scientific Corp., P.O. Box 143, Princeton, NJ. 08542, www.princetonscientific.com

[10] EP30FL epoxy, Master Bond Inc., 154 Hobart Street, Hackensack, NJ 07601 USA.

[11] KL-5 Vacuum Leak sealant, Kurt J. Lesker Company, PO Box 10, 1925 Route 51, Clairton, PA 15025-3681 http://www.lesker.com/newweb/fluids/sealants_leaksealant_kjlc.cfm?pgid=kl5.

[12] Hypres, Inc. "Hypres Niobium Integrated Circuit Fabrication - Design Rules", Revision #19, (Elmsford, NY, 2003).

[13] STYCAST 2850FT, Emerson & Cuming, 46 Manning Road, Billerica, MA 01821.

[14] Sapphire Engineering, 53 Portside Drive, Pocasset, MA 02559.

[15] Puratronic from Alfa Aesar, 30 Bond Street, Ward Hill, MA 01835.

[16] Pobell, Frank, *Matter and Methods at Low temperatures*, 2nd ed. (Springer Verlag, New York, USA 1995), Chap. 3, pp. 61.

[17] CS Hyde Company, High temperature and high performance threads data sheet for Kevlar thread (size 207), http://www.cshyde.com/Threadspec.htm.

[18] G. Ventura, M. Barucci, E. Got ardi, I. Peroni, Cryogenics, **40**, 489 (2000).

[19] L. Risegari, M. Barucci, E. Olivieri, E. Pasca, G. Ventura, World Scientific Proc. ICATPP 8th, (2003).

[20] White, G. K. and Meeson, P., *Experimental Techniques in Low-Temperature Physics*, 3rd edition, (Oxford University Press, USA 2001).

[21] 850G Series, Newport Corporation, Irvine, CA.

[22] Newport, *ESP6000 PC-Based High-Performance Motion Controller – User's Manual* (Irvine, 2000).

[23] ESP6000DCIB, Newport Corporation, Irvine, CA.

[24] LabVIEW ver. 6.0.1, National Instruments Corporation, 11500 Mopac Expressway, Austin, TX 78759-3504.

[25] Model 5840B amplifier, Picosecond Pulse Labs, 2500 55th Street, Boulder, Co. 80301, USA.

[26] Model CX-1010-SD, Lake Shore Cryotronics, Inc., 575 McCorkle Boulevard, Westerville, OH 43082, www.lakeshore.com.

[27] Model LTC-21 Temperature Controller, Neocera, 10000 Virginia Manor Road, Suite 300, Beltville, MD 20705-4215, USA.

[28] KJLC 979 ATV gauge and KPDR900 controller, Kurt J. Lesker Company, PO Box 10, 1925 Route 51, Clairton, PA 15025-3681.

[29] Cryomech PT405 Cryogenic Refrigerator – Installation, operation and routine maintenance manual, revised 4/22/2005, URL:http://www.cryomech.com/CRYOREFRIGERATORS/Model%20PT405%20Manual.pdf.

Chapter 7

[1] Micro-Coax, *Semi-Rigid Coaxial Cable* (Pottstown PA, 2003), UT-034-SS.

[2] Huber+Suhner, *Suhner Coaxial Connectors General Catalogue* (Herisau Switzerland, 2001).

[3] Stanford Research Systems, *MODEL DG535 Digital Delay / Pulse Generator* rev. 2.6 (Sunnyvale CA, 2000).

[4] Model 5840B amplifier, Picosecond Pulse Labs, 2500 55th Street, Boulder, Co. 80301, USA.

[5] Agilent 53132A Universal Counter, Agilent Technologies, Palo Alto, CA.

[6] J. Matthews, C. P. Vlahacos, S. P. Kwon, and F. C. Wellstood, IEEE Trans Appl. Supercond. **15**, 688 (2005).

[7] S.P. Kwon, Ph.D. thesis, University of Maryland, College Park, 2005.

Chapter 8

[1] S. Ramo, J. R. Whinnery, and T. van Duzer, *Fields and Waves in Communication Electronics*, John Wiley & Sons, Inc., New York, 1994.

[2] D. Pozar, *Microwave Engineering*, 3rd edition, John Wiley and Sons, Inc. New York, 2005, chapter 2.

[3] R. E. Collin, Foundations for Microwave Engineering, 2nd edition, McGraw-Hill, Inc. New York, 1992, pp. 125-164.

[4] I. J. Bahl and D. K. Trivedi, "A Designer's Guide to Microstrip Line," Microwaves, May 1977, pp. 174-182.

[5] K. C. Gupta, R. Garg, and I. J. Bahl, *Microstrip Lines and Striplines*, Artech House, Dedham, Mass., 1979.

[6] J. D. Jackson, Classical Electrodynamics, 3rd edition, John Wiley and Sons, Inc. New York, 1999, pg. 247, equation (6.56).

Chapter 9

[1] D. Drung and M. Mück, "SQUID Electronics," in J. Clarke, A. I. Braginski (Eds.), *The SQUID Handbook, Vol. I: Fundamentals and Technology of SQUIDs and SQUID systems*, *Wiley-VCH Verlag GmbH &Co*., (KGaA, Weunheim, 2004), pp. 127-170.

[2] Microstock, Inc. Semi-Rigid Coaxial Cable, UT-85-C. http://www.micro-coax.com/pages/products/ProductTypes/CableTypes/Semi-RigidCoaxial/Semi-RigidDetails.asp?ID=UT-085C

[3] K. C. Gupta, R. Garg, and I. J. Bahl, *Microstrip Lines and Striplines*, Artech House, Dedham, Mass., 1979.

[4] S. Chatraphorn, E. F. Fleet, and F. C. Wellstood, IEEE. Trans. Appl. Supercond. **9**, 4381 (1999).

[5] S. Chatraphorn, Ph.D. thesis, University of Maryland, College Park, 2000.

[6] FEKO suite version 5.4, EM Software & Systems, 2003-2008.
URL: http://www.feko.info or http://www.emss.co.za/

[7] Davidson, D.B.; Theron, I.P.; Jakobus, U.; Landstorfer, F.M.; Meyer, F.J.C.; Mostert, J.; Van Tonder, J.J. (September 1998), "Recent progress on the antenna simulation program FEKO", *Proceedings of the 1998 South African Symposium on Communications and Signal Processing*, pp. 427-430

[8] Jakobus, U.; Van Tonder, J.J. (2005), "Fast Multipole Solution of Metallic and Dielectric Scattering Problems in FEKO", *21st Annual Review of Progress in Applied Computational Electromagnetics*, Applied Computational Electromagnetics Society (ACES)

[9] Jakobus, U.; Van Tonder, J.J. (2005), "Fast Multipole Acceleration of a MoM Code for the Solution of Composed Metallic/Dielectric Scattering Problems", *Advances in Radio Science 3*, Copernicus GmbH, pp. 189-194

[10] Jakobus, U.; Van Tonder, J.J. (2006), "Challenges Regarding the Commercial Implementation of the Parallel MLFMM in FEKO", *IEEE Antennas and Propagation Society International Symposium 2006*, IEEE, pp. 95-98

[11] Jakobus, U.; Theron, I.P. (2003), "Analysis of Coated Metallic Surfaces with Physical Optics for the Solution of High-Frequency EMC Problems", *15th International Zurich Symposium on Electromagnetic Compatibility*, pp. 257-261

[12] D. B. Davidson, *Computational Electromagnetic for RF and Microwave Engineering*. Cambridge University Press, Cambridge, UK, 2005.

[13] R. F. Harrington, *Time-Harmonic Electromagnetic Fields*. New York: McGraw Hill 1961.

[14] T. Itoh, *Numerical Techniques for Microwave and Millimeter-Wave Passive Structures*, John Wiley & Sons, Inc., New York, 1989, chapters 2-4.

Chapter 10

[1] W. C. Stewart, “Current-voltage characteristics of Josephson Junctions,” *Appl. Phys. Lett*. **12**, 277-280 (1968).

[2] *Mathematica*, Version 6.0, Wolfram Research, Inc., Champaign, Illinois, 2007.

[3] A. C. Hindmarsh, "ODEpack, a systematized collection of ODE solvers". In *Scientific Computing*, R. S. Stepleman *et al*. eds., North-Holland, Amsterdam, 1983, 55-64.

[4] L. R. Petzold, SIAM J. Sci. Stat. Comput. **4**, 136-148 (1983).

[5] C. W. Gear and O. Osterby, ACM Trans. Math Soft. **10**, 23-44 (1984).

[6] C. D. Tesche, "Noise and Optimization of the dc SQUID," Thesis, University of California Berkeley, Lawrence Berkeley laboratory, LBL-8510, 1978, section III.

[7] J. Matthews, C. P. Vlahacos, S. P. Kwon, and F. C. Wellstood, IEEE Trans Appl. Super. 15, 688 (2005).

[8] S. M. Faris, Appl. Phys. Lett. **36**, 1005 (1980).

[9] D. B. Tuckerman, Appl. Phys. Lett. **36**, 1008 (1980).

[10] O. A. Mukhanov, V. K. Semenov, and K. K. Likharev, IEEE Trans. Magn. **23**, 759 (1987).

[11] O. A. Mukhanov, S. Sarwana, D. Gupta, A. F. Kirichenko, and S. V. Rylov, Physica C **368**, 196 (2002).

[12] M. Kenyon, Ph.D. thesis, University of Maryland, College Park, 2001.